Three-dimensional hydrodynamic simulations of deep convection in massive stars

Andréa Cristini

PhD in Astrophysics

December 2017

Keele University

Abstract

Convection plays a key role in the evolution of massive stars. Despite many decades of work on this topic, the treatment of convection (convective boundary mixing in particular) is still one of the major uncertainties in stellar evolution modelling. Fortunately computing power has reached a level that enables detailed three-dimensional hydrodynamic simulations, these can provide valuable insights into the processes and phenomena that occur during stellar convection. The aim of this thesis is to explore the physics responsible for convective boundary mixing within the deep interiors of massive stars, through the calculation of stellar evolution and three-dimensional hydrodynamic models. The latter focus on carbon shell burning and are the first of their kind within the stellar hydrodynamic community.

To prepare the input models as well as study the evolution of convective boundaries, a $15\,\mathrm{M}_{\odot}$ stellar model was computed and a parameter study was undertaken on the convective regions of this model. The carbon shell was chosen as an input model for three-dimensional simulations. Two sets of simulations were calculated with the aim of conducting a resolution study and luminosity study. The simulations were analysed using the Reynolds-averaged Navier-Stokes (RANS) framework and within the context of the entrainment law.

The following is a summary of the key findings. The lower convective boundary was found to be 'stiffer' (according to the bulk Richardson number) than the upper boundary. The boundaries are shown to have a significant width which is likely formed through Kelvin-Helmholtz instabilities, the width of the lower boundary is much narrower than the upper. The shape of the boundaries (interpreted through the composition) is smooth and sigmoid-like, whereas in the one-dimensional models it is sharp and discontinuous. Finally, these simulations confirm the scaling of the bulk Richardson number with both the entrainment rate and the driving luminosity.

Acknowledgements

All of my collaborators - Raphael Hirschi (RH), Casey Meakin (CM), David Arnett (DA), Cyril Georgy (CG), Maxime Viallet (MV) and Ian Walkington (IW) - have contributed to the preparation and interpretation of the data contained in this thesis. In addition, they and also Clare Carson (CC) have provided many corrections and comments which have improved the thesis to its current state. CC has also edited a number of figures and tables in this thesis, these are: Figs. 1.2, 5.2, 5.4 and 5.17 and Table 5.3.

The work presented in chapter 4 is based on the published (and peer-reviewed) conference proceedings from Cristini et al. (2016*b*). This work was completed by myself but would not have been possible without the help and guidance from my collaborators.

Chapter 5 is an extension of the work recently accepted for publication in MNRAS (Cristini et al., 2016*a*), most of this work was carried out by myself (again with the necessary help and guidance from my collaborators). Credit for some parts of this chapter go to my collaborators though: CM produced Fig. 5.1, and ran the lrez, mrez and hrez models; RH ran the vhrez model, and all Kippenhahn diagrams were created from adapted versions of his scripts; DA wrote the majority of the content on the temporal constraint of turbulence in §5.1.3; CG ran the $15\,M_{\odot}$ stellar model; and IW produced Fig. 5.4.

The work presented in chapter 6 is not published but this chapter will form the core of a subsequent paper. IW provided the script from which Fig. 6.5 was produced. All of the models and content of chapter 6 were produced by myself, but the relevant interpretation and conclusions made from the data would not have been possible without the help of my collaborators.

My thanks go to the following people for having an influence (although not always a positive one!) on my PhD. Firstly, I'd like to thank my supervisor, Raphael Hirschi, for his continued support, encouragement and guidance (both academic and personal) during my four years at Keele. Secondly, I'd like to thank my girlfriend for her relentless care and support during my PhD, through both the celebratory and the hard times. She has undoubtedly kept me sane during the PhD. Without her none of this would have been possible, including this refined thesis, for which she helped in improving every word and detail. I'd like to thank my dad, sister, Dee, Liam, Aunty Angie and all other members of my family, who have provided loving support throughout my PhD and especially during the tougher times. Particularly, I'd like to thank my Nanny whom I loved very much and sadly lost during my PhD, I dedicate this thesis to her memory. Unusual thanks goes to my best friend and faithful companion, Togo, who although can't understand these words, has helped me through his overwhelming love and company in the office. Thanks also goes to the guys at Primordial radio (formerly Team Rock radio), in particular Moose, Dews, Jrock and Pete, who provided me with hours of uplifting and new music as well as hilarious banter. I'd like to thank all of my fellow PhD students who I have shared beers with and also many inspiring scientific and humorous conversations. I also owe my thanks to my friends for the many beers and laughs that have helped me to unwind after a hard day in the office, namely: Aaron, Chris, Joe, Tay and many others.

Contents

List of Figures

List of Tables

Chapter 1

Introduction

Massive stars have a large impact on the dynamics and composition of the universe, throughout all stages of their life cycle. Their radiation represents a significant fraction of the radiation emitted from their host galaxy, and ionises the gas that surrounds them, forming H II (ionised hydrogen) regions (Wood and Churchwell, 1989).

The internal temperature and neutron density during certain phases of massive star evolution are high enough for the synthesis of weak s-process isotopes[1] (e.g. Langer, Arcoragi and Arnould, 1989; Käppeler et al., 2011).

At the end of the star's life the majority of the interior matter (including s-process isotopes) is expelled into the inter-stellar medium (ISM) through a dramatic core-collapse supernova (CC-SN) explosion. Such events are also responsible for the formation of primordial dust grains, providing that they survive the reverse shockwave (Todini and Ferrara, 2001), and are considered a candidate for the site[2] of r-process nucleosynthesis (Nishimura et al., 2012; Winteler et al., 2012), where large neutron fluxes are required to produce the heaviest elements. The feedback of energy (both kinetic and thermal) from SN events to the surrounding ISM is thought to have a significant impact on galaxy formation (e.g. Simpson et al., 2015). Stellar winds also affect galaxy structure and composition through the deposition of kinetic energy and nucleosynthesis products (e.g. Garay and Lizano, 1999).

Massive stars leave behind neutron stars or black holes depending on the final

[1] These are isotopes of the heavy elements in the mass range $60 \lesssim A \lesssim 90$ (e.g. Pignatari et al., 2010).

[2] A more favoured astrophysical site for r-process nucleosynthesis is neutron star mergers (Wanajo et al., 2014).

mass of the heavy element core (e.g. Woosley, Heger and Weaver, 2002). In addition, massive stars are an astrophysical laboratory where physical processes at such high temperatures and densities can be studied. Similar studies are possible terrestrially but only in small volumes, for example in NIF[3] (Kuranz et al., 2011) and z-pinch device[4] (Miernik et al., 2013) experiments.

1.1 The life and death of a massive star

Massive stars are generally defined as those with an initial mass large enough such that they will go through all of the burning stages to form an iron core, which will eventually collapse. According to Woosley, Heger and Weaver (2002); Heger et al. (2003) and Jones et al. (2013) the lower mass threshold is around $8\,\mathrm{M}_{\odot}$. These mass limits are determined from 1D stellar evolution calculations, and so the inclusion of new convective boundary mixing prescriptions could affect these limits.

1.1.1 Early stages

Consider a significantly massive gas cloud, due to its self-gravity the gas (assumed to be perfect) is gravitationally accelerated towards the centre but is balanced by the pressure gradient between the centre and surface of the star. This mechanical equilibrium is referred to as hydrostatic equilibrium, and the star is in such a state for most of its life. If the gas pressure is not large enough to balance the gravitational forces, the star will contract, reducing the gravitational potential energy and increasing the internal energy (as the internal pressure and temperature increase).

Upon reaching temperatures of around $10^7\,\mathrm{K}$ hydrogen fusion is possible predominantly through the CNO cycle[5]. Each cycle produces an alpha particle (He) and around $4{\times}10^{-5}\,\mathrm{erg}$ of energy (from 6 different reactions during each cycle) in the form

[3]The National Ignition Facility at the Lawrence Livermore National Laboratory in California is the world's largest and most energetic laser facility. Ongoing experiments are conducted in the attempt to achieve inertial confinement fusion.

[4]A z-pinch device uses strong magnets to induce a current in the conductive plasma, which when appropriately aligned can compress the plasma through the Lorentz force. The largest generator that can undertake such experiments is the 'Z-machine' located at Sandia National Laboratory, New Mexico.

[5]Energy is also produced through the p-p chain but is only around 5% of the energy produced from the CNO cycle at a temperature of $2 \times 10^7\,\mathrm{K}$ (see Fig. 18.8 of Kippenhahn, Weigert and Weiss 2013).

of photons. These photons travel towards the surface of the star through collisions with the surrounding matter and in doing so exert a radiative pressure. This increase in local pressure prevents the star from collapsing further. Hydrogen fusion eventually ceases in the core once all of the hydrogen fuel has been depleted. The reduction in the nuclear energy generation rate removes the energy source and the pressure is no longer great enough to prevent the star from contracting (due to its self-gravity). The gas contracts and its temperature and density increase. Once temperatures of around 10^8 K are reached the fusion of helium into carbon is possible, through the triple-α process, producing around 2×10^{-5} erg per three helium nuclei and restoring the pressure balance. Carbon nuclei can capture alpha particles to produce oxygen[6] and this provides a similar amount of energy to helium fusion. These alpha captures are possible once a sufficient amount of carbon has been produced. Once helium is exhausted the carbon- and oxygen-rich core will contract again.

1.1.2 Advanced phases

Following the end of helium burning, if the carbon-oxygen rich core is below around $1\,M_\odot$, the temperatures reached are not high enough in the core for carbon nuclei to fuse. These stars instead lose their envelope (at the end of their life via a stellar wind) leaving a carbon-oxygen white dwarf (CO-WD) remnant. For stars with initial masses between around $8\,M_\odot$ and $10\,M_\odot$ competition between carbon burning (under degenerate conditions) and mass loss due to thermal pulses in the helium burning shell will determine the final evolutionary state of the star. For stars with initial masses[7] around $9\,M_\odot$ (Siess and Pumo, 2006; Jones et al., 2013), once core contraction begins due to carbon exhaustion, the presence of a temperature inversion in the core, allows a Ne/O flame[8] to develop, which propagates towards the centre of the star. The contraction of the core occurs faster than the flame propagation, and once densities are reached sufficient for electron captures on ^{24}Mg and ^{20}Ne, these stars then explode

[6]Oxygen nuclei can also capture alpha particles to produce neon, but the production is low in comparison.

[7]Some studies suggest this ignition mass is closer to $7\,M_\odot$ (Jones, 2014).

[8]In this sense, a flame is defined as the ignition of nuclear fusion at an off-centre position. The heating of the surrounding material mainly through convective heat transport then helps to push this flame front further towards the centre of the star.

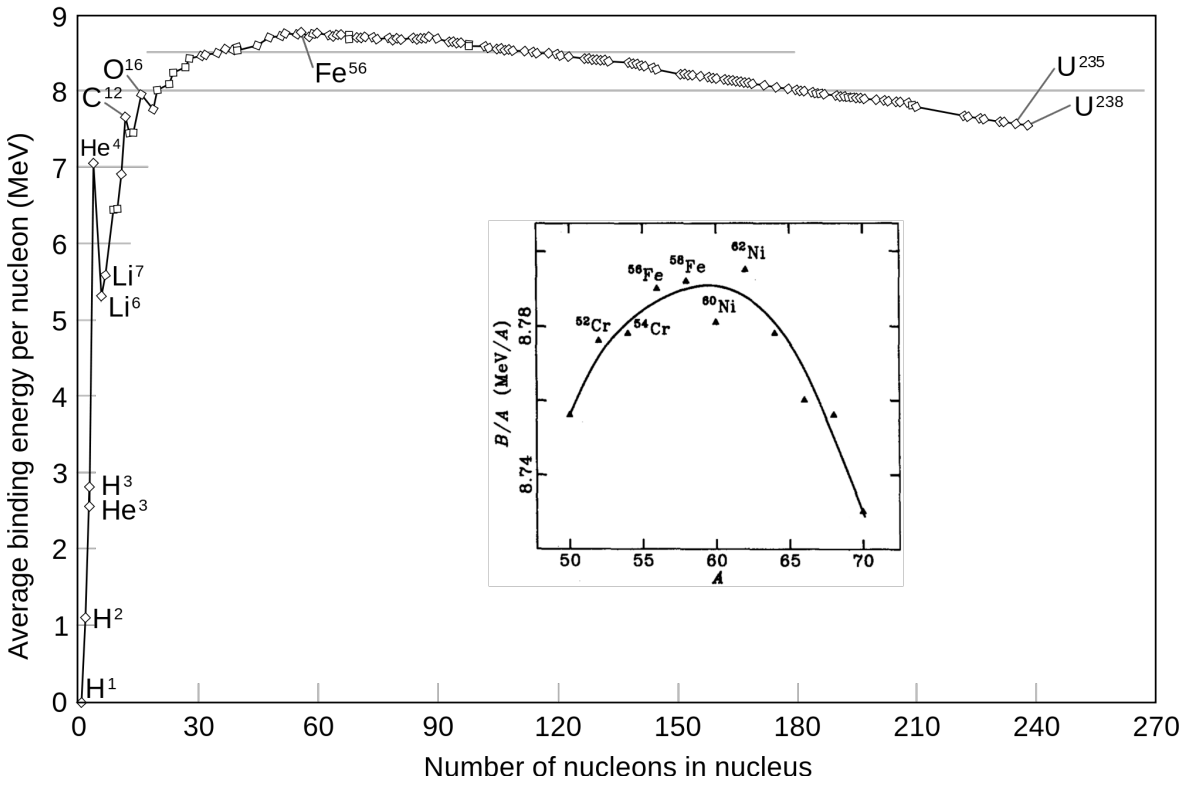

Figure 1.1: Average binding energy per nucleon as a function of the atomic mass number. Common isotopes are noted, including ^{56}Fe which has the lowest mass per nucleon. Despite many textbooks stating that ^{56}Fe is the isotope with the highest binding energy per nucleon, it is actually ^{62}Ni. This is shown by the inset which shows the binding energy per nucleon of the iron-group elements. Alpha captures during silicon burning cease at ^{62}Ni, but much more ^{56}Ni is produced (not shown), which later decays to ^{56}Fe. *Credit:* Wikimedia Commons; inset adapted from Fig. 2 in Fewell 1995.

Phase	Hydrogen	Helium	Carbon	Neon	Oxygen	Silicon
Lifetime (yrs)	1.1×10^7	2.0×10^6	2.0×10^3	0.7	2.6	0.05

Table 1.1: Approximate lifetimes (in years) of the various nuclear burning phases within a $15\,M_\odot$ star. Adapted from Woosley and Janka (2005).

through an electron-capture supernova (EC-SN).

For stars within this mass range (8-10 $M_\odot$) which have ignited carbon in the core but do not have densities great enough to permit electron captures, their now oxygen-neon rich core becomes completely degenerate, and the star ends as an oxygen-neon white dwarf (ONe-WD). Stars greater than around $10\,M_\odot$ can ignite carbon non-degenerately, where carbon burning continues until the carbon fuel is depleted. Stellar models show that the exact value of this mass limit is sensitive to the input physics used (e.g. convective boundary mixing, and rotation).

For carbon burning and beyond, photons emitted from nuclear burning still provide a radiative component to the pressure but the high temperatures and densities lead to significant neutrino emissions from the plasma. These neutrinos do not contribute to the pressure balance as their mean free path is larger than the radius of the star and so directly remove energy from the star, this accelerates the evolution during the advanced burning stages compared to the earlier hydrogen and helium burning phases (Arnett, 1996). The approximate lifetimes of each burning phase for a $15\,M_\odot$ star are shown in Table 1.1, here it can be seen that there is an acceleration in lifetime for the more advanced phases.

Following the depletion of the carbon fuel, heating of the core continues to temperatures above 10^9 K. At this temperature the photons are so energetic that neon is photodissociated into oxygen, the energy lost from this endothermic reaction is compensated for by the capture of alpha particles onto neon creating magnesium. The net result is a production of around 7×10^{-6} erg (from the reaction $^{20}\mathrm{Ne}(\alpha,\gamma)^{24}\mathrm{Mg}$) per two neon nuclei (the photodissociation of one Ne nucleus provides the alpha particle for fusion with the second). Further heating to temperatures of 1.5×10^9 K results in the fusion of oxygen into mainly silicon, producing around 1.25×10^{-5} erg per oxygen

nucleus. Once oxygen has depleted in the core, and the temperature rises to 3×10^9 K, many nuclei are photodisintegrated. This allows alpha particles to be captured by silicon and heavier elements producing many iron group elements. Further fusion beyond the iron group is not possible (without an input of energy) as the production of heavier isotopes would result in a decreased binding energy per nucleon (see Fig. 1.1). With no further fusion possible in the core, a pressure imbalance exists once again and the star begins to contract.

1.1.3 Final fate

As mentioned earlier, the fate of low mass massive stars ($8\,M_\odot$ - $10\,M_\odot$) is either to cool into a WD or explode through an EC-SN.

For massive stars with initial masses greater than around $10\,M_\odot$, the exhaustion of the silicon fuel leads to temperatures in the core beyond 10^{10} K. Large densities in the core facilitate electron captures, reducing the Chandrasekhar mass[9] (Chandrasekhar, 1931), M_{ch}, of the core. Once M_{ch} becomes smaller than the mass of the core, electron degeneracy pressure can no longer support the weight of the star and collapse ensues on an almost free-fall time-scale ($\sim$40 ms; Kippenhahn, Weigert and Weiss 2013). The stellar remnant following the core-collapse will be either a neutron star (NS) or black hole (BH).

Ergma and van den Heuvel (1998) argue based on observations of high mass X-ray binary systems[10] that for progenitor masses between $8\,M_\odot$ and $20\,M_\odot$, a NS remnant will most likely form. Whereas for progenitor masses greater than $50\,M_\odot$ a BH remnant will most likely form, and for intermediate masses the remnant could be either. A similar uncertainty in the NS and BH progenitor masses is demonstrated in Fig. 1.2, adapted from Woosley, Heger and Weaver (2002), whereby the final (pre-supernova) and remnant masses cannot be accurately determined (not shown in this plot) due to the uncertainties surrounding the mass loss rates for stars of initial masses $\gtrsim 30\,M_\odot$.

[9]The theoretical mass limit of a core supported by the degeneracy pressure of relativistic electrons, beyond which the core will collapse. For a mean molecular weight (see also Eq. 2.1.2) per electron of 2 (generally relevant for hydrogen free gas), the Chandrasekhar mass is $1.44\,M_\odot$ (Chandrasekhar, 1967).

[10]These consist of a massive star with a NS or BH companion. Mass lost from the massive star is accreted onto the compact object in the form of a disc. Friction in this accretion disc heats up the material to energies relevant for X-ray emission.

O'Connor and Ott (2011) show that BHs likely form without a SN explosion for a compactness parameter, $\xi_{2.5} \gtrsim 0.45$, where the compactness is defined as the ratio of mass to radius (inside a mass of $2.5\,\mathrm{M}_{\odot}$) at the time when the core 'bounces', once nuclear densities of $\rho \sim 10^{14}\,\mathrm{g\,cm^{-3}}$ are reached. Using this definition for BH formation, from four sets of stellar models at solar metallicity, they find that the percentage of BHs formed assuming a Salpeter (Salpeter, 1955) initial mass function over the initial mass range of $8 \leq \mathrm{M/M}_{\odot} \leq 120$ range from 0% to 7%. Ertl et al. (2016) define two parameters that help in determining the explodability of massive stars. The first, M_4, is the mass inside the dimensionless entropy per nucleon of $s = 4$ (normalised by a solar mass), the second, μ_4 is the spatial derivative of the mass at this point. They find that a higher value of M_4 in association with a lower value of μ_4 favours explosions and NS remnants. While, BH formation is generally associated with local minima and maxima in M_4 and μ_4, respectively.

1.2 Convection in massive stars

Convection is expected to occur in stars as the necessary ingredients for convective heat transport are present: a gravitational field; a fluid (mostly plasma); and a heat source (nuclear fusion or material with a high radiative opacity). The gravitational field allows relatively less dense material to become buoyant (through Archimedes' principle; see §2.1.1 for more details). As this material is a fluid it can be continually displaced with large velocities. The heat source provides the local increase/decrease in temperature/density.

Convection therefore occurs in the deep interiors and envelopes of massive stars (see e.g. Fig. 1.3), and is a major transport process of kinetic energy throughout these regions of the star. The extent of convection within stellar evolution models is approximated by the Schwarzschild or Ledoux criteria (see §2.1.1). The local fluid velocity associated with convective instability is usually obtained through the assumption of adibaticity in the deep interior or the use of the mixing length theory[11] near the surface (see §2.1.2).

[11]Alternative theories do exist, such as the full spectrum of turbulence pioneered by Canuto and Mazzitelli (1991); Canuto, Goldman and Mazzitelli (1996).

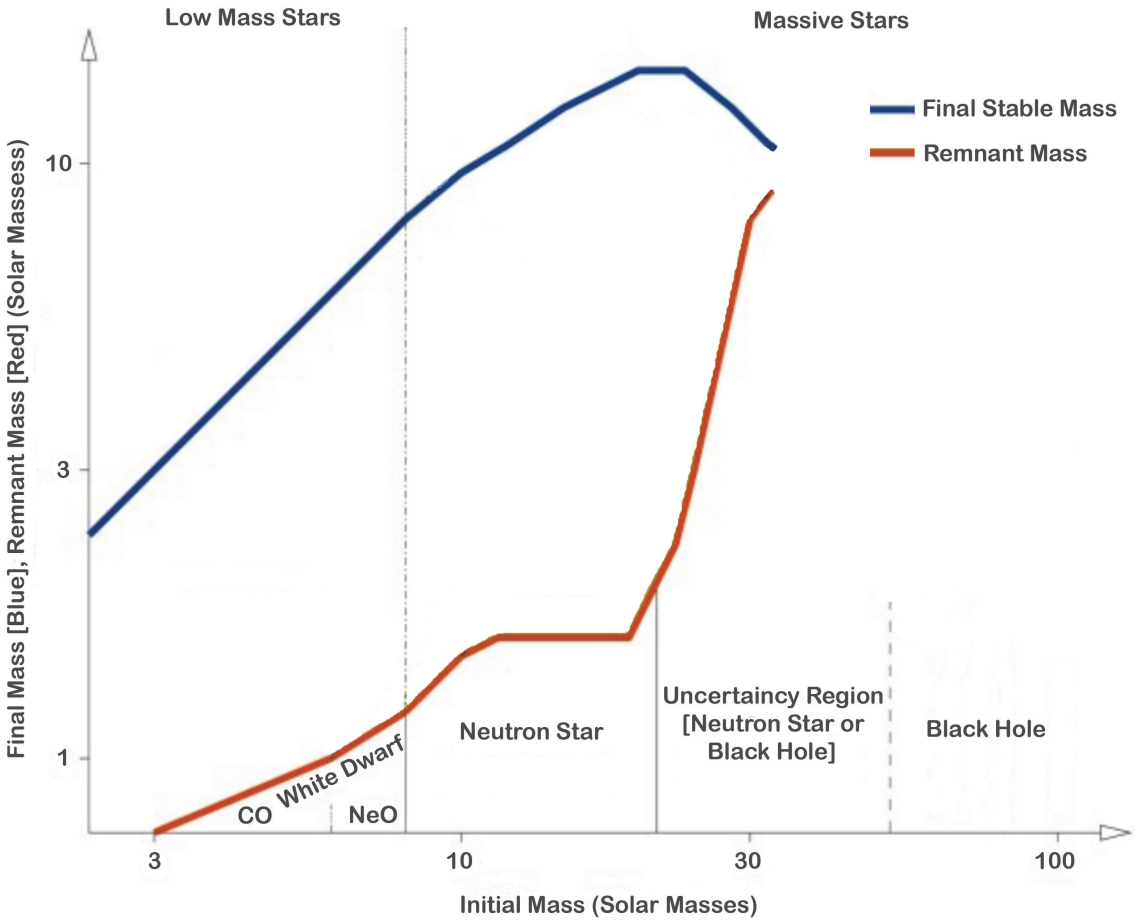

Figure 1.2: Initial mass function of non-rotating, solar metallicity, single stars. The horizontal axis shows the initial mass in solar masses on a logarithmic scale. The vertical axis denotes the final (blue) and remnant (red) masses in solar masses. The final mass is the mass of the star before it becomes unstable, either through mass loss during the planetary nebula phase for low-mass stars, or through core-collapse for massive stars. The remnant mass is the mass left behind following this dynamical event, the type of remnant is annotated along the horizontal axis for various initial masses. Final and remnant masses beyond initial masses $\sim 30\,\mathrm{M}_{\odot}$ are not shown due to the uncertainty in mass loss rates for these stars. Figure adapted from Woosley, Heger and Weaver (2002).

The time-scale for the transport of heat and composition by convection can be compared to other time-scales relevant for stellar evolution and stellar structure. The following time-scales were estimated for a $15\,M_{\odot}$ star on the zero-age main sequence (ZAMS). Turbulent convection mixes composition over dynamical time-scales ($\sim 10^3$ s), whereas diffusive processes such as radiative transport occur over longer thermal time-scales ($\sim 10^5$ yrs) and the production of new nuclei (through fusion) generally occurs over even longer evolutionary time-scales ($\sim 10^8$ yrs). Therefore, in most cases the composition over the convective region can be considered homogeneous, however at the boundary between a convective and stable region, mixing of material can lead to inhomogeneities in composition.

1.2.1 Driving processes

There are two main driving processes for convection in stars; convection driven by the absorption and scattering of radiation (or opacity) which occurs in the envelope (sub-surface convection) and convection driven by nuclear fusion which occurs in the deep interior.

Opacity driven convection

Photons that are produced in the deep interior travel to the surface of the star. Below the photosphere[12], the opacity of the material is much higher due to the lower local temperature of the gas and the subsequent recombination (the capturing of electrons by nuclei) of hydrogen, helium and iron as well as other metals (e.g. Phillips, 1999). The re-ionisation of these metals by high energy photons leads to a substantial increase in heat and the production of a thermal boundary layer near the photosphere. Colder material above the photosphere, sinks towards the thermal boundary layer in thin down-drafts and breaks up due to turbulent instabilities. This sinking fluid is replaced by hot rising fluid which 'condenses' and cools at the surface. The overall result is the turning over of matter in the form of convective instability which eventually extends over several orders of magnitude in density below the photosphere ($\sim$4 for a $5\,M_{\odot}$ star, for example; Viallet et al. 2013). An example of a convectively unstable region driven by

[12]A surface above which matter is transparent to radiation.

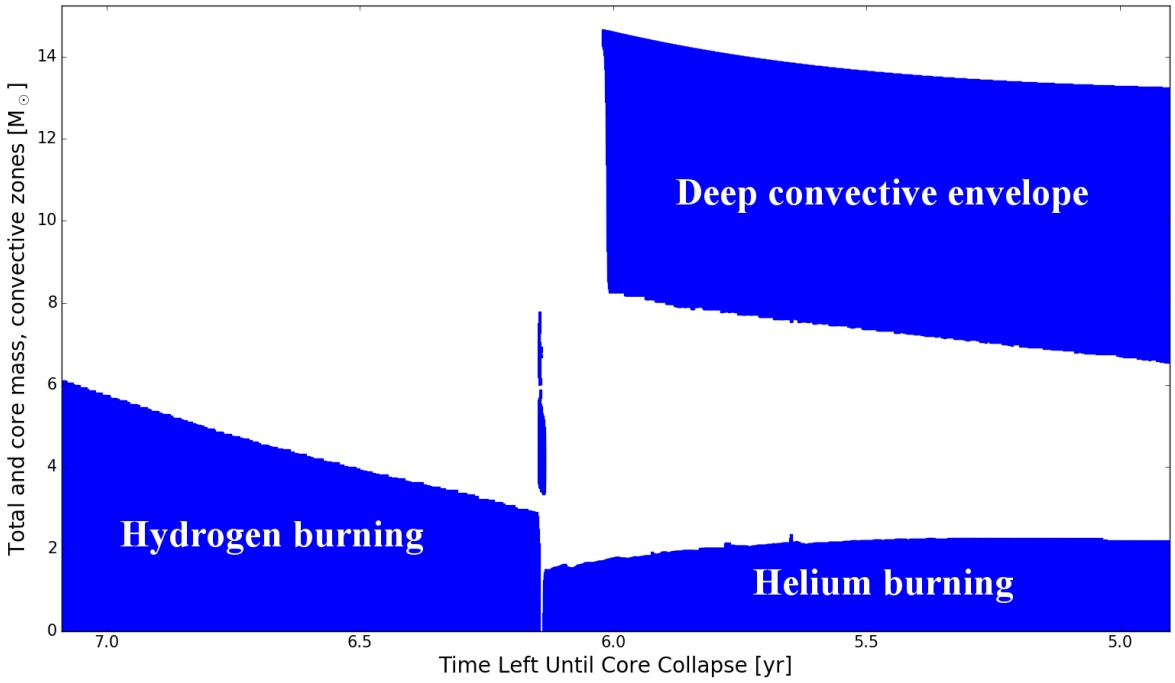

Figure 1.3: Convective structure evolution (Kippenhahn diagram) of a $15\,M_\odot$ solar metallicity, non-rotating, single star model. The vertical axis shows the mass in solar masses. The horizontal axis shows the estimated time left until collapse in years, on a logarithmic scale. Blue regions indicate convective instability. The initial convective region which extends out to $6\,M_\odot$ is the hydrogen burning core, an example of fusion driven convection. The later convective region which initially extends between 8 and $14.5\,M_\odot$ is the deep convective envelope which develops during core helium burning, and is an example of opacity driven convection. The reduction in mass of the outer boundary is a result of mass loss from the surface of the star.

opacity is shown in Fig. 1.3, extending initially in mass between 8 and $14.5\,M_\odot$. Here, the envelope of the star has become convectively unstable via the process described above.

Fusion driven convection

Nuclear fusion is generally localised due to the strong temperature dependencies (e.g. temperature to the power of the order 20 for the CNO cycle; Kippenhahn, Weigert and Weiss 2013) of the energy generation rate and also the availability of the nuclei fuel. The radiation or conduction of the energy produced from fusion throughout the plasma is much less efficient than convection due to the diffusive nature of these mechanisms[13]. Convection is very efficient due to the large stratification in density over the convective region, and heat is therefore advected almost adiabatically over the unstable region. The material at higher temperatures (locally) becomes buoyant, rises and overturns

[13]Diffusive mechanisms transport matter slowly over gradients in concentration, whereas, convection is predominantly advective which transports matter via the bulk motion of the fluid.

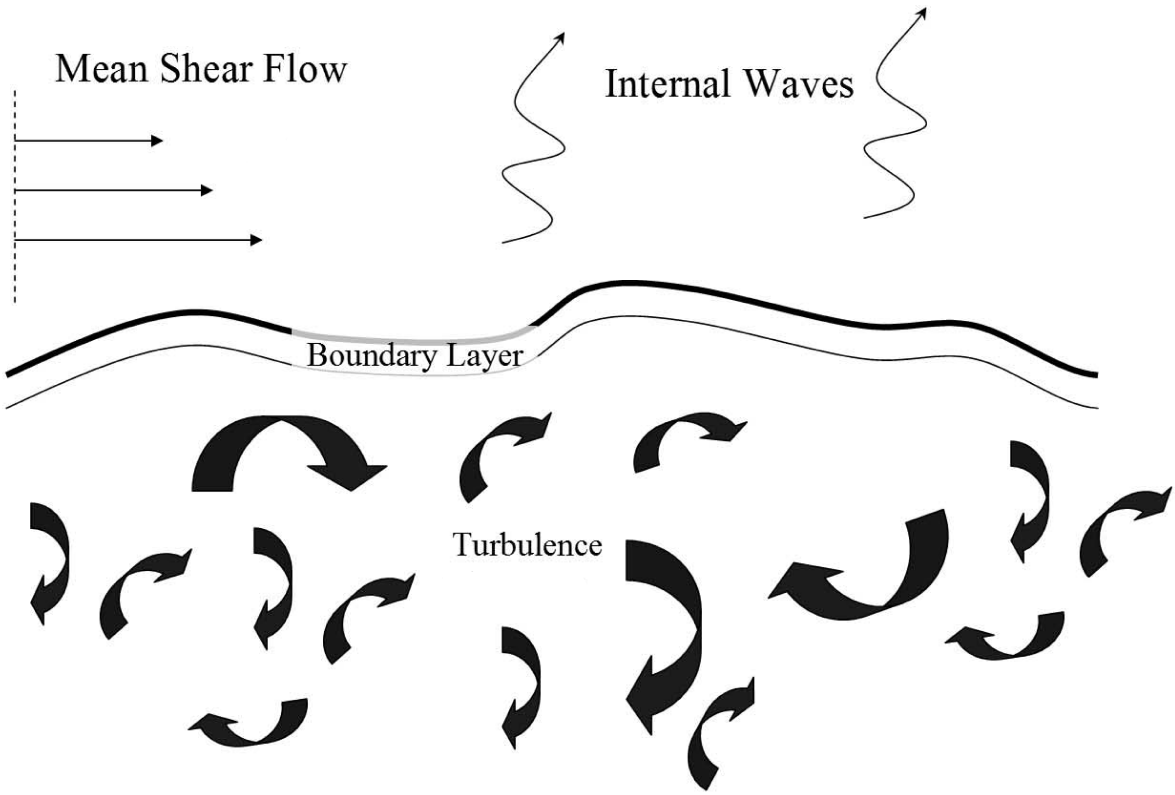

Figure 1.4: Illustration of a convective boundary layer, separating a turbulent region below and a stably stratified region above. Other features include internal gravity waves generated by turbulent motions below the boundary layer, and a mean shear flow that may develop between the turbulent and stable regions due to the over-turning of fluid elements near the boundary. Figure adapted from Meakin and Arnett (2007*b*).

as it is decelerated near the convective-radiative boundary, this material then cools and sinks back towards the temperature peak (e.g. Arnett et al., 2015; Cristini et al., 2016*a*). Convective velocities are large and the flow becomes turbulent, typically, the Mach number varies from 10^{-4} to 10^{-1} (see Fig. 4.5). These features of buoyant material rising and overturning are depicted in Fig. 1.4, where a turbulent region is separated from a stably stratified region by a boundary layer; the overturning of fluid elements may generate shear at the boundary. This figure also illustrates how turbulent elements which impact the boundary region can generate gravity mode waves which propagate through the stable region above (see also Figs. 5.8 and 5.12). An example of fusion driven convection is shown in Fig. 1.3, where a high flux of energy during core hydrogen burning leads to the development of a convectively unstable region which initially extends in mass out to $6\,\mathrm{M}_{\odot}$. Fusion driven convection also occurs during helium, carbon, oxygen and silicon burning (see Fig. 4.1). Convection is also driven by photodissociation during neon burning.

1.2.2 Compositional mixing

Turbulent convection mixes the composition over dynamical time-scales due to the large convective velocities, therefore, for most of the burning stages, the distribution of nuclear species (including those newly created from fusion) can be considered homogeneous, due to the much longer nuclear time-scales over which they are created or destroyed[14] (e.g. Kippenhahn, Weigert and Weiss, 2013).

The homogeneity of the composition within the convective region, can lead to sharp spatial gradients in composition at the boundary between the convective and stable regions, due to the lack of mixing within the stable regions. These gradients can even become discontinuous. The development of such sharp gradients can be seen in the composition profiles of Fig. 1.5. This figure shows the abundance in mass fractions (as a function of the interior mass of the star) for a $15\,M_\odot$ model. The model is part way through carbon shell burning, where the core is composed of mostly neon and oxygen and is radiative. Given that the time-scale for mixing (dynamical) is much shorter than the time-scale for nuclear processes (evolutionary) the assumption of homogeneity (instantaneous mixing) is valid. Such an assumption, however, leads to sharp discontinuities in the abundance profiles ($\sim 1.9\,M_\odot$), which may not be physically representative of the star (see §5.2.5).

A relative increase in convective boundary mixing above the core will lead to an increased core mass, which will extend the lifetime of the burning phase. Also, the ashes of previous nuclear burning phases can be mixed into the convective envelope and advected to the surface of the star. Frischknecht et al. (2010) show this effect in models of 9, 12 and $15\,M_\odot$ stars through a combination of turbulent convection and rotationally induced mixing.

[14]The time-scale of the most advanced burning stages can become comparable to the dynamical time-scale.

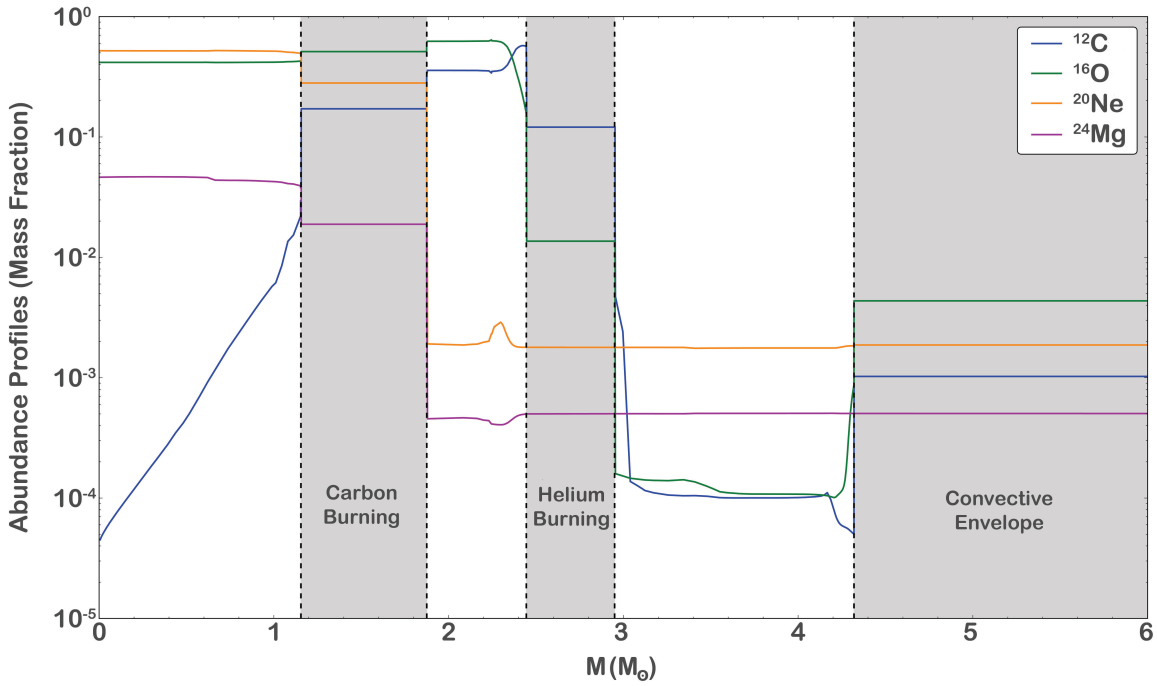

Figure 1.5: Abundance profiles in units of mass fractions (fraction of the total mass within that region) versus interior mass for a $15\,M_\odot$, solar metallicity, non-rotating, single star model. The model represents the carbon burning phase, where convective carbon burning occurs in a convective shell. The abundances of carbon (blue), oxygen (green), neon (orange) and magnesium (magenta) are plotted. The carbon burning convective shell can be seen to extend between around $1.2\,M_\odot$ and $1.9\,M_\odot$. The assumption of homogeneous mixing is illustrated by flat abundance profiles in the convective zones. This leads to sharp gradients at the boundaries.

1.3 The necessity of predictive modelling

Observations of massive stars are key to determine how and why many processes occur. However, until the recent advances in asteroseismology (see e.g. Aerts, Christensen-Dalsgaard and Kurtz, 2010) it has been difficult to directly observe what occurs in the interiors of massive stars. Even asteroseismology, with these advances can only provide information up to the edge of the convective core. As such, currently detailed analysis of massive star interiors can only be achieved through numerical modelling. Such models can be used in conjunction with observations to provide estimates for: masses of real stars (e.g. Bersten et al., 2014); nucleosynthesis yields (Pignatari et al., 2016); supernova progenitor structures (Arnett and Meakin, 2011*a*); and evolutionary ages (e.g. Nieva and Przybilla, 2014). Models are not only directly applicable to understanding stellar evolution and structure, but such information can also be used in many other aspects of astrophysics, for example in galactic chemical evolution models (Nomoto, Kobayashi and Tominaga, 2013).

1.3.1 Modelling deep interiors

The construction of a stellar model at a single instance in time first requires the specification of the initial total mass and compositional fractions, usually specified through the fraction of metals (all species heavier than helium).

The equations of stellar structure are essentially given by four equations (see §3.1 for a full account of these), which provide a local description (within a Lagrangian framework) of the radius, pressure, luminosity and temperature. These are the equations of mass conservation, hydrostatic equilibrium, energy conservation and energy transport. Several auxiliary equations are also required, these are: the equation of state; temperature gradients for heat transport via radiation (and conduction); adiabatic convection; and super-adiabatic convection (the latter requires a theory of convection such as mixing length theory[15], to calculate the temperature gradient, see §2.1.2). The opacity of material is calculated through the interpolation of tabulated values, given the local density, temperature and composition. The change in composition is calculated

[15]Such a procedure does not account for the convective boundary sub-structure, or the effects of convective boundary mixing.

based on the production and destruction of nuclear species, given reaction rates for each species. Finally, two boundary conditions at the centre and surface of the star are required. The central conditions are usually taken as zero radius and luminosity. The surface conditions are defined by the location of the photosphere which can be found at a radius, R, where the optical depth (a function of density and opacity) is $2/3$ and the luminosity at the effective temperature is, $L = 4\pi R^2 \sigma T_{eff}^2$, where σ is the Stefan-Boltzmann constant.

A first principles approach to stellar modelling (in one dimension) is not attainable, as several physical aspects of the model must be obtained through numerical approximations and heuristic theory (based on observations). In addition to this, there are many different approaches to prescribing much of the micro-physics contained within stellar models and the increasing number of combinations of these approaches leads to (Martins and Palacios, 2013) different predicted evolutionary paths for stellar models of the same initial mass, and an increase in the number of free parameters used which are not globally constrained.

Stellar models therefore require the convergence of solutions between codes that are physically representative of the problem at hand. This can be achieved through verification and validation (V&V) of the codes (Calder et al., 2006). V&V are the principal testing procedures for the development of any code that is designed to meaningfully describe nature through simulations, and should be continually used throughout the code development.

The American Institute of Aeronautics and Astronautics (AIAA, 1998) define verification as "the process of determining that a model implementation accurately represents the developer's conceptual description of the model and the solution of the model." They define validation as "the process of determining the degree to which a model is an accurate representation of the real world from the perspective of the intended uses of the model."

Verification in stellar models can be achieved by comparing the same model over varying mesh and time resolutions, or by comparing models using the same initial conditions between independent codes (Jones et al., 2015). Errors and uncertainties in the numerical solution can easily be identified through verification, or other constraints.

Validation ultimately requires the comparison of stellar models with observations,

and tests the underlying physical assumptions in the models. There are two ways in which the validation of stellar models can be achieved; either through empirical or theoretical tests. Generally, V&V should be completed for stellar interior models before they are considered to be predictive, although the act of fine-tuning stellar evolution model parameterisations in order to match observations renders them postdictive rather than predictive.

Empirical validation

The comparison of complete stellar models with relevant observations of real stars is the most obvious form of empirical validation. Such comparisons are also necessary in order to constrain certain aspects of stellar models such as the free parameter in the mixing length theory. Ekström et al. (2012) compare Geneva stellar evolution code (GENEC; Eggenberger et al. 2008) models using a mixing length of, $\alpha_{ml} = 1.6$ (see Eq. 2.1.15), to observations of stars in the red super giant (RSG) stage. This comparison is shown in Fig. 1.6, where the evolution of stellar models and observations are compared in the Hertzsprung-Russell diagram. The evolutionary tracks of various stellar models (solid lines) of different initial masses are compared to observations of stars from various clusters (grey shading) and RSG stars in the Milky Way (red circles). The agreement between theory and observation is good for the post main sequence evolution, and justifies the choice of mixing length for these models at these evolutionary stages.

Comparison of theory and observation can also reveal the non-universality (and non-locality) of theoretical prescriptions for physical processes. Tayar et al. (2017) find that stellar models of red giants using the Yale rotating stellar evolution code (YREC; Demarque et al. 2008) and the Padova-Trieste stellar evolution code (PARSEC; Bressan et al. 2012) only agree with observations from the Apache Point observatory galactic evolution experiment (APOGEE)-Kepler catalogue (Fleming et al., 2015) when a metallicity dependent mixing length is used.

The parameterised physical processes used in stellar models can also be tested by comparison to the results from the meteorology (e.g. Garcia and Mellado, 2014) and oceanography (e.g. Large, McWilliams and Doney, 1994) communities, with the caveat that the fluid in stars is high energy-density plasma, not air or water. For example, parameterisations in stellar models for convective boundary mixing through turbulent

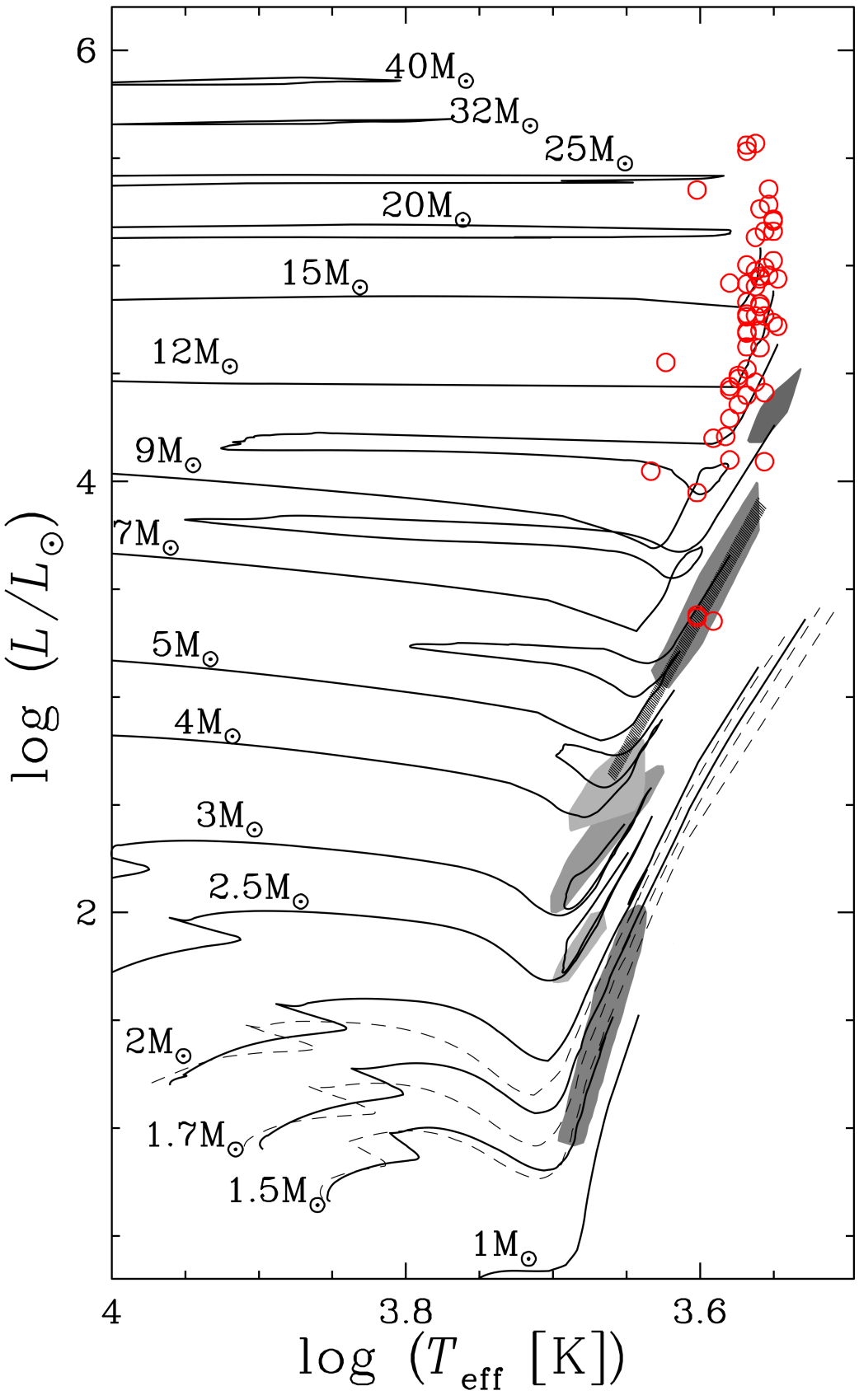

Figure 1.6: Hertzsprung-Russell diagram showing evolutionary tracks for rotating (solid lines) and non-rotating (dashed lines) stellar models calculated using the Geneva stellar evolution code. Grey shaded areas are observations of various clusters and associations, and red circles are observations of RSGs in the Milky Way. The agreement between theory and observation is good for the post main sequence evolution. These observations are used to constrain the mixing length free parameter used in the stellar evolution models. Adapted from Ekström et al. (2012).

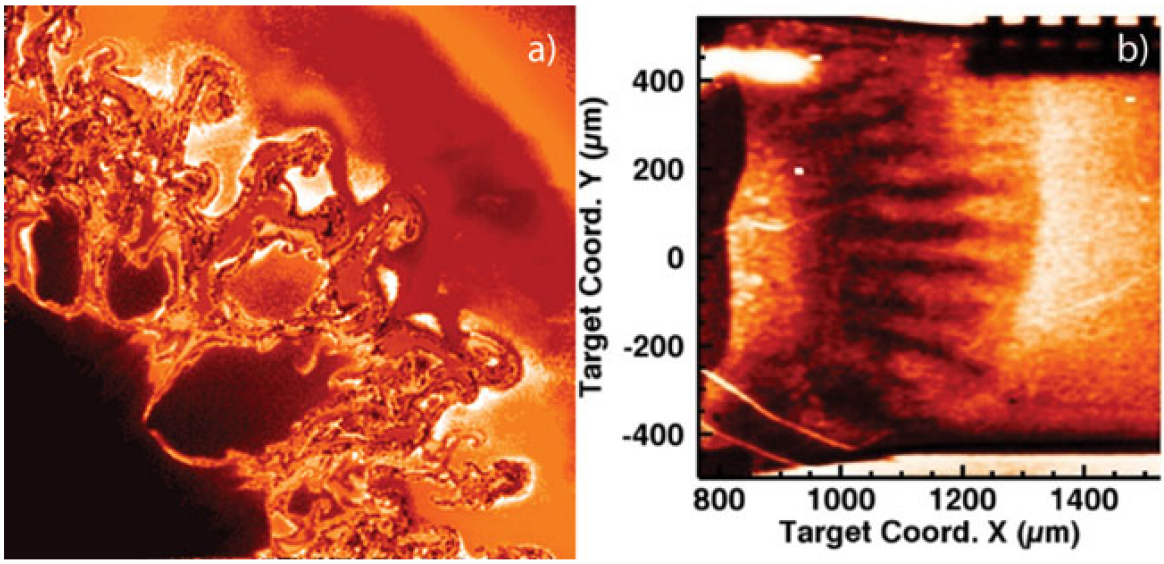

Figure 1.7: *Left:* two-dimensional simulation of the SN1987A supernova using the PROMETHEUS (Fryxell, Müller and Arnett, 1989) code, the scale is approximately 10^9 cm. *Right:* radiograph of a laser-induced hydrodynamic experiment (scaled to SN1987A) using the Omega laser (Boehly et al., 1995). Images taken from Kuranz et al. (2011).

entrainment can be guided by the entrainment law famous to these communities.

Additionally, the results from laboratory studies on fluids with similar properties (extremely high temperature and pressure plasmas) to that of stars can be compared to simulations of stellar interiors, although the volumes of such fluids are much smaller than those in stars. A two-dimensional simulation of the interior of a supernova progenitor is compared to the results of a laser experiment in Fig. 1.7. Although the separation in scales between the simulation and experiment is huge, similarities in the developing hydrodynamic instabilities can be seen.

Theoretical validation

Phenomena such as turbulent convection within the deep interior of massive stars, particularly during their advanced evolution, occur in extreme regimes far from the regimes observed terrestrially. For the deep interiors of massive stars, particularly during the later evolution, there are no observations or terrestrial experiments that can validate simulations. Testing the predictability of stellar models concerning the deep interiors therefore requires validation through theory.

According to Shu (1992), "there is no rigorous general procedure starting from first principles, that exists for the non-linear resolution of the development of convection in

stars, and the consequences of its back reaction on the basic state." As such, there is no complete theoretical picture for the presence of convective instability within stellar interiors.

The alternative then is to turn to the numerical modelling of the governing equations of fluid dynamics (e.g. the Navier-Stokes equations of motion), through the use of multi-dimensional hydrodynamic simulations. These can test the stellar models and their prescriptions for multi-dimensional physical processes under semi-realistic astrophysical, macroscopic, but not necessarily microscopic conditions (the spectrum of length-scales is too small to represent all of the motions between the macroscopic and microscopic scales in stellar convection).

Such simulations are extremely computationally expensive, and the dynamical time-scales over which they evolve are much shorter than the evolutionary time-scales of the star. It is therefore difficult to extrapolate such results over the entire evolution of the star[16], but nevertheless, the results over these short time-scales are usually enlightening.

1.4 A brief history of stellar interior simulations

Henyey et al. (1959) were among the first to produce stellar configurations at multiple epochs using a computer (see Fig. 1.8); they discretised the stellar evolution equations (see §3.1) onto a one-dimensional Lagrangian computational grid. The differential equations were replaced with finite difference approximations and solved using the Newton-Raphson scheme[17]. This scheme was later generalised by Henyey, Forbes and Gould (1964). They used implicit time-stepping, where all the quantities can be calculated at an advanced epoch. In order to ensure numerical convergence and no loss of temporal information, the time-step, Δt, must be limited. This upper limit on the time-step is the time taken for the fluid to cross a single cell of width, Δx (assuming some flow velocity).

Such a restriction on the permitted time-step is described by the Courant-Friedrichs-Lewy (CFL; Courant, Friedrichs and Lewy, 1928) condition,

[16]An apt analogy is the attempt to extrapolate a local climate from a weather forecast.

[17]This method calculates successive approximations to the root of a function. Generally, iterations stop after a pre-defined number of successive estimates or once a solution is found to within a pre-defined tolerance.

$$\frac{U\,\Delta t}{\Delta x} = C_{max}, \tag{1.4.1}$$

where U in this case is the flow velocity and C_{max} is the Courant factor, which has a maximum value of unity. The maximum time-step size is usually chosen with a Courant factor smaller than one, in order to ensure numerical accuracy, while still providing an acceptable margin of error if the flow velocity, U, increases during the simulation compared to the initially adopted value.

Following the success of these calculations, Henyey, Lelevier and Levee (1959) calculated stellar evolution models during the main sequence for stars of mass 1.5, 2, 3.5, 6, 11, 20 and 30 $\mathrm{M}_{\odot}$. This was done by using tabulated values for the opacity based on local values of the temperature, density and composition, a non-relativistic degenerate equation of state and interpolation formulae for the nuclear energy generation rates.

One of the first 2D simulations of stellar interiors was calculated by Deupree (1976). Rather than simulate the entire star at different epochs, their aim was to simulate part of the star with greater detail within a computational box (see §1.5.2 for details on these two types of modelling). They simulated adiabatic stellar pulsations in convective envelopes, where an implicit time-stepping scheme would not be suitable, due to the unsteadiness of these types of flows. Instead, an explicit time-step was taken which resolves all of the relevant transport processes. Hence, in order to temporally resolve acoustic motions, the time-step had a stricter limit than for implicit schemes. The upper limit on this time-step is the time taken for a sound wave to cross a single cell (assuming the local speed of sound), this is equivalent to replacing the flow velocity, U, in Eq. 1.4.1 by $U + c_s$, where c_s is the local sound speed. Deupree (1976) observed the formation and breakup of convective cells in the convective envelope of a 1.5 $\mathrm{M}_{\odot}$ star (see Fig. 1.9).

As computing power increased, simulations of stellar interiors were extended to three dimensions. One of the first groups to calculate such a model were Young et al. (2005) who simulated shell oxygen burning within a 23 $\mathrm{M}_{\odot}$ star, again by placing a computational box within the area of interest of the star.

Figure 1.8: *Left:* UNIVAC 1, the first commercial computer produced in the United States, first installed in 1951. It weighed 7 tons and was capable of performing 1905 floating point operations per second (FLOPS). *Right:* Sunway TaihuLight, as of November 2016, the fastest supercomputer in the world (Dongarra, 2014). Installed at the National Supercomputing Centre in Wuxi, China. It has over 10 million cores, weighs over 150 tons and is capable of performing at over 100 peta-FLOPS.

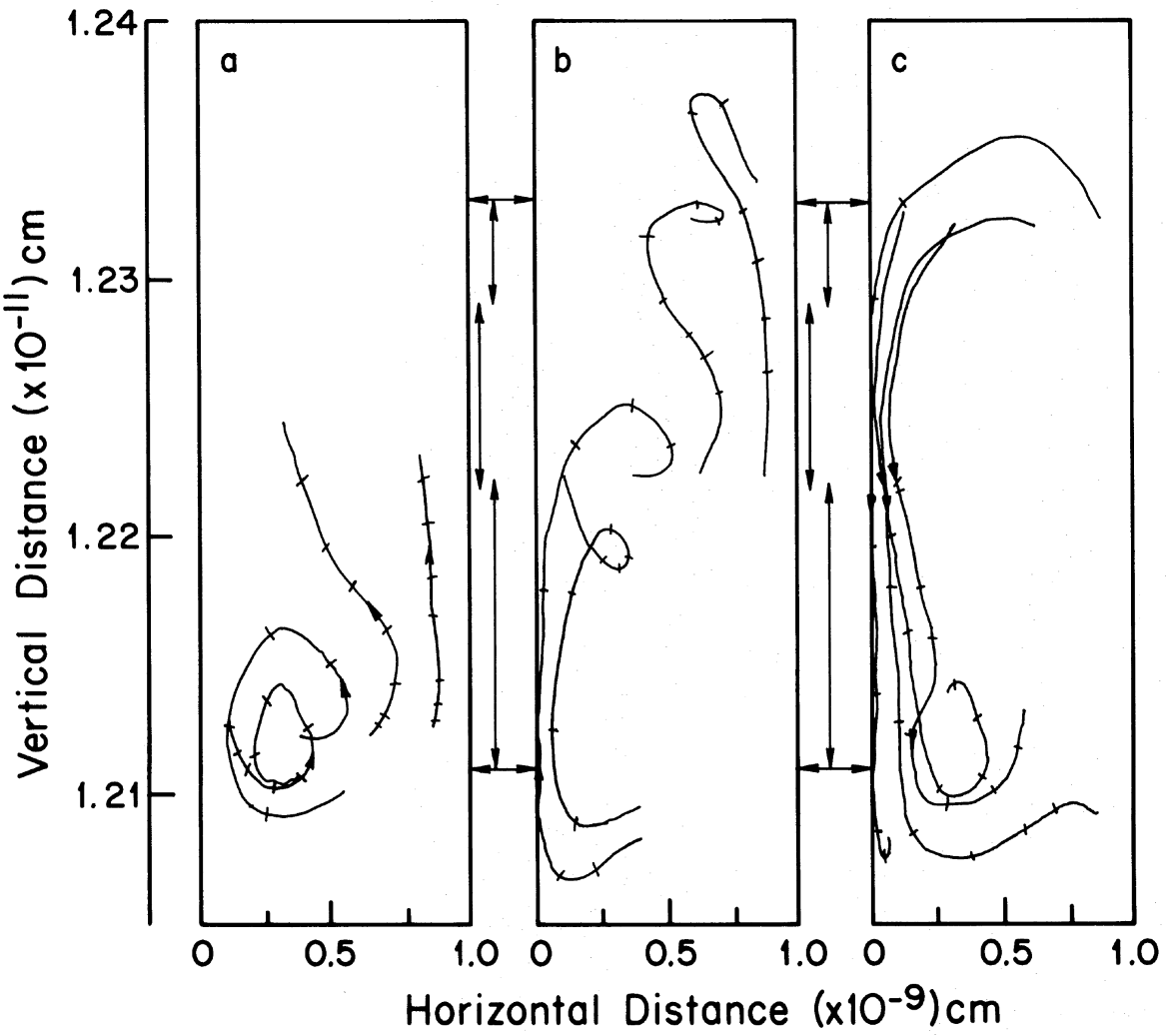

Figure 1.9: Convective motions shown by test particles from 2D simulations (N-body, non-hydrostatic) of adiabatic envelope convection by Deupree (1976). Particles were released from the bottom (left panel), middle (centre panel) and top (right panel) of the convection zone. Horizontal arrows denote convective boundary positions and vertical arrows denote pressure scale heights. Dashes along each profile indicate time intervals of 1000 s. Figure taken from Deupree (1976).

1.5 Modern simulations of massive stellar interiors

Sophisticated simulations sampling a broad range of relevant and increasingly realistic astrophysical conditions have been undertaken thanks to the continuous increase in computing power (see Fig. 1.8).

These simulations fall into two categories: one-dimensional stellar evolution models, which are designed to simulate the entire life-cycle of the star (from the ZAMS to pre-collapse) using spherical symmetry and parameterised micro-physics; and multi-dimensional hydrodynamic simulations, which are designed to simulate short phases of stellar evolution (over shorter dynamical time-scales) from first principles and a minimal number of approximations.

1.5.1 One dimensional simulations

Several groups have calculated grids of multiple stellar models, which provide evolutionary tracks in the Hertzsprung-Russell diagram for models with varying mass, metallicity and rotation rate. Observations can then be over-layed onto these models, in order to estimate those quantities for the observed stars. Recent efforts have focussed on the implementation of axial rotation into such grids. Rotation has been shown to have an impact on many properties of stellar models, mainly through rotationally induced mixing. Namely, these are stellar lifetimes, evolutionary paths and nucleosynthesis (Maeder and Meynet, 2010). Such influences will also directly affect population synthesis models and galactic chemical evolution models. Four independent groups have calculated such grids, the properties of which are summarised in Table 1.2. There is a range of masses, metallicities and rotation rates between the four studies. In addition to this, there will be inherent differences in each code regarding certain physical assumptions, e.g. the specific treatment of rotation, calibration of extra chemical mixing etc.

There are other notable stellar evolution codes which are suitable for studying massive star evolution. These are STAREVOL (Decressin et al., 2009), PADOVA[18] (Bertelli et al., 2009) and KEPLER (Heger, Langer and Woosley, 2000).

[18]Rotation is not included in the PADOVA stellar evolution code.

Reference	Code	Mass $M_\odot$	Metallicity Z	Rotation $v_{zams}/\mathrm{km\,s^{-1}}$	Rotation v_{ini}/v_{crit}
Brott et al. (2011)	STERN	5 - 60	0.0021 - 0.0088	0 - 540	-
Ekström et al. (2012)	GENEC	0.8 - 120	0.014	110 - 220	0.4
Chieffi and Limongi (2013)	FRANEC	13 - 120	0.014	300	0.6
Choi et al. (2016)	MESA	0.1 - 300	0.00012 - 0.037	-	0.4

Table 1.2: Properties of four sets of stellar model grids: reference to the publication; stellar evolution code used; mass range in solar masses of models; metallicity range in mass fractions of models; rotation range of models in terms of both the equatorial rotational rate on the ZAMS, v_{zams} and the ratio of initial rotation rate, v_{ini}, to the critical rotation rate, v_{crit}.

1.5.2 Multi dimensional

Almost all phases of stellar evolution have been simulated using multi-dimensional hydrodynamic simulations. The following is a summary of notable efforts to simulate various burning stages of massive stars.

Oxygen burning

Oxygen burning has been studied by numerous groups at different resolutions. Oxygen, as well as the other advanced burning phases (carbon to silicon burning), are preferable for hydrodynamic simulations, due to the short nuclear burning time scale, allowing a significant fraction of the burning stage to be simulated. Furthermore, neutrino losses dominate over radiative losses of energy, such that radiative cooling due to photon losses is negligible, the computational cost is therefore reduced. Two types of simulations are generally adopted, box-in-a-star simulations which model a small section of the star within the computational domain, and star-in-a-box simulations which model the entire geometric volume (4π sphere) of the part of the star considered. Oxygen burning simulations are chronologically tabulated in Table 1.3. Unless otherwise stated, all computational grids consist of uniform cells within a Cartesian geometry.

Until very high-resolution simulations ($> 1536 \times 1536 \times 1536$) can be routinely undertaken, both 'box-in-a-star' and 'star-in-a-box' simulations are needed and provide

Reference	Zoning	Type	Notes
Arnett (1994)	200×40	Box-in-a-star	a
Bazan and Arnett (1994)	200×40	Star-in-a-box	b
Bazán and Arnett (1998)	460×128	Box-in-a-star	c
Asida and Arnett (2000)	172×60	Box-in-a-star	d
Kuhlen, Woosley and Glatzmaier (2003)	$241 \times 63 \times 31$	Anelastic	e
Young et al. (2005)	$400 \times 100 \times 100$	Box-in-a-star	-
Meakin and Arnett (2006)	800×320	Box-in-a-star	f
Meakin and Arnett (2007a)	$400 \times 100 \times 100$	Box-in-a-star	-
Meakin and Arnett (2007b)	$400 \times 100 \times 100$	Box-in-a-star	-
Arnett and Meakin (2011a)	800×320	Box-in-a-star	g
Viallet et al. (2013)	$786 \times 512 \times 512$	Box-in-a-star	-
Chatzopoulos, Graziani and Couch (2014)	$8 \times 8 \times 8$	Box-in-a-star	h
Arnett et al. (2015)	$1536 \times 1024 \times 1024$	Box-in-a-star	-
Jones et al. (2017)	$1536 \times 1536 \times 1536$	Star-in-a-box	-

a Box-in-a-star simulations maximise local resolution.
b Star-in-a-box simulations have lower local resolution but provide all of the low-order modes in a full circular/spherical (4π) domain.
c The computational domain was taken from the edge of the silicon shell to the start of the hydrogen envelope.
d The radial resolution is logarithmic, while the horizontal resolution is linear.
e The resolution describes $n_{max} \times l_{max} \times m_{max}$ which are the Chebyshev polynomials and spherical harmonics l and m, respectively.
f In addition to the oxygen shell the overlying carbon shell was also simulated.
g In addition to the oxygen shell the carbon, neon and silicon shells were also included.
h Although this was the initial size of the grid, this simulation utilised adaptive mesh refinement, whereby the grid zoning is increased in areas requiring higher resolution, resulting in a maximum mesh size of $6250 \times 6250 \times 6250$.

Table 1.3: Chronological summary of oxygen burning simulations, detailing the reference, grid zoning, type of simulation (box-in-a-star, star-in-a-box or anelastic) and any additional information about the simulation.

complementary information on convection in stars.

Anelastic simulations allow longer time-steps than fully compressible simulations. However, their use of impermeable and stress-free boundary conditions mean that convective boundary mixing (see §2.1.3) can not be studied and the overall flow pattern in the convective region will be restricted (Meakin and Arnett, 2007*a*).

Silicon burning

Silicon burning is the most complicated burning phase and requires a large computational effort. Here the neutrino losses are very high and the evolution time-scale is down to the order of days. Early simulations of silicon burning on a numerical grid of 256×64 were performed by Bazán and Arnett (1997) using a nuclear reaction network consisting of 123 nuclei. Couch et al. (2015) simulated (in three dimensions) the final three minutes of silicon burning in a $15\,\mathrm{M}_\odot$ star[19]. They show that asphericities in the progenitor structures may have a strong impact on the core-collapse supernova mechanism (e.g. Müller and Janka 2015) and should not be ignored. An initial study of silicon burning in three dimensions with a large network ($\sim$ 120 nuclei) has been carried out by Meakin & Arnett (in prep.). The carbon, oxygen and part of the silicon shell of an $18\,\mathrm{M}_\odot$ star preceding its collapse have also been simulated as a full-sphere, with a resolution of $400 \times 148 \times 56$ in $(\log(\mathrm{r}), \phi, \theta)$ by Müller et al. (2016).

Hydrogen burning

Early phases of stellar evolution are harder to simulate because they are generally characterised by their large size, very long nuclear time scales and strong cooling due to photon losses, meaning that radiative effects cannot be ignored. Despite these added difficulties, several studies have targeted hydrogen or helium burning phases. Meakin and Arnett (2007*b*) performed a fully-compressible simulation of core hydrogen burning on a numerical grid of $400 \times 100 \times 100$, with the driving luminosity boosted by a factor of 10. Gilet et al. (2013) adopted the low Mach number solver MAESTRO (Almgren, Bell and Zingale, 2007) to simulate core hydrogen burning on a numerical grid of $512 \times 512 \times 512$. This type of solver removes the need to follow the propagation of

[19]This simulation used the FLASH code (Fryxell et al., 2000) with adaptive mesh refinement and a small nuclear reaction network.

acoustic waves. Such a solver allows for longer time-steps than a fully compressible one, but may neglect important kinetic energy (KE) transfer due to acoustic fluxes (see Eq. A.2).

Helium burning

Herwig et al. (2014) and Woodward, Herwig and Lin (2015) performed idealised full-sphere hydrodynamic simulations of H-ingestion into the He-burning shell of a post asymptotic giant branch (AGB) star on a numerical grid of 1536^3. The rapidity of such events violate the assumptions inherent in the mixing length theory (see §2.1.2) of stellar convection and therefore requires hydrodynamic simulations for lack of an alternative model.

1.6 Thesis outline

The first three-dimensional hydrodynamic simulations of carbon shell burning in a massive star are presented in this thesis. In chapter 2, the necessary theoretical aspects are introduced for the numerical modelling of turbulent convection in stellar interiors, as well as the prescriptions that are used to describe such processes in stellar evolution models. Descriptions of the computational tools that are used are presented in chapter 3. These tools are used to calculate the stellar evolution and hydrodynamical models which are presented in later chapters. Chapter 4 presents new results from a boundary parameter study of various convective boundaries within a $15\,\mathrm{M}_\odot$ stellar evolution model. In chapter 5, new results from a resolution study using hydrodynamic simulations of the carbon burning shell are shown. The initial conditions used for these models are provided by the stellar model introduced in chapter 4. Convergence to a physical solution is tested, and emphasis is placed on analysing the convective boundaries. Turbulent entrainment[20] is investigated and the width of the convective boundary regions is estimated. The same initial conditions introduced in chapter 4 are used in a luminosity study, where the nominal carbon burning nuclear energy generation rate is multiplied by 8 different factors within the range $1 - 3 \times 10^4$. The results

[20]Turner (1973) defines entrainment as the transport of fluid across an interface between two bodies of fluid by a shear-induced turbulent flux.

of this study are presented in chapter 6. Here, the scaling between turbulent driving, convective velocities and boundary stiffness as well as the entrainment law are tested by varying the driving luminosity of each model. Finally, in chapter 7, the findings from each study are summarised and the potential future implementations and plans for the further study of turbulent convection within massive stars is discussed.

Chapter 2

Analytical tools and prescriptions for numerical modelling of convection in stellar interiors

2.1 Stellar model prescriptions for turbulent convection

In stellar evolution codes the treatment of convection is split into three aspects: boundary location; mixing within the convective region; and convective boundary mixing. I look at each of these aspects in turn.

2.1.1 Criterion for stability against convection

In a broad sense, when radiation is not efficient enough to transport energy, matter becomes convectively unstable. This convective transport of energy can be very efficient and nearly fully adiabatic, or conversely radiative losses can occur during convective transport leading to super-adiabatic convection. The extent of convection is determined in the following from a thermodynamical point of view. The derivations shown here are based on those from Maeder (2009) and Kippenhahn, Weigert and Weiss (2013).

The thermodynamic properties of a system are related to each other through an equation of state (EOS), for which a general form is

$$p^{\alpha} = \frac{\rho}{\mu^{\phi}} k_B T^{\delta}, \tag{2.1.1}$$

where p, ρ, μ, k_B and T are the pressure, density, mean molecular weight, Boltzmann's constant and temperature, respectively. α, ϕ and δ are defined in Eq. 2.1.3. The mean molecular weight for a mixture of nuclei of type i is

$$\mu = \left(\sum_i \frac{X_i(1 + Z_i)}{\mu_i} \right)^{-1}, \tag{2.1.2}$$

for molecular weight, μ_i, atomic number, X_i and charge number, Z_i. The exponents in Eq. 2.1.1 are given by

$$\alpha = \left(\frac{\partial \ln \rho}{\partial \ln p} \right)_{\mu,T}, \quad \phi = \left(\frac{\partial \ln \rho}{\partial \ln \mu} \right)_{p,T}, \quad \delta = -\left(\frac{\partial \ln \rho}{\partial \ln T} \right)_{p,\mu}, \tag{2.1.3}$$

the usual ideal gas EOS is retrieved with $\alpha = \phi = \delta = 1$.

Taking the logarithm and then the radial derivative (assuming α, ϕ and δ are constant) of Eq. 2.1.1 gives

$$\frac{1}{\rho}\frac{\partial \rho}{\partial r} = \frac{\alpha}{p}\frac{\partial p}{\partial r} + \frac{\phi}{\mu}\frac{\partial \mu}{\partial r} - \frac{\delta}{T}\frac{\partial T}{\partial r}. \tag{2.1.4}$$

Considering a fluid element (e) within its surroundings (s), if the element is heated and assumed to be in hydrostatic equilibrium with its surroundings then its density will decrease (according to Eq. 2.1.1). The fluid element will subsequently feel a buoyant acceleration (according to Archimedes' principle; e.g. Lautrup 2011) and will move upwards by some distance. If the change in distance is a small perturbation in radius, δr, then the change in density of the fluid element and its surroundings over this distance can be expressed as

$$\left(\frac{\partial \rho}{\partial r} \right)_e \delta r \quad \text{and} \quad \left(\frac{\partial \rho}{\partial r} \right)_s \delta r, \quad \text{respectively.} \tag{2.1.5}$$

If the change in density of the fluid element (a reduction due to heating) is greater than the change in density of the surroundings over the distance, δr, then the fluid element will continue to rise and becomes convectively unstable. This can be expressed as (remembering that the radial density gradient is negative for a stable stratification)

$$\left(\frac{\partial \rho}{\partial r}\right)_e < \left(\frac{\partial \rho}{\partial r}\right)_s . \tag{2.1.6}$$

Substituting Eq. 2.1.4 into the instability criterion given by Eq. 2.1.6, while assuming that the fluid element is in pressure equilibrium with its surroundings, $(\partial p/\partial r)_e = (\partial p/\partial r)_s$, and that the composition of the fluid element remains constant, $(\partial \mu/\partial r)_e = 0$, yields

$$-\left(\frac{\delta}{T}\frac{\partial T}{\partial r}\right)_e < \left(\frac{\phi}{\mu}\frac{\partial \mu}{\partial r}\right)_s - \left(\frac{\delta}{T}\frac{\partial T}{\partial r}\right)_s . \tag{2.1.7}$$

This criterion is more commonly expressed using the nabla notation (see Eq. 2.1.9). This notation uses the pressure scale height, which describes the characteristic length scale for a radial variation in the pressure[21] of the order of the exponential function 'e' (e.g. Kippenhahn, Weigert and Weiss, 2013); in hydrostatic equilibrium this can be expressed as

$$H_p = -\frac{dr}{d\ln p} \approx \frac{p}{g\rho}, \tag{2.1.8}$$

$H_p > 0$ as pressure decreases radially from the centre, for a dynamically stable star. The nabla notation is then defined as

$$-\frac{H_p}{T}\frac{\partial T}{\partial r} = \frac{\partial \ln T}{\partial \ln p} = \nabla. \tag{2.1.9}$$

Using this notation in Eq. 2.1.7 yields the Ledoux (Ledoux, 1947) criterion for stability against convection

$$\nabla_e - \nabla_s < -\frac{\phi}{\delta}\nabla_\mu, \tag{2.1.10}$$

where $\nabla_\mu = \partial \ln \mu / \partial \ln p$ is the compositional gradient.

In the absence of convection the temperature gradient in the surrounding medium is determined by radiative and conductive heat transport. Therefore, $\nabla_s = \nabla_{rad}$, where ∇_{rad} is the radiative temperature gradient due to the transport of heat by photons; this transport can be assumed to be diffusive throughout the star as the photonic mean

[21] A similar definition also exists for the density scale height, describing the radial variation in the density.

free path is much smaller than the stellar radius. The radiative temperature gradient is given by (see Appendix A.1 for the derivation)

$$\nabla_{rad} = \frac{3}{16\pi ac\,G}\frac{\kappa\, pL}{mT^4}, \tag{2.1.11}$$

where a, c and G are the radiation density constant, speed of light and gravitational constant, respectively. m and L are the mass and luminosity of the star, respectively, and κ is the combined radiative and conductive opacity.

If a fluid element is convectively unstable, then it will rise adiabatically (to a good approximation, in most cases the fluid element is actually super-adiabatic, as it will radiate some energy to the surroundings; see §2.1.2); the temperature gradient of the fluid element is then the adiabatic one, $\nabla_e = \nabla_{ad}$ where (e.g. Maeder, 2009)

$$\nabla_{ad} = \frac{p\,\delta}{T\rho\, c_p}, \tag{2.1.12}$$

and c_p is the specific heat at constant pressure. Replacing the temperature gradients in Eq. 2.1.10 with those from Eqs. 2.1.11 and 2.1.12 leads to a calculable expression for the extent of convective instability

$$\nabla_{rad} > \nabla_{ad} + \frac{\phi}{\delta}\nabla_{\mu}. \tag{2.1.13}$$

If the surrounding medium is assumed to be of uniform chemical composition (or if the stabilising effects of composition gradients are ignored) the composition gradient, ∇_μ, is zero, and the Ledoux criterion for convective instability simplifies to the Schwarzschild (Schwarzschild, 1992) criterion

$$\nabla_{rad} > \nabla_{ad}. \tag{2.1.14}$$

2.1.2 Böhm-Vitense's convective flux

In order for a star with a non-zero nuclear energy generation rate to remain in thermal balance, it must radiate energy at some radiative flux, F_r. The kinetic energy (KE) flux, F_k, of the star in a localised region can become greater than the maximum possible radiative flux of the star, for example during nuclear burning phases. If this

happens, then this region of the star will become convectively unstable as the radiative flux alone is not efficient enough to provide thermal stability. For deep interior convection, transport of KE by a convective flux, F_c, is very efficient and is almost entirely adiabatic. For sub-surface convection in the envelopes of red giants, for example, the convective flux is less efficient as some of the energy is radiated to the surroundings and is therefore super-adiabatic.

One common way to estimate this super-adiabatic convective flux in stellar evolution models is to use the mixing length theory (MLT; Böhm-Vitense 1958). In MLT, convective fluid elements are assumed to be transported over some mean free path known as the mixing length, beyond which they diffuse and deposit their internal energy into the ambient medium. The mixing length is given as

$$\ell_{ml} = \alpha_{ml} H_p, \tag{2.1.15}$$

where α_{ml} is of order unity and is tuned in such a way that stellar models match observations (e.g. Ekström et al., 2012).

By combining the Schwarzschild criterion (Eq. 2.1.14) with Eq. 2.1.11, a critical luminosity can be derived, above which heat transport must be convective. The total flux of the star can be associated with some 'fictitious' radiative temperature gradient[22] (as given by Eq. 2.1.11 and the derivation in Appendix A.1)

$$F_{tot} = F_{rad} + F_{conv} = \frac{4acG}{3}\frac{mT^4}{\kappa p r^2}\nabla_{rad}, \tag{2.1.16}$$

where the radiative flux, F_{rad}, is determined by the background temperature gradient, ∇ (if there is a non-zero convective flux)

$$F_{rad} = \frac{4acG}{3}\frac{mT^4}{\kappa p r^2}\nabla. \tag{2.1.17}$$

The convective flux is calculated by following the MLT formalism. A convective fluid element will travel the mixing length distance, ℓ_{ml}, through a background stratification of density, ρ, before diffusing with the background fluid depositing an average specific energy of $c_p\,\overline{\Delta T}$, where $\overline{\Delta T}$ is the average temperature excess of the fluid element with

[22]This gradient is not fictitious if the convective flux is zero, in such a situation the total flux is equal to the radiative flux only and $\nabla = \nabla_{rad}$.

respect to the background. If the average velocity of (up-flowing and down-flowing) convective elements over this distance is v_{mlt}, then the average convective flux is

$$F_{conv} = c_p \, \rho \, v_{mlt} \, \overline{\Delta T}. \tag{2.1.18}$$

In a similar manner to that described by Eq. 2.1.5, the average temperature excess ($\overline{\Delta T}$) of a fluid element (e) with respect to its background (s) after traversing the mixing length (ℓ_{ml}) is approximated as the temperature excess at half of this distance

$$\overline{\Delta T} \approx \Delta T(\ell_{ml}/2) = \left[\left(\frac{\partial T}{\partial r} \right)_e - \left(\frac{\partial T}{\partial r} \right)_s \right] \frac{\ell_{ml}}{2}. \tag{2.1.19}$$

In order to estimate the average convective flux of a fluid element its average buoyancy per unit volume, B, over the mixing length is considered

$$B = -g\overline{\Delta\rho}, \tag{2.1.20}$$

where the average density excess is related to the temperature excess through Eq. 2.1.4 (assuming hydrostatic equilibrium and uniform composition) and is

$$\frac{\Delta\rho}{\rho} = -\delta \frac{\Delta T}{T}. \tag{2.1.21}$$

The average work done by a convective fluid element moving a distance of the mixing length, ℓ_{ml}, is assumed to be equal to the work done at half this distance. Half of this work done by the fluid element is assumed to be lost to the background through displacement of other fluid elements. The remaining half is associated with the KE of the fluid element; this can be written as

$$\begin{aligned} \frac{1}{2}\,\overline{W} \;&=\; \frac{1}{2}\,W(\ell_{ml}/2) \;=\; \frac{1}{2}\,B(\ell_{ml}/2)\,\frac{\ell_{ml}}{2} \\ &=\; -\frac{1}{2}\,g\,\overline{\Delta\rho}(\ell_{ml}/2)\,\frac{\ell_{ml}}{2} \;=\; \frac{1}{2}\,\rho\,v_{mlt}^2. \end{aligned} \tag{2.1.22}$$

Hence, using Eqs. 2.1.19 - 2.1.22, the average convective velocity of a fluid can be calculated using

$$v_{mlt}^2 = \frac{g\,\delta\,\ell_{ml}^2}{8\,H_p}\,(\nabla - \nabla_e)\,, \tag{2.1.23}$$

and the convective flux given by Eq. 2.1.18 becomes

$$\mathbf{F_{conv}} = \ell_{\mathbf{ml}}^{\mathbf{2}}\rho\,\mathbf{T c_p}\,\frac{\sqrt{\mathbf{g}\,\delta}}{\mathbf{4\sqrt{2}}}\,\mathbf{H_p^{-3/2}}\,(\nabla - \nabla_{\mathbf{e}})^{\mathbf{3/2}}. \tag{2.1.24}$$

For deep interior convection, where heat transport is very efficient, the temperature gradient of the fluid elements can be taken as the adiabatic one, $\nabla_e = \nabla_{ad}$, but for less efficient convection, at the surface, for example, corrections for radiative losses of the fluid element must be accounted for.

A fluid element of surface area, S, and radial thickness, d, will radiate energy at a rate, $\lambda = F_\lambda S$, where F_λ is the absolute value of the element's radiative flux

$$F_\lambda = \frac{4acT^3}{3\kappa\rho}\left|\frac{\partial T}{\partial n}\right|, \tag{2.1.25}$$

and $\partial T/\partial n$ is the temperature gradient in the direction perpendicular to the surface and can be approximated, using Eq. 2.1.19, as $\partial T/\partial n \approx 2\,\overline{\Delta T}/d$. If the fluid element has an average velocity, v_{mlt}, then its temperature loss per unit length is

$$\left(\frac{\partial T}{\partial r}\right)_\lambda = \left(\frac{\partial T}{\partial r}\right)_{ad} - \left(\frac{\partial T}{\partial r}\right)_e = \frac{\lambda}{\rho V c_p v_{mlt}}, \tag{2.1.26}$$

where V is the volume of the fluid element. The temperature change per unit length due to radiative losses in nabla notation is then

$$\nabla_e - \nabla_{ad} = \frac{\lambda H_p}{\rho V c_p v_{mlt} T}. \tag{2.1.27}$$

Inserting the expression $\lambda = F_\lambda S$ into Eq. 2.1.27, using $S\ell_{ml}/Vd \approx 9/2\ell_{ml}$ (from the original formulation in Böhm-Vitense, 1958) and rearranging yields

$$\frac{\nabla_e - \nabla_{ad}}{\nabla - \nabla_e} = \frac{6acT^3}{\kappa\rho^2 c_p v_{mlt}\ell_{ml}}. \tag{2.1.28}$$

Then using Eqs. 2.1.16 - 2.1.18, 2.1.23 and 2.1.28 the radiative and convective fluxes, convective velocity and temperature gradients of the background and of the fluid element can be calculated. Finally, the strength of diffusive mixing due to convection

can be determined through an appropriate diffusion coefficient:

$$D_{mlt} = \frac{1}{3} v_{mlt} \ell_{ml}. \tag{2.1.29}$$

2.1.3 Convective boundary mixing prescriptions

One prescription used in stellar evolution modelling of convective boundary mixing (CBM) is penetrative convection. This is the motion of a fluid element from a convectively unstable region into a surrounding stable region. Such motions weaken the sub-adiabatic stratification in the stable region, resulting in growth of the convective region over time. Penetrative convection is believed to occur in the fluids of stars due to the abundance of this phenomenon terrestrially. It is observed in: fluid dynamics experiments (Moroni and Cenedese, 2006; Dore et al., 2009); the Earth's oceans (Turner, 1986); and the Earth's atmosphere (Frey et al., 2014). Zahn (1991) made the distinction between convective penetration and overshooting[23] for stellar models. They also showed that penetrative convection into the stable region above a convective core, will remove the sub-adiabatic stratification in all but a thin thermal boundary layer. One standard CBM prescription for convective cores is an adiabatic extension of the core by a fraction of the local pressure scale height. Schaller et al. (1992) showed that an extension of 20% provided the best fit for the main sequence envelope of 65 star clusters. Such a value is adopted for CBM during hydrogen and helium burning cores in GENEC models (Eggenberger et al. 2008; see §3.2 for a description of the GENEC code).

Another approach is to consider a non-zero velocity at the formal convective boundary, unlike the predictions given by MLT. Freytag, Ludwig and Steffen (1996) computed 2D radiative hydrodynamic simulations of surface convection. They found that the velocity profiles decayed exponentially and extended well beyond the convective bound-

[23]Overshooting occurs when the efficiency of convection is low (when thermal dissipation is significant); such penetration mixes abundances and transports momentum, but cannot alter the stable temperature gradient.

Mixing type	Entropy mixing?	Diffusion or advection?	Composition profile shape
Penetration	Yes	Diffusion	Step function
Overshoot	No	Diffusion	Step function
Diffusive	No	Diffusion	Exponential
Double-diffusive	No	Diffusion	Double exponential
Entrainment	Yes	Both	Sigmoid

Table 2.1: Summary of the various convective boundary mixing prescriptions that are commonly implemented into stellar evolution codes. Details include: whether the entropy structure is affected by the mixing process; if the mixing is primarily due to diffusion or advection; and the function which best describes the compositional profile shape.

ary. They attributed this to the propagation of linear g-modes[24] (e.g. Christensen-Dalsgaard, 2003) in the stable region. They modelled the position of tracer particles in the overshot region by an exponentially decaying diffusive process, with a suitable diffusion coefficient of the form

$$D = D_0 \, exp\left(-\frac{2z}{fH_{p,0}}\right), \tag{2.1.30}$$

where D_0 can be taken as the diffusion coefficient calculated by MLT at a suitable distance inside the convectively unstable region, i.e. at a position where the convective velocity (Eq. 2.1.23) is high and is not affected by buoyant deceleration near the convective boundary region. z is the distance from the formal convective boundary (i.e. that determined by the Schwarzschild or Ledoux criteria), $H_{p,0}$ was originally taken as the velocity scale height at the convective boundary, but is commonly replaced (for example, in the MESA code; Paxton et al., 2011) by a fraction, f, of the pressure scale height at the same position where D_0 is evaluated. This fraction is fine-tuned so that the models reproduce observed main sequence widths (Herwig, 2000; Jones et al., 2015), and often different values are taken for different convective boundaries. Such a type of diffusive CBM is similar to classical (non-adiabatic) overshooting in the sense that they do not affect the entropy structure of the mixed region.

[24]These waves occur within fluids or at fluid interfaces. They are produced from the restoring force of gravity when the fluid is perturbed, such that the perturbation is not strong enough to result in the fluid becoming buoyant.

A modified diffusive CBM approach was first introduced by Herwig et al. (2007), who used the same tracer particle method[25] as Freytag, Ludwig and Steffen (1996). This method was used to fit an exponentially decaying diffusion coefficient to diffusive mixing within the convective region and near the boundary of the helium shell in a $2\,M_\odot$ AGB star. A separate method was used to derive diffusion coefficients for diffusive mixing in the stable region, based on the vertical spread of the entropy. This approach is then a 'double-diffusive' mixing parameterisation that uses two exponential decays of different slopes. The first decay can be thought of as physically representative of shear mixing near the convective boundary, while the second decay of a shallower slope is representative of the mixing due to propagating gravity waves. Battino et al. (2016) applied this 'double diffusive' method to two regions within 2 and $3\,M_\odot$ AGB stars: at the bottom of the thermal pulse-driven convective zone[26] above the core; and during the third dredge up[27] below the convective envelope. They used free parameters that were fixed according to the results of simulations by Herwig et al. (2007) and theoretical work by Denissenkov and Tout (2003).

A recent study by Viallet et al. (2015) suggests the combination of the two types of CBM previously mentioned (penetrative and diffusive) as well as a third type, turbulent entrainment (turbulence leads to shear mixing at convective boundaries; see §2.2.2) for the modelling of CBM in stellar evolution calculations. The suggested use of each prescription depends on the specific regime of mixing, and in particular the importance of radiative effects, which can be determined using the Péclet number (Pe; the ratio of time-scales for heat transport through conduction and advection; see §4.2). For $\mathrm{Pe} < 1$, such as in surface convection, thermal diffusion is the dominant form of mixing and so a parameterisation such as Eq. 2.1.30 can be used. For deeper internal convection that is still affected by thermal diffusion, such as CBM during core hydrogen and helium burning and the envelopes of red giants (Viallet et al., 2013), a transition occurs

[25]This method consists of using a scalar quantity as a tracer particle, by allowing the particles position to change based on the local fluid velocity.

[26]This refers to a convection zone which arises for a relatively short amount of time, caused by a helium flash. This flash occurs when helium is ignited under degenerate conditions, resulting in an increase in temperature with no expansion due to the prevailing pressure component from degenerate electrons.

[27]Following a helium flash, the opacity driven convective envelope can extend down to the region where helium was processed into carbon and nitrogen. These newly created elements can then be advected to the surface. This process is known as the third dredge up.

whereby penetrative convection mixes both entropy and composition until thermal effects can inhibit this process. Such mixing would be best represented by penetrative convection (Schaller et al., 1992) immediately followed by a diffusive CBM prescription. Finally, the third case is where radiative effects are negligible (Pe $\gg 1$), such as in the advanced burning stages of massive stars where neutrino losses dominate the cooling. In this case, mixing of composition and entropy proceeds through turbulent entrainment and shear mixing, extending the convective region. Such mixing has been observed in simulations of oxygen shell burning by Meakin and Arnett (2007*b*), carbon shell burning by Cristini et al. (2016*a*) and the core helium flash by Mocák, Siess and Müller (2011). Also, results of turbulent entrainment in the carbon shell of a $15\,\mathrm{M}_{\odot}$ star are presented in §5.2 and §6.2. All of the CBM prescriptions mentioned above are summarised in Table 2.1, where their effect on entropy, mixing type (diffusive/advective) and the subsequent shape of the composition profile are detailed.

2.2 Analytical tools for studying turbulent convection

There have been considerable efforts into understanding turbulence from a theoretical perspective. Such perspectives are incredibly useful when analysing multi-dimensional hydrodynamic simulations of turbulent convection. In the following sections I detail the turbulent cascade of energy, the entrainment of material from dynamically stable regions due to turbulence and the analysis of the mean evolution and fluctuations in the turbulent flow properties.

2.2.1 Kolmogorov's turbulent cascade

From dimensional analysis of a turbulent system, given a root-mean-square (RMS) velocity of the largest energy-containing fluid elements, v_{rms}, at the integral length scale, ℓ, the approximate specific KE of the system is, v_{rms}^2, and will vary over a time scale of ℓ/v_{rms}. Hence, as Kolmogorov (1941) showed, the rate of energy dissipation at the largest (integral) length-scale of the system is

$$\epsilon \sim v_{rms}^3/\ell. \tag{2.2.1}$$

The turbulent velocity, v_{rms}, can be calculated using a spatially (horizontal) and temporally averaged velocity magnitude in the following way:

$$v_{rms} = \sqrt{\overline{\langle v_{mag}^2 \rangle} - \overline{\langle v_{mag} \rangle}^2}, \tag{2.2.2}$$

where v_{mag} is the magnitude of the velocity over the three dimensions; a description of this notation is given in §2.2.3.

At any other scale, λ, where the velocity is v_λ, the energy dissipation will be

$$\epsilon_\lambda \sim v_\lambda^3/\lambda. \tag{2.2.3}$$

For a system in a statistically steady state, Kolmogorov (1962) showed that $\epsilon_\lambda = \epsilon$ for any scale (within the inertial sub-range), λ, meaning that the same amount of energy is transferred down through to fluid elements at increasingly smaller scales, i.e. a turbulent cascade of KE from large to small scales. Equating Eqs. 2.2.1 and 2.2.3 reveals that

$$v_\lambda = v_{rms} \left(\frac{\lambda}{\ell} \right)^{1/3}, \tag{2.2.4}$$

hence the largest fluid elements have the highest velocities ($\lambda/\ell = 1$), while the smallest fluid elements have the highest vorticities ($v_\lambda/\lambda \gg 1$). This spectrum of velocities extends to smaller and smaller scales until a length scale, λ_0, is reached, where the viscous dissipation rate is comparable to the turbulent kinetic energy (TKE) dissipation rate[28]. At this scale the KE of the fluid elements is small enough to be affected by viscous actions of the fluid, thereby damping out their motions.

The approximate dissipation of KE through viscous actions at this scale over a time-scale λ/v_λ could be written as

$$\mathbf{v}_\lambda^\mathbf{2} \frac{\lambda}{\mathbf{v}_\lambda} = \nu, \tag{2.2.5}$$

[28]To quote the verse by Richardson (1922), "Big whorls have smaller whorls that feed on their velocity, and little whorls have lesser whorls and so on to viscosity (in a molecular sense)."

where ν is the kinematic viscosity. By equating Eqs. 2.2.1 and 2.2.4 and using Eq. 2.2.5, this can be expressed as

$$\lambda_0 = \left(\frac{\nu^3}{\epsilon}\right)^{1/4}. \tag{2.2.6}$$

This length-scale is otherwise known as the Kolmogorov length-scale.

2.2.2 Turbulent entrainment at convective boundary regions

Fluid flows can become turbulent when inertial forces become greater than the viscous forces of the fluid. In a similar manner to the turbulent cascade, the Reynolds number determines the separation between the smallest and largest scales of the flow, where the largest scales are least affected by viscosity. The Reynolds number is therefore a diagnostic for the relative importance of the inertial and viscous forces at a certain scale, and can be expressed as

$$\mathrm{Re} = \frac{v_{rms}\,\ell}{\nu}. \tag{2.2.7}$$

It is generally considered that fluid flow transitions from laminar to turbulent at $\mathrm{Re_c} \gtrsim 2000$ ($\mathrm{Re_c} = 2722$ - 2870, Reynolds 1883; $\mathrm{Re_c} = 2250$ - 2900, Pavelyev et al. 2003; $\mathrm{Re_c} = 2000$ - 3500, Durst and Ünsal 2006), but this limit is often approximated to be around 1000. Stellar flows are highly turbulent with $\mathrm{Re} \sim 10^{12}$ (Cristini et al., 2016*b*), which is due mainly to the length scales (10^9 cm) over which KE is transported, despite the high viscosity ($\nu \sim 320$) which is similar to that of tomato sauce. Turbulence within a convectively unstable region results in chaotic changes in the flow velocity, and near the convective boundary region has the overall effect of drawing in and mixing material from the surrounding convectively stable region. This mixing due to turbulence is referred to as turbulent entrainment. Turner (1973) defines entrainment as the transport of fluid across an interface between two bodies of fluid by a shear-induced turbulent flux. Examples of turbulent entrainment are shown in §5.2 and §6.2. Over time, the entrainment of material into the convective region across boundaries leads to a growth in the convective region. In turn, this shifts the boundary positions into the surrounding convectively stable regions over time. If the turbulent system is in a

quasi-steady state then this entrainment can occur within an equilibrium regime (see below for more details on the equilibrium entrainment regime). Although the boundary is not a flat surface, but an undulating one, and by tracking the centre of the boundary surface over time an entrainment velocity can be obtained.

Convective boundary stiffness

I refer to the stiffness of a convective boundary as its susceptibility to turbulent mixing over the boundary. The bulk Richardson number is one way to determine the stiffness of a boundary, it is the ratio of the specific stabilisation potential (analogous to the work done against convective motions by the boundary) to the specific TKE within the convective region. It is written as

$$\mathrm{Ri}_B = \frac{\Delta B \ell}{v_{rms}^2}, \tag{2.2.8}$$

where ℓ is the integral length scale which represents the size of the largest fluid elements and v_{rms} is the turbulent RMS velocity and represents the velocity of the largest fluid elements (at the integral scale) carrying most of the energy. ΔB is the buoyancy jump local acceleration over the boundary and is estimated by integrating the square of the buoyancy frequency over a suitable distance (Δr) either side of the boundary centre, r_c,

$$\Delta B = \int_{r_c-\Delta r}^{r_c+\Delta r} N^2 dr. \tag{2.2.9}$$

The integration distance Δr is not well defined theoretically but it should be large enough to capture the dynamics of the boundary region and the distance over which fluid elements are decelerated.

The buoyancy or Brunt-Väisälä frequency, N, is the frequency with which a perturbed fluid element will oscillate if it is surrounded by a stably stratified medium. This frequency is imaginary for a convectively unstable fluid element and is defined as:

$$N^2 = -g \left(\frac{\partial \ln\rho}{\partial r}\Big|_e - \frac{\partial \ln\rho}{\partial r}\Big|_s \right). \tag{2.2.10}$$

Bulk Richardson numbers less than 10 are associated with relatively soft convective

boundaries, whereas bulk Richardson numbers greater than 100 are associated with relatively stiff convective boundaries.

The equilibrium entrainment regime

If entrainment and the subsequent mixing of material occurs on a time scale similar to or smaller than the convective turnover time, then such mixing may be dominated by strong, individual outlier events. The convective turnover time is defined as:

$$\tau_c = \frac{2\ell_{cz}}{v_c}, \tag{2.2.11}$$

where ℓ_{cz} is the height of the convective region and for 1D stellar evolution equations v_c is given by Eq. 4.2.2, whereas for 3D hydrodynamic simulations v_c is replaced by the RMS velocity, v_{rms}, given by Eq. 2.2.2. If the time scale for the boundary migration due to entrainment, τ_b, is comparable to or larger than the convective turnover time scale, τ_c, then the turbulent mixing at the boundary is within the equilibrium entrainment regime (Fedorovich, Conzemius and Mironov, 2004; Garcia and Mellado, 2014).

Within this regime, the entrainment process is sampling the entire spectrum of turbulent motions rather than being sensitive to individual fluid elements, as mentioned earlier. This simplifies the development of mixing models within this regime, as the adopted prescription can be assumed to hold over the quasi-steady state of turbulence.

The entrainment law

The time rate of change of the boundary position through turbulent entrainment (the entrainment velocity), v_e, is known to have a power law dependence on the bulk Richardson number (Eq. 2.2.8), when the ratio of the entrainment velocity with the velocity of the large-scale fluid elements, $E = v_e/v_{rms}$, is considered (e. g. Garcia and Mellado, 2014). This relationship between the relative entrainment rate and the bulk Richardson number is referred to throughout the meteorological and atmospheric science fields as the entrainment law, and is typically given as:

$$E = \frac{v_e}{v_{rms}} = A\,\mathrm{Ri}_\mathrm{B}^{-n}, \tag{2.2.12}$$

where A and n are constants. A positive entrainment rate implies the radially

outward migration of the convective boundary over time, while a negative entrainment rate implies that the convective boundary is receding over time. Many simulations (e. g. Deardorff 1980) and laboratory (e. g. Chemel, Staquet and Chollet 2010) studies of a well-mixed thermally convecting layer within a stable stratification have found similar values for the coefficient, A, typically between 0.2 and 0.25. The exponent, n, is generally taken to be 1 for convectively driven turbulence with bulk Richardson numbers in the range $7 < \mathrm{Ri_B} < 100$ and $\mathrm{Pe} \gg 1$ (e. g. Turner, 1986; Fernando, 1991; Stevens and Lenschow, 2001). On the other hand, in a recent direct numerical simulation (DNS) study, Jonker et al. (2013) showed that $A \approx 0.35$ and $n = 1/2$ for small Péclet number, shear-driven entrainment. Entrainment rates for stellar convection typically vary between 10^{-1} and 10^{-5} (e.g. see Fig. 5.15).

2.2.3 Mean field analysis in the Reynolds-averaged Navier-Stokes framework

Turbulence is inherently a chaotic process, whereby energy is transferred from the largest scale turbulent elements down through to the smallest scale. Fluid elements at the largest scale determine the overall energy of the system, while those at the smallest scale are responsible for the dissipation of KE and where viscosity dominates the flow dynamics. It is common therefore, when studying turbulent flows to average them both spatially, to obtain a mean turbulent state over two dimensions, and temporally, to smooth out the stochastic nature of turbulence and provide a statistical average. In the hydrodynamics code that I use (see §3.4), the Euler equations are solved, which are an inviscid form of the Navier-Stokes equations of motion. When taking a Reynolds average (see Eq. 2.2.3) of the Euler equations, a new 'mean evolution' of the fluid flow can be represented, by averaging the three-dimensional profiles into a one-dimensional radial profile. Through Reynolds averaging, new correlations of fluctuating terms will appear, which sometimes provide new physical interpretations of this mean evolution of the fluid flow, and are often different from the physical interpretation of terms in the original equation (Ch.5 of Chassaing, 2002). Reynolds decomposition by construction separates the mean flow component from the fluctuating component, and so physically relevant terms can be constructed that represent competing processes for a given

conservation law. These include fluxes, sinks, sources and numerical effects (implied momentum diffusion). The mean radial (x) field is calculated by averaging over the horizontal plane (y-z), i.e. for a quantity ω

$$\langle\omega\rangle = \frac{1}{\Delta A}\int_{\Delta A} \omega \, \mathrm{d}A, \tag{2.2.13}$$

where $\mathrm{d}A = \mathrm{d}y\,\mathrm{d}z$ and $\Delta A = \Delta y\,\Delta z$ is the area of the computational domain along the radial axis. The original quantity can then be expressed as the sum of the mean and fluctuating components

$$\omega = \overline{\langle\omega\rangle} + \omega', \tag{2.2.14}$$

where the Reynolds average of the fluctuation is by definition zero, i.e. $\overline{\langle\omega'\rangle} = 0$. The over-bar notation denotes a temporal average and is defined below.

I apply this horizontal averaging to most[29] of the quantities that describe the flow. The simulations are set up in such a way that they begin with a violent turbulent transient phase, which 'kick-starts' the thermodynamic system, and turbulence begins to develop. Such a phase is initiated through random and equal (but small) perturbations in the density and temperature of the flow. As mentioned, this is a transient phase, and so following this the flow enters a quasi-steady state of turbulent convection, which is analogous to the physical fluid flow of the star. In such a state the kinetic energy driving is closely balanced by the viscous dissipation (e.g. see Fig. 5.10). As turbulence and turbulent events such as entrainment are chaotic by nature, I temporally average the fluid flow over this quasi-steady period of the hydrodynamic simulation. This provides a more statistically valid representation of the flow, and also smooths out many of the instantaneous fluctuations, provided the number of convective turnovers is large enough ($\gtrsim 3$). Of course, if the evolutionary time-scale becomes comparable to the convective turnover time-scale (e.g. during silicon burning) then such temporal averaging is not valid, as the quasi-steady state approximation breaks down in such cases. This temporal averaging is defined in the following way:

[29]The gravitational acceleration only has a mean component as the fluctuating component is zero, i.e. $g = \overline{\langle g\rangle}$. Such an assertion is made under the Cowling approximation, which states that the perturbations in the gravitational potential are negligible with respect to the local density.

$$\overline{\omega} = \frac{1}{\Delta t} \int_{t_1}^{t_2} \omega(t) dt \tag{2.2.15}$$

for an averaging window $\Delta t = t_2 - t_1$. I take averages of the TKE equation, and construct energy flux, source and dissipation terms. This averaged equation and the physical meaning of all of the terms are presented in Appendix A.2. This reduction of multi-dimensional data into horizontally- and temporally-averaged one-dimensional (1D) radial profiles allows the representation of the data obtained from hydrodynamic simulations within the context of 1D stellar evolution models. This is because stellar evolution models already implicitly include temporal and spatial averaging. Temporal averaging is included through the use of time-steps in 1D stellar evolution that are much larger than the convective turnover time, and spatial averaging due to the assumption of spherical symmetry. Such a comparison of averaged 3D data to 1D data allows the determination of the suitability of currently used prescriptions for convection in stellar evolution calculations (extent, additional mixing etc.), and also the ability to test new prescriptions based on the results of these multi-dimensional hydrodynamical simulations.

Chapter 3

Computational tools

3.1 1D stellar evolution models

The following information on the initial conditions and equations required to begin a stellar evolution calculation is adapted from Kippenhahn, Weigert and Weiss (2013) and Hansen and Kawaler (1994). The main parameters governing the evolution of stars are the initial mass, M, and metallicity, Z (or more accurately the abundances, X, of a pre-determined list of nuclear species). In addition to the mass and metallicity, initial estimations of the pressure, p_0, temperature, T_0, radius, r_0, and luminosity, L_0, are required. There are four main differential equations that can be used to describe the structure of the star. The independent coordinate for these equations is chosen to be the mass, m, within a radial distance, r. This allows an easier discretisation of the equations as the variation of mass is smoother than the variation of radius. These describe mass conservation, hydrostatic equilibrium, energy conservation and energy transport. These equations are:

$$\frac{\partial r}{\partial m} = \frac{1}{4\pi r^2 \rho}; \tag{3.1.1}$$

$$\frac{\partial p}{\partial m} = -\frac{Gm}{4\pi r^4}; \tag{3.1.2}$$

$$\frac{\partial L}{\partial m} = \epsilon_n - \epsilon_\nu - c_p \frac{\partial T}{\partial t} + \frac{\delta}{\rho}\frac{\partial p}{\partial t}; \tag{3.1.3}$$

$$\frac{\partial T}{\partial m} = -\frac{GmT}{4\pi r^4 p}\nabla, \tag{3.1.4}$$

where ϵ_n and ϵ_ν are the specific energy generation rate due to nuclear reactions and

neutrinos, respectively, the remaining variables have their usual meaning. A description of the composition evolution is also required

$$\frac{\partial X_i}{\partial t} = \frac{m_i}{\rho}\left(\sum_j R_{ji} - \sum_k R_{ik}\right), \quad i = 1, ..., I, \tag{3.1.5}$$

where X_i is the mass fraction of nuclear species i with mass m_i; R_{ji} and R_{ik} are the reaction rates for nuclear species $j \to i$ and $i \to k$, respectively.

The background temperature gradient, ∇, is taken to be equal to the radiative temperature gradient given by Eq. 2.1.11 if energy transport is dominated by radiation (and conduction). If the energy transport is dominated by convection then the temperature gradient, ∇, can be approximated as the adiabatic one given by Eq. 2.1.12, or more accurately obtained through a theory of convection such as the mixing length theory (see §2.1.2), for example.

In addition, an equation of state detailing the relationship between density, pressure, temperature and composition is needed, as well as boundary conditions for the star. Taking the radius and luminosity to be zero at the centre of the star ($m = 0$) would lead to a singularity, so in practice, the mass, luminosity and radius are said to be approaching zero at the centre. The first zone at a small radius contains non-zero values for these structure variables which are then extrapolated to the centre.

At the 'surface' of the star both the density and temperature are assumed to be approximately that of the surrounding vacuum, $\rho = T = 0$. To be precise, the surface of the star is taken to be the photosphere, and the surrounding features of the star such as the stellar wind are ignored and assumed to have no direct dynamical effect on the stellar interior, other than to reduce the total mass.

The stellar structure and composition are discretised onto a finite, one-dimensional grid, usually of non-uniform spacing. The resolution of the grid is adjusted over time based on the changes in certain stellar properties between grid points, if these changes exceed a pre-determined threshold[30] for that variable then the number of grid points in that region is increased. This helps to avoid discontinuities in the stellar profiles

[30]The grid mesh can be automatically adjusted based on the local change of the pressure, luminosity or abundance between adjacent grid cells. This adjustment can be set to occur when this change exceeds a value of typically a few percent.

and ensures a sufficiently resolved numerical representation of the problem.

Some codes (GENEC, for example, Eggenberger et al. 2008; see §3.2) will change the independent variable in Eqs. 3.1.1 - 3.1.4 from mass to pressure when computing solutions to these equations in the stellar envelope. In this region of the star, the pressure varies more than the mass with increasing radius, and this allows a better discretisation of the star onto the computational grid.

In order to calculate the initial stellar model, Eqs. 3.1.1 - 3.1.4 must be integrated over the mass of the star. This is not possible though, as the four boundary conditions mentioned earlier are split between the centre and the surface. Instead, a 'shooting method' is sometimes employed, whereby the structure is integrated from the surface inwards and the centre outwards, simultaneously, until a suitable fitting point is reached. This fitting point is usually chosen as the boundary between the stellar core and the envelope, as this is a natural position where the stellar profiles may become discontinuous. Kippenhahn, Weigert and Hofmeister (1967) defined an efficient method for calculating the boundary conditions over the $L - T$ parameter space used in the integration of the outer regions.

An alternative to the shooting method is to integrate the structure from the centre to a suitable fitting point, and the values of the structure variables over the remaining mass up to the surface are obtained through extrapolation.

It is more computationally efficient to spatially integrate Eqs. 3.1.1 - 3.1.4 first and then temporally integrate from Eq. 3.1.5 in an operator split approach. The exact method differs between codes, though, with some codes coupling both the structure and composition during the integration (e.g. MESA; Paxton et al. 2011). Although more computationally efficient, an operator split approach is inconsistent. For example, if following the spatial integration (given an initial composition), certain layers of the star become convectively unstable, this would then affect the compositional stratification during the temporal integration, i.e. convective motions will homogeneously mix the chemical components over those layers. Whereas, if the structure and composition were integrated simultaneously then the effect of a convectively unstable layer would be coupled to both the structure and the composition, and the resulting solution may be different than in the case where the composition and structure are de-coupled. This inconsistency due to operator splitting can be reduced by minimising the employed

time-step, but an underlying inconsistency will still be apparent, and the operator coupled approach is the more accurate. In the operator split approach in GENEC for example, in order to achieve a converged solution, the structure is first calculated, followed by a separate burning (fusion) and mixing (instantaneous or diffusive) phase of the composition. These two phases of the calculation are repeated in an iterative fashion until convergence is reached.

The next two subsections describe the numerical procedures for spatially and temporally integrating a stellar model beyond its initial conditions, respectively.

3.1.1 Spatial integration

The following is a description of the Henyey method (Henyey, Forbes and Gould, 1964), commonly adopted to solve the stellar evolution equations and follows the derivation presented in Kippenhahn, Weigert and Weiss (2013). Equations 3.1.1 - 3.1.4 can be more compactly written as

$$\frac{dy_j}{dm} = f_j\left(y_1, ..., y_4\right), \qquad j = 1, ..., 4, \tag{3.1.6}$$

where $y_1 = r,\ y_2 = p,\ y_3 = L,\ y_4 = T$. The derivatives on the left hand side of Eq. 3.1.6 can be replaced with finite differences between adjacent grid points on the mesh, and the arguments on the right hand side, y_j $(j = 1, ..., 4)$, can be evaluated at the geometric centre of each grid cell,

$$A_j^k = \frac{y_j^k - y_j^{k+1}}{m_j^k - m_j^{k+1}} - f_j\left(y_1^{k+1/2}, ..., y_4^{k+1/2}\right) = 0, \qquad j = 1, ..., 4,\ k = n, ..., 1, \tag{3.1.7}$$

where the index k represents the grid points of the model from the centre, $k = n$, to the surface, $k = 1$. The index $k + 1/2$ refers to the value between adjacent grid points and is usually represented by an average of those grid points. Suppose that the solution to Eq. 3.1.6 given some initial conditions, $M,\ X_i,\ p_0,\ T_0,\ r_0$ and L_0, results in $A_j^k \neq 0$. Corrections can then be added to each variable such that, $y_j^k(2) = y_j^k(1) + \delta y_j^k$, where (1) and (2) denote the first and second iterations, respectively. Equation 3.1.6 can then be written in such a way that

$$A_j^k(1) + \delta A_j^k = 0, \tag{3.1.8}$$

where if δA_j^k is sufficiently small, it can be expanded using a Taylor series up to first order, so that the corrections are linearised,

$$\delta A_j^k \approx \frac{\delta A_j^k}{\delta y_j^k}\, \delta y_j^k. \tag{3.1.9}$$

By inserting Eq. 3.1.9 into Eq. 3.1.8, it can be rewritten in matrix form as

$$HY = -X, \tag{3.1.10}$$

where H is called the Henyey matrix and contains the $4n-2$ ($j = 1, ..., 4$ with $k = n-1, ..., 2$, i.e. excluding the central and surface zones, there are also four boundary conditions for each variable at the centre, and two for the radius and luminosity at the surface, giving a total of $2 + 4(n-2) + 2 = 4n - 2$ equations) derivatives, $\delta A_j^k / \delta y_j^k$; Y is a vector containing the $4n-2$ corrections, δA_j^k; and X is a vector containing the equations A_j^k.

If Eq. 3.1.8 is still not satisfied, then another correction is made and the same process followed. These iteration steps are continued until a solution is obtained to within a chosen accuracy.

Of course, there may be instances where convergence to a solution is not possible. This could depend on several factors, such as: how different the initial approximation is from an attainable solution (expanding the corrections, δ_j^k, to second order may remedy this); the suitability of the mesh; or whether there is unphysical noise when interpolating lookup tables (for example in opacity tables). If a converged solution is found, then the whole process is repeated at the next time step.

3.1.2 Temporal integration

Generally, when integrating the composition in time, an implicit scheme is used, whereby the composition at the future time-step is calculated based on the rate of composition change at the future time-step. For a stellar model at the n^{th} time-step of the calculation this can be written as (ignoring specific grid points for now)

$$X_i^{n+1} = X_i^n + \Delta t \dot{X}_i^{n+1}, \qquad i = 1, ..., I, \tag{3.1.11}$$

where $\Delta t = t^{n+1} - t^n$, $\dot{X} = \partial X / \partial t$ and again the accuracy of such a method is determined by the size of the employed time-step.

In addition to the chemical composition, the last two terms in Eq. 3.1.3 also include time derivatives, and so the same implicit scheme (as in Eq. 3.1.11) is also used to obtain these differentials at the future time-step during the spatial integration. These two terms describe a change in the internal energy of the star due to local expansion or contraction.

The above describes the fundamental methodologies that are employed for discretising and solving the stellar evolution equations over multiple time-steps. In addition, a description or parameterisation for the various input physics of the models should be defined. Opacities, mass loss, nuclear reaction networks and the equation of state, among others are required to calculate a stellar model. As the employed methods for describing such input physics can vary greatly between stellar evolution codes, all of the possible options will not be described in this thesis, but instead a description of the specific stellar evolution code that is used in this study is described. Other notable stellar evolution codes which are used actively within the community are: MESA (Paxton et al., 2011); STERN (Brott et al., 2011); FRANEC (Chieffi and Limongi, 2013); KEPLER (Heger, Langer and Woosley, 2000); STAREVOL (Decressin et al., 2009); and PARSEC (Bressan et al., 2012).

3.2 The GENeva stellar Evolution Code

The Geneva stellar evolution code (GENEC; Eggenberger et al., 2008; Ekström et al., 2012) solves the stellar evolution equations given by Eqs. 3.1.1 - 3.1.5 using a finite differencing, de-coupled, time implicit method.

Up to the start of core oxygen burning it is assumed that the chemical composition is homogeneously mixed between time-steps in convective regions only; this is a valid assumption provided that the time-steps are longer than the convective turnover time

(Eq. 2.2.11). From oxygen burning and onwards compositional mixing is treated diffusively, and nuclear species are mixed according to their number concentration, C, given by (Eggenberger et al., 2008)

$$\rho \frac{\partial C}{\partial t} = \frac{1}{r^2} \frac{\partial}{\partial r} \left(r^2 \rho D \frac{\partial C}{\partial r} - r^2 \rho C v_D \right), \tag{3.2.1}$$

where D is the diffusion coefficient and v_D is the diffusion velocity.

In GENEC, the structure equations are de-coupled from the abundance equations; changes in abundances due to nuclear burning and diffusive mixing are calculated separately.

Reaction rates are calculated for a nuclear reaction network of 23 isotopes; these are: ^{1}H, ^{3,4}He, ^{12,13}C, ^{14,15}N, ^{16,17,18}O, ^{20,22}Ne, ^{24,25,26}Mg, ^{28}Si, ^{32}S, ^{36}Ar, ^{40}Ca, ^{44}Ti, ^{48}Cr, ^{52}Fe, and ^{56}Ni. These reaction rates are interpolated (based on the temperature) from the reaction tables by NACRE (Angulo et al., 1999); screening factors are also included through the prescription by Graboske et al. (1973). Using these rates, the nuclear energy generation rate can be calculated for the relevant channels. Energy losses due to the production and loss of neutrinos through the following mechanisms are also included (see Fig. 3.1): pair creation reactions; photo-neutrino reactions (Compton scattering); and plasma neutrino reactions (Itoh et al., 1989, 1996). The equation of state relates the pressure, density and temperature assuming a perfect gas, and includes radiation and partial degeneracy. Opacities are interpolated given the density and temperature from tables provided by the OPAL group (Rogers, Swenson and Iglesias, 1996) and Alexander and Ferguson (1994) for high and low temperatures, respectively. With these opacities, the energy transport due to radiative transfer of photons on nuclei can be calculated, see Eq. 2.1.17. The employed mass loss estimates are a function of metallicity, and calculated according to the prescriptions by Vink, de Koter and Lamers (2001) and de Jager, Nieuwenhuijzen and van der Hucht (1988) for massive stars. Energy transport due to convection is assumed to be adiabatic for deep internal convection, up to the start of core oxygen burning. For convective envelopes, and other diffusively mixed convective regions, energy transport is modelled using the mixing length theory with $\alpha_{ml} = 1.6$ (Schaller et al., 1992), as described in §2.1.2. The extent of convectively unstable regions, is determined by the Schwarzschild criterion

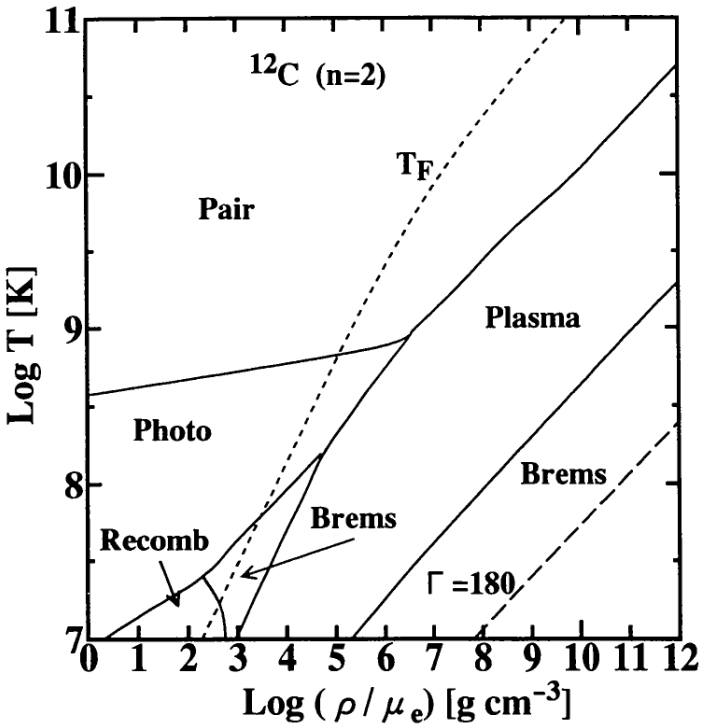

Figure 3.1: Dominant neutrino production mechanisms over the density-temperature plane for ^{12}C matter, including neutrino production through recombination and bremsstrahlung. Figure taken from Itoh et al. (1996).

(Eq. 2.1.14), along with penetrative convection (§2.1.3) of up to 20% (Stothers and Chin, 1991) of the local pressure scale height (for core hydrogen and helium burning phases). For the stellar model presented in §4.2 the extent of penetrative convection is shortened to 10% of the pressure scale height.

3.3 3D stellar hydrodynamic models

Unlike one-dimensional stellar evolution models, three-dimensional stellar hydrodynamic models generally focus on modelling the fluid dynamics of the stellar material while the star is dynamically stable. This requires much smaller time-steps. Such models typically use an initial structure determined from a stellar evolution model, and then calculate the flow dynamics, typically through solving some variation of the Navier-Stokes equations. The Navier-Stokes equation of motion for a viscous, compressible and homogeneous flow is

$$\rho\left(\frac{\partial \boldsymbol{v}}{\partial t} + (\boldsymbol{v}\cdot\boldsymbol{\nabla})\,\boldsymbol{v}\right) = \eta\boldsymbol{\nabla}^2\boldsymbol{v} + (\eta+\lambda)\,\boldsymbol{\nabla}\,(\boldsymbol{\nabla}\cdot\boldsymbol{v}) - \boldsymbol{\nabla}p + \rho\boldsymbol{g}, \tag{3.3.1}$$

where $\boldsymbol{v} = v(v_r, v_y, v_z, t)$ and $\boldsymbol{g} = g(0, 0, -g_0, t)$. η and λ are the first and second coefficients of viscosity, respectively. The kinematic viscosity, ν, is the ratio of the first coefficient (dynamic viscosity), η, to the fluid density, ρ. There are generally two approaches to turbulent fluid modelling; direct numerical simulations and large eddy simulations. The suitability of each approach to stellar interior simulations will be discussed.

3.3.1 Direct numerical simulations

Direct numerical simulations (DNS) are designed to have a grid spacing fine enough to capture the smallest turbulent length scales (i.e. the Kolmogorov scale, see §2.2.1), at which the dissipation of momentum through viscous forces becomes important. The difficulty comes in simultaneously modelling the largest length scales (at the integral scale) at which TKE is first generated and fed into the turbulent cascade, and also the dissipative scale. Often, the range of scales adopted in DNS is some subset between the two extremes which includes the Kolmogorov scale.

The number of grid points required for DNS of homogeneous, isotropic turbulence, which captures both the integral scale and the Kolmogorov scale (while maintaining a reasonable Courant number; see Eq. 1.4.1), is a function of the Reynolds number, $N^3 \sim \mathrm{Re}^3$. As an example, DNS of the (often assumed) transition from laminar to turbulent flow at $\mathrm{Re} \sim 1000$, would thus require 10^9 grid points, whereas the effective Reynolds number (see §3.3.2) that can be achieved for an equivalent number of grid points using a large eddy simulation (LES) is an order of magnitude higher ($\mathrm{Re} \sim 10^4$). Realistic DNS of stellar interiors are therefore not possible, as the integral scale cannot be effectively modelled. The integral scale is a required characteristic of the system, as it sets the scale and rate at which kinetic energy is dissipated into the turbulent cascade.

3.3.2 Large eddy simulations

LES type schemes focus on modelling the integral scale motions. In a similar manner to DNS, the imposed inertial sub-range is entirely modelled within the computational domain. Such an inertial sub-range is imposed because the dissipative scale coincides

with the grid-scale, whereby numerical dissipation is represented by a sub-grid scale (SGS) model. This means that the effective Reynolds number (a measure of the number of eddy sizes between advective and dissipative length scales) is smaller than the physical Reynolds number, as the dissipation range is encountered at the grid scale which does not usually coincide with the Kolmogorov scale. A physical representation then requires extrapolation of the model to realistic Reynolds numbers. This is possible for LES as the integral scale is correctly modelled and the rate of TKE dissipation is the same at all scales (see §2.2.2), with the caveat that the dissipation of energy below the grid scale (as detailed by the SGS model), must be physically realistic (energy conserving) and coupled smoothly to the resolved scales. Commonly adopted explicit SGS models are often a combination of two distinct methods: 'functional' models which utilise the addition of an artificial viscosity to the equations of motion (e.g. Garnier, Adams and Sagaut, 2009); and 'structural' models which use various methods to represent the stress tensor in the equation of motion, for example, approximate deconvolution (San et al., 2011), scale similarity (Bardina, Ferziger and Reynolds, 1980) or series expansions (Clark, Ferziger and Reynolds, 1979).

An alternative to using an explicit SGS model for the dissipation of energy below the grid scale is an implicit LES (ILES) scheme, where the SGS model is implied through the adopted numerical model (Garnier, Adams and Sagaut, 2009), rather than being explicitly defined as part of the physical model. The numerical errors in LES schemes are associated with the difference between the solutions to the Navier-Stokes equations on a finite grid and the exact, analytical solutions. Ghosal (1996) showed that these errors can be large in comparison to the sub-grid term which represents the SGS dissipation model. They also showed that if the order of the scheme is increased (up to eighth order), these errors can be reduced and can even be comparable to the sub-grid term at certain wave-numbers (see their figs. 4 and 7). This was the premise with which to develop the ILES scheme, whereby such errors due to the discretisation of the problem represent the numerical dissipation of the model.

Implicit large eddy simulations

ILES usually solve the inviscid Euler equations (Eqs. 3.4.1a - 3.4.1d), where focus is placed on the representation of the integral scale (largest eddies which are roughly the

size of the convective region) and the inertial range. In most turbulent systems the full inertial range and the scales at the Kolmogorov length can not be modelled while simultaneously modelling the integral scale. This is especially true in stars where the ratio of the integral scale (10^9 cm) to the Kolmogorov length-scale (1 cm; see Eq. 2.2.1) is of the order of 10^9, considering that the current limit of the number of vertical zones in 3D (cubic/spherical) simulations is approximately 2000 zones (e.g. Radice et al., 2016).

Kolmogorov (1962) showed that the rate of TKE dissipation at all scales does not depend on the details of the dissipative process. This implies that it may be unnecessary to resolve the dissipation sub-range of the cascade, providing that the sub-grid dissipation reproduces the Kolmogorov length, through its implied viscosity. In a turbulent flow the momentum diffusion (viscosity) is negligible in comparison to the advection of KE at all scales except near the Kolmogorov scale and below it. In ILES, the minimum amount of dissipation required in order to maintain monotonicity and energy conservation is adopted (Grinstein, Margolin and Rider, 2007). The implicit SGS model used in ILES is the leading order term in the truncation error, which is a result of discretising the Euler equations. This method incorporates the qualitative effects of dissipation at the grid scale, i.e. energy conservation, but information such as the time-scale[31] (e.g. cascade time over the unresolved inertial range) for such processes is lost in the numerics. Energy conservation is built into the ILES scheme; KE that cascades down to the sub-grid scales from the resolved scales is damped as the velocity fluctuations are dissipated. The internal energy of the fluid is suitably increased in such a way that it mimics viscosity at the Kolmogorov scale, which would dissipate the structures at this scale into heat.

Beyond the broad categories of the LES and DNS paradigms, many methods exist which are used to solve the Navier-Stokes or Euler equations. Here, the discussion is limited to just the piecewise parabolic method (PPM), as this is the only method that is incorporated into the hydrodynamic solver that is used.

[31]This time-scale for energy dissipation is generally much smaller than the convective turnover time for well resolved simulations.

3.3.3 Piecewise parabolic method

A description of the piecewise parabolic method (PPM) first requires an introduction to Godunov's method.

Godunov's Method

Godunov's method (Godunov, 1959; Godunov, Zabrodin and Prokopov, 1962) is a type of finite-volume method (FVM; see Eymard, Gallouët and Herbin 2003). FVMs are used to represent partial differential equations on a discretised geometry (such as a uniformly spaced mesh), where finite volume refers to the volume surrounding the centre of each grid cell. They utilise Gauss's theorem, in order to represent the integral of the divergence of a variable over the volume of the grid cell, with the integral of the flux of that variable (which is perpendicular to each cell wall), i.e. for a variable f, $\int_V (\nabla \cdot f) dV = \oint_S (f \cdot n) dS$, where V and S are the volume and surface area of the grid cell, and n is the normal vector of the cell interface. The fluxes at each cell wall can be reconstructed through interpolation of the cell's centre value. This method is easily applicable to two and three dimensions by calculating the flux over each cell edge in each dimension. The FVM also has the advantage of being a conservative method.

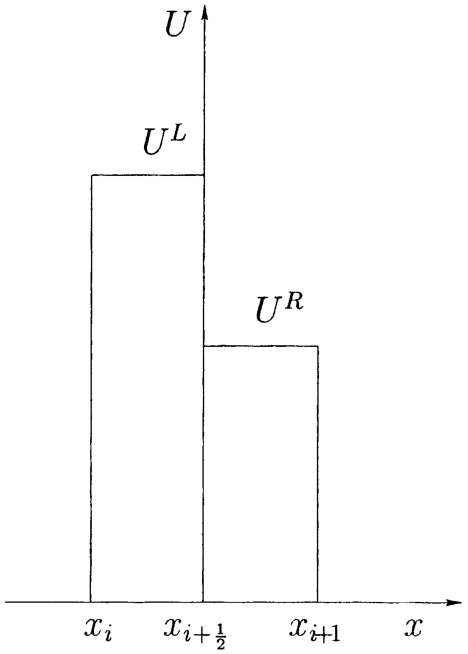

Figure 3.2: Example of a Riemann problem
Values of a variable, U, between two grid points: $U = U_L(x_i)$ and $U = U_R(x_{i+1})$. A discontinuity arises at the interface of the two grid points. This is an example of a Riemann problem. Adapted from Brocchini et al. (2001).

Godunov's method is an application of the FVM to discretised grids, where Riemann problems (see e.g. Toro, 1999) naturally arise. Riemann problems are initial value problems of conservation equations (e.g. an advection equation) that consist of piecewise data and discontinuities (see Fig. 3.2). Hence, they arise in FVMs due to the interpolation of cell values to the cell edges, resulting in discontinuities between cell interfaces.

PPM is a higher order extension of Godunov's method generally applicable to non-uniform computational grids. The PPM is reviewed to a high level of detail in Colella and Woodward (1984). Given initial conditions of zone centred average values, the values at the cell edges are interpolated over the cell using a 3^{rd} order polynomial in the form of a cubic parabola. An example of this interpolation is given by the density profiles in Fig. 3.3. Here it can be seen that the interpolations result in a profile that 'overshoots' ($r \sim 3.85 \times 10^8$ cm in the top panel) and 'undershoots' ($r \sim 4.25 \times 10^8$ cm in the top panel) at the boundaries; the advection of such profiles would result in numerical instability. The interpolation is therefore constrained further by disallowing the production of any new extrema, and forced to be a monotonous function between edge values (bottom panel of Fig. 3.3); this introduces discontinuities at the cell edges (Riemann problem). The same is done for all cells on the grid, so that the resulting profiles are piecewise continuous. If such a discontinuity is detected at one or both cell edges, then the cell boundary values are redefined by linear interpolations of the values in adjacent cells in order to remove the discontinuity at the interface.

The future time-step solution is calculated explicitly from the previous one. Considering the advection equation

$$\partial f/\partial t + \nabla \cdot (fu) = 0, \tag{3.3.2}$$

for a variable f, the spatial increment of f over the time-step is calculated by integrating from the cell edges over the advection distance. This distance is calculated from the local flow velocity, u, and the employed time-step; effectively this time-averages the flux of the variable f over the time-step. Calculated fluxes at each cell interface and each time-step can be discretised over the computational domain in order to be used in approximate conservation equations, e.g. a finite difference version of Eq. 3.3.2.

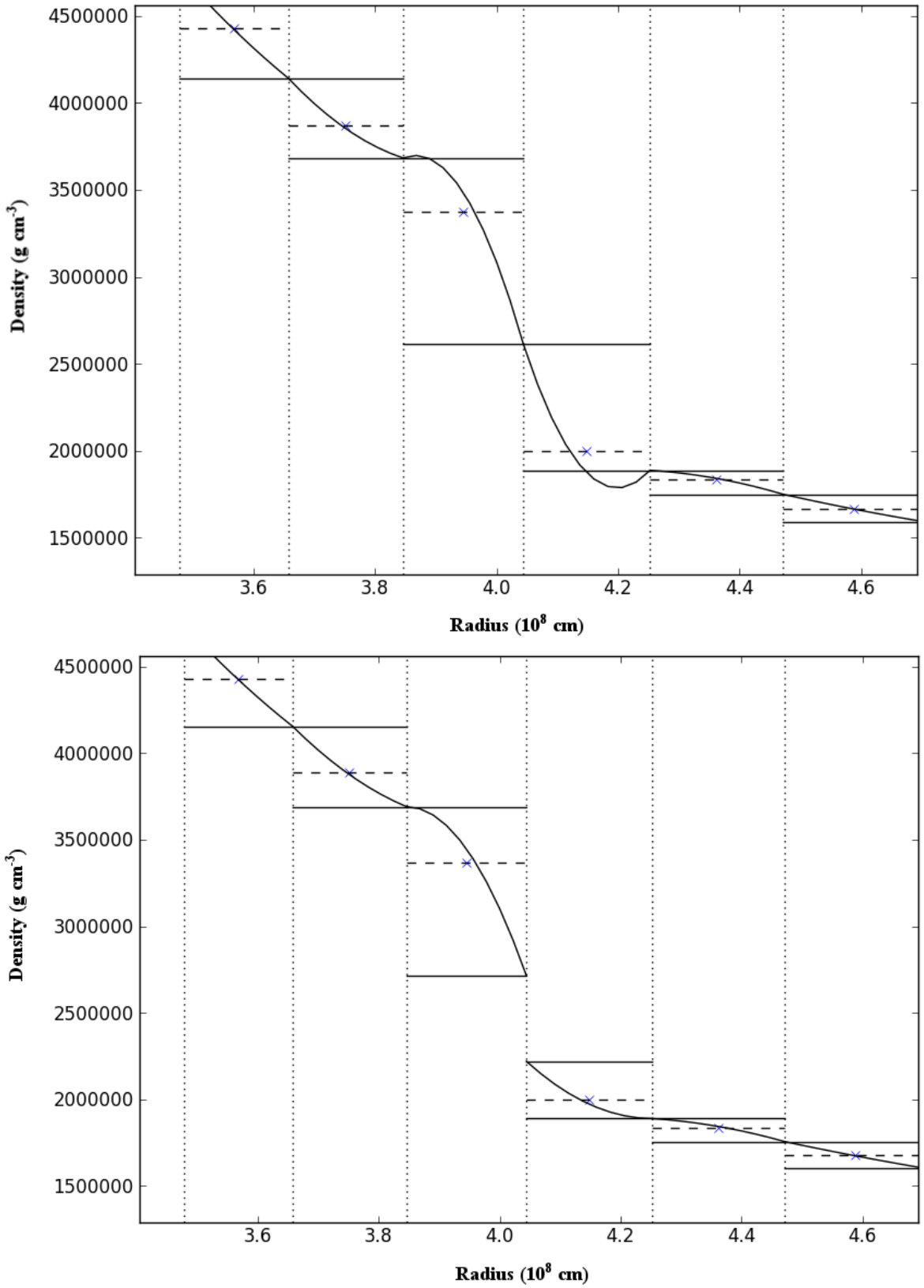

Figure 3.3: Radial density profiles calculated using a parabolic reconstruction, without enforcing monotonicity (top) and with monotonicity enforced (bottom). Vertical dotted lines denote the cell interfaces, blue crosses and horizontal dashed lines show the cell-centred values of the density and horizontal solid lines show the radial extent over which each parabola is defined. In the bottom panel monotonicity enforcement results in discontinuities at the cell interfaces, these discontinuities would be removed by redefining the boundary values before the solution is advected to the next time-step. Figures obtained from Viallet (2015).

The above steps in calculating the advection of variables over the domain, can be done within a Lagrangian framework and then remapped onto a spatial grid, or calculated directly within a Eulerian framework. Dissipation algorithms are also introduced in order to help capture shocks (super-sonic motion) in the gas, although the fluids studied here are universally sub-sonic.

PPM has been used extensively in different fluid dynamical problems, including numerous stellar hydrodynamic applications. Examples of recent studies that have used PPM to model stellar fluids are: Woodward, Herwig and Lin (2015); Cristini et al. (2016*a*); Jones et al. (2017). A more complete, but non-exhaustive list of studies which have utilised PPM is given in Appendix B.1.

3.4 The PROmetheus MPI code

The Prometheus MPI (PROMPI; Meakin and Arnett 2007*b*; where MPI is an acronym for message passing interface) code is a finite-volume, time explicit, Eulerian, PPM implementation of Colella and Woodward (1984) derived from the legacy astrophysics code PROMETHEUS (Fryxell, Müller and Arnett, 1989). PROMPI utilises domain decomposition in order to be parallelised over multiple processors. Communication between computational nodes is handled by MPI. PROMPI solves the Euler equations (inviscid approximation), given by:

$$\frac{\partial \rho}{\partial t} + \boldsymbol{\nabla} \cdot (\rho \mathbf{v}) = 0 \tag{3.4.1a}$$

$$\rho \frac{\partial \mathbf{v}}{\partial t} + \rho(\mathbf{v} \cdot \boldsymbol{\nabla})\mathbf{v} = -\boldsymbol{\nabla} p + \rho \mathbf{g} \tag{3.4.1b}$$

$$\rho \frac{\partial E_t}{\partial t} + \rho(\mathbf{v} \cdot \boldsymbol{\nabla})E_t + \boldsymbol{\nabla} \cdot (p\mathbf{v}) = \rho \mathbf{v} \cdot \mathbf{g} + \rho(\epsilon_{nuc} + \epsilon_{\nu}) \tag{3.4.1c}$$

$$\rho \frac{\partial X_i}{\partial t} + \rho(\mathbf{v} \cdot \boldsymbol{\nabla})X_i = R_i \tag{3.4.1d}$$

where E_t is the total energy, R_i is the rate of change of a nuclear species i, and the remaining variables have their usual meaning. These equations are solved within the ILES paradigm, where dissipation below the grid scale is implicitly implemented as the leading order term in the truncation errors; this is due to the discretisation of the Euler equations.

Domain boundary conditions are implemented for each dimension of the geometry. For a Cartesian geometry, a reflective[32] boundary condition is used in the vertical direction and periodic[33] boundary conditions are used in the horizontal directions. In the case of reflective boundary conditions, the velocities are damped near the domain boundaries either through an exponentially decaying or sinusoidal function. To ensure that structural changes within cells are temporally resolved, the time-step should be shorter than the local sound crossing time across the cell. PROMPI therefore employs a time-step that is in accordance with the CFL condition with a Courant factor of 0.8.

PROMPI also calculates Reynolds averages of 106 quantities during each calculation, removing the need for any post-process averaging of the raw data. Spatial averages are taken in the horizontal directions (y and z coordinates in the cubic Cartesian geometry) and running temporal averages are updated between each data output write sequence.

3.4.1 Micro-physics

The base hydrodynamics solver in PROMPI is complemented by various implementations of micro-physics.

Nuclear reaction network

A 25 isotope nuclear reaction network is included. These isotopes are: ^{1}H; ^{4}He; ^{12}C; ^{16}O; ^{20}Ne; ^{23}Na; ^{24}Mg; ^{28}Si; ^{31}P; ^{32,34}S; ^{35}Cl; ^{36,38}Ar; ^{39}K; ^{40,42}Ca; ^{44,46}Ti; ^{48,50}Cr; ^{52,54}Fe; and ^{56}Ni. Reaction rates are calculated using data from Rauscher and Thielemann (2000). Energy generation due to nuclear burning can then be calculated using these rates, or alternatively, estimated through a volumetric parameterisation of the main nuclear interaction branches (see e.g. §5.1).

Equation of state

The Helmholtz EOS (Timmes and Arnett, 1999; Timmes and Swesty, 2000) is used to describe the thermodynamic state of the plasma. Input variables are: temperature; density; average atomic mass; and average atomic number. Output variables include:

[32]The fluid flow has an elastic collision with the computational domain boundary.

[33]The fluid flow exits one side of the computational domain and enters through the opposite side of the computational domain along the same dimension.

pressure; total energy; entropy; many thermodynamical derivatives; and other useful quantities such as the local sound speed. This EOS assumes a Planck distribution of photon energies; an ideal gas of ions; and an electron-positron gas with arbitrary degrees of relativity and degeneracy. Corrections to the Coulomb potential (due to effects such as electron screening) are also included and implemented according to the work by Yakovlev and Shalybkov (1989).

Other physics

Self-gravity can be included for a variety of different geometries, and the effects of gravity perturbations are ignored under the Cowling approximation ($g' = 0$). Self-gravity is not included in the models presented here, but instead the gravitational acceleration is parameterised over the radius. The advection of multi-species fluids is also included. Opacities can be calculated analytically, by assuming Thomson scattering or more accurately interpolated given the density and temperature from data tables provided by the OPAL group (Kurucz, 1991; Iglesias and Rogers, 1996). The resulting diffusive flux of radiative energy throughout the plasma can also be calculated. In these models however, radiation transport is not considered as the convective heat transport is almost purely adiabatic. Convective heat transport is initiated in the model through small, random and equal perturbations in temperature and density. The loss of energy due to escaping neutrinos is parameterised using the analytical formula[34] provided by Beaudet, Petrosian and Salpeter (1967). This includes all of the relevant neutrino production processes: pair creation reactions; Compton scattering; and plasma neutrino reactions (see e.g. Fig. 3.1).

[34]The formula for the specific energy generation rate for neutrino cooling is:

$$\begin{aligned}\epsilon_\nu =& \frac{1.590\times10^{14}\lambda^8}{2(1+25.22\lambda)} + \frac{21.6\rho^2\lambda^2}{\rho+8.6\times10^5}(1+2.215\times10^{-6}\xi^2)e^{-4.5855\times10^{-3}\xi} \\ &+ 4.772\times10^2\lambda^2\rho\, e^{-2.5817\times10^{-5}\rho^{2/3}\lambda^{-1}},\end{aligned}$$

where $\lambda = k_B T/mc^2$ and $\xi = \rho^{1/3}\lambda^{-1}$.

Chapter 4

Parameter study of convectively unstable regions in a 15 $M_\odot$ stellar model

4.1 Motivations and methodologies

Convective boundary locations and convective boundary mixing has always been a well researched area within stellar evolution. This is because the extent of the convective region determines important aspects of the evolution, such as the lifetime of a burning phase and the mass of the core below the shell burning regions. This is particularly important for the final core masses in supernova progenitor models, but has also been shown to have importance in the onset of novae[35] and the propagation of flame fronts in degenerate cores. The correct choice of prescriptions for the extent of convection in stellar evolution codes, has always been a topic of debate and has been specifically questioned by several authors.

Renzini (1987) discusses the improper use of MLT and penetrative convection (referred to as overshooting). He reminds the reader that the mixing length in MLT, is the average length scale for the size of convective elements and also the average distance convective elements will travel before dissipating. Penetrative convection beyond the

[35]Novae occur when a white dwarf in a binary system with a low mass star accretes a critical amount of mass. Once this mass is reached, the temperatures are high enough for the CNO cycle to operate. As the matter is degenerate, this heating continues without expansion until the Eddington luminosity is reached, whereby the ignited layers are ejected, and the process can eventually recur.

convective boundary location is usually taken up to a distance of around 10% or 20% of a pressure scale height, i.e. a small fraction of the size of the convective elements which are penetrating the stable region. This leads to a physical limitation of the MLT, in that detailed information of the extra mixing processes that occur at the boundary of the order of a *fraction* of a pressure scale height, cannot be attained if the resolving power of the theory (the length-scale over which convective heat transport occurs) is of the order of *one* pressure scale height.

Gabriel et al. (2014) comment on the incorrect identification of the mass coordinate of the convective boundary, through two common methods used in stellar evolution codes. They show that a spherical convective boundary, can be defined as the position where the radial velocity, convective flux and kinetic energy flux are all zero, due to the absence of radial convective motions and the overturning of the flow. Correspondingly, the total flux at the boundary is equal to the radiative flux; this fact can be used in stellar models to determine the convective boundary position. However, due to the discretisation of the problem, the exact mass coordinate where the luminosity is entirely radiative must be obtained through interpolation, and this interpolation should be carried out from within the convective region. If the interpolation is carried out from the radiative side of the boundary, then the inferred mass coordinate of the boundary will be incorrect, and leads to an over-prediction of the core mass (Castellani, Giannone and Renzini, 1971).

A more common method of identifying the mass co-ordinate of the boundary is by searching for a change in sign of $\nabla_{rad} - \nabla_{ad}$ (Schwarzschild criterion; Eq. 2.1.14), and then interpolating to the exact mass coordinate where this function is zero. Again, if this interpolation is carried out on the radiative side of the boundary this will result in either an under-estimated or over-estimated mass for the convective region.

Viallet et al. (2015) do not point out the incorrect use of prescriptions for determining convective boundary locations, but instead suggest specific prescriptions for different mixing regimes within stars, based on the Péclet number (see §4.2). The various regimes and suggested implementations are discussed in §2.1.3.

An uncertainty between stellar models of the same mass has also been demonstrated, due to the use of different prescriptions for the extent of convective instability. Martins and Palacios (2013) show a large uncertainty in the post main sequence

evolution of six stellar models of a $20\,M_\odot$ star from different codes. While Georgy, Saio and Meynet (2014) demonstrate the differences that arise when using either the Schwarzschild or Ledoux criteria to determine the extent of the intermediate hydrogen burning shell in a massive star. They show the onset of core helium burning is delayed in the case that uses the Ledoux criterion, and the mass and position of the intermediate hydrogen burning shell is also changed, which in turn affects the morphology of the convective envelope.

The above demonstrates that there are many uncertainties on how the convective boundaries should be treated in 1D stellar evolution codes. This further confirms that the use of 3D hydrodynamical simulations is required in order to accurately follow the fluid flow, instabilities and mixing processes that occur in stars from first principles. This area is explored in this thesis by evolving a 3D hydrodynamical model using a 1D stellar evolution model as the initial conditions (§5 and §6). In order to decide which convective phase was best suited to study, given the available resources (physical time and CPU time), a parameter study on the various convective boundaries that appear during the evolution of a 1D stellar evolution model was performed. As well as providing insight into which boundaries are most suited for a 3D hydrodynamical study, this parameter study can help identify possible trends over the stellar lifetime.

4.2 Results and discussions

A $15\,M_\odot$, solar metallicity, non-rotating stellar model was chosen to perform the parameter study. This stellar model was evolved using GENEC (§3.2), up to the end of the oxygen burning phase. All the convective boundaries that were present during the model were analysed, including convective cores and shells[36], with the exceptions of the hydrogen and neon burning shells and the convective envelope[37]. The structure was analysed at the start, maximum mass extent (for all cores except hydrogen and helium) and the end of each burning phase. Fig. 4.1 shows the evolution of the con-

[36]Convective shells appear at higher mass co-ordinates than cores and usually ignite after the extinction of the related core burning region.

[37]These shells were not included as their structure was complicated, and the envelope was not included as only deep interior convection was of interest.

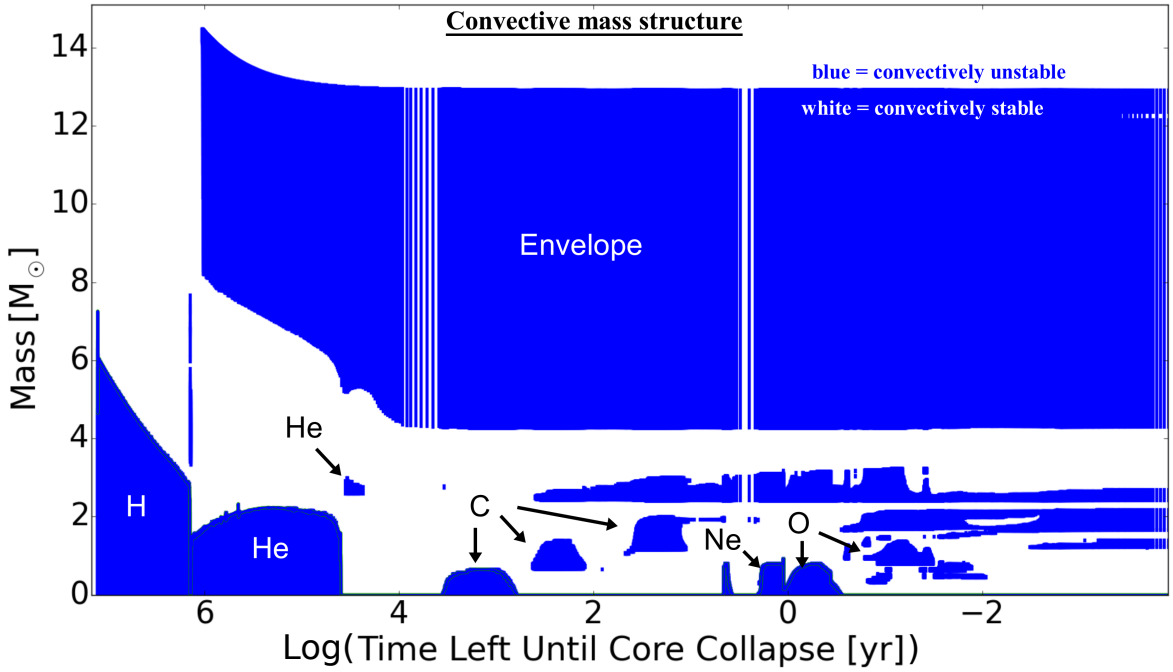

Figure 4.1: Convective structure evolution (Kippenhahn) diagram of a $15\,M_\odot$ stellar model up to the end of oxygen burning. The interior mass is plotted on the vertical axis in units of solar masses and the log of the time remaining until the predicted collapse of the star in units of years is on the horizontal axis. Coloured areas represent convectively unstable regions, with the corresponding labels denoting the nuclear species that serves as fuel in the most dominant nuclear reaction. There is no nuclear burning in the envelope; convection arises due to the opacity of the material (see §1.2.1). Note that, these plots are produced by drawing blue vertical lines which represent convectively unstable regions at various time-steps of the model. Thus, the vertical white lines at 'time left until core collapse' ~ 4 and other times are a consequence of the plotting technique, hence the regions between neighbouring blue lines remain convective.

vective mass structure of the stellar model (see also Fig. 4.5). The nuclear species that serves as fuel in the most dominant nuclear reaction is annotated for the majority of the convective regions.

The following quantities were considered to be informative of the structure and evolution of the various convective regions within the model: the gravitational acceleration; convective velocity; MLT velocity (Eq. 2.1.23); buoyancy jump (Eq. 2.2.9); pressure scale height (Eq. 2.1.8); total luminosity; mean molecular weight (Eq. 2.1.2); and the number of convective turnovers. Several important dimensionless numbers were also calculated: the bulk Richardson number (Eq. 2.2.8); Mach number (Eq. 4.2.4); Péclet number (Eq. 4.2.5); and Damköhler number (Eq. 4.2.7). Except for the bulk Richardson number and total luminosity all of the quantities were mass averaged over the convective region. The total luminosity was taken as the peak radial value and the bulk Richardson number is a property of each boundary. The mass average of a quantity A is defined as:

$$A_{\text{avg}} = \sqrt{\frac{1}{m_2 - m_1} \int_{m_1}^{m_2} A^2(m)\, dm}, \tag{4.2.1}$$

where m_1 and m_2 are the masses at the lower and upper convective boundaries, respectively.

The convective velocity is estimated from the convective flux and is given by (Arnett, 2016):

$$v_c = \left(\frac{F_c}{\rho} \right)^{\frac{1}{3}}, \tag{4.2.2}$$

where F_c is the convective flux. The approximate number of convective turnovers during each burning phase is estimated according to:

$$N_t = \frac{\tau_{burn}}{\tau_c} \tag{4.2.3}$$

where τ_{burn} is the approximate lifetime of each burning phase and τ_c is the convective turnover time.

The flow speed and sound speed, c_s, are needed to calculate the Mach number. The convective velocity was used for the former, and the latter was calculated using the

Helmholtz EOS (§3.4.1). The Mach number is

$$\mathrm{Ma} = \frac{v_c}{c_s}. \tag{4.2.4}$$

The Péclet number (Pe) is defined as the ratio of heat transfer through conduction, to heat transfer through advective motions, using characteristic time-scales for each process. In the stellar case, thermal diffusion dominates over molecular diffusion. For the deep interior, conductive heat transfer plays a minor role, so typically $\mathrm{Pe} \gg 1$. The Péclet number was determined from a ratio of diffusivities using the following formula:

$$\mathrm{Pe} = \frac{3D_{mlt}}{\chi}, \tag{4.2.5}$$

where D_{mlt} is the diffusion coefficient determined from MLT (Eq. 2.1.2) and χ is the thermal diffusivity, defined as

$$\chi = \frac{16\sigma\, T^3}{3\kappa\, \rho^2\, c_p} \tag{4.2.6}$$

where κ is the opacity and c_p is the specific heat at constant pressure.

The Damköhler number (Da) is defined as the ratio of the advective time-scale to the nuclear reaction time-scale. Generally, this is a small value in deep convective regions as the time-scale for nuclear reactions is long, but during the advanced stages of massive star evolution the two time-scales can become comparable. The Damköhler number was determined using the following formula:

$$\mathrm{Da} = \frac{\tau_c}{\tau_{nuc}} = \left(\frac{2\ell_{cz}}{v_c}\right)\left(\frac{\epsilon_{nuc}}{qX_i}\right), \tag{4.2.7}$$

where ℓ_{cz} is the height of convective region, q is the specific energy released for the dominating reactions, X_i is the mass abundance of the interacting particle and ϵ_{nuc} is the nuclear energy generation rate.

One additional key property of the advanced convective regions in massive stars is the radial extent (see Fig. 4.2 and the radial contours in Fig. 4.5). It is often easier to express the extent of the convective regions in terms of an average of the pressure scale height over the convective region. For the mass range that was considered ($15\,\mathrm{M}_\odot$), such deep convective regions typically span only a few pressure scale heights

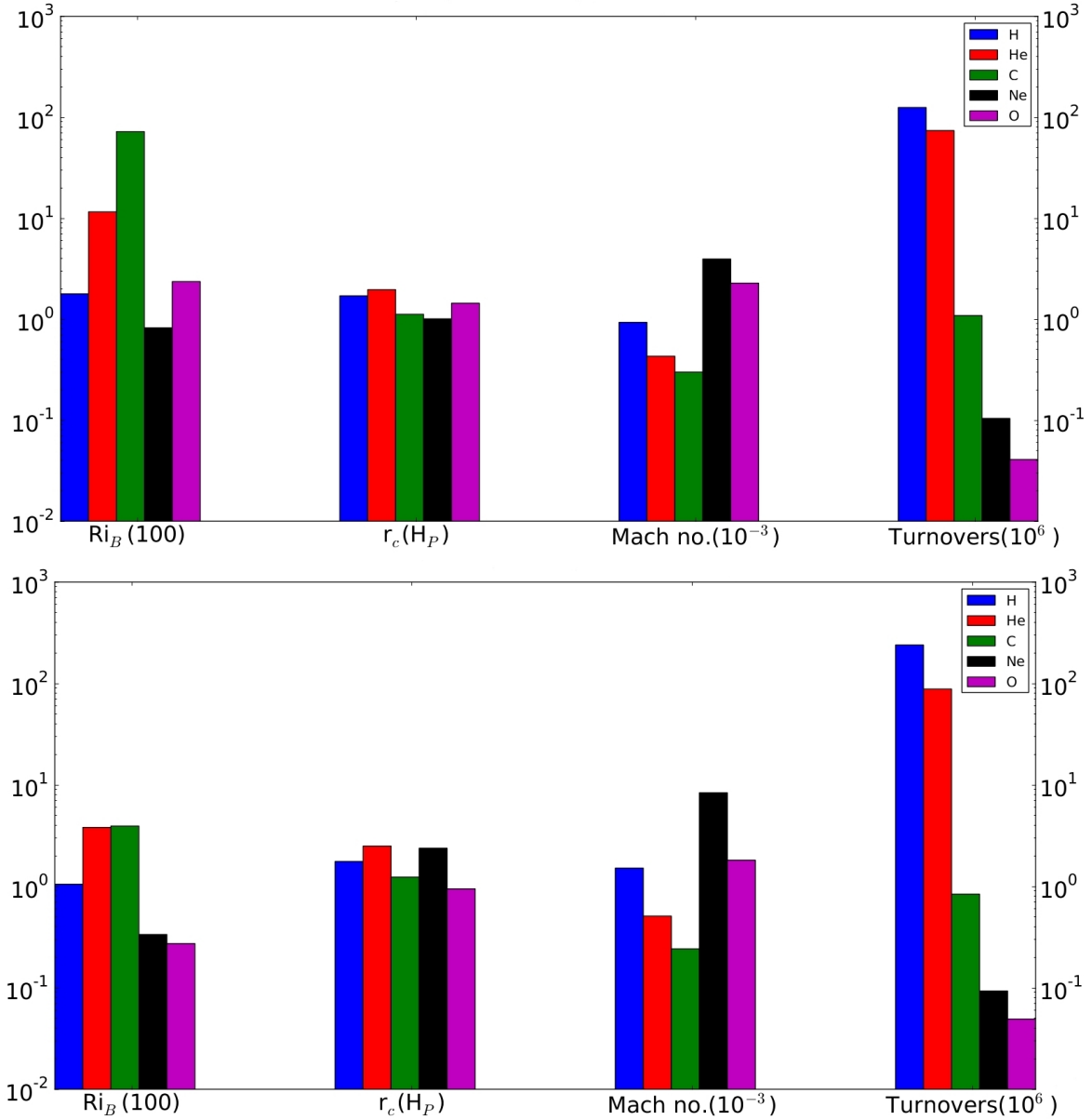

Figure 4.2: Initial (top panel) and final (bottom panel) core properties of different burning phases: hydrogen (blue); helium (red); carbon (green); neon (black); and oxygen (magenta). From left to right along the horizontal axis are: the bulk Richardson number (normalised by 100); core radius normalised by the mass averaged pressure scale height in the core; mass averaged Mach number within the core (normalised by 10^{-3}); and the estimated number of turnovers for the entire phase (normalised by 10^{6}).

$(0.2 - 5)$. Consequently, convective motions might be expected to resemble at least some characteristics of the classical description of convective rolls[38] proposed by Lorenz (1963), a hypothesis that shows some validity according to the results of Arnett and Meakin (2011*b*).

The above quantities are summarised throughout Tables 4.1 and 4.2 and Figs. 4.2 - 4.4. It is important to note that these quantities are only approximations to the physical case and thus should only be used as order of magnitude estimates.

From Table 4.1, it can be seen that the general trend is for the gravitational acceleration, peak luminosity and mean molecular weight to increase as the star evolves. The gravitational acceleration ranges from around $10^5\,\mathrm{cm\,s^{-2}}$ in the early stages to around $10^9\,\mathrm{cm\,s^{-2}}$ during the later stages. The peak luminosity ranges from around $5 \times 10^{37}\,\mathrm{erg\,s^{-1}}$ during the start of helium core burning up to $2 \times 10^{44}\,\mathrm{erg\,s^{-1}}$ at the end of neon core burning. The mean molecular weight ranges from 0.627 at the start of core hydrogen burning up to 1.92 at the end of oxygen shell burning. These increasing trends are due to the centre of the star becoming denser as the star evolves. In turn, this leads to higher temperatures (and therefore luminosities), which facilitates the fusion of heavier nuclei (thermal kinetic energy overcomes the Coulomb potential barrier), resulting in an increase in the mean molecular weight. The general trend for the pressure scale height is a decrease over the stellar lifetime. It ranges from $5 \times 10^{10}\,\mathrm{cm}$ during core hydrogen burning down to $1 \times 10^8\,\mathrm{cm}$ during shell oxygen burning. This decreasing trend is a result of the increase in pressure and its radial gradient as the interior regions become denser, and therefore the distance between pressure e-foldings becomes shorter (a smaller pressure scale height).

From Table 4.2 it can be seen that the general trend is for the convective velocities and the Mach, Péclet and Damköhler numbers to increase as the star evolves. The convective velocities range from about $5 \times 10^4\,\mathrm{cm\,s^{-1}}$ during the early phases, to several times $10^6\,\mathrm{cm\,s^{-1}}$ during the advanced phases. The Mach number ranges from a few times 10^{-4} (values lowest for helium and carbon burning) to close to 10^{-2}. Note that, the Mach number may still increase further during silicon burning as the core region becomes denser, and also during the early collapse as found by Müller et al. (2016).

[38]These are two-dimensional global convective motions induced by buoyancy, which represent the rolling of matter.

Phase	g ($\mathrm{cm\,s^{-2}}$)	L ($\mathrm{erg\,s^{-1}}$)	H_P (cm)	μ
H Core Start	8.7×10^{4}	7.5×10^{37}	5.1×10^{10}	0.627
H Core End	9.0×10^{4}	1.5×10^{38}	3.6×10^{10}	1.21
He Core Start	1.8×10^{6}	4.6×10^{37}	5.1×10^{9}	1.36
He Core End	2.4×10^{6}	1.2×10^{38}	4.2×10^{9}	1.71
C Core Start	4.3×10^{7}	5.9×10^{38}	8.9×10^{8}	1.77
C Core Max	4.6×10^{7}	5.6×10^{38}	8.3×10^{8}	1.78
C Core End	5.0×10^{7}	6.1×10^{38}	8.8×10^{8}	1.87
Ne Core Start	4.8×10^{8}	1.7×10^{43}	2.3×10^{8}	1.81
Ne Core Max	4.1×10^{8}	1.4×10^{44}	2.1×10^{8}	1.83
Ne Core End	4.2×10^{8}	2.1×10^{44}	2.1×10^{8}	1.83
O Core Start	4.5×10^{8}	5.2×10^{42}	2.3×10^{8}	1.84
O Core Max	5.0×10^{8}	7.4×10^{42}	2.0×10^{8}	1.86
O Core End	5.1×10^{8}	3.1×10^{42}	2.5×10^{8}	1.91
He Shell Start	7.4×10^{7}	5.2×10^{39}	5.5×10^{8}	1.76
He Shell End	7.2×10^{7}	1.6×10^{39}	6.3×10^{8}	1.74
C Shell Start	2.3×10^{8}	2.0×10^{41}	2.5×10^{8}	1.8
C Shell IC[a]	2.0×10^{8}	1.0×10^{41}	2.8×10^{8}	1.8
C Shell End	2.1×10^{8}	3.3×10^{40}	2.9×10^{8}	1.8
O Shell Start	1.3×10^{9}	1.6×10^{41}	1.2×10^{8}	1.88
O Shell End	1.5×10^{9}	3.7×10^{42}	1.0×10^{8}	1.92

[a] Properties of the 1D model used as initial conditions for the 3D simulations.

Table 4.1: Gravitational acceleration ($\mathrm{cm\,s^{-2}}$), luminosity ($\mathrm{erg\,s^{-1}}$), pressure scale height (cm) and mean molecular weight at different times during core and shell burning phases of a $15\,\mathrm{M}_\odot$ stellar model. Except for the luminosity which is the peak value, all other values were mass averaged over the convective region.

Phase	v_c ($\mathrm{cm\,s^{-1}}$)	$\mathrm{Ri_B}$	Ma	Pe	Da
H Core Start	6.9×10^4	1.8×10^2	9.3×10^{-4}	$\sim 10^3$	3.8×10^{-8}
H Core End	9.7×10^4	1.1×10^2	1.5×10^{-3}	$\sim 10^3$	7.2×10^{-7}
He Core Start	4.7×10^4	1.2×10^3	4.3×10^{-4}	$\sim 10^4$	1.8×10^{-7}
He Core End	5.9×10^4	3.8×10^2	5.1×10^{-4}	$\sim 10^5$	3.0×10^{-6}
C Core Start	6.9×10^4	7.2×10^3	3.0×10^{-4}	$\sim 10^6$	3.4×10^{-6}
C Core Max	5.6×10^4	1.2×10^4	2.4×10^{-4}	$\sim 10^7$	1.2×10^{-5}
C Core End	5.8×10^4	3.9×10^2	2.4×10^{-4}	$\sim 10^7$	1.8×10^{-5}
Ne Core Start	1.5×10^6	82	3.9×10^{-3}	$\sim 10^{10}$	3.3×10^{-3}
Ne Core Max	6.4×10^5	3.6×10^2	1.9×10^{-3}	$\sim 10^{10}$	5.5×10^{-3}
Ne Core End	4.1×10^5	62	1.1×10^{-3}	$\sim 10^{10}$	2.6×10^{-3}
O Core Start	8.8×10^5	2.4×10^2	2.2×10^{-3}	$\sim 10^{10}$	6.3×10^{-4}
O Core Max	7.9×10^5	8.5×10^4	2.0×10^{-3}	$\sim 10^{10}$	2.4×10^{-3}
O Core End	7.5×10^5	27	1.8×10^{-3}	$\sim 10^{10}$	2.0×10^{-3}
He Shell Start	1.4×10^5	46 (20)	8.9×10^{-4}	$\sim 10^6$	5.7×10^{-8}
He Shell End	1.3×10^5	14 (1.8×10^3)	9.1×10^{-4}	$\sim 10^6$	1.0×10^{-7}
C Shell Start	3.6×10^5	4.2×10^2 (6.0×10^3)	1.3×10^{-3}	$\sim 10^8$	1.3×10^{-4}
C Shell IC[a]	2.9×10^5	6.9×10^2 (1.5×10^4)	1.2×10^{-3}	$\sim 10^8$	2.0×10^{-4}
C Shell End	1.6×10^5	59 (6.5×10^4)	5.7×10^{-4}	$\sim 10^7$	1.3×10^{-4}
O Shell Start	1.5×10^5	3.7×10^4 (4.0×10^4)	3.4×10^{-4}	$\sim 10^{10}$	2.7×10^{-4}
O Shell End	5.7×10^5	1.2×10^2 (3.4×10^4)	1.3×10^{-3}	$\sim 10^{10}$	1.4×10^{-3}

[a] Properties of the 1D model used as initial conditions for the 3D simulations.

Table 4.2: Estimates of the convective velocity ($\mathrm{cm\,s^{-1}}$), Bulk Richardson number, Mach number, Péclet number and Damköhler number of different times during core and shell burning phases of a $15\,\mathrm{M_\odot}$ stellar model. Bulk Richardson numbers are boundary values, brackets indicate values at the lower boundary, all other values were mass averaged over the convective region.

The Péclet number is always much larger than one, with a minimum of around 1000 during hydrogen burning and up to 10^{10} during the advanced phases. Radiative effects may still dominate at smaller scales. One can define a length scale, ℓ_d where eddies of this size would be strongly affected by thermal diffusion (Viallet et al., 2015). Within the entrainment regime, this length scale is small and close to the Kolmogorov length scale. Viallet et al. (2015) categorise the early stages of stellar evolution to be within a 'penetrative regime' where this length-scale is much larger, therefore the convective boundary layer consists of a well mixed nearly adiabatic layer above which a layer dominated by thermal diffusion lies. As mentioned in §1.5.2, for most of the convective phases the evolutionary (or nuclear) time-scale is much larger than the advective time-scale (Da $\sim 10^{-7}$ for hydrogen burning). Only during the later stages of evolution do these time-scales become closer (Table 4.2; Da $> 10^{-4}$).

From Fig. 4.2 it can be seen that the radial extent is on the order of a few pressure scale heights for each burning region, and does not change significantly during their evolution. The number of convective turnovers during hydrogen and helium burning is roughly the same, but decreases as the star evolves through the advanced burning phases. This is due to a very large increase in the number of plasma neutrinos produced during the advanced phases, in combination with increased energy generation rates. This leads to shorter evolutionary time-scales and faster extinction of the convective region (see also Arnett, 1996, pg. 284 - 292).

4.2.1 Convective boundary evolution

Another important result relates to the bulk Richardson number ($\mathrm{Ri_B}$). In order to approximate $\mathrm{Ri_B}$ from a 1D model, its defining quantities must be substituted with quantities from a stellar model that are physically analogous. The integration distance, Δr, is not well defined theoretically but it should be large enough to capture the dynamics of the boundary region and the distance over which the fluid elements are decelerated. The integration length, Δr, is hence taken to be one quarter of the local pressure scale height. As the integral length scale, ℓ, is often taken to be the horizontal correlation length and Meakin and Arnett (2007*b*) show that the horizontal correlation length scale and pressure scale height are similar to within a factor ~ 3, I approximate

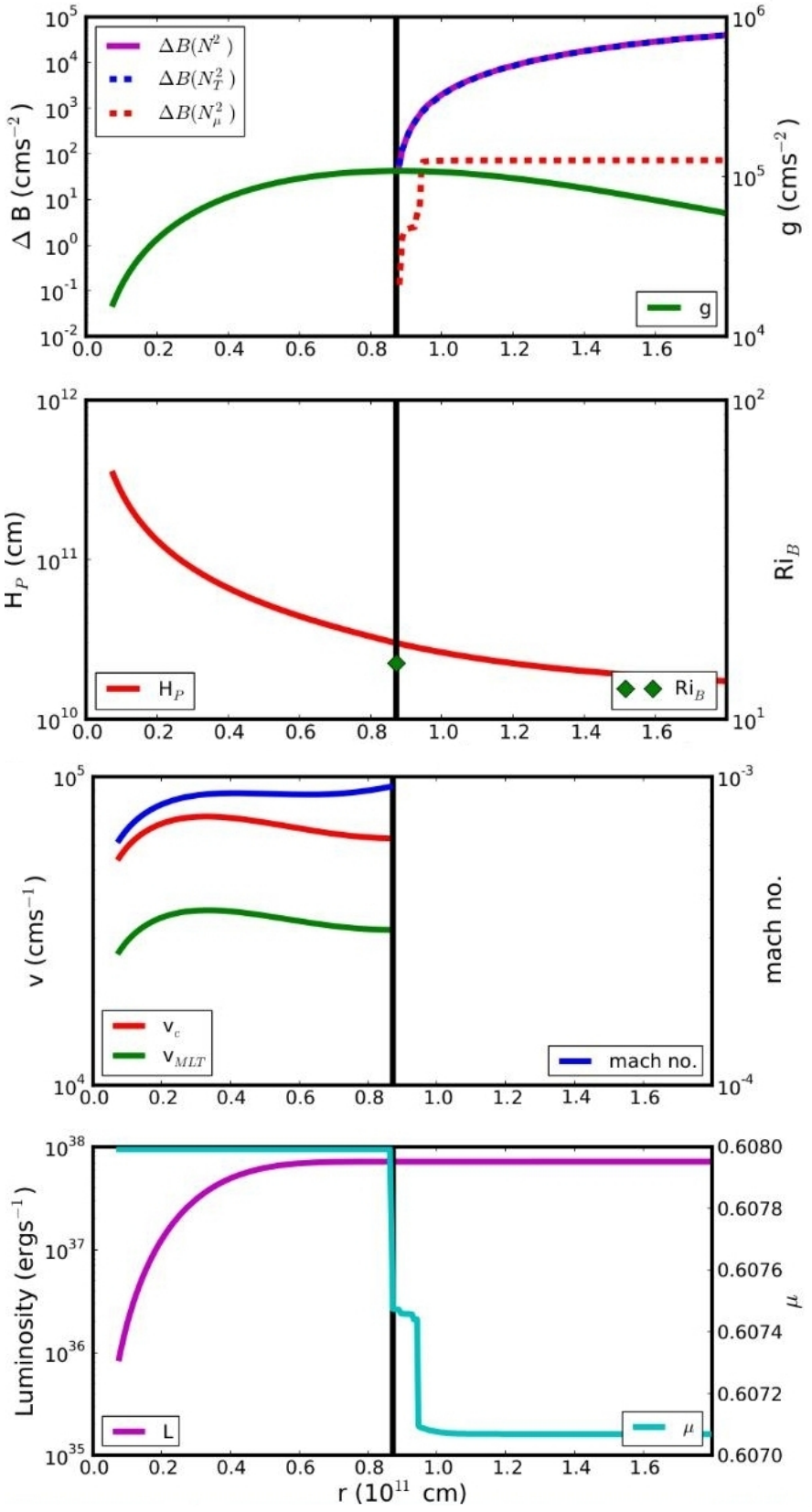

Figure 4.3: Structure properties of the start of core hydrogen burning as a function of radius (0.3% of fuel burnt). *Top panel* - Buoyancy jump (ΔB; magenta) and its components, thermal ($\Delta B(N_T^2)$; blue dashed) and compositional ($\Delta B(N_\mu^2)$; red dashed) and gravitational acceleration (g; green). *Second panel* - Pressure scale height (H_P; red) and bulk Richardson number (Ri$_B$; green diamond). *Third panel* - Convective (v_c; red), mixing length theory (v_{mlt}; green) velocities and Mach number (Ma; blue). *Bottom panel* - Luminosity (L; magenta) and mean molecular weight (μ; cyan). Vertical black lines represent radial positions of convective boundaries.

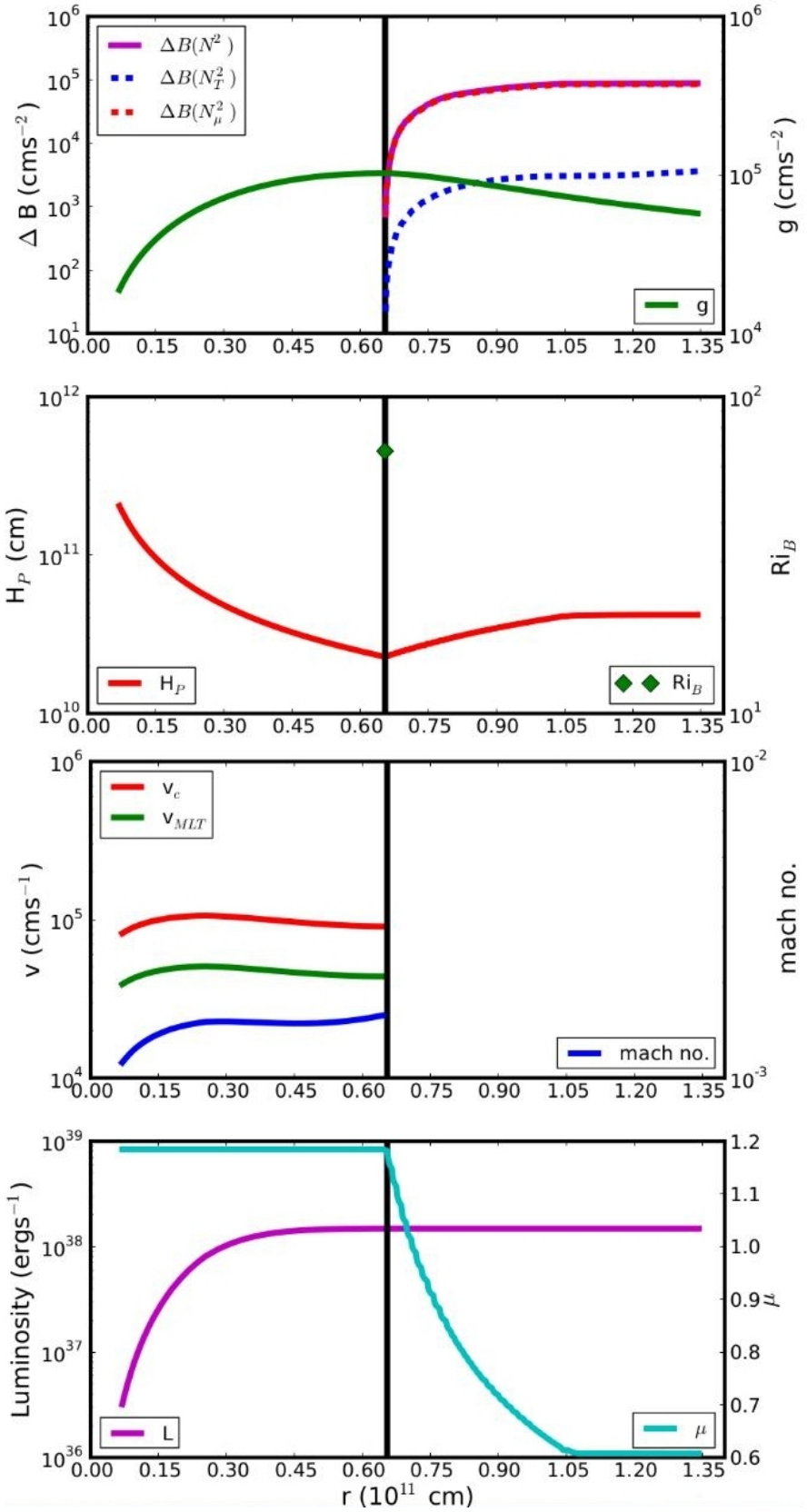

Figure 4.4: Structure properties of the end of core hydrogen burning as a function of radius (90.5% of fuel burnt). Curves, colours and lines are the same as in Fig. 4.3.

the integral scale as half of the local pressure scale height. The RMS turbulent velocity is approximated as the convective velocity, v_c, as this is one of only two choices (the other being the mixing length velocity) for the flow velocity in 1D stellar evolution models.

A key factor in the $\mathrm{Ri_B}$ is the buoyancy jump at the boundary (Eq. 2.2.9) which has contributions from both entropy and mean molecular weight (μ) gradients. At the start of burning stages, the entropy gradient or thermal component of N^2 dominates (e.g. see top panel of Fig. 4.3). However, as nuclear burning proceeds, the μ gradient increases and this compositional component starts to dominate over the thermal component. Even during the hydrogen burning phase where the convective core continuously recedes, the μ gradient ultimately dominates over the thermal component. This can be seen in Fig. 4.4, where at the end of core hydrogen burning, the molecular weight has risen due to the production of a helium rich core. This leaves behind a large molecular weight gradient, due to the recession of the core revealing previous mixing signatures. The jump in buoyancy across the boundary is due mainly to this large compositional gradient, and acts as a barrier against CBM. The magnitude of the buoyancy jump increases during the evolution of the core, resulting in a stiffening of the boundary as shown by an increase in $\mathrm{Ri_B}$.

During the advanced burning stages (C, Ne, O, and Si burning), the convective core grows throughout most of each stage and the boundary becomes stiffer as μ gradients increase. As the end of the burning stage is approached, the convective regions recede and the boundary stiffness decreases as the μ gradient is weakened. These trends can explain the evolution of $\mathrm{Ri_B}$ observed in the model (see Table 4.2).

Comparing values of $\mathrm{Ri_B}$ between all of the different phases, it was found in general that the boundary was at its stiffest during the maximum mass extent of the convective cores and the start of the convective shells. The boundaries were softest at the very end of each burning stage. The values estimated for the $\mathrm{Ri_B}$ for core carbon and oxygen burning agree well with the trend described above. The evolution of $\mathrm{Ri_B}$ for the other core burning stages, however, does not necessarily follow the same trend. This is partly due to the fact that it is not straightforward to estimate $\mathrm{Ri_B}$ from a 1D model. In particular, it is not easy to define the integration length, Δr in Eq. 2.2.9 which is used to calculate the buoyancy jump over the boundary. Estimates were used for

this integration length, the turbulent velocity and the integral scale in the calculation of Ri_B, which produces some inaccuracies. The numerical values for Ri_B presented in Table 4.2 should therefore be taken with caution and only as estimates. Nevertheless the values of Ri_B between different phases of a burning stage are comparable (as the same approximations are used in each case).

$\mathrm{Ri_B}$ and thus the character of stellar convective boundaries, can be expected to vary significantly during the course of stellar evolution. This is an indication that a globally applicable and predictive model for CBM could be developed for use in stellar evolution models, which would depend a priori on $\mathrm{Ri_B}$.

Interestingly, the lower boundaries of the convective shells, are consistently found to be stiffer than the upper boundaries. This has important implications for astrophysical phenomena that involve CBM. For example, Denissenkov, Herwig, Bildsten and Paxton (2013) showed that MESA models of novae, do not produce the observed ejecta associated with novae unless some CBM is included at the interface between the carbon-oxygen white dwarf and the accreted hydrogen envelope. They observe that this interface is stiff, a similarity with the lower boundary of convective shells in massive stars. Therefore, the $\mathrm{Ri_B}$ may not only form a predictive model for CBM during massive star evolution, but also may be important for the modelling of nova explosions.

Jones et al. (2013) demonstrate that the transition masses for super-AGBs ending their lives as either electron-capture supernova (EC-SN) or core-collapse supernova (CC-SN) are shifted when CBM is included in their stellar evolution models, due to an increase in the convective core size. The relative increase in stiffness at lower convective boundaries of shells compared to the upper boundaries, could also affect the dynamics of flame front propagation in these models, further affecting their predicted end-points.

Denissenkov, Herwig, Truran and Paxton (2013) reveal that when including CBM, the propagation of a carbon burning flame (see §1.1.2) is quenched throughout the carbon-oxygen core of a super-AGB model. This could have important consequences for type Ia SNe, as this opens up another channel for single degenerate progenitors. The amount of un-burnt carbon that is left in these models depends on the CBM prescriptions used, and so the stiffness of the lower boundary of the carbon shell would therefore directly affect the amount of CBM that occurs.

Average Temperature K	Average Density $\mathrm{g\,cm^{-3}}$	Shell radius cm	Turbulent velocity $\mathrm{cm\,s^{-1}}$	Radiative viscosity $\mathrm{cm^2\,s^{-1}}$	Opacity $\mathrm{cm^2\,g^{-1}}$	Thermal diffusivity $\mathrm{cm^2\,s^{-1}}$	Gravitational acceleration $\mathrm{cm\,s^{-2}}$	Diffusion coefficient $\mathrm{cm^2\,s^{-1}}$	Reynolds number	Péclet number	Mach number
5×10^{8}	2×10^{4}	1×10^{9}	2×10^{5}	320	0.1	2×10^{6}	7×10^{7}	5×10^{13}	1×10^{12}	2×10^{8}	9×10^{-4}

Table 4.3: Structural and flow properties for the carbon burning shell of the $15\,\mathrm{M}_\odot$ stellar model. The table shows various structural properties of the shell and various useful dimensionless numbers.

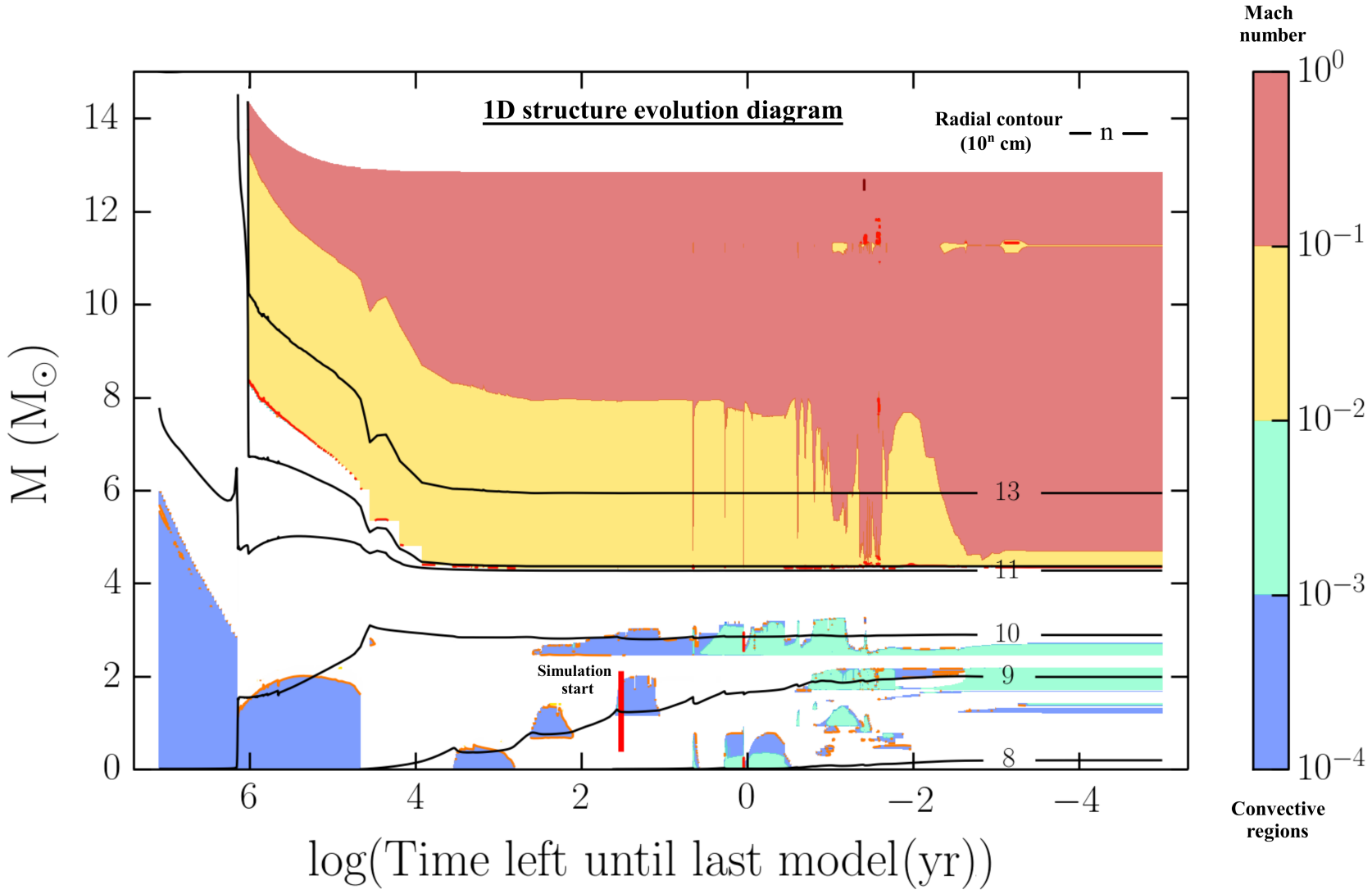

Figure 4.5: Structure evolution diagram of the 15 $M_\odot$ 1D input stellar model. The horizontal axis is a logarithmic scale of the time left before the predicted collapse of the star in years (this stellar model was only calculated up to the end of oxygen burning) and the vertical axis is the mass in solar masses. The total mass and radial contours (in the form $\log_{10}$(r) in cm), are drawn as solid black lines. Shaded areas correspond to convective regions. The colour indicates the value of the Mach number. The orange and red outlines represent the edge of the interior and envelope convective zones, respectively. The red vertical bar at around log[time left in years]$\sim$ 1.5 represents the domain simulated in 3D and the time at which the 3D simulations start.

4.2.2 Carbon shell burning

The second carbon shell (shown in Fig. 4.5 at mass coordinate $\sim 2\,\mathrm{M}_{\odot}$) was chosen as the convective region to study in greater detail using 3D hydrodynamic simulations. Structural properties and some useful dimensionless numbers are presented for the carbon shell in Table 4.3.

The carbon shell is an interesting choice for the following reasons, in addition to the fact that (at the time of writing) it has not been studied before in detail. It is the first neutrino-cooled burning shell, thus allowing radiative diffusion to be neglected (large Péclet number) and hence simplifying the numerical model. Earlier phases of stellar evolution are harder to simulate, as they are generally characterised by very small Damköhler numbers (slow burning) and very low convective Mach numbers (slow mixing). The carbon shell is characterised by a larger Damköhler number than these earlier, radiatively cooled stages, helping to alleviate the computational cost. The initial composition and structural profiles are also simpler than those of the more advanced stages. This is a result of the region in which the shell forms, being smoothed by the preceding convective helium-burning core. As carbon burning is the first neutrino dominated phase of nuclear burning, it plays an important role in setting the size of the heavy element core which subsequently forms and in which the core-collapse event will take place. Finally, the choice of the carbon shell (as opposed to the core) affords the study of two physically distinct convective boundaries rather than just one.

The structural properties of the second carbon shell at a time where it has burnt 31% of its fuel is summarised in Fig. 4.6. Here it can be seen that the lower convective boundary ($\sim 0.9 \times 10^9$) is stiffer, according to the value of $\mathrm{Ri_B}$, than the upper convective boundary ($\sim 2.3 \times 10^9$).

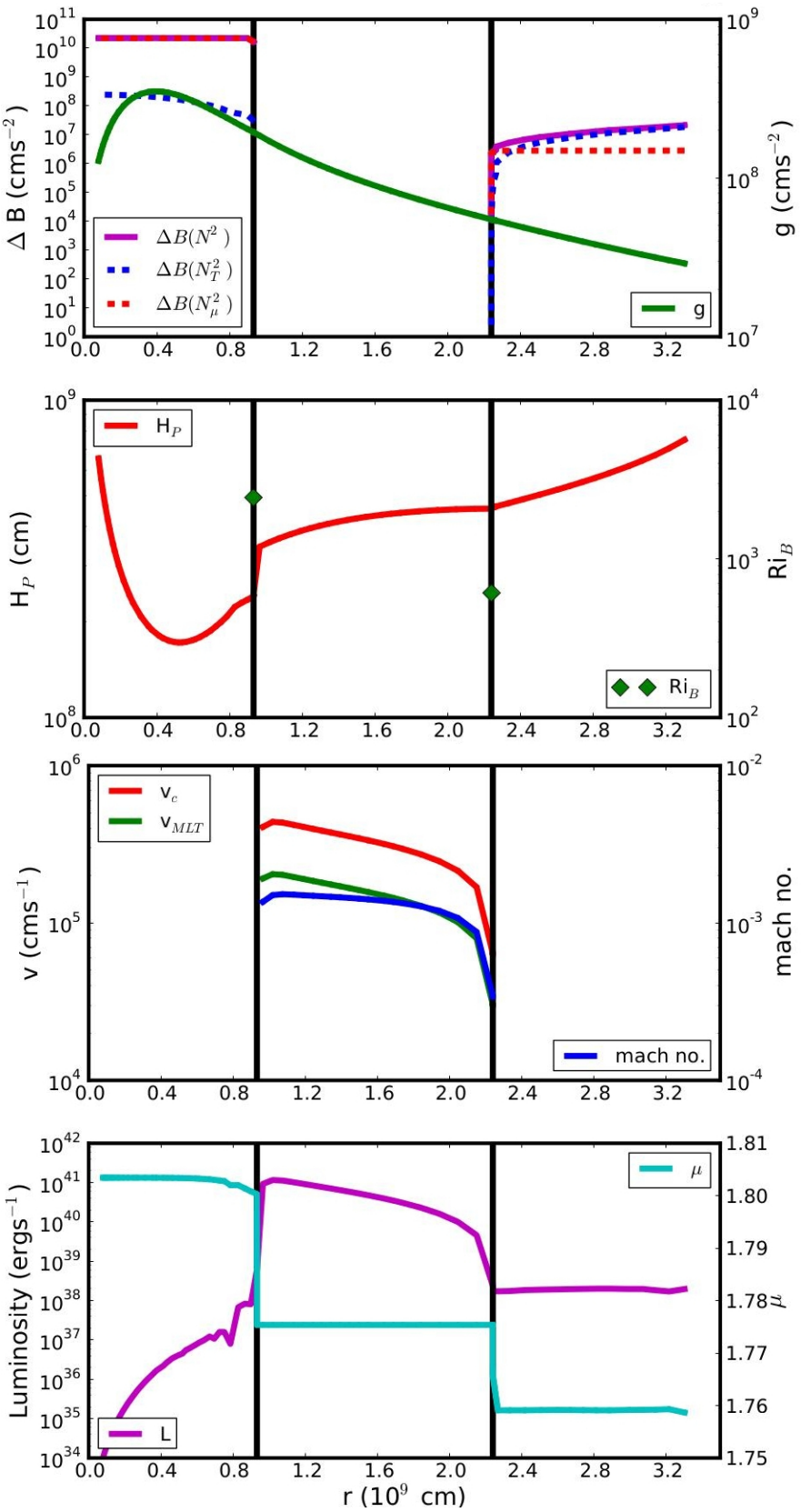

Figure 4.6: Structure properties of carbon shell burning as a function of radius (at 31% of the shell's lifetime). Central regions between vertical black lines are convective, areas outside of these lines are convectively stable. Curves, colours and lines are the same as in Fig. 4.3.

Chapter 5

Implicit large eddy simulations of a carbon burning shell and their dependence on resolution

5.1 Physical model set-up

3D hydrodynamical simulations have been computed using the PROMPI code, as described in §3.4. Models were evolved from initial conditions provided by a stellar model snapshot of the start of carbon shell burning (see Fig. 4.5) within a $15\,M_\odot$ star (see §4.2.2). The fluid flow is then solved for using the inviscid Euler equations (Eqs. 3.4.1a - d). While there is evidence that magnetic fields will be generated in deep interior convective regions (e. g. Boldyrev and Cattaneo, 2004) and that rotational instabilities (e. g. Maeder et al., 2013) may play an important role in shaping convection, it was decided to focus purely on the hydrodynamic problem in the current study, which remains a problem of significant complexity with many outstanding issues, such as unresolved convective boundary regions.

Energy generation during carbon burning proceeds mainly via fusion of two ^{12}C nuclei. For stellar conditions, considering only the main exit channels (α and p channels) will result in no significant errors (Arnett, 1996). The n exit channel branching ratio is only $b_n = 0.02$. Thus, for this study, its effect on the energy generation is neglected and only the α and p channels are considered. Rather than calculating the reaction rates through interpolation of reaction rates from tables in the literature (e.g.

the REACLIB database; Cyburt et al. 2010), the carbon burning energy generation rate was estimated using a slightly modified version of the parameterisation given by Audouze, Chiosi and Woosley (1986); Maeder (2009):

$$\epsilon_{^{12}C} \sim 4.8 \times 10^{18}\, Y_{12}^2\, \rho\, \lambda_{12,12}, \tag{5.1.1}$$

where $Y_{12} = X_{^{12}C}/12$, $X_{^{12}C}$ is the mass fraction of ^{12}C, $\lambda_{12,12} = 5.2 \times 10^{-11}\, {T_9}^{30}$ and $T_9 = T/10^9$. This approach is simpler than the former and more computationally efficient. Additionally, only the abundance of ^{12}C needs to be followed when using this parameterisation. There are thus only three compositional variables required for the model: the abundance of ^{12}C; the average atomic mass ($\bar{A}$); and average atomic number ($\bar{Z}$). The mean mass and charge are required for the EOS (§3.4.1) and to represent the mean properties of all other species besides ^{12}C. Thus the composition is an active scalar, coupled through the EOS and composition transport. A further simplification of the simulations is that the change of ^{12}C abundance due to nuclear burning is ignored because of its negligible rate of change relative to advective mixing (i. e. the carbon shell is characterised by a small Damköhler number, Da $\sim 10^{-4}$, see Table 4.2). The key important feature retained with this prescription of nuclear burning is the interaction and feedback between the nuclear burning and hydrodynamic mixing, while keeping computational costs to a minimum.

Cooling via neutrino losses is parameterised using the analytical formula provided by Beaudet, Petrosian and Salpeter (1967) which includes all of the relevant processes: pair creation reactions; Compton scattering; and plasma neutrino reactions. Other neutrino production processes such as recombination and bremsstrahlung are not relevant for typical carbon burning temperatures and densities.

5.1.1 The Computational Domain

Rather than simulate the star within a spherical geometry, a Cartesian geometry was chosen. This was done by employing the plane-parallel approximation; the simulations are therefore of the "box-in-a-star" type rather than a "star-in-a-box" type (see e.g. Jones et al., 2017). The main advantage of adopting a Cartesian geometry under

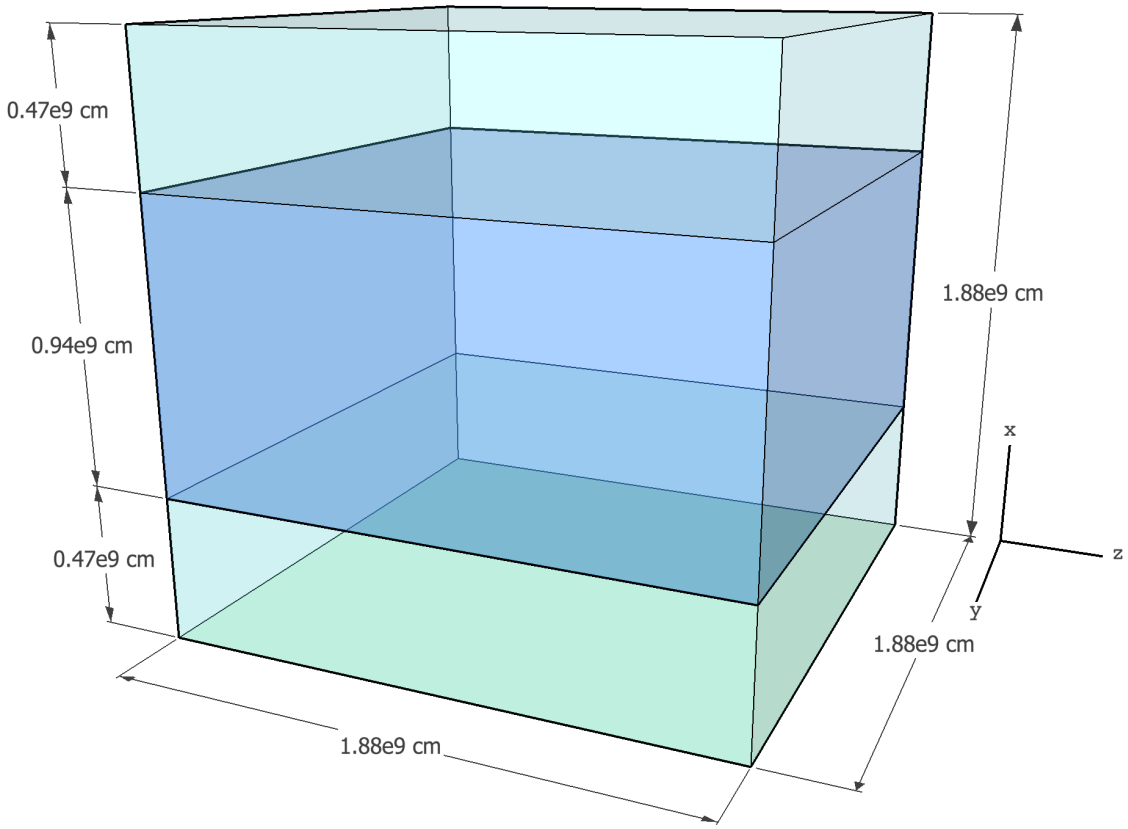

Figure 5.1: The geometry of the computational domain. Gravity is aligned with the x-axis. The blue region depicts the approximate location of the convectively unstable layer at the start of the simulation while the surrounding green volumes depict the locations of the bounding stably stratified layers.

the plane-parallel approximation, rather than a full spherical approximation is the increased resolution available at the convective boundaries. This is important in this study as the dynamics of mixing at the boundaries (and the boundaries themselves) are the main focus. Utilising a Cartesian geometry with a plane-parallel approximation rather than a spherical one also affords an increase in computational efficiency, as the Courant time scale[39] at the inner boundary of the domain will be eased.

The computational domain (for this box-in-a-star simulation) encompasses the convective region of thickness, t, and is bounded either side by radiative regions of thickness, $t/2$. The width of the computational domain is $2t$ in both horizontal directions; this allows the formation of two large scale convective eddies within the convective region. The geometry of the computational domain is illustrated in Fig. 5.1, where the convective region is coloured blue and the stably stratified regions are coloured green. The aspect ratio of the convective zone is 2:1 (width:height), and so a plane-parallel

[39]The models of this thesis are evolved explicitly in time with time-steps determined by the Courant condition (Eq. 1.4.1), using a Courant factor of 0.8.

approximation is not ideal and is one major simplification of the set-up[40]. This geometry allows for maximum effective resolution of the convective boundary regions but high order modes may not be present in the simulation. In spite of this, when these plane parallel simulations are compared to spherical simulations of the oxygen burning shell (Arnett et al., 2015), the change in geometry seems to have no significant effect on the velocity profiles and mean turbulent kinetic energy budget. On the other hand, by not simulating the shell within a full sphere (4π), some global convective motions may be inhibited by the restricted geometry (e.g. Herwig et al., 2014, and references therein), but as mentioned above this disadvantage is accepted in favour of maximum effective resolution at the boundaries.

In order to study the convective region, and also stable region dynamics, the entire convection zone and portions of the adjacent stable regions are included in the simulations. The mass and radial extent of the domain in relation to the stellar model initial conditions are illustrated by the vertical red bars in Figs. 4.5 and 5.2, respectively. The computational domain extends in the vertical direction from 0.42×10^9 cm to 2.30×10^9 cm, and in the two horizontal directions from 0 to 1.88×10^9 cm, see Fig. 5.1. The vertical mass extent of the computational domain is $0.4\,\mathrm{M}_\odot < m < 2.1\,\mathrm{M}_\odot$. During initial studies on the optimal aspect ratio for the computational domain, it was found that an aspect ratio for the convection zone of 2:1 (horizontal:vertical) was the required minimum for unrestricted circulation of the turbulent fluid elements. An aspect ratio of 3:1 did not change the morphology or circulation of fluid elements significantly.

The computational domain utilises reflective boundary conditions in the vertical direction (x), with the assumption that beyond this boundary the same physical processes exist. Periodic boundary conditions are used in the two horizontal directions (y, z) in order to mimic the continued fluid flow over planes of constant height. Although the material in the radiative regions is stable against convection, it has oscillatory gravity-modes (e.g. Christensen-Dalsgaard, 2003) propagating from the convective boundary, which are excited by the turbulence in the adjacent convection zone. In order to mimic the propagation of these waves out of the domain, a damping region is employed that extends radially 0.18×10^9 cm above the lower domain boundary at 0.42×10^9 cm (and

[40]In relation to the total radius of the star, which is 4.6×10^{13} cm, the radial extent of the computational domain is 4×10^{-3}% of this.

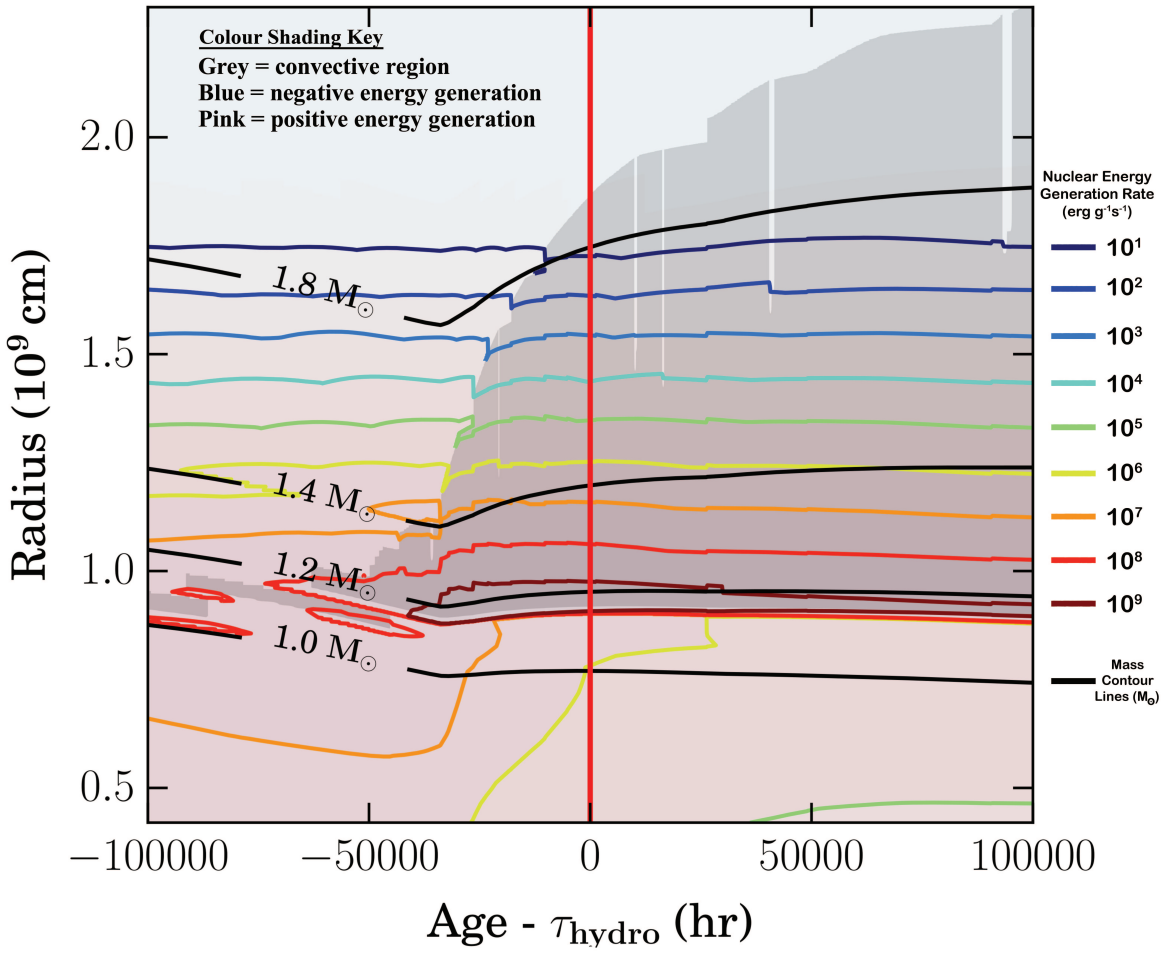

Figure 5.2: Structure evolution diagram of the $15\,\mathrm{M}_\odot$ stellar model used as initial conditions in the 3D hydrodynamic simulations, this is an expanded view of Fig. 4.5. The horizontal axis is the time relative to the start of the 3D simulations (τ_{hydro}). The vertical axis is the radius ($10^9\,\mathrm{cm}$). Mass contours (in solar masses) are shown by black lines and nuclear energy generation rate contours by coloured lines, brown corresponds to $10^9\,\mathrm{erg\,g^{-1}\,s^{-1}}$, the remaining colours decrease by one order of magnitude. Blue and pink shading represent regions of negative and positive net energy generation, respectively. Grey shaded areas correspond to convective regions. The vertical red bar indicates the relative start time and radial extent of the hydrodynamical 3D simulation. The physical time of the simulation is on the order of 1 hour, still much shorter than the time-scale of this plot.

covers the entire domain horizontally). Within this region all velocity components are reduced by a common damping factor, f, resulting in damped velocities over the computational domain, $\mathbf{v_d} = f\mathbf{v}$. The damping factor is defined as

$$f = (1 + \Delta t\, \omega f_d)^{-1}\,, \tag{5.1.2}$$

where $\omega = 0.01$ and is a free scaling parameter; and $f_d = 0.5\, \cos(\pi r/r_0) + 1$, where r is the radial position in the vertical direction (x-coordinate in this set-up) and $r_0 = 0.6 \times 10^9$ cm is the edge of the damping region in the vertical direction. The change in internal energy due to the dissipation of the damped wave energy is not included, as it is assumed that such effects are negligible on the overall energy budget[41].

The vertical red bar in Fig. 5.2 (a zoom in of Fig. 4.5) shows the time at which the simulations start and the vertical extent of the computational domain included in the simulations. The horizontal axis represents the age of the star relative to the age of the star at the start of the simulations. The chosen point in time corresponds to the start of the carbon burning shell, where the shell is still growing in mass according to the 1D stellar evolution model, and the large convective luminosity is driven by a peak in nuclear energy generation of $\sim 10^9\,\mathrm{erg\,g^{-1}\,s^{-1}}$ at 0.9×10^9 cm. The physical time of the 3D hydrodynamical simulations, however, is of the order of hours, much shorter than the time-scale shown by the horizontal axis. Furthermore, the bottom of the convective shell is stable over time (horizontal mass contour for $1.2\,\mathrm{M_\odot}$ in Fig. 5.2). Thus, it is not expected that there will be any strong structural re-arrangements that occur over the time-scale of the 3D simulations. This is also a justification for excluding modelling of the gravitational acceleration evolution over the course of the simulation (see §5.1.2 for details).

5.1.2 Initial Conditions and Runtime Parameters

The initial structure of the convective region can be seen through the entropy, buoyancy and composition profiles in Fig. 5.3. The convective region is apparent through the homogeneity of these quantities due to strong mixing, while the boundaries are

[41] Although not relevant for these models, Fuller et al. (2015) showed that internal gravity waves excited by the convective shells in massive stars can increase core rotation rates and thereby reduce the spin period of the post-supernova neutron star remnant.

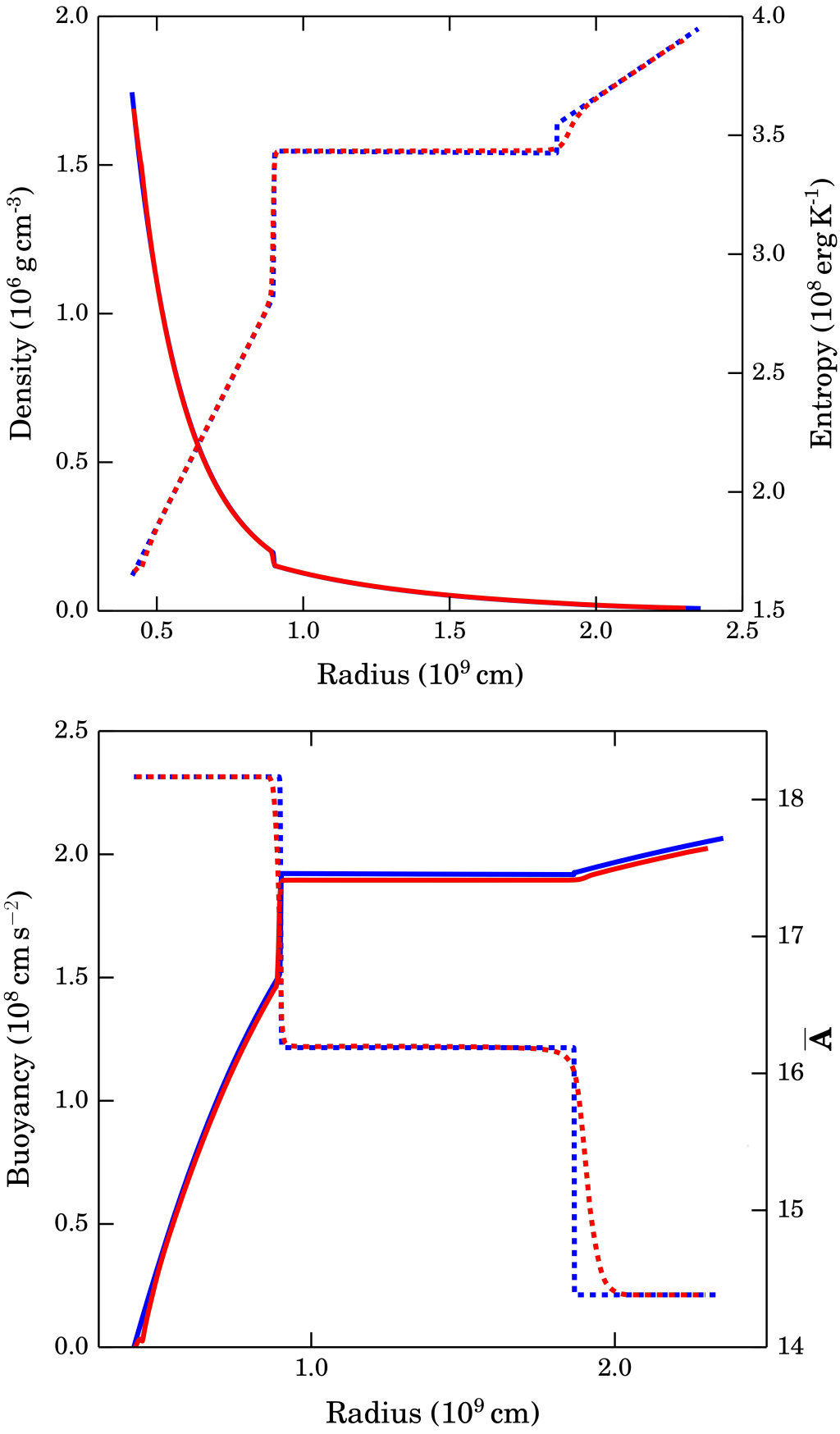

Figure 5.3: *Top panel:* Initial radial density (solid) and entropy (dashed) profiles. *Bottom panel:* Initial radial buoyancy (solid) and composition (dashed) profiles. One dimensional (1D) stellar evolution profiles calculated using GENEC (blue) are compared with the same profiles integrated and mapped onto the Eulerian Cartesian grid in PROMPI (red).

defined by sharp jumps due to the placement of the convective boundary using the Schwarzschild criterion (Eq. 2.1.14).

An initial hydrostatic structure in PROMPI was reconstructed from the entropy, composition and gravitational acceleration profiles taken from the GENEC 1D model. Stellar models do not have regularly spaced mesh points in the radial direction, given the fact that they use a Lagrangian method which utilises adaptive mesh refinement. The spatial resolution therefore can be quite coarse, especially at the convective boundaries. For this reason, the 1D GENEC entropy (s), average atomic mass ($\bar{A}$) and average atomic number ($\bar{Z}$) profiles are first remapped onto a finer, uniform mesh before being linearly interpolated onto the Eulerian grid in PROMPI. The details of this re-mapping can be found in Appendix A.3. To ensure the re-mapped model is in hydrostatic equilibrium and is thermodynamically self-consistent, the density $\rho(s, p, \bar{A}, \bar{Z})$ is integrated along the new radial grid according to:

$$\frac{\partial \rho}{\partial r} = \frac{ds}{dr}\left(\frac{\partial \rho}{\partial s}\right)_{p,\bar{A},\bar{Z}} + \frac{dp}{dr}\left(\frac{\partial \rho}{\partial p}\right)_{s,\bar{A},\bar{Z}} + \frac{d\bar{A}}{dr}\left(\frac{\partial \rho}{\partial \bar{A}}\right)_{s,p,\bar{Z}} + \frac{d\bar{Z}}{dr}\left(\frac{\partial \rho}{\partial \bar{Z}}\right)_{s,p,\bar{A}}, \tag{5.1.3}$$

the second term is simplified by enforcing hydrostatic equilibrium to within a tolerance of 10^{-10}, given by:

$$\frac{dp}{dr} = -\rho g. \tag{5.1.4}$$

For this plane-parallel geometry set-up, the gravitational acceleration is parameterised by a function of the form $g(r) = A/r$, with constant $A = 1.5 \times 10^{17}\,\mathrm{cm^2\,s^{-2}}$. As mentioned above, this is not expected to have any adverse effects on the model, as there should not be any secular changes in the stellar structure on such a short time-scale ($\lesssim 10^4\,\mathrm{s}$). The total derivatives $\frac{ds}{dr}$, $\frac{d\bar{A}}{dr}$ and $\frac{d\bar{Z}}{dr}$ are calculated from the fitted profiles introduced earlier. The partial derivatives $\frac{\partial \rho}{\partial s}$, $\frac{\partial \rho}{\partial p}$, $\frac{\partial \rho}{\partial \bar{A}}$ and $\frac{\partial \rho}{\partial \bar{Z}}$ are calculated from the Helmholtz EOS. The initial profiles (density, entropy, buoyancy and average atomic mass) for the stellar model initial conditions (Fig. 5.3) were mapped onto the Eulerian grid in PROMPI. There is good agreement between the 1D and 3D initial conditions.

	lrez	mrez	hrez	vhrez
N_{xyz}	128^3	256^3	512^3	$1{,}024^3$
$\boldsymbol{\tau_{sim}}$(s)	3,213	3,062	2,841	986 †
$\boldsymbol{v_{rms}}$(cm/s)	3.76×10^6	4.36×10^6	4.34×10^6	3.93×10^6
$\boldsymbol{\tau_c}$(s)	554	474	471	513
$\boldsymbol{N_c}$	4.0	4.4	3.9	1.9
$\mathrm{Ri_B}$	29 (370)	21 (259)	20 (251)	23 (299)
Ma	0.0152	0.0176	0.0175	0.0159

† If the initial transient time of the hrez model is also included, then the total physical time for this model is 1966 s, as the vhrez model was restarted from the end of this phase in the hrez model.

Table 5.1: Summary of simulation properties. N_{xyz}: Total number of zones in the computational domain ($N_x \times N_y \times N_z$); $\tau_{\rm sim}$: simulated physical time; $v_{\rm rms}$: global RMS convective velocity; τ_c: convective turnover time; N_c: number of convective turnovers; $\mathrm{Ri_B}$: bulk Richardson number (values in brackets are representative of the lower convective boundary region); Ma: Mach number.

Carbon shell simulations

The carbon shell was simulated at four different resolutions named according to their resolution: lrez - 128^3, mrez - 256^3, hrez - 512^3 and vhrez - 1024^3, and their global properties are summarised in Table 5.1, which includes physical time simulated, resolution, convective turnover time, as well as a variety of other physical parameters estimated for the flows. Simulation time is typically measured relative to the number of convective turnovers, where the convective turnover time, τ_c, is given by Eq. 2.2.11. The four simulations typically span 2 to 4 convective turnovers, following an initial transient phase of around 1,000 s. By comparing the different simulations, the dependence of the results on the numerical resolution can be tested. If the results vary significantly as the resolution is increased, then this would suggest that the results are sensitive to the numerics in some way. Whereas, if the results appear to converge to a common value or trend over certain resolutions, then this would suggest the simulations are modelling a physical process and that the results are independent of those resolutions.

The vhrez model was restarted from the hrez model at 980 s, rather than beginning with the stellar model initial conditions as in the other three simulations. This approach (restarting one model from another) is achieved by duplicating every cell in each direction, effectively representing the same physical model on twice the number of grid points, hence, the new grid scale is halved, and the resolution doubled. The time chosen to restart the hrez model at double the resolution is roughly coincident with the beginning of the quasi-steady state, therefore removing the need to simulate the transient phase, which is mostly converged (except for the peak in total kinetic energy) when varying the resolution. Due to the limited number of computational resources available for this study, the vhrez model could not be simulated for the desired number of convective turnovers in order for any temporal averaging of the turbulent processes to be statistically valid. As a result, this model is not included in any detailed analysis but serves only as a higher resolution comparison to the other models.

Convection is seeded in these models through equal and random perturbations in temperature and density in the same manner described by Meakin and Arnett (2007*b*). They also show that the subsequent nature of the flow is independent of these seed perturbations.

5.1.3 Problems with sustaining turbulence

During initial test calculations, it was apparent that turbulent motions were not being sustained throughout the simulation following the initial transient phase. The following discussion explores, heuristically, the modelling of turbulence on a discrete grid to determine whether a computed flow will exhibit turbulence based on the spatial and temporal discretisation used.

Spatial constraint of turbulence

A useful dimensionless number for determining the extent of turbulence in a simulation is the effective Reynolds number. This is the discrete analogue of the Reynolds number (Eq. 2.2.7). It is defined using the following arguments. From Eq. 2.2.3, one can state the rate of energy dissipation at the extreme scales of the simulation, i.e. at the integral scale and the grid scale. These energy dissipation rates are

$$\epsilon_\ell = \frac{v_{rms}^3}{\ell} \quad \text{and} \quad \epsilon_{\Delta x} = \frac{\Delta u^3}{\Delta\, x}, \quad \text{respectively,} \tag{5.1.5}$$

where Δu is the flow velocity across a grid cell; this velocity can also be used to define an effective numerical viscosity at the grid scale

$$\nu_{eff} = \Delta u \Delta x. \tag{5.1.6}$$

For a turbulent system within a statistically steady state, Kolmogorov (1962) showed that the rate of energy dissipation is equal at all scales; applying this equality to Eq. 5.1.5 yields (with the use of Eq. 5.1.6)

$$\nu_{eff} = v_{rms}\ell \left(\frac{\Delta x}{\ell}\right)^{4/3}. \tag{5.1.7}$$

Assuming the integral scale is the size of the convective region, ℓ_{cz}, then the effective Reynolds number can be expressed as (to within a factor of 2)

$$\mathrm{Re}_{eff} = \left(\frac{\ell}{\Delta x}\right)^{4/3} \sim N_x^{4/3}, \tag{5.1.8}$$

where N_x is the number of grid points in the vertical direction. In these simulations this is a slight over-estimate as in the vertical direction only half of the grid points represent the convective region.

Within the ILES paradigm the effective Reynolds number is therefore limited by the momentum diffusivity[42] at the grid scale (Eq. 5.1.6), and as demonstrated by Eq. 5.1.8 it is the choice of spatial zoning that sets a limit on the degree of turbulence. This is essentially because the grid scale sets an effective Kolmogorov length-scale which is larger than the physical one, therefore 'shortening' the inertial sub-range, and reducing the ensemble of eddies with different sizes within this sub-range. The effective Reynolds numbers of the current simulations ($N_x = 128 - 1024$) range from around 650 to 10^4, suggesting that the simulations with finer grids are within the turbulent

[42]The actual numerical dissipation of the PPM method is highly complex and non-linear (Sytine et al., 2000); the higher resolution simulations presented here seem to capture the effective dissipation accurately.

regime[43] ($\mathrm{Re}_{eff} \gtrsim 1000$).

Temporal constraint of turbulence

The peak energy generation rate, ϵ_{peak}, can be larger than the mean energy generation rate, ϵ, by a considerable factor, due to the strong temperature dependence. For carbon burning, $\epsilon_{peak} \sim 40\epsilon$ (Arnett, 1996). This heating will induce buoyancy and drive convective motion, which is turbulent, and will carry the super-adiabatic energy down to the smaller scales where it is dissipated.

The turbulent velocity can be estimated using Eq. 2.2.1. For carbon burning, $\epsilon_{peak} \sim 10^9\,\mathrm{erg\,g^{-1}\,s^{-1}}$ and the integral scale can be approximated as the height of the convective region ($\ell_{cz} \sim 10^9\,\mathrm{cm}$), thus, $v_{rms} = (\ell\epsilon)^{1/3} \sim 3 \times 10^5\,\mathrm{cm\,s^{-1}}$, which agrees with the value calculated by the stellar evolution model, given in Table 4.2. The convective turnover time, τ_c, is the time needed to establish the turbulent velocity field (Meakin and Arnett, 2007*b*) following the initial perturbations in temperature and density. Hence, it is the temporal constraint for modelling turbulence in these simulations; for carbon burning the turnover time (using the velocity calculated above) is $\tau_c \sim 6.7 \times 10^3\,\mathrm{s}$. The maximum time step size is $\Delta t_{max} = \Delta x / c_s$, where the local sound speed is approximately $c_s \sim 4.5 \times 10^8\,\mathrm{cm\,s^{-1}}$. Thus (adopting the number of grid zones as $N_x = 2\ell_{cz}/\Delta x$) the maximum time-step is $\Delta t_{max} = 2\ell_{cz}/c_s N_x \sim 4.4/N_x$. This implies that the minimum number of time steps needed to establish a turbulent flow (roughly one convective turnover time) is $N_{\Delta t} \sim 1.5 \times 10^3 N_x$.

For the hrez zoning (512^3), the required number of time-steps equates to 7.7×10^5, which would have exceeded the available computer resource budget. The modelling of smaller velocities therefore requires more time steps. One option to overcome this issue is to scale the velocity up, by scaling the nuclear energy generation rate up. By scaling the burning rate (energy generation) by a factor of 1000 (this only scales the velocity, $v_{rms} \propto \epsilon^{1/3}$ up by a factor of 10), the convective turnover time becomes $\tau_c \sim 667\,\mathrm{s}$, and the minimum number of time-steps required to establish a turbulent flow decreases to $N_{\Delta t} \sim 150 N_x$. For a zoning of 512^3, this is $\sim 7.68 \times 10^4$ time-steps, which was comfortably attainable given the available computational resources.

[43] This is supported by visual comparison of the simulations with experimental data (e.g. van Dyke, 1982).

Boosting factor

The chosen boosting factor[44,45] for the nuclear energy generation rate was 1000. This boosting increases the flow velocity, v_{rms} (see Eq. 2.2.1), by a factor of 10. A key advantage to this approach is that more convective turn-over times can be computed for the same computational cost, but it does highlight an important sensitivity of the hydrodynamic flow to the numerical set-up. Additionally, as the nuclear luminosity has been boosted the neutrino losses contribute negligibly to the thermal evolution of the model. Interestingly, the boosted nuclear energy generation rate is close to the natural oxygen burning one ($\sim 10^{12}\,\mathrm{erg\,g^{-1}\,s^{-1}}$; Meakin and Arnett, 2007*b*).

5.2 Results and discussions

5.2.1 The Onset of Convection

All of the models represent some fraction of the inertial range. A similar representation was demonstrated by Sytine et al. (2000) in their PPM simulations of homogeneous turbulence on grids of sizes 64^3, 128^3, 256^3, 512^3, 1024^3, see their Fig. 11. In this figure they compute the velocity power spectra of the models and show their agreement with Kolmogorov's $k^{-5/3}$ power law for the inertial range, where k is the wave-number of turbulent fluid elements. In order to independently test whether the PROMPI carbon shell simulations correctly model turbulence (with the inclusion of an inertial range), the velocity power spectra for the four models was computed in this thesis.

Turbulent velocity spectrum

In order to visualise the specific kinetic energy of the simulations over a range of wave-numbers the velocity power spectra is calculated for the four models. This is

[44]In such simulations, the effect of such a boost in driving will not alter the thermal diffusion in the model. This is because thermal diffusivity is negligible in comparison to the loss of heat through escaping neutrinos produced in the plasma (Arnett, 1996, pg. 284 - 292), and so thermal diffusion only becomes important at the sub-grid scale.

[45]An argument for why thermal diffusivity is also negligible in the boundary regions of the oxygen burning shell (which would also apply to the boosted carbon shell) has been presented in Arnett et al. (2015). They show that a large Péclet number leads to an adiabatic expansion of the convective boundary.

achieved by performing a horizontal 2D fast Fourier transform[46] (FFT) of the vertical velocity at a constant height, within the centre of the convection zone. The results of this transform are presented in Fig. 5.4, where the square of the transform, $\hat{V}^2(k)$, is plotted as a function of the wave-number. These spectra are time-averaged over several convective turnover times, and the 1D profile is obtained by binning the 2D transform within the $k_y - k_z$ plane, where k_y and k_z are the wave-numbers in the y and z directions, respectively ($k_y, k_z = 0, 2\pi, 4\pi, ..., 2\pi(N/2)$, where N is the number of grid points in one dimension, i.e. the resolution). A scaling of $(k^{5/3}/N_x)$ is applied, to allow a visual determination of the inertial range shown by a $k^{-5/3}$ power law (Kolmogorov, 1941). The inertial range is therefore represented by the roughly horizontal regions of the profiles, for example, $k = 10 - 500$ in the vhrez (green) simulation. This wave-number range represents the scales within the simulation that are free from the effects of the driving force, numerical dissipation, boundary conditions and initial conditions. The steep decline in each model ($500 < k < 3000$, for the vhrez model) represents the dissipation of TKE at a rate that departs from the Kolmogorov $k^{-5/3}$ scaling; this is because at these length scales the numerical dissipation inherent to these PPM simulations indirectly affects the flow. Porter, Woodward and Pouquet (1998); Sytine et al. (2000) show that this is the case in their highest resolution simulations for up to 16 and 32 cell widths, respectively. The same effect is observed at $k \sim 500$, which corresponds to around 8 cell widths in the highest resolution simulation. At the end of each profile there is a small 'lip' (i.e. the feature at $k \sim 3000$ in the vhrez simulation) which represents the wave-number of the grid-scale. The discretisation of the profiles produces this feature due to the sudden increase in numerical dissipation at the grid-scale.

These velocity spectra thus demonstrate that the two highest resolution PPM simulations possess the essential characteristics of a turbulent flow – an integral scale, an inertial range obeying the $k^{-5/3}$ power law, and an effective Kolmogorov length-scale (represented by the grid scale). In the two lowest resolution models, on the other hand, the plateau is either very short or not present, indicating that models with fewer than 512^3 zones are probably not very accurate models of turbulence. This minimum desired resolution is in reasonable agreement with the estimates of the numerical Reynolds

[46]Using the Python package NUMPY.FFT.FFT2.

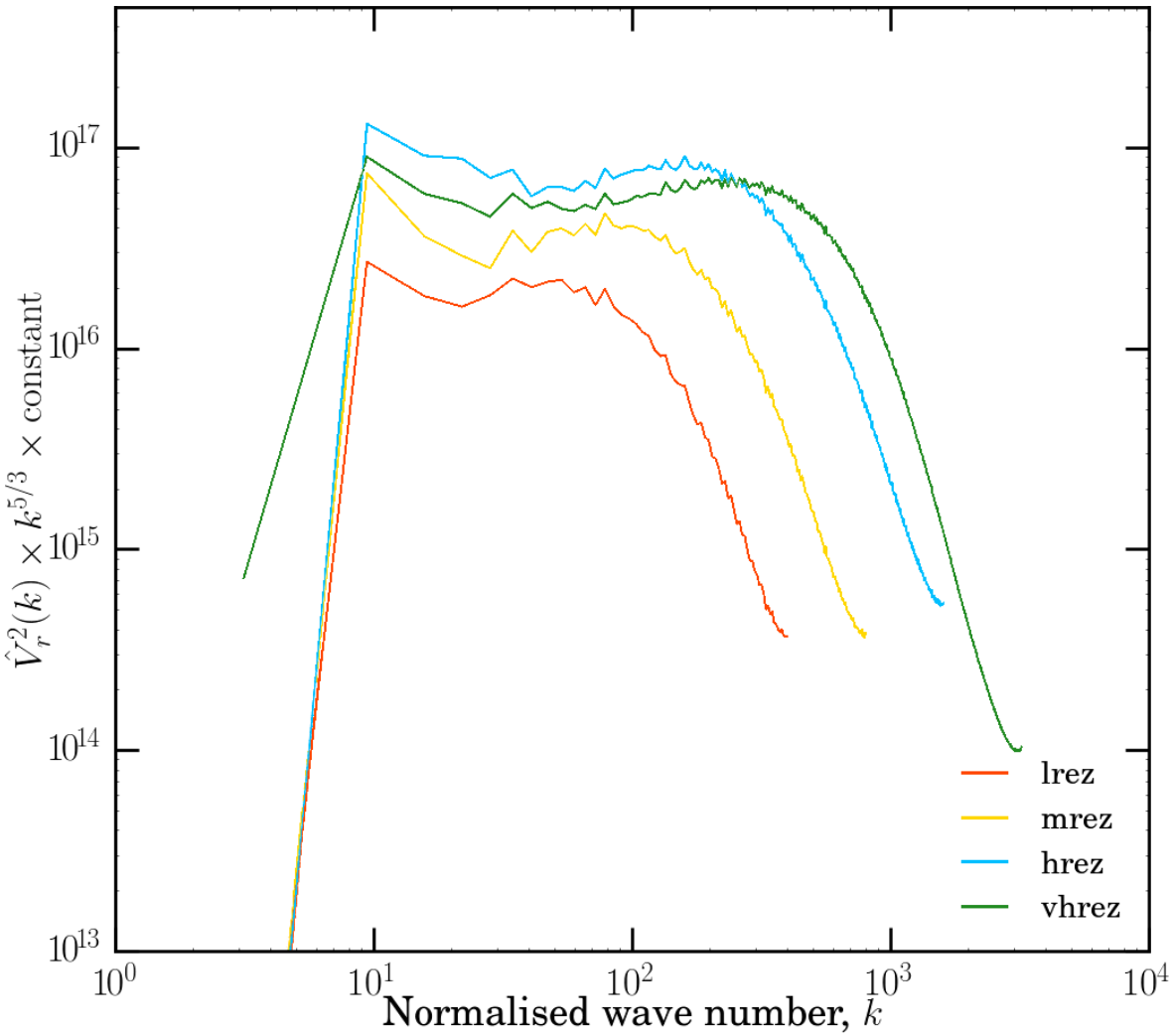

Figure 5.4: Specific kinetic energy spectrum of the four simulations. Spectra were obtained from a 2D Fourier transform of the vertical velocity (at the mid-height of the convective region), averaged over several convective turnovers. The vertical axis is the square of the Fourier transform, scaled by a 'Kolmogorov factor', $k^{5/3}$, multiplied by a constant (N_x^{-1}) to allow easier comparison between resolutions. This scaling means that the inertial range corresponds to the horizontal part of the curve. The horizontal axis is the wave-number, k. See text for more details.

numbers presented in §5.1.3 ($\mathrm{Re}_{eff} \sim N_x^{4/3}$).

Temporal evolution of convection

The temporal evolution of the global (integrated over the convective zone) specific kinetic energy for all of the models is presented in Fig. 5.5. The first ∼1,000 seconds of evolution are characterised by an initial transient associated with the onset of convection. Beyond this time, all of the models settle into a quasi-steady state, characterised by semi-regular pulses in kinetic energy, occurring on a time scale of the order of the convective turnover time. These pulses are associated with the formation and eventual breakup of semi-coherent, large-scale eddies (or plumes), that traverse a good fraction

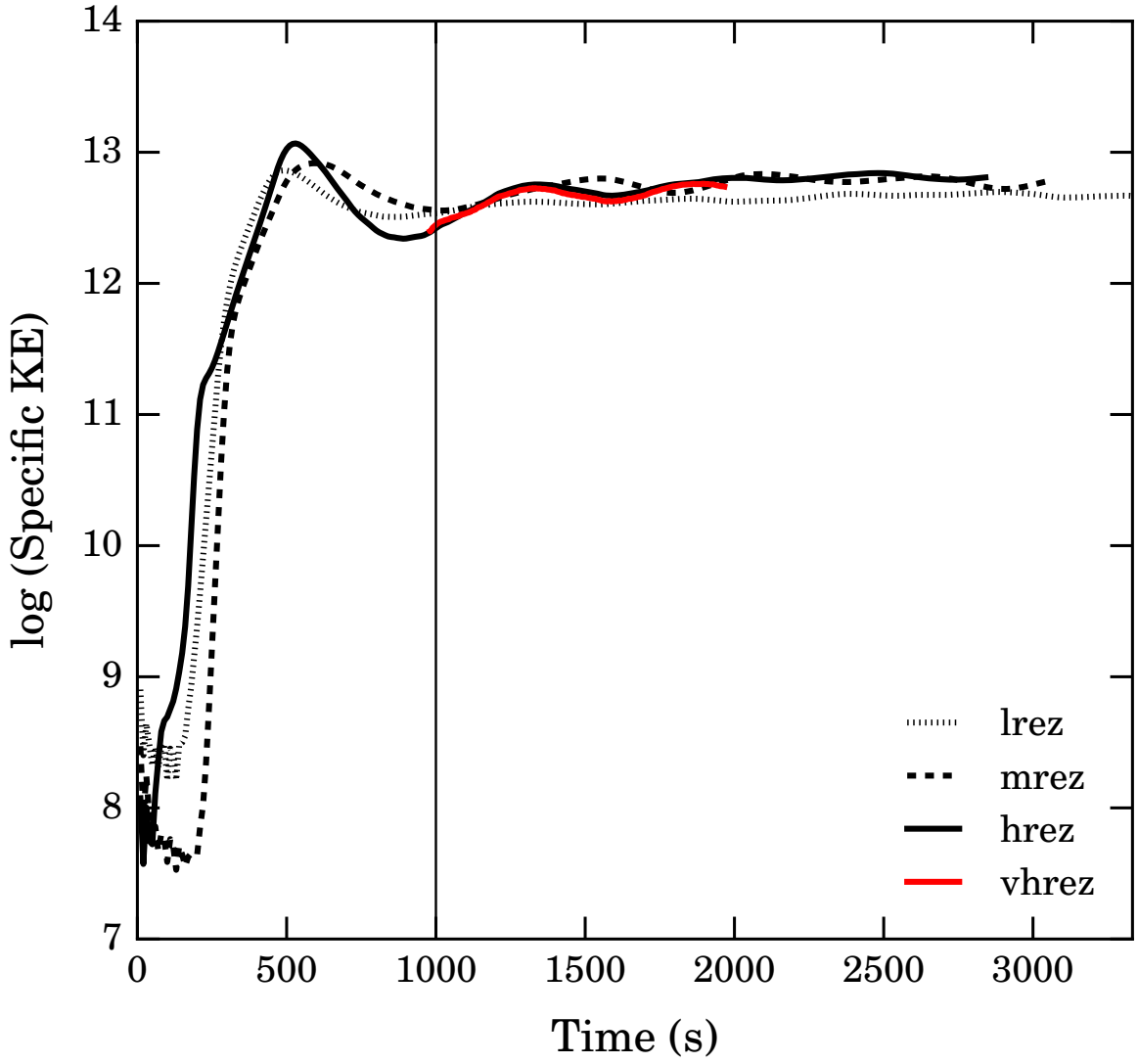

Figure 5.5: Temporal evolution of the global specific kinetic energy: thin dashed - lrez; thick dashed - mrez; black solid - hrez; red solid - vhrez. The quasi-steady state begins after approximately 1,000 s, and is shown by the vertical solid black line.

of the convection zone before dissipating and are a phenomenon that is typical of stellar convective flow (Meakin and Arnett, 2007*b*; Arnett and Meakin, 2011*a*,*b*; Viallet et al., 2013; Arnett et al., 2015).

As discussed in §5.1.2, the evolution of the highest resolution model, vhrez, begins at ∼1,000s, the time at which it was restarted from the hrez model by sampling the underlying flow field onto a higher resolution mesh. As is typical of turbulent flow, this model relaxes in approximately one large-eddy crossing time as evidenced by the re-establishment of the TKE balance which is discussed further in §5.2.3.

Although these simulations do not sample a large number of convective turnover times (between ∼2 and ∼4), resolution trends are still apparent. The most prominent trend seen in Fig. 5.5 is the kinetic energy peak associated with the initial transient,

which increases as the grid is refined. This is not linked to the initial seed perturbations and is most likely related to the decreased numerical dissipation at finer zoning.

A similar trend can also be seen in the quasi-steady turbulent state that follows the initial transient. Interestingly, in this case, a resolution dependence only appears to manifest for the lowest resolution model, lrez. This has an overall smaller amplitude of kinetic energy as well as a much smaller variance associated with the formation and destruction of pulses. These properties can be naturally attributed to a higher numerical dissipation at a lower resolution.

5.2.2 Properties of the Quasi-Steady State

Thermodynamic fluctuations around the mean states are considered by expanding the Taylor series of thermodynamic variables up to the second order. These variables are then given by the sum of the mean background state and the linear fluctuations from this state. These fluctuations are small enough so that the expansion up to second order is reasonably accurate. RMS fluctuations in density, pressure, entropy, temperature and composition centred around their mean background states are shown for the hrez model in Fig. 5.6. Fluctuations in the convective region are small and of a similar magnitude for all quantities except the composition. Near the convective boundary regions, the relative amplitude of the fluctuations is highest, reaching values up to around 1% of the mean background state.

Pressure fluctuations can be grouped into a compressible and an incompressible component. The former describes the acoustic nature of pressure fluctuations such as when the flow turns and is compressed. The latter describes the advective nature of pressure perturbations due to buoyancy effects. The compressible component of the pressure fluctuations is proportional to a pseudo-sound term, $\rho_0 \, v'^2/p_0$, shown by the dashed line in Fig. 5.6. This term is highest in the convective region and has a magnitude similar to the square of the Mach number, $\sim 3 \times 10^{-4}$.

Horizontally averaged RMS velocity components for the hrez model are shown in Fig. 5.7. These profiles represent an average over the quasi-steady state period of the simulation, which is estimated to occur over four convective turnover times. The total RMS velocity reaches a maximum of around 4.8×10^6 cm s^{-1} both in the centre of the

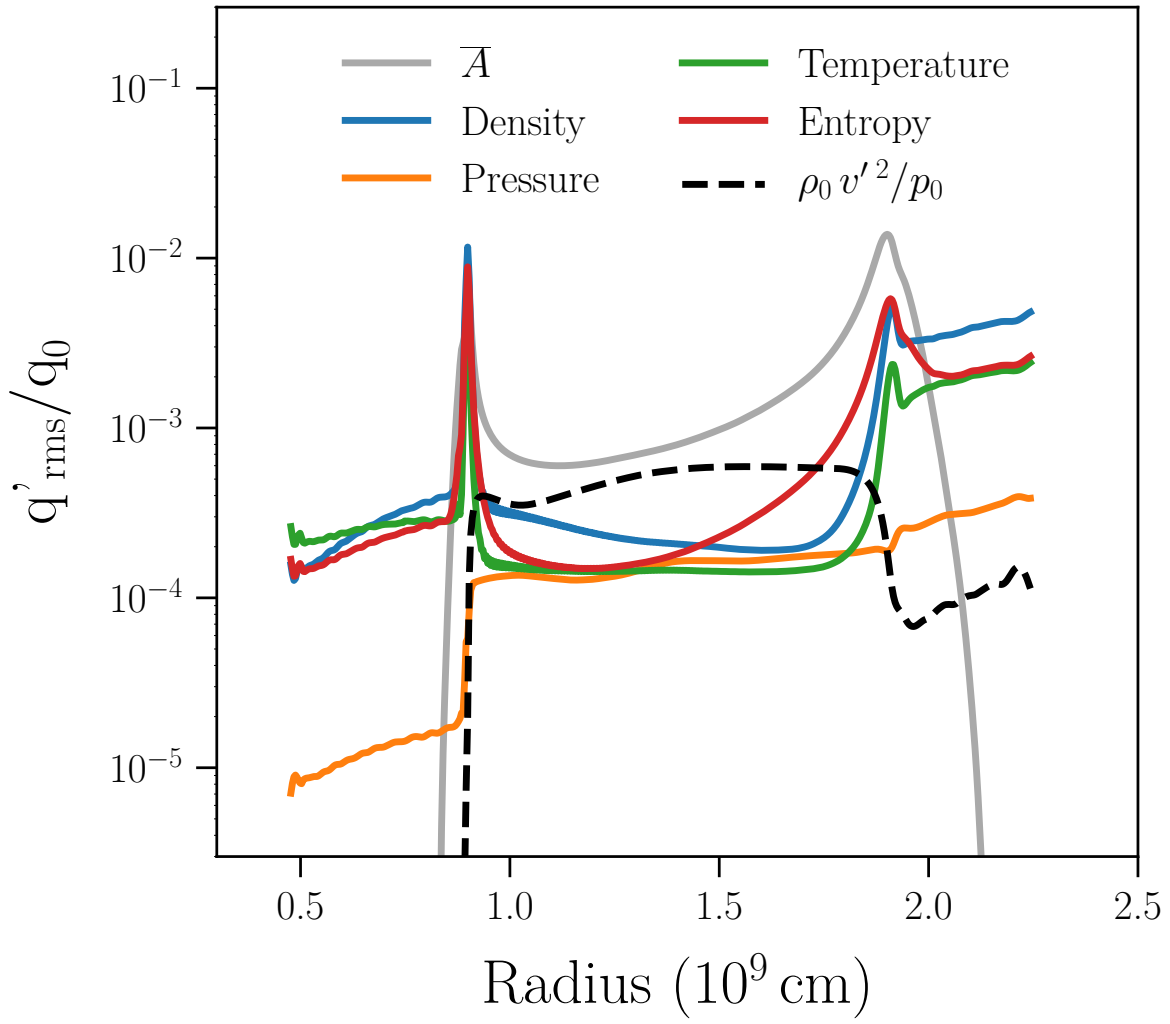

Figure 5.6: Horizontally averaged RMS fluctuations of composition, density, pressure, temperature and entropy weighted by their average values. The dashed curve represents a pseudo-sound term. These fluctuations were time averaged over 4 convective turnover times of the hrez model.

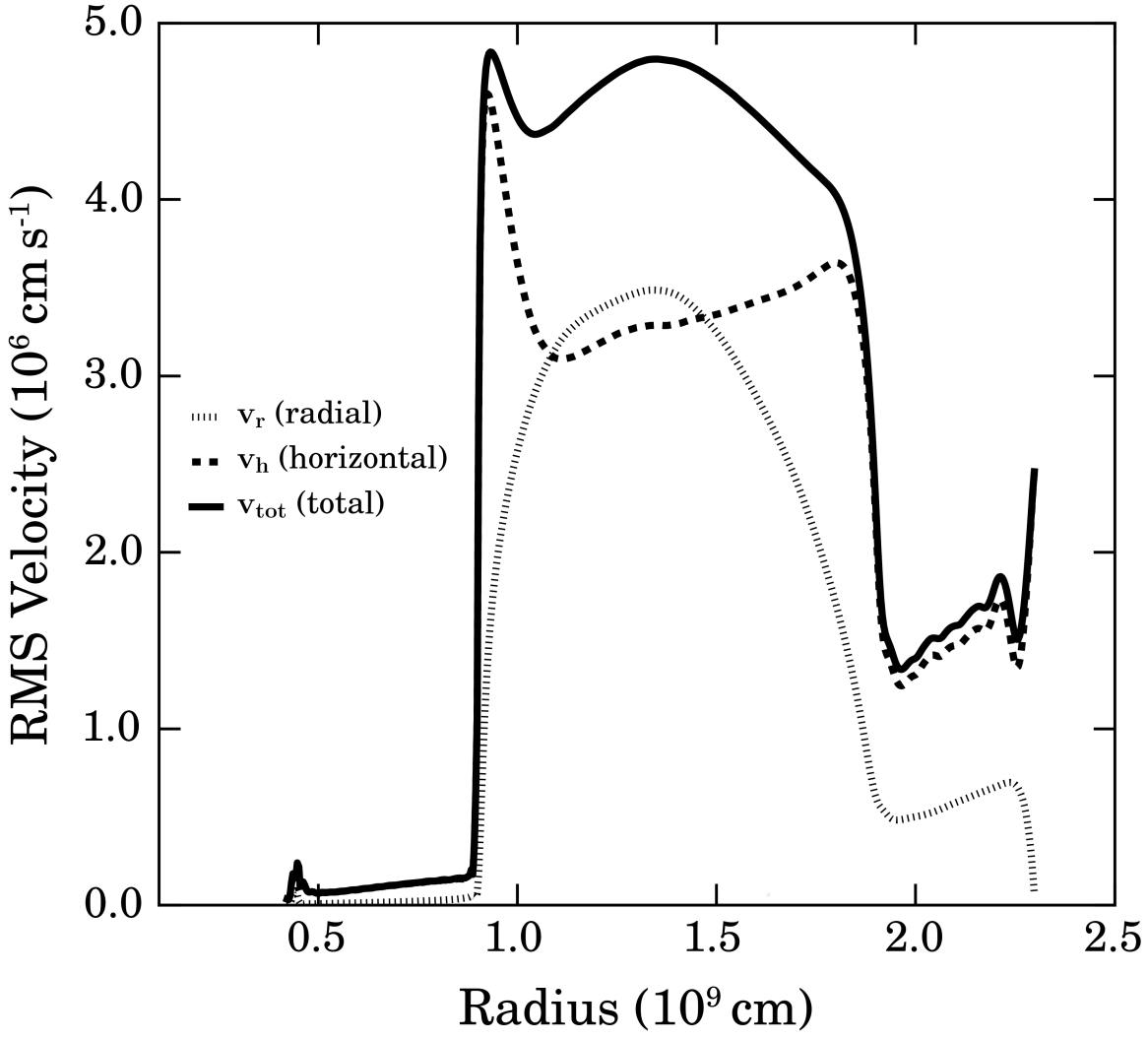

Figure 5.7: RMS radial (thin dashed), horizontal (thick dashed) and total (solid) velocity components, time averaged over four convective turnover times for the hrez model. Local maxima (minima) in the horizontal (vertical) velocity indicate the approximate convective boundary locations.

convective region ($r \sim 1.4 \times 10^9$ cm) and also near the lower convective boundary ($r \sim 0.9 \times 10^9$ cm). Contributions to the total velocity are dominated by the radial velocity over the central part of the convective region, while close to the convective boundaries the horizontal velocity ($v_h = \sqrt{v_y^2 + v_z^2}$) is the largest component. The local maxima in horizontal velocities and coincidental local minima in vertical velocities correspond to the radial deceleration and eventual turning of the flow near the convective boundaries. Similar features are reported in simulations of the oxygen burning shell by Meakin and Arnett (2007*b*) and Jones et al. (2017), see their Figs. 6 and 11, respectively.

The components of the flow velocity for the hrez model are illustrated by contour plots in Fig. 5.8. These snapshots of the flow were taken at 1,480 s into the simulation, where the quasi-steady state has already developed. Each vertical 2D slice in Fig. 5.8 is taken at the same horizontal (z) position in the $x - y$ plane, at $z = 0.94 \times 10^9$ cm (i. e. in the middle of the domain). The top, middle and bottom panels of Fig. 5.8 show the x, y and z components of the velocity, respectively. In the top panel, strong, buoyant up-flows are shown in shades of red, while cooler, dense down-drafts are shown in shades of blue. The convective boundaries are apparent in all the velocity components from the sudden drop in velocity magnitude. The lower convective boundary is clearly distinguishable, but the upper boundary is more subtle with velocities above the boundary represented by slightly lighter shades of red and blue. In the middle and bottom panels, horizontal velocities are strongest near the convective boundaries (shown by extended patches of dark red and dark blue colours). This is indicative of the flow turning as it approaches the boundary. Gravity mode waves excited by turbulence in the convective region can be seen in the stable region above, and are shown by lighter shades of red and blue in the upper part of each panel.

5.2.3 Mean Field Analysis of Kinetic Energy

The Reynolds-averaged Navier-Stokes (RANS) framework (introduced in §2.2.3) was used to calculate the terms of the turbulent kinetic energy (TKE) equation (details given in Appendix A.2) and to analyse them, by spatially averaging over the horizontal directions and temporally averaging over the quasi-steady turbulent state. Such a time integration is valid at the convective boundaries, despite their dynamic behaviour,

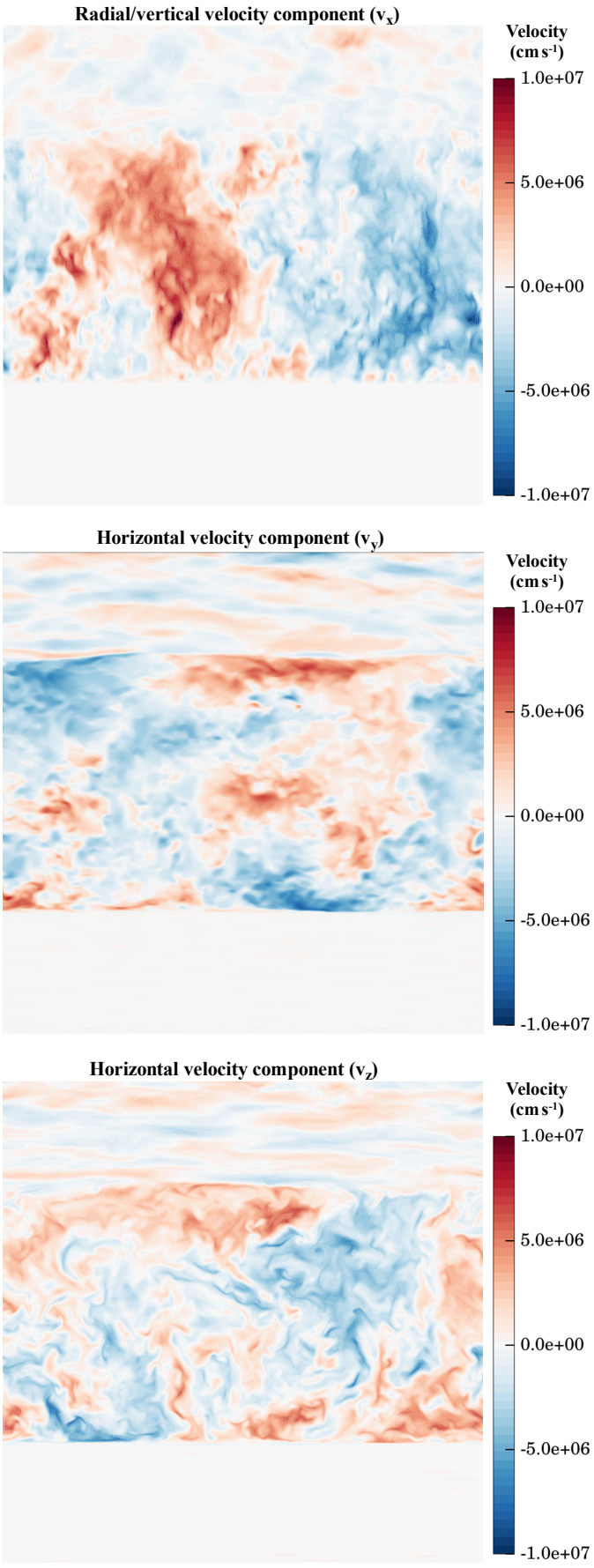

Figure 5.8: Velocity components within a vertical 2D plane, at $z = 0.94 \times 10^9$ cm, 1480s into the hrez simulation. Plotted from top to bottom are the radial velocity component (v_r) and horizontal velocity components (v_y and v_z), respectively. Reds represent positive values, while blues represent negative values and white represents velocities around zero. Velocity values corresponding to certain colours are also shown in the colour-bars.

as the characteristic expansion time of the boundaries is smaller than the convective turnover time. Such a situation occurs within the equilibrium entrainment regime[47] (e.g. Fedorovich, Conzemius and Mironov, 2004). The ratios of the boundary migration time-scales to the convective turnover time-scales, τ_b/τ_c, are 13.4, 13.1, 9.8 and 11.7 for the upper convective boundaries and 42.2, 27.6, 23.4, 12.3 for the lower convective boundaries of the lrez, mrez, hrez and vhrez models, respectively. These models, therefore, are considered to be within the equilibrium entrainment regime. The data from these simulations is interpreted within this framework (see §2.2.2 for details).

Momentum diffusion is not included in these simulations as the inviscid Euler equations are solved within the ILES paradigm. Instead, TKE dissipation is inferred through the loss of information below the grid scale, this provides an effective numerical viscosity (ϵ_k in Eq. A.2). Each term in Eq. A.2 is computed, apart from the numerical dissipation which is associated with the residual TKE from the energy budget.

Time-Averaged Properties of the TKE Budget

The profiles of the mean TKE equation terms (Eq. A.2) for the lrez, mrez, hrez and vhrez models are shown in the left panels of Figs. 5.9 and 5.10, with the inferred viscous dissipation shown by the black dashed lines. These profiles are time integrated over multiple convective turnovers (excluding the initial transient phase) and normalised by the surface area of the domain. Bar charts of the mean fields integrated over the domain are shown in the right panels. Comparing the left panels of these figures to Fig. 8 of Viallet et al. (2013), it can be seen that the properties of convection during carbon burning are very similar to oxygen burning.

Time Evolution. — The Eulerian time derivative of the kinetic energy, $\rho\mathbf{D_t}E_k$, is small or negligible over the simulation domain, implying that over the chosen time-scale, the model is in a statistically steady state.

Transport Terms. — The transport of kinetic energy throughout the convective

[47]This regime also assumes that the energy lost from exciting g-modes in the stable region is negligible in comparison to the turbulent kinetic energy. See Fig. 5.7, where the wave velocities at $r < 0.9 \times 10^9$ cm are around 40 times smaller than the velocities in the convective region, but at radii $r > 2 \times 10^9$ cm the velocities are around 2-3 times smaller than those in the convective region, and so are not negligible.

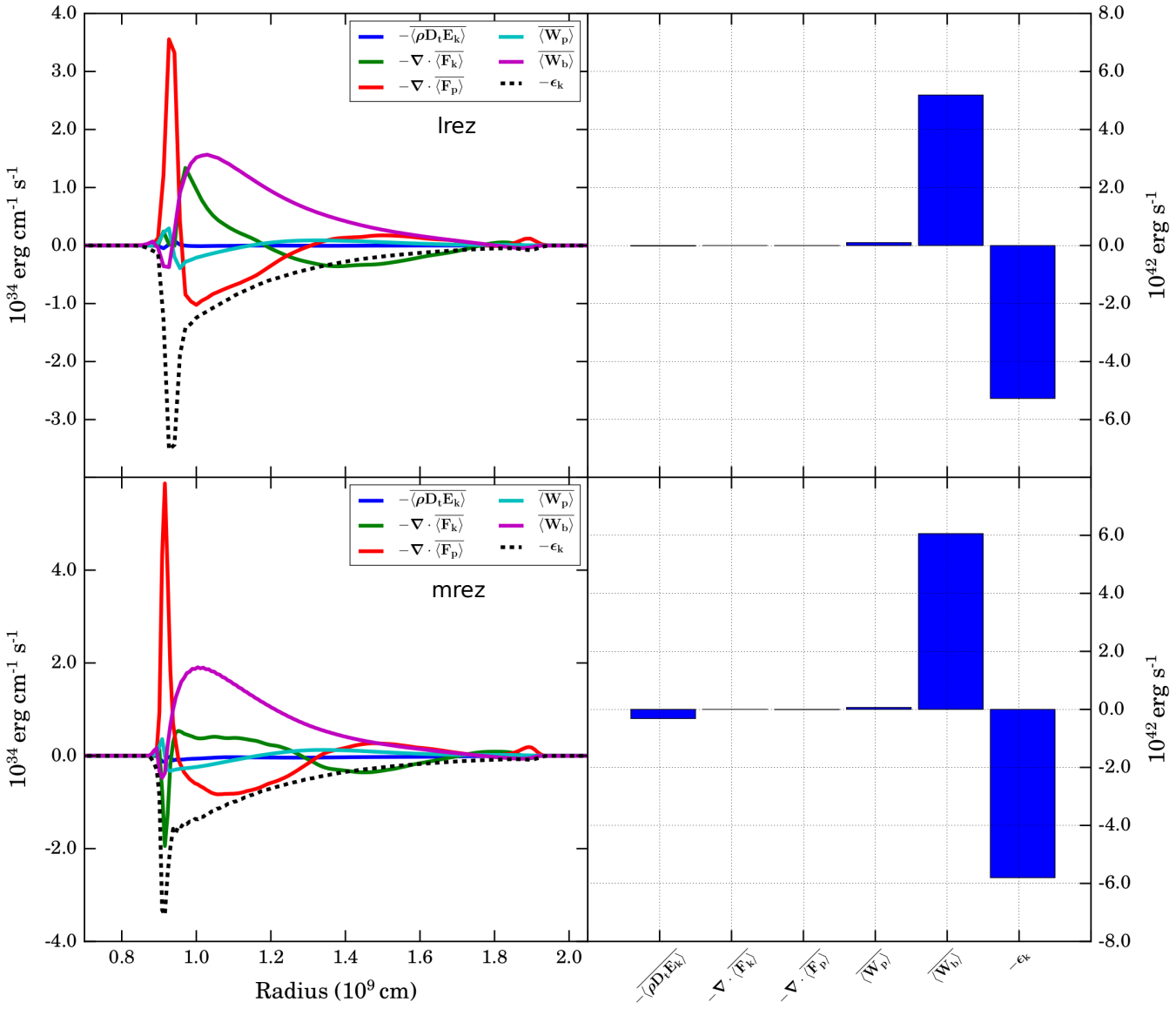

Figure 5.9: Left: Decomposed terms of the mean kinetic energy equation (Eq. A.2) over the simulation domain for the lrez (top) and mrez (bottom) models. These models have been horizontally averaged, normalised by the domain surface area and time averaged over the quasi-steady state. Time averaging windows are over 2,200 s and 2,100 s for the lrez and mrez models, respectively. Right: Bar charts representing the radial integration of the profiles in the left panel. This plot is analogous to Fig. 8 of Viallet et al. (2013).

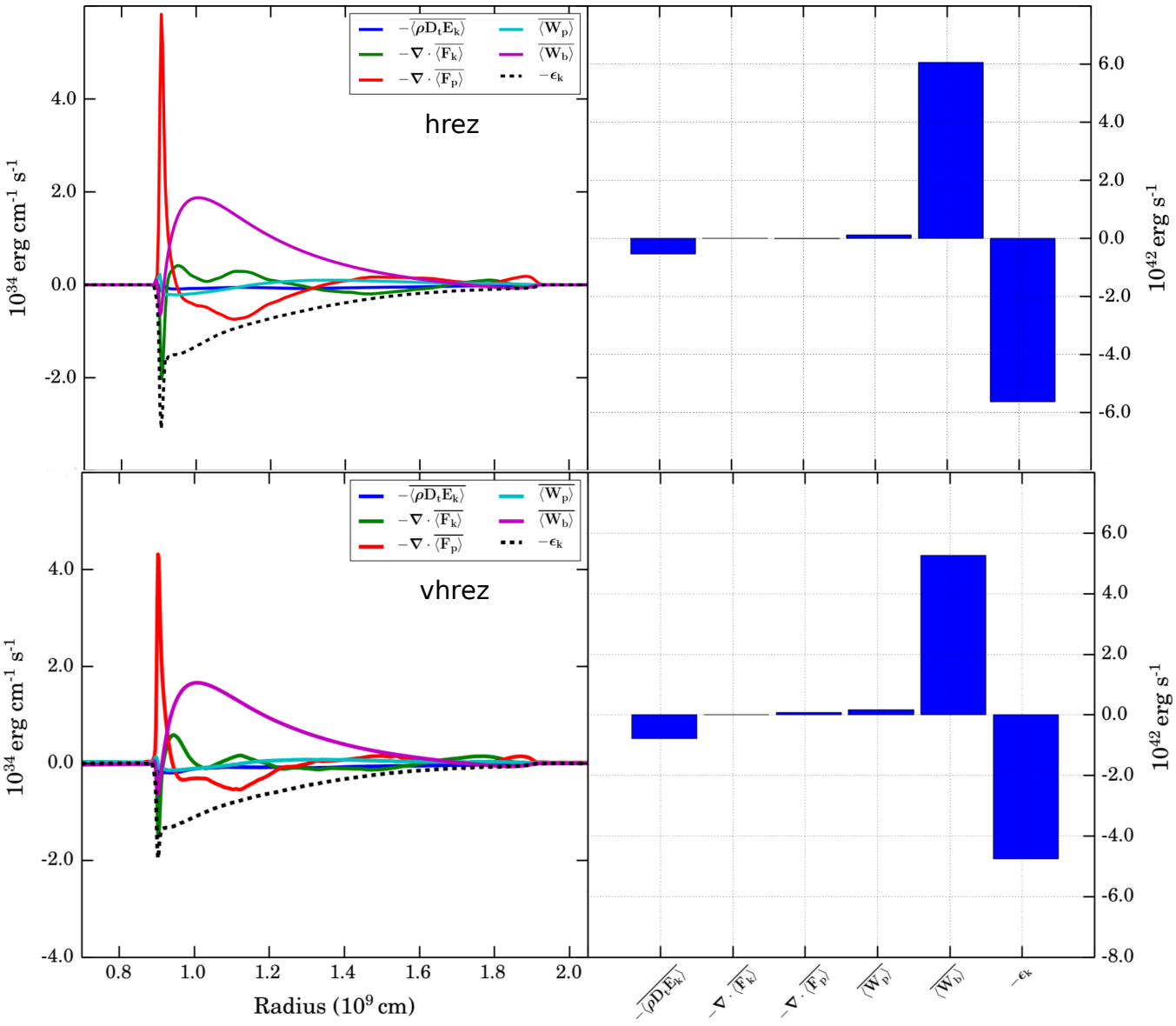

Figure 5.10: Left: Decomposed terms of the mean kinetic energy equation (Eq. A.2) over the simulation domain for the hrez (top) and vhrez (bottom) models. These models have been horizontally averaged, normalised by the domain surface area and time averaged over the quasi-steady state. Time averaging windows are over 1,850 s and 1,000 s for the hrez and vhrez models, respectively. Right: Bar charts representing the radial integration of the profiles in the left panel. This plot is analogous to Fig. 8 of Viallet et al. (2013).

region is determined by the two transport terms: the TKE flux, $\mathbf{F_k}$; and the acoustic flux, $\mathbf{F_p}$ (see Viallet et al., 2013, for a detailed discussion on these terms).

Source Terms. — Turbulence is driven by two kinetic energy source terms, $\mathbf{W_b}$ and $\mathbf{W_p}$. The rate of work due to buoyancy (density fluctuations), $\mathbf{W_b}$ is the main source of kinetic energy within the convective region, while the rate of work due to compression (pressure fluctuations or dilatation), $\mathbf{W_p}$, is small, suggesting that the fluid in this region of the star is almost incompressible. In the convective zone, generally $\mathbf{W_b} > 0$ as expected since it is the main driving term. Near the boundaries, however, there is a region where $\mathbf{W_b} < 0$. These regions are where the flow decelerates (braking layer) as it approaches the boundary, as already found and discussed for oxygen burning in Meakin and Arnett (2007*b*) and Arnett et al. (2015). Interestingly, the top braking layer and convective boundary width is more extended than the bottom one; this point is explored more in §5.2.5.

Dissipation. — Kinetic energy driving is found to be closely balanced by viscous dissipation, ϵ_k; a property consistent with the statistical steady state observed. The time and horizontally averaged dissipation can be seen to extend roughly uniformly throughout the convective region but increases slowly in its amplitude with depth, tracking the RMS velocities. There is almost no dissipation in the stable layers, where velocity amplitudes are low and turbulence is absent. Finally, there are notable peaks in dissipation localised at the convective boundaries. The dependence of these peaks on resolution is discussed next.

Resolution Dependence

The four models are compared - lrez, mrez, hrez and vhrez models - to determine if any of the physical results depend on the chosen mesh size. Over the four resolutions, the profiles in Figs. 5.9 and 5.10 are qualitatively similar. Within the turbulent regions of the higher resolution models, the cascade of kinetic energy over the inertial range appears to be resolution independent (Fig. 5.4). This suggests, as expected that the dissipation rate of kinetic energy is set by the dissipation of kinetic energy at the largest scales, which is sufficiently modelled at these resolutions. This is apparent from the

convergence of the inertial range within the kinetic energy spectrum in Fig. 5.4. An example of this dissipation is the breakup of large scale turbulent elements into smaller elements through shear forces.

In the left panels of Figs. 5.9 and 5.10 there is a significant deviation between models at the lower boundary region ($\sim 0.9 \times 10^9$ cm). This region is narrow in radius, and so the lrez model has an insufficient number of grid points to be representative (see Table 5.3 for approximate boundary widths and §5.2.5 for their definition). Also, the kinetic energy dissipation at the lower convective boundaries is clearly resolution dependent; this point is addressed next.

Dissipation at Convective Boundaries

At the lower convective boundary ($\sim 0.9 \times 10^9$ cm) a peak in dissipation appears at all resolutions in Figs. 5.9 and 5.10. This peak appears to be numerical, but the general behaviour of the numerical dissipation is sane, and the discrepancy is localised. The peak reduces in amplitude and width with increasing resolution, suggesting convergence to a physically relevant solution. A comparison of the dissipation in the lower boundary region for all resolutions is given in the bottom panel of Fig. 5.11. Here the TKE dissipation is normalised by a value at a common position within the convective region near to the boundary. This highlights the relative decrease in this numerical peak with respect to a converged value in the convective region. A similar plot for the upper boundary in the top panel of Fig. 5.11 shows that the dissipation at the upper boundary is smooth for both hrez and vhrez models. There is, however, some noise in the vhrez profile of the upper boundary, which is due to the lack of a sufficient number of convective turnovers for this model.

5.2.4 Convective Boundary Mixing

Entrainment events (similar to entrainment events found for oxygen burning, see Fig. 23 in Meakin and Arnett, 2007*b*) in the hrez model can be seen in both panels of Fig. 5.12. The upper panel shows the 2D velocity magnitude ($\sqrt{v_r^2 + v_y^2}$) in the (x, y) plane during a snapshot of the hrez model. The lower panel shows the logarithm of the average atomic weight fluctuations relative to their mean of the same snapshot, with

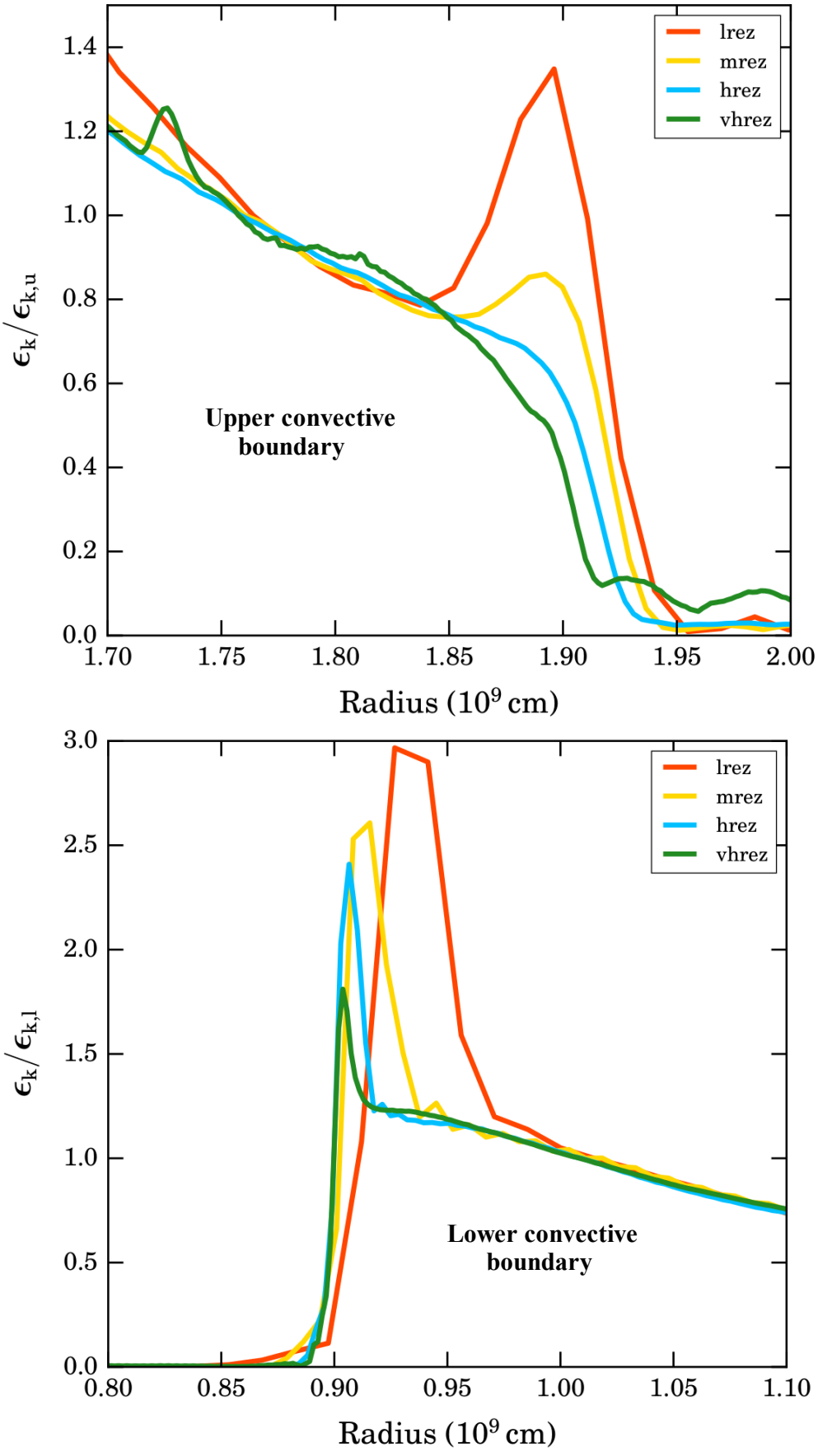

Figure 5.11: Turbulent kinetic energy residual dissipation curves of the upper (top) and lower (bottom) convective boundary regions for the lrez (red), mrez (yellow), hrez (cyan) and vhrez (green) models. The dissipation at each boundary has been normalised by a value at a common position within the convective region near to the boundary. The hrez and vhrez residual profiles appear to be converging at the upper boundary, suggesting that the representative numerical dissipation here is physically relevant.

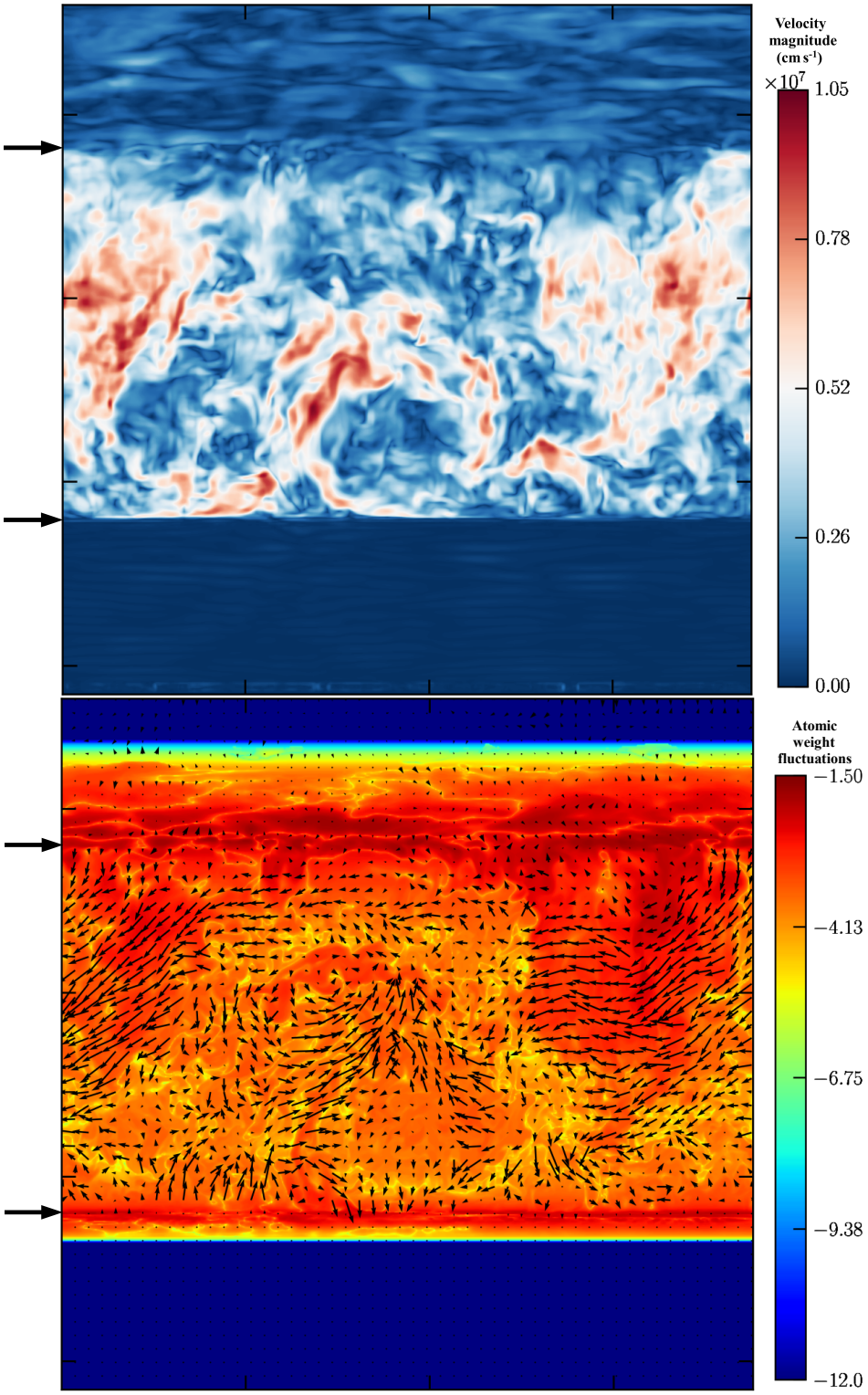

Figure 5.12: Upper: Vertical cross-section of the radial component and one horizontal component of the velocity vector field magnitude, $\sqrt{v_r^2 + v_y^2}$. The colour-map represents the velocity magnitude in $\mathrm{cm\,s^{-1}}$. Lower: Vertical cross-section of the logarithm of the absolute average atomic weight fluctuations relative to their mean within the convective region. The colour map represents the logarithm of compositional fluctuations ($|\overline{A}'/\overline{A}_0|$) relative to the mean. Arrows within the plot show the velocity vector field plotted in the upper panel. The direction of the arrows indicates the direction of this vector field in the x-y plane, and their length the magnitude of the velocity vector at that grid point.
Both snapshots were taken at 2,820 s into the hrez simulation. The horizontal black arrows on the left of each panel denote the vertical positions of the convective boundaries.

the velocity field over-plotted as arrow vectors, and with the magnitude and direction of the velocity vector at that point represented by the length and direction of the arrows, respectively. In the lower panel, the convective zone is represented by the orange/red region. At the bottom of this region material from below the convective zone is entrained upwards, resulting in an entrained region of thickness $0.26\,H_{p,l}$, where $H_{p,l}$ is the pressure scale height at the lower convective boundary. In the top corners of the convective region material is entrained from the stable layer above, resulting in an entrained region of thickness $0.7\,H_{p,u}$, where $H_{p,u}$ is the pressure scale height at the upper convective boundary. In both panels, strong flows can be seen in the centre of the convective region (centre of image/panel) and shear flows can be seen over the entire convective region. These shear flows have the greatest impact at the convective boundaries, where composition and entropy are mixed between the convective and radiative regions.

The production of Kelvin-Helmholtz (KH) instabilities[48] due to the effects of the shear flow at the boundary can be seen in Fig. 5.13. This plot shows the velocity magnitude for the vhrez simulation, focused on one section of the upper boundary region. Several rolls (or waves) of fluid can be seen (as is typical of KH instabilities) just above the boundary interface due to their increased velocity relative to the slower stable region. The behaviour of the flow at the boundary is a very different picture from the parameterisations that are used to describe CBM in stellar evolution models[49]. Such differences in the flow behaviour are also seen in oxygen burning simulations (e.g. Meakin and Arnett, 2007*b*; Arnett et al., 2015).

Entrainment at both boundaries, pushes the boundary position over time into the surrounding previously stable regions. This is due to the entrainment of fuel from the upper stable region, which is quickly mixed and burnt near the bottom of the convection zone, increasing the internal energy and convective flux of the shell. In order to calculate the boundary entrainment velocities, first, the convective boundary positions must be determined for each model. In the 3D simulations, the boundary is

[48]These types of instabilities arise when there is a velocity difference at the interface of two fluids, and are most prominent when the fluids are flowing in opposite directions (along the horizontal plane of the interface).

[49]Although most paramaterisations for CBM in stellar models are based on the results of 3D hydrodynamic simulations, they cannot capture multi-dimensional processes such as the KH instability.

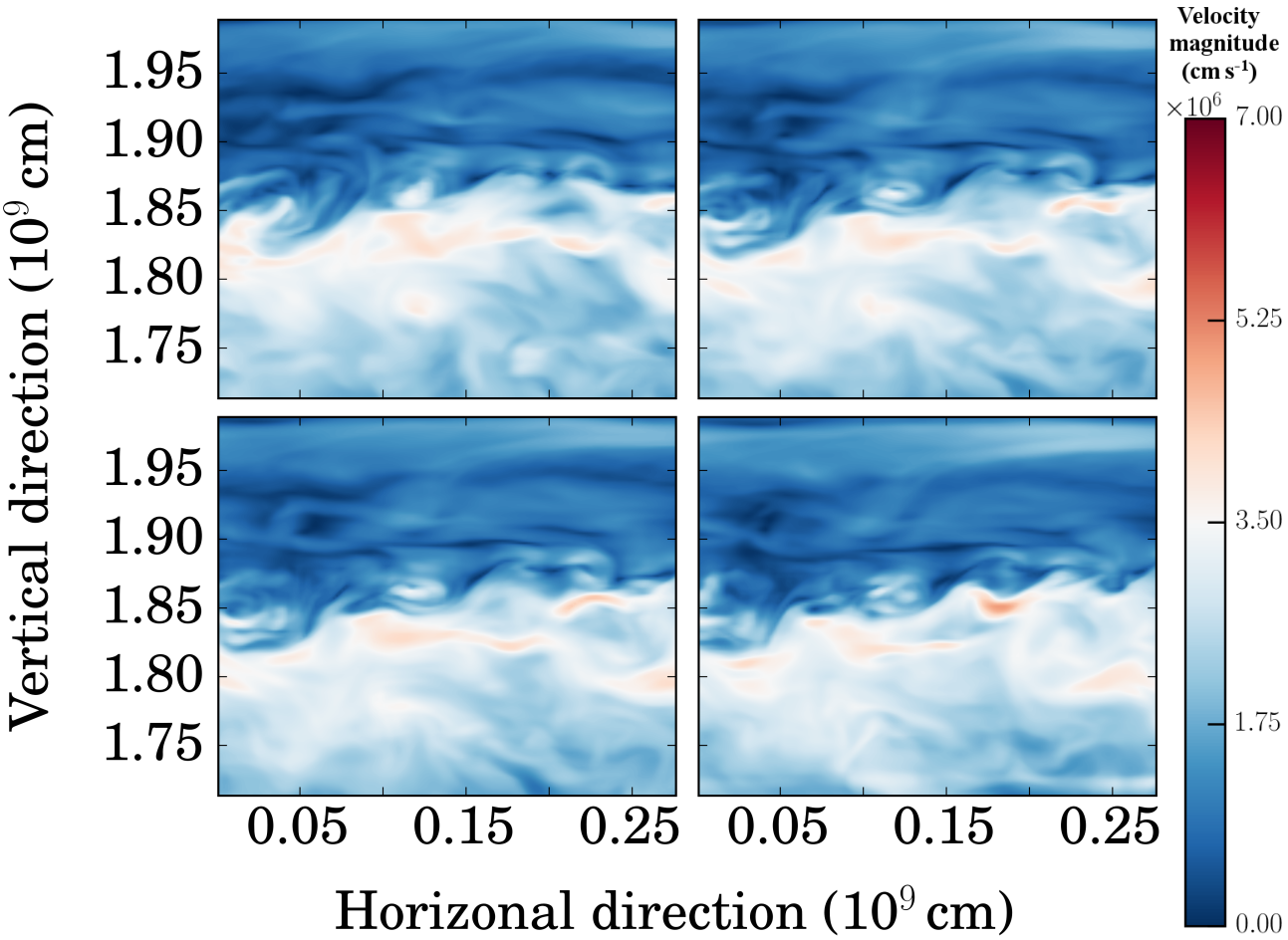

Figure 5.13: Sequential vertical cross-sections in the x-y plane of the velocity magnitude, $\sqrt{v_r^2 + v_y^2 + v_z^2}$, across the left section of the upper convective boundary for the vhrez simulation. Snapshots are taken at 1565 s (upper left), 1570 s (upper right), 1575 s (lower left) and 1580 s (lower right). The colour bar presents the values of the velocity magnitude in units of cm s^{-1}. The convective boundary is located at approximately 1.85×10^9 cm in the vertical direction. Each panel reveals shear mixing occurring across the boundary interface. The Kelvin-Helmholtz instability is a promising candidate for generating this type of mixing.

a two-dimensional surface with a varying thickness and is not spherically symmetric as in 1D stellar models.

Estimating Convective Boundary Locations

In order to estimate the radial position of a convective boundary, the boundary surface must first be mapped out. Consider the two-dimensional horizontal boundary surface, $r_{j,k} = r(j,k)$, for $j = 1, n_y$; $k = 1, n_z$, where n_y and n_z are the number of grid points in the horizontal y and z directions. The radial position of the boundary at each horizontal coordinate, is defined as the position which coincides with a pre-defined composition, using the average atomic weight, $\bar{A}$. This value of the composition is the average of the mean values of $\bar{A}$ in the convective and the corresponding radiative zones for each boundary, and is defined as

$$\overline{A}_{th} = \frac{\overline{A}_{conv} + \overline{A}_{rad}}{2}, \tag{5.2.1}$$

where $\overline{A}_{conv}$ and $\overline{A}_{rad}$ are the averages of $\overline{A}$ in the convective and relevant stable regions, respectively. This method is similar to the one adopted by Meakin and Arnett (2007*b*), who use the maximum radial gradient of the composition to define the location of the convective boundaries in their oxygen shell simulations. Once the 2D boundary surface, $r_{j,k}$, has been mapped out using the compositional constraint given by Eq. 5.2.1, the radial position (x) of the centre of the boundary region is taken as the mean of the surface position over the $y - z$ plane, $\overline{r}_{j,k}$, henceforth denoted as $\overline{r}$.

The error in the estimated boundary position is defined as the standard deviation (σ) from the horizontal surface mean, $\overline{r}$. As the composition, $\bar{A}$, is used as an input variable in the EOS, the value of A_{th} is updated as the models evolve, and hence new boundary surface positions, $r_{j,k}$, (and their means) are calculated. The method chosen here is a valid, but not unique, procedure in which to calculate the convective boundary positions. Examples of various other methods can be found in the following texts: Sullivan et al. (1998); Fedorovich, Conzemius and Mironov (2004); Meakin and Arnett (2007*b*); Liu and Ecke (2011); Sullivan and Patton (2011); van Reeuwijk, Hunt and Jonker (2011); Garcia and Mellado (2014); Gastine, Wicht and Aurnou (2015).

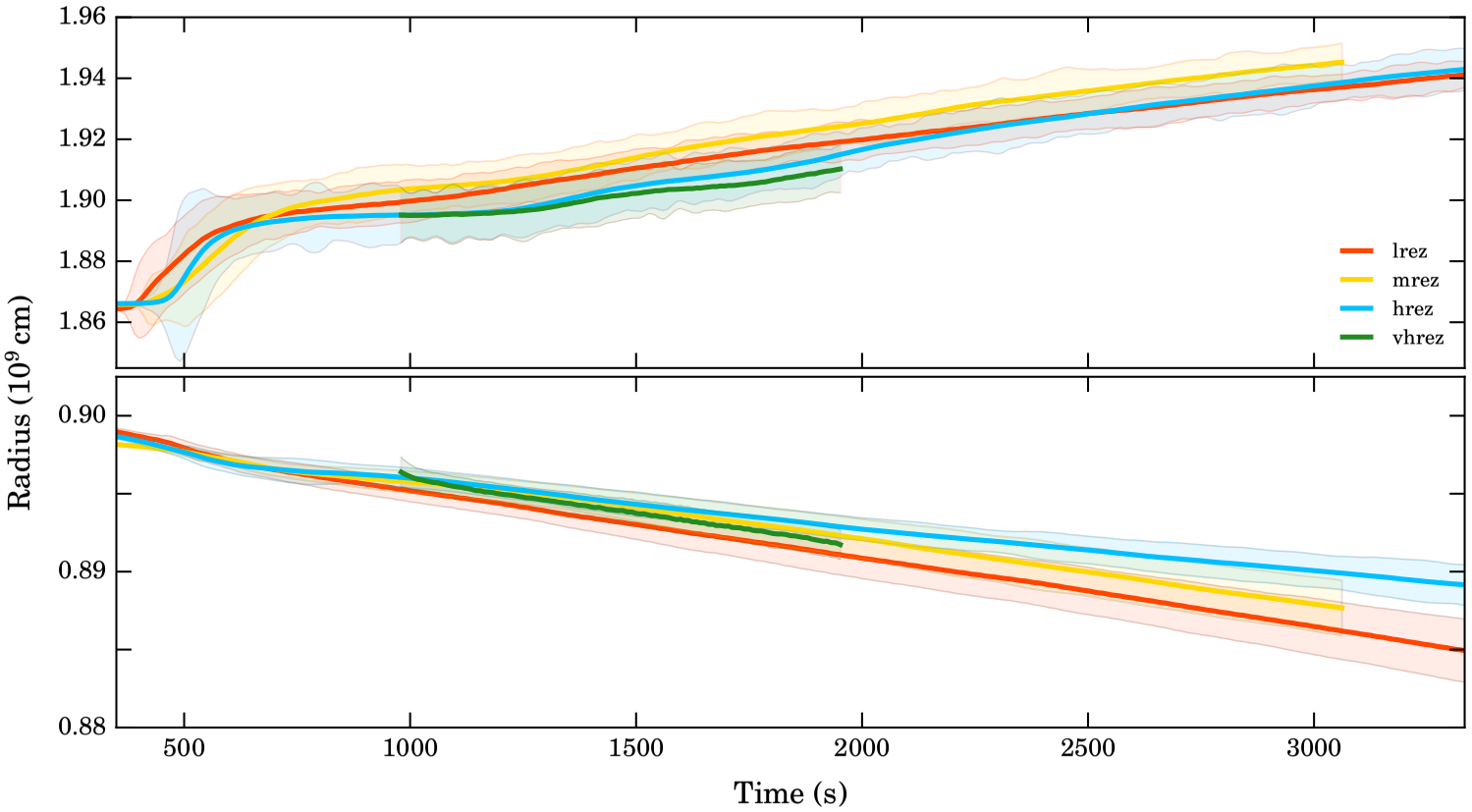

Figure 5.14: Time evolution of the mean radial position of the convective boundaries, $\overline{r}$, horizontally averaged over the boundary surface, $r_{j,k}$, for all four resolutions. Shaded envelopes are twice the standard deviation from the boundary mean. *Top*: upper convective boundary region. For increasing resolution the average standard deviation in the estimated boundary position are the following percentages of the local pressure scale heights: 3.3%; 3.8%; 4.3%; and 4.5%. *Bottom*: lower convective boundary region. For increasing resolution the average standard deviation in the estimated boundary position are the following percentages of the local pressure scale heights: 0.8%; 0.7%; 0.4%; and 0.6%. The shaded areas represent the variation in the boundary height due to the fact that the boundary is not a flat surface. This can be compared to the surface of the ocean not being flat due to the presence of waves.

	lrez	mrez	hrez	vhrez
Entrainment velocity ($10^4\,\mathrm{cm\,s^{-1}}$)	1.78 (-0.44)	2.01 (-0.39)	2.15 (-0.30)	1.59 (-0.46)
RMS velocity ($10^6\,\mathrm{cm\,s^{-1}}$)	3.76	4.36	4.34	3.93
Convective height ($10^9\,\mathrm{cm}$)	1.08	1.04	1.03	1.09
Boundary entrainment time ($10^3\,\mathrm{s}$)	7.4 (23.4)	6.2 (13.1)	4.6 (11.0)	6.0 (6.3)
Convective turnover time (s)	554	474	471	513
Bulk Richardson number	29 (370)	21 (259)	20 (251)	23 (299)

Table 5.2: Table summarising bulk and boundary region properties for each model. Values in brackets correspond to the lower boundary.

Convective Boundary Evolution and Entrainment Velocities

The variation in time of the average surface position, $\overline{r}$, of both boundaries is shown for all models in Fig. 5.14. Positions are shown as solid lines and the surrounding shaded envelopes are twice the standard deviation. This small variance is due to the vertical extent of the boundary surface, which is not flat as explained above. Following the initial transient ($> 1,000\,\mathrm{s}$), a quasi-steady expansion of the convective shell proceeds. The entrainment velocities, v_e, are calculated using a linear fit to the time evolution of the boundary position plotted in Fig. 5.14, and are given in Table 5.2. These velocities are very high. If one multiplies them by the lifetime of the carbon shell (of the order of 10 years), the convective boundaries would move by more than $10^{10}\,\mathrm{cm}$, which would lead to dramatic consequences for the evolution of the star. Note, though, that the driving luminosity of the shell was boosted by a factor of 1,000, in order to increase the

physical time of the simulations given limited resources. Hence the entrainment is also accelerated, although it is difficult to quantify by how much, the convective velocities are boosted by a factor of 10.

Turbulent entrainment

It is interesting to interpret the carbon shell simulations within the framework of the entrainment law (see Eq. 2.2.12), and ascertain the corresponding numerical values for A and n. Before doing this, it is instructive to compare the bulk Richardson numbers (Eq. 2.2.8) of the 3D simulations (of this thesis) to the initial conditions from the 1D stellar model (§4.2.2) and check that these simulations are indeed within the entrainment regime.

From the 1D $15\,\mathrm{M}_{\odot}$ stellar model introduced in §4.2, the carbon shell that was used as initial conditions in the 3D simulations (see Table 4.2) has bulk Richardson numbers of $\mathrm{Ri}_{\mathrm{B}}^{u} \sim 1,440$ and $\mathrm{Ri}_{\mathrm{B}}^{l} \sim 2.0 \times 10^{4}$ for the upper and lower convective boundaries, respectively. While, for the 3D vhrez model (see Table 5.2), $\mathrm{Ri}_{\mathrm{B}}^{u} \sim 23$ and $\mathrm{Ri}_{\mathrm{B}}^{l} \sim 299$. The lower values obtained in 3D are mainly the result of boosting the luminosity by a factor of 1,000, as this will increase the flow velocity by a factor of ~ 10 (as $\mathrm{Ri}_{B} \propto v_{c}^{-2}$; see §6.2 for a detailed study on the effects of varying the driving luminosity).

As the boundaries possess reasonable values for the bulk Richardson number (given the boosted energy generation rate), the four models are interpreted within the framework of the entrainment law (Eq. 2.2.12). A best fit entrainment coefficient of $A = 0.03\,(+0.02/-0.01)$ and exponent of $n = 0.60\,(+0.13/-0.14)$ is obtained over the four models (see Fig. 5.15). The value obtained for the entrainment exponent, n, falls between two scaling relations, $1/2 \leq n \leq 1$ (e.g. Jonker et al., 2013; Turner, 1986, respectively).

The value for the coefficient, A, for the simulations however, differs from all of the values found in the literature. A larger dataset is required to explore in more detail the parameter space; this is achieved in §6.2 where eight different simulations (16 convective boundaries) are compared within the $E - \mathrm{Ri}_{B}$ plane. Despite the discrepancies with the literature, this data set is compared with that from the oxygen burning study by Meakin and Arnett (2007*b*), in Fig. 5.15. The bulk Richardson numbers are similar for both datasets, and in particular, the lower convective boundaries both have higher

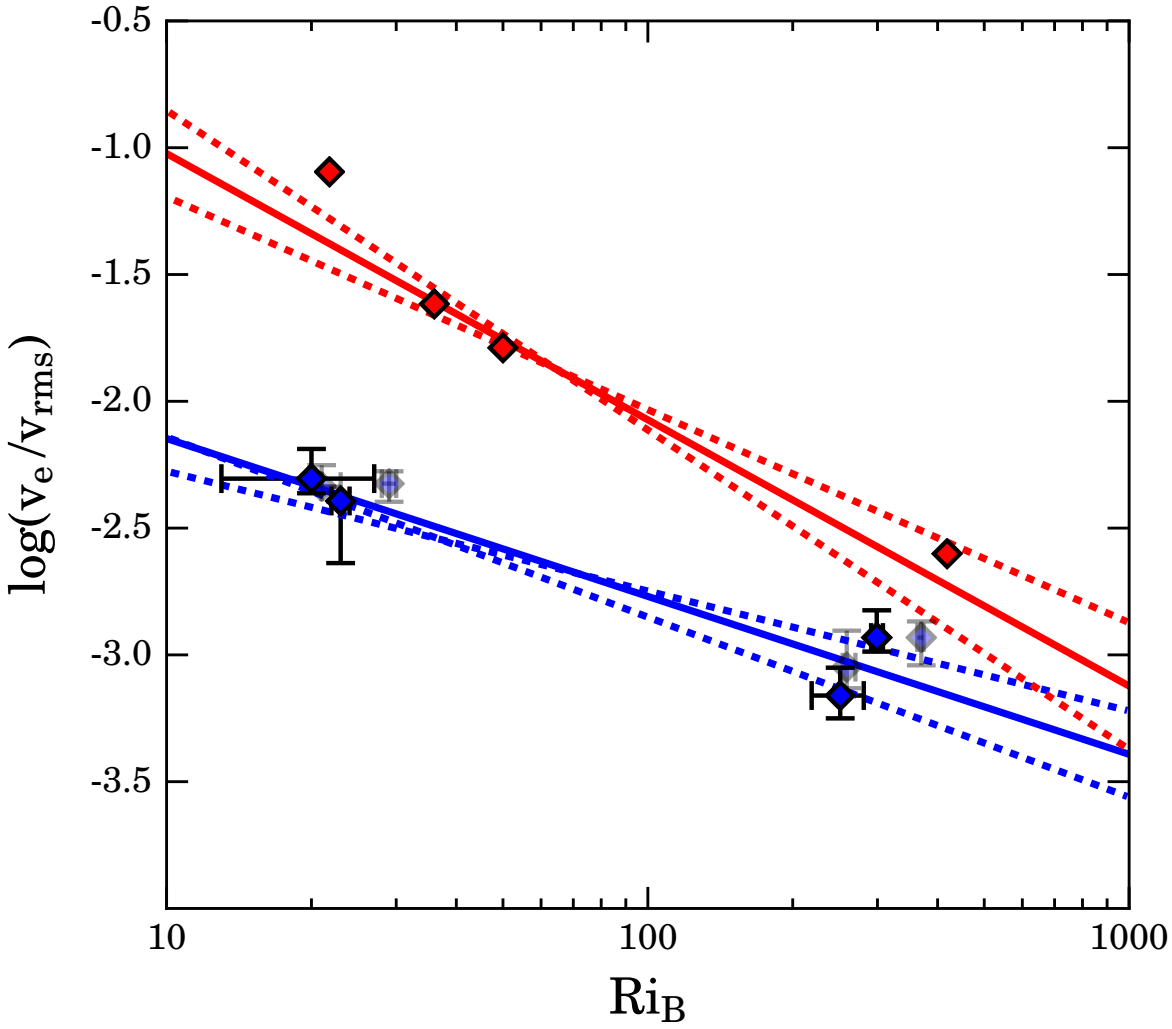

Figure 5.15: Logarithm of the entrainment speed for high Péclet number simulations, normalised by the RMS turbulent velocity versus the bulk Richardson number. Red points represent data obtained in the study by Meakin and Arnett (2007*b*) and blue points represent data obtained in this study. Transparent points represent the values for the lrez and mrez models, which are not included in the best fit power law shown by the blue solid line. The blue dashed lines show the best fit to the extremes of the error bars of the hrez and vhrez models. The red solid line is the best fit power law from a linear regression of the oxygen shell data and the red dashed lines show the error in the computed slope.

values than the corresponding upper boundaries. Entrainment velocities for the carbon shell are smaller than the oxygen shell, but this is partly expected due to the slightly lower turbulent driving.

5.2.5 Convective Boundary Structure

While stellar evolution codes describe a convective boundary as a discontinuity (see the blue composition profile in the bottom panel of Fig. 5.3, for example), 3D hydrodynamic simulations show a more complex structure. A boundary layer structure is formed between the convective and stably stratified regions. This can be seen from the

apparent structure of the mean fields, at $\sim 0.9 \times 10^9$ cm and $\sim 1.9 \times 10^9$ cm, in the left panels of Fig. 5.10, which represent the approximate locations of the lower and upper convective boundaries, respectively.

Figure 5.16 presents time-averaged profiles for various quantities over the upper (top panel) and lower (bottom panel) convective boundary regions for the vhrez model. These profiles have been normalised (see the caption of Fig. 5.16) to make comparison of their qualitative behaviour easier. It is apparent that a sub-structure exists within these boundary regions. For example, in the bottom panel of Fig. 5.16, the region that is most stable against convection (where there is a maximum in N^2), lies below the region of maximum deceleration of the incoming fluid elements (i.e. below where there is a minimum in $\overline{\langle W_b \rangle}$). Within this region of deceleration, radial velocities are lower. This effect is also shown by the lower RMS velocity compared with velocities at larger radii. The fluid elements approach a 'wall of stability' when the radial velocity is low, this is represented by the peak in the N^2 profile. At this position, the horizontal velocities are high; the fluid elements turn around and re-enter the convective region. This picture of over-turning fluid elements is similar to the description given by Arnett et al. (2015) (see their Fig. 5 and text therein).

Convective Boundary Thickness Estimates

The thickness of the convective boundaries is estimated using the jump in composition, $\bar{A}$, between convective and stable regions. This jump represents the transition between the fully mixed convectively unstable region and the convectively stable, stratified region. Due to the fusion of fuel into ashes, the average atomic weight difference between regions containing mostly ash or mostly fuel is considerable. The average composition (averaging removes stochastic fluctuations in composition) in the lower stable, convective and upper stable regions are denoted as, A_l, A_c and A_u, respectively. The width of the boundary region is considered to extend between 99% and 101% of the respective positions coincident with such compositional values, for example the outer position (greatest radius) of the upper convective boundary is considered to coincide with the position where the composition is equal to $1.01A_u$. For each boundary, the various threshold values are denoted with the appendage of a subscript $-$ (99%) or $+$ (101%) to the composition of each region, i.e. $\bar{A}_{u_+}$, for the previous example. Explicitly

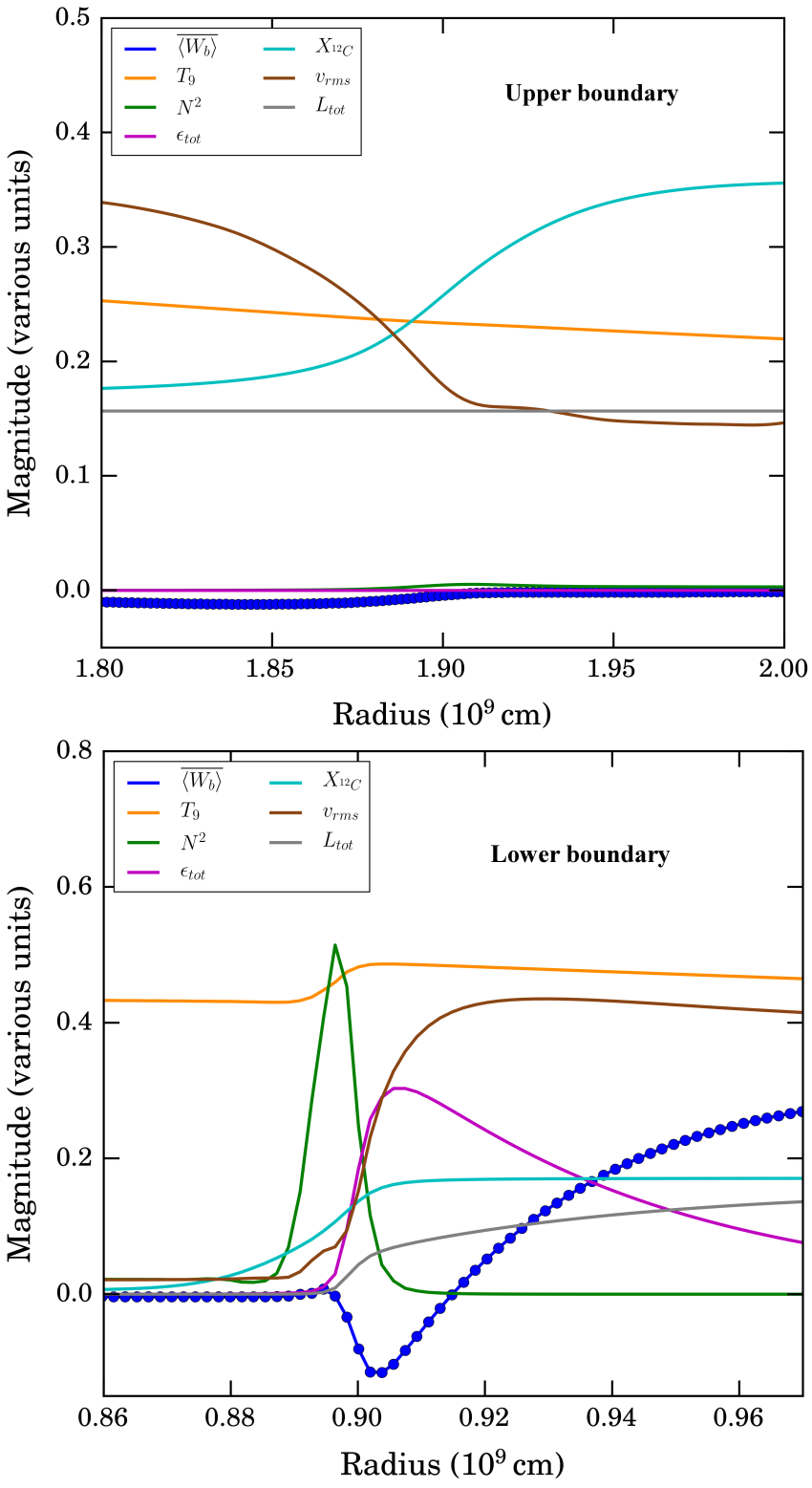

Figure 5.16: Time averaged profiles for the upper (top panel) and lower (bottom panel) convective boundaries of the vhrez model.
The following quantities are plotted: buoyancy work ($\overline{\langle W_b \rangle}$, normalised by 10^{35}; blue); temperature ($T_9 = T/2 \times 10^9$; orange); Brunt-Väisälä frequency (N^2, normalised by 10; green); total energy generation rate ($\epsilon_{tot} = \epsilon_{nuc} - \epsilon_\nu$, normalised by 10^{13}; magenta); carbon mass fraction ($X_{^{12}C}$, cyan); RMS velocity magnitude (v_{rms}, normalised by 10^7; brown); and total cumulative luminosity (L_{tot}, normalised by 10^{42}; grey).
Filled circles in the buoyancy work profile represent the grid spacing. The slight misalignment of the profile minima/maxima (especially for the lower boundary), demonstrates that there is a sub-structure within the boundary region. Also, the effect of ϵ_ν on the total energy generation rate is small due to the artificial boosting of ϵ_{nuc} by a factor of 1,000.

then, the thickness of the lower and upper boundaries are defined as:

$$\delta r_l = r\left(\bar{A}_{c_+}\right) - r\left(\bar{A}_{l_-}\right); \quad \text{and} \tag{5.2.2}$$

$$\delta r_u = r\left(\bar{A}_{u_+}\right) - r\left(\bar{A}_{c_-}\right), \quad \text{respectively.} \tag{5.2.3}$$

In addition, the boundary thickness was defined using radial gradients in the composition and entropy, and also the jump in entropy at the boundary. These other methods gave quantitatively similar results to the jump in composition at the boundary. In Fig. 5.17, the estimation of the thickness of the boundaries (using Eqs. 5.2.2 and 5.2.3) is illustrated for the final time-step of each simulation. The radius of each model has been shifted, such that the boundary position, $\overline{r}$ (see §5.2.4), of each model coincides with the boundary position of the vhrez model. With such a translation, it is easier to assess the convergence of the representations of the boundaries from each model. The thickness of the boundaries are denoted by the distance between filled squares for each simulation and also by the corresponding arrowed lines. Filled circles represent the individual mesh points, indicating the resolution of each simulation (a closer spacing between circles indicates a greater resolution). Note that, the composition profile labelled as model GENEC is from the 1D stellar model (bottom panel of Fig. 5.3), and was used as part of the initial conditions for all of the 3D models, so serves only as a qualitative comparison. The use of instantaneous mixing in stellar models (black) leads to compositional gradients at convective boundaries that are very different from the gradients obtained in hydrodynamic models (e.g. green) which calculate the fluid flow from first principles. Numerical estimates of the thickness of the boundaries are shown in Table 5.3, along with their ratio of the local pressure scale height.

In Fig. 5.17, it can be seen that the composition gradient varies little with resolution at the upper boundary. The composition gradient at the lower boundary varies significantly between the lrez and hrez models, while between the hrez and vhrez the gradient appears to be converging and generally becomes narrower with increasing resolution. These trends are confirmed by the boundary widths presented in Table 5.3, but a further increase in resolution is desired in order to be sure that the representation of the boundaries (including their position and width) is physical and not dependent

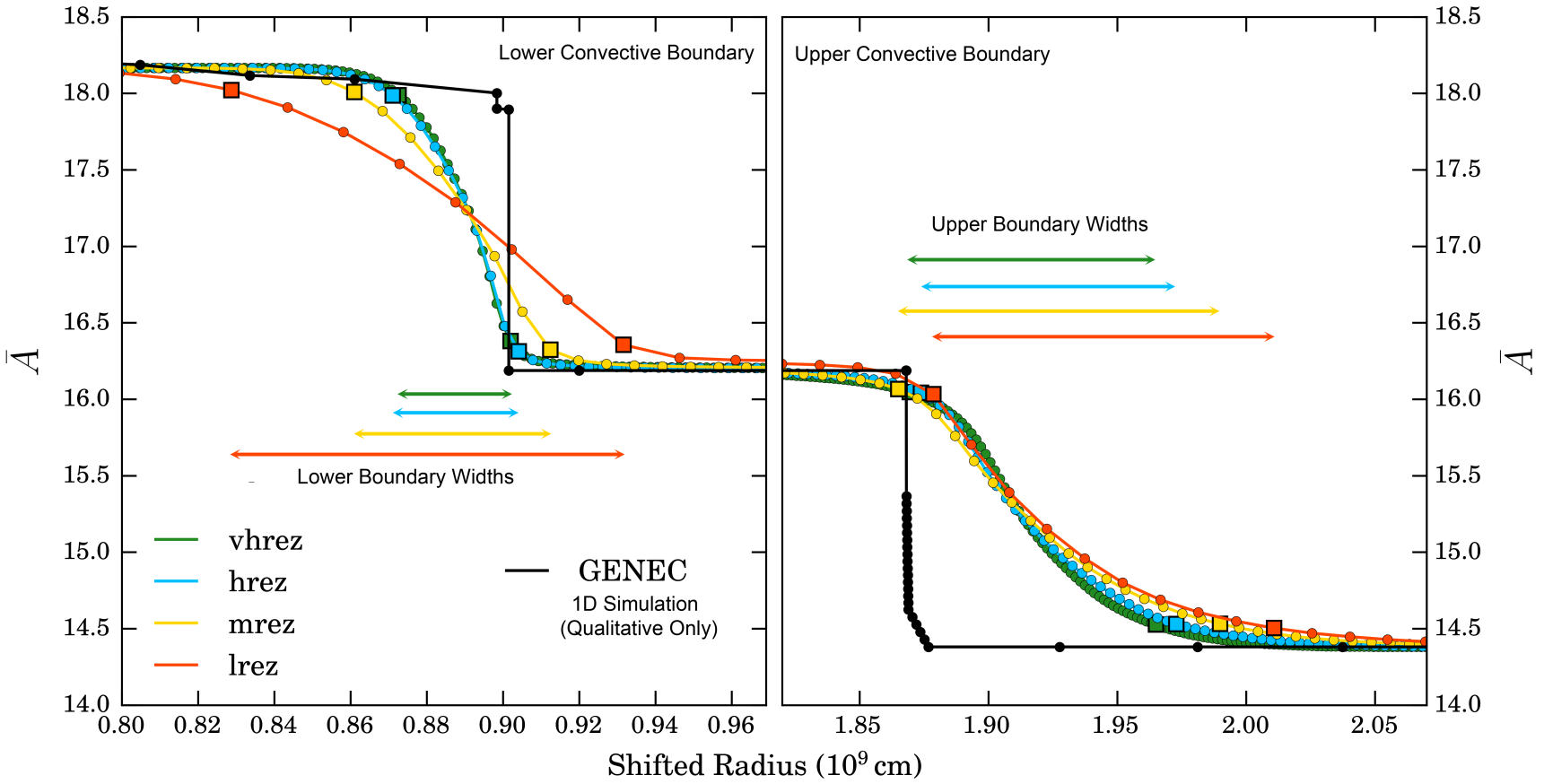

Figure 5.17: Radial compositional profiles at the lower (*left*) and upper (*right*) convective boundary regions for the last time step of each model. The radius of each model is shifted such that the boundary position, $\overline{r}$ (see §5.2.4), coincides with the boundary position of the vhrez model. In this sense, it is easier to assess the convergence of each model's representation of the boundary at the final time-step. Individual mesh points are denoted by filled circles. Approximate boundary extent (width) is the distance between two filled squares for each model and is indicated by the arrowed lines. The initial composition profile calculated using GENEC is shown in black (for a qualitative comparison only). See Eqs. 5.2.2 and 5.2.3 and the corresponding text for details of the definition of the boundary width.

	Boundary Width		Pressure Scale Height		Width : Scale Height	
	Lower	Upper	Lower	Upper	Lower	Upper
	δr_l(cm)	δr_u(cm)	$H_{p,l}$(cm)	$H_{p,u}$(cm)	$\delta r_l / H_{p,l}$	$\delta r_u / H_{p,u}$
lrez	1.0×10^8	1.3×10^8	2.9×10^8	3.3×10^8	0.36	0.41
mrez	5.1×10^7	1.3×10^8	3.0×10^8	3.4×10^8	0.17	0.36
hrez	3.3×10^7	9.9×10^7	3.0×10^8	3.5×10^8	0.11	0.29
vhrez	3.0×10^7	9.6×10^7	3.0×10^8	3.4×10^8	0.10	0.28

Table 5.3: δr_l and δr_u are the approximate boundary widths determined from the composition profiles of the lower and upper convective boundaries, respectively (see Fig. 5.17). $H_{p,l}$ and $H_{p,u}$ are the average pressure scale heights across the lower and upper convective boundary regions, respectively.

on the resolution that is used.

The widths determined from the abundance gradients (shown in Fig. 5.17 and given in Table 5.3) are larger than the fluctuations of the boundary locations (corresponding to the mid-point of the abundance gradients plotted in Fig. 5.17) shown as shaded areas in Fig. 5.14. This is expected since the fluctuations of the boundary location do not take into account its thickness or width, but only the location of its centre (mid-point). As a physical validity, these fluctuations in the location can be compared to the fluctuations in the position of the ocean surface due to the presence of waves. The fact that the width determined from the abundance gradients (given in Table 5.3) is significantly larger than the fluctuations, means that there is mixing across the boundary. This mixing is most likely due to shear (Kelvin-Helmholtz instability) induced by plumes rising from the bottom of the convective region and turning around at the boundary. Such instabilities can be seen in Fig. 5.13, which shows sequential slices of the flow velocity across the left section of the upper convective boundary region, where the characteristic Kelvin-Helmholtz rolls can be seen (see also the shear layer in Fig. 5 of Arnett et al., 2015). Mixing also occurs through plume impingement or penetration with the boundary. Some mixing may also occur through the presence of gravity waves which propagate through the stable region (e.g. Denissenkov and Tout, 2003). It is not expected that the upper boundary gradient will steepen, as this would support more

violent surface waves whose non-linear dissipation would tend to broaden the gradient, resulting in a negative feedback loop between these two processes.

It is important to note though, that the boundary widths given in Table 5.3 are only estimates. The key findings are (1) that the lower boundary has a narrower width compared to the upper boundary, and (2) the widths are relatively well converged between the hrez and vhrez models.

Comparison of Convective Boundaries

In order to visualise and understand how the shape of the boundaries changes over time, the composition ($\bar{A}$) of the hrez model has been over-plotted for each boundary over all points in time in Fig. 5.18, with the radial position of each profile (the boundary position at that time) shifted by its distance from the initial position of the boundary centre such that all the mid-points align, using the data from Fig. 5.14. At both boundaries, the initial, relatively narrow composition jump plotted in blue, is quickly broadened during the initial transient phase (up to 1,000 s) due to the turbulent flow. In the following quasi-steady state phase ($\gtrsim$ 1,000 s), the upper convective boundary becomes slightly 'softer' over time, broadening the composition jump in the stable region. Similarly, the lower boundary is slightly broadened over time into the stable region, but the overall width of the lower boundary is much smaller than the upper boundary.

Summarising the boundary properties determined so far for the hrez model (see Tables 5.2 and 5.3), the upper boundary region has a typical width of 9.9×10^7 cm, entrainment speed of $2.2 \times 10^4\,\mathrm{cm\,s^{-1}}$ and bulk Richardson number of 20. The lower boundary region typically has a width of 3.3×10^7 cm, entrainment speed of $3 \times 10^3\,\mathrm{cm\,s^{-1}}$ and bulk Richardson number of 251. There is thus a consistent picture of the lower boundary being narrower, having a slower entrainment velocity and being stiffer (higher $\mathrm{Ri_B}$) than the upper boundary by a factor of about 3, 7 and 13, respectively. Due to the sharpness and small extent of the lower boundary region, the resolution of the current simulations is not high enough to sufficiently resolve the lower boundary, whereas the upper boundary is sufficiently resolved with a resolution of 512^3. This can be seen from Fig. 5.11 where the residual TKE is compared for each resolution and at each boundary. Each profile is normalised by a converged value from within the convective region;

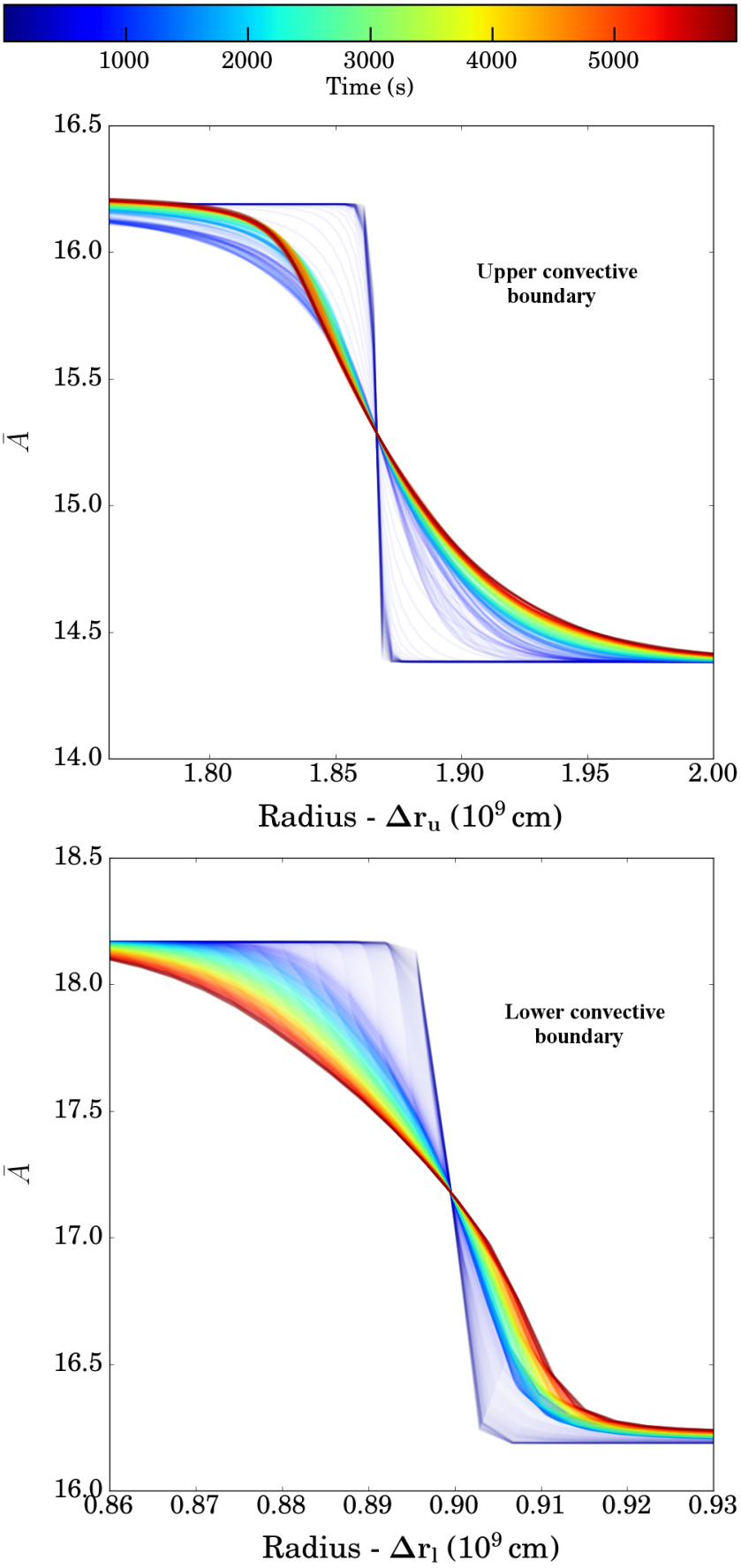

Figure 5.18: Composition ($\bar{A}$) profiles of the hrez model, over-plotted and coloured based on the time of the simulation. The radius of each profile is shifted by the distance from the initial boundary centre, using the data from Fig. 5.14, i.e. the boundary centre of each profile coincides with the boundary centre of the initial profile. The colour bar illustrates the time evolution of the profiles. *Top*: upper convective boundary composition profiles. *Bottom*: lower convective boundary composition profiles.

it is therefore easy to see that models with poor resolution at the boundaries possess sharp peaks in dissipation which decrease with increasing resolution. It is predicted then that a resolution of 1536^3 would be large enough to adequately resolve the lower boundary region.

5.3 Comparisons to similar studies

Here, I compare the results of the hydrodynamic simulations of the carbon shell within this resolution study, to other hydrodynamic simulations from the community. Such a comparison allows the process of entrainment and the dynamics of the boundary regions to be tested between different stages of stellar evolution, using different codes and analytical approaches.

The oxygen shell of a $23\,\mathrm{M}_\odot$ star was simulated by Meakin and Arnett (2007*b*) in spherical coordinates, also using the PROMPI code. The boosted luminosity of the carbon shell simulations in the resolution study, is similar in magnitude to the natural luminosity of their oxygen shell. The profiles of the velocity components are similar between the two models, despite the differences in geometry. Estimates of the bulk Richardson numbers obtained for the relevant convective boundaries in each study are similar. The predicted values of the constants in the entrainment law (Eq. 2.2.12) differ between the two shells (see Fig. 5.15). For the carbon shell these are $A = 0.03\,(+0.02/-0.01)$ and $n = 0.60\,(+0.13/-0.14)$. While for the oxygen shell these are $A = 1.06\,(\pm 2.40)$ and $n = 1.05\,(\pm 0.21)$. Higher values of A in the oxygen shell models points to more efficient entrainment of material across the boundaries, while a value for n which departs from 1 in the carbon shell models suggests that there may be additional mixing processes besides entrainment occurring within the carbon shell.

The TKE budget obtained in these Cartesian simulations of the carbon shell is in qualitative agreement with the spherical simulations of the oxygen shell in a $23\,\mathrm{M}_\odot$ star by Viallet et al. (2013) also computed with PROMPI. In both sets of simulations a statistically steady state of turbulence is achieved where TKE is driven by an overall positive rate of work due to buoyancy; this driving is balanced by dissipation at the grid scale through numerical viscosity. This suggests, in terms of the TKE budget, that the chosen geometry (spherical or plane-parallel) does not affect the results significantly.

However, the lack of a full spherical geometry may lead to missing low-order modes which could affect the energetics in other ways.

In a recent full spherical simulation of the oxygen burning shell in a $25\,M_\odot$ star, Jones et al. (2017) find a 2σ fluctuation in their calculation of the convective boundary position of 17% of the local pressure scale height. This is larger than the horizontal fluctuation in the estimation of the upper boundary position of the carbon shell - a 2σ fluctuation of 4.3% of the local pressure scale height (Fig. 5.14). This difference could be due to the maximum tangential velocity gradient method[50] which Jones et al. (2017) use to estimate the boundary positions, which differs from the method described in §5.2.4. In practice, there is no commonly accepted method for determining the position of the convective boundary. The magnitudes of the velocity components are comparable between the two simulations (see Fig. 5.7, and their Fig. 11), and so are the Mach numbers of the flow (see Table 5.1, and their Table 1). This could be in part due to the fact that the boosted energy generation rate used in the PROMPI carbon shell simulations ($\sim 3 \times 10^{12}\,\mathrm{erg\,g^{-1}\,s^{-1}}$) is comparable to the rate used in their PPMSTAR (Woodward, Herwig and Lin, 2015) simulations. The relative magnitude of the radial velocity component in Fig. 5.7 is higher than that of Jones et al. (2017), and the horizontal velocity does not possess the same symmetry as their tangential velocity. The latter is likely due to the difference in geometries between the two simulations.

Jones et al. (2017) also observe entrainment at the upper convective boundary of their oxygen shell; their velocity of the upper boundary due to entrainment is lower than the entrainment velocity estimated in the carbon shell simulations by over an order of magnitude. One reason for this difference could be that their oxygen shell boundary is much stiffer than the carbon shell boundary of this thesis. Such a prediction could be confirmed by calculating the bulk Richardson numbers of these oxygen shell boundaries. Stiffer boundaries in the oxygen shell would point to a larger jump in buoyancy over the boundary, as their value for the RMS turbulent velocity is similar to the value obtained in the carbon shell simulations. This difference in boundary stability could be confirmed through a difference in the peak squared Brunt-Väisälä frequencies, N^2. The value at the upper boundary of the carbon shell ($N^2 \sim 0.05\,\mathrm{rad\,s^{-2}}$) is an

[50]The tangential velocity drops rapidly where the steep entropy gradient forces the flow to overturn. The boundary position is then assumed to coincide with the position where the velocity slope is steepest.

order of magnitude smaller than that of the oxygen shell. This could then explain the order of magnitude difference in entrainment velocity assuming that the oxygen shell simulations follow an entrainment law similar to Eq. 2.2.12.

The comparison between the carbon shell simulations and these three simulations shows that entrainment is common to both carbon and oxygen shell burning.

Chapter 6

Investigation of the buoyancy driving strength within the context of a carbon burning shell

6.1 Motivations and methodologies

Following the realisation that 3D hydrodynamical simulations of carbon burning at natural luminosities are not easily attainable given the available computational resources (see §5.1.3), it seems befitting to further investigate the effects of varying the driving luminosity while retaining the same stellar structure. For this purpose, the driving luminosities are varied from natural carbon burning rates, up to oxygen burning rates and beyond. Despite boosting the luminosities of the models by such amounts, simulations are still possible as PROMPI is capable of modelling fluids over a wide range of Mach numbers. The most energetic of these models is the furthest from realistic stellar conditions, given the initial structure of the shell, but the aim in such a study is to explore the effects that varying the driving luminosity will have on the convective boundary dynamics and global properties of the shell.

Previous works (e.g. Porter and Woodward, 2000; Arnett et al., 2015) have shown that the RMS radial velocities of convective regions have a universal dependence on the driving luminosity (from Eq. 5.1.3), $v_{x,rms} \propto L^{1/3}$, where $v_{x,rms}$ is the vertical/radial RMS velocity. The simulations presented in this thesis were tested for these conditions and follow the same scaling relation. Jones et al. (2017) also show that the entrainment

rate of oxygen across the upper boundary of their oxygen shell burning simulations, is directly proportional to the driving luminosity. In these carbon burning simulations the fluid composition is defined by the average value of the atomic weight of all species in the fluid; as such it is not possible to obtain a similar mass entrainment rate for carbon. Instead, the scaling relation between the bulk Richardson number and the energy generation rate was determined. The bulk Richardson number is a useful diagnostic for the susceptibility of a boundary region to the entrainment of material through turbulent motions.

Many laboratory and computational studies have explored the entrainment law (Eq. 2.2.12) in various terrestrial situations (e.g. atmospheres, oceans and confined plasmas), but only recently has attention turned to stellar turbulent flows within the context of an entrainment law. Terrestrially there is already much debate on the universality of turbulence within the framework of an entrainment law, based on the TKE and stabilisation potential of the convective boundary (see §5.2.4). The initial result on turbulent dynamics within the carbon shell (e.g. Fig. 5.15) suggests that the standard scalings for entrainment are similar to those of stellar entrainment, but such results are far from conclusive. This makes a luminosity study of stellar convective mixing processes such as entrainment very attractive as, currently, the parameter space of the entrainment law ($E-\mathrm{Ri}_B$) is sparsely populated with data points from multi-dimensional stellar simulations. A larger study, over a range of driving luminosities could therefore help determine the appropriate scaling for turbulent entrainment within a stellar environment.

These models were also calculated using the PROMPI code, as described in §3.4 and evolved from the same initial conditions described in §4.2.2, within the same geometry and under the assumption of the plane-parallel approximation, as described in §5.1.1. The only change in the physical set-up between models is the driving luminosity, which is set by the carbon burning nuclear energy generation rate. This energy generation rate is the same prescription as described by Eq. 5.1, with the addition of a constant boosting factor, ϵ_{fac}, varying between 1 and 3.3×10^4. The radial profile of the nuclear energy generation rate is plotted for all models in Fig. 6.1, and is normalised to the maximum energy generation rate for the original `eps1` model. The energy generation rate due to neutrino losses is unchanged for each model, as over such short (dynam-

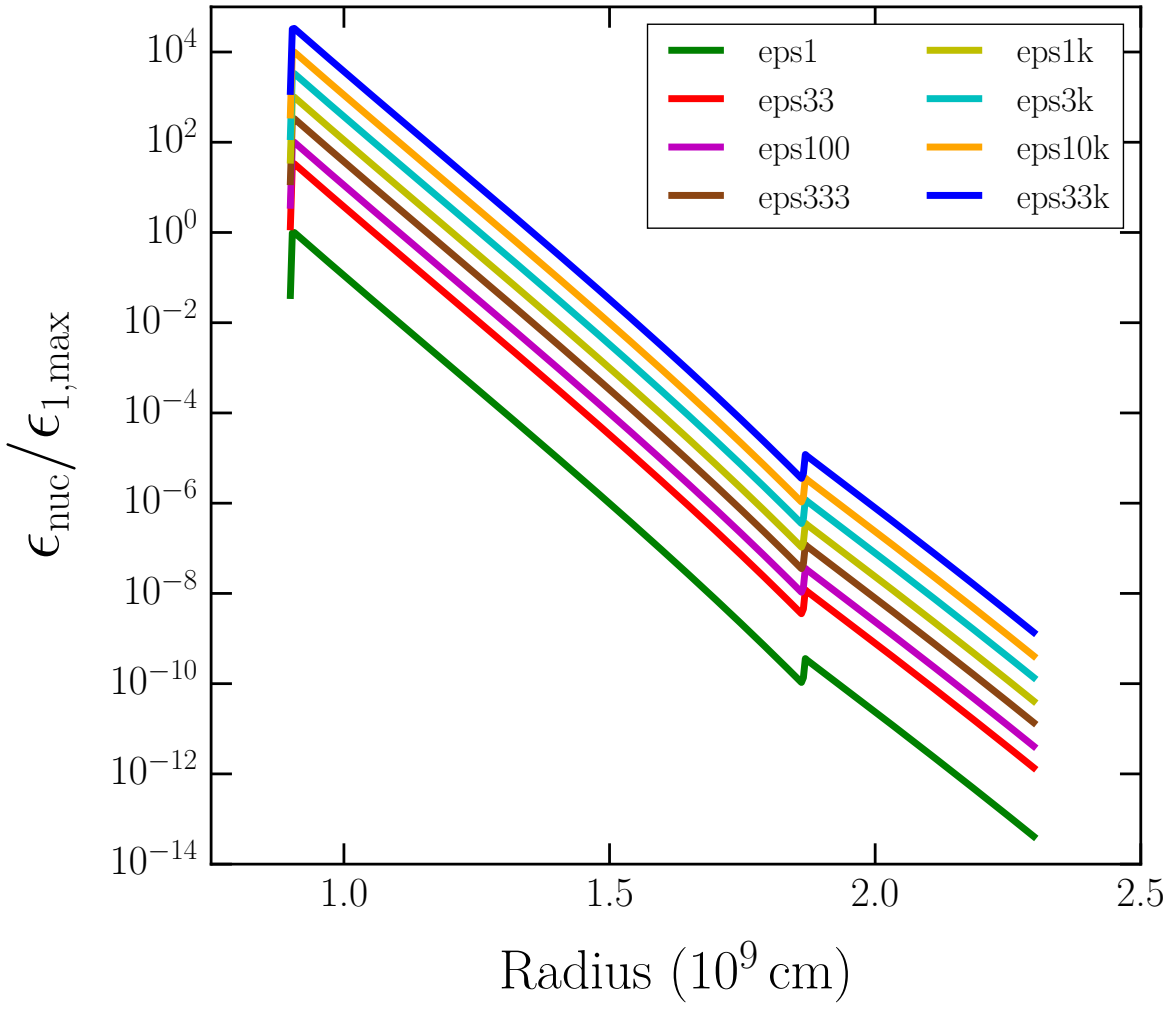

Figure 6.1: Radial profiles of the nuclear energy generation rate for each model. Each profile is normalised to the maximum energy generation rate in the original eps1 model, to allow an easier comparison between the models.

ical) time-scales it is not expected that changes in the energy generation rate due to neutrino losses will have an effect on the structure of the shell, even in the case of the natural luminosity model, eps1, where cooling due to neutrino losses cannot be neglected relative to the nuclear energy generation rate.

In order to be computationally efficient while maximising the resolution, a mesh size of 512^3 was chosen for all of these models. This resolution is sufficient to model the upper convective boundary for the hrez model (a subset of the eps1k model with $\epsilon_{fac} = 1000$), e.g. see the top panel of Fig. 5.11. It would be too computationally expensive to compute several models at a resolution of 1024^3. Eight models are computed and are named according to the value used for ϵ_{fac}, see Table 6.1. The model eps1k is an extension of the hrez model (introduced in §5.1.2) up to 6000 s. All other models were computed from the same stellar model initial conditions; this was in order to

	eps1	eps33	eps100	eps333	eps1k	eps3k	eps10k	eps33k
ϵ_{fac}	1	33	100	333	1000	3000	1×10^4	3.3×10^4
τ_{sim}	5000	5000	3600	1640	6000	3635	2000	1190
v_{rms}	6.80×10^5	1.15×10^6	1.59×10^6	1.92×10^6	4.56×10^6	6.93×10^6	1.03×10^7	1.57×10^7
τ_c	3257	1789	1317	1025	465	316	219	153
τ_q/τ_c	1.20	2.18	1.89	0.62	10.76	8.68	6.84	3.87
Ri_B	1876 (2.93×10^4)	559 (8089)	310 (4203)	200 (3101)	42 (435)	19 (188)	7 (101)	4 (44)
Ma	0.0028	0.0048	0.0070	0.0074	0.0209	0.0321	0.0481	0.0727

Table 6.1: Summary of simulation properties. ϵ_{fac}: nuclear energy generation rate boosting factor, τ_sim: simulated physical time, v_rms: global RMS convective velocity, τ_c: convective turnover time, τ_q: quasi-steady state time, $\mathrm{Ri_B}$: bulk Richardson number (values in brackets are representative of the lower convective boundary region), Ma: Mach number.

study the effect of varying ϵ_{fac} on the initial transient stage. In particular, the time required to reach a quasi-steady state, where an equilibrium is reached between the driving luminosity and numerical dissipation was of interest. The highest energy model eps33k, was difficult to evolve as the energies were so extreme that the structure of the shell was disrupted, which made the shell become dynamically unstable. As such, the physical simulation time for this model is relatively shorter than the other models. The physical time of the eps333 model is also particularly short, but this was due to a lack of computational resources. The global properties of each model are summarised in Table 6.1.

6.2 Results and discussions

6.2.1 General flow properties

Similarly to the majority of models presented in §5.1.2, the eight models for this study were evolved from the initial conditions given in §4.2.2. They first passed through an initial transient phase (whereby the turbulent velocity field was established) and the models eventually reached a quasi-steady turbulent state, where there was no longer any influence from the initial conditions. The transition to the quasi-steady state for each model can be seen most easily in Fig. 6.2, where the specific total kinetic energy (KE) for each model is plotted against the simulation time. The initial transient phase begins with a characteristic sharp rise in the KE up to a local maximum, which is then followed by a steady decrease. This marks the end of the initial transient, and the beginning of the quasi-steady state, and is indicated by a vertical dashed line for each model. From Fig. 6.2 it can be seen that the local maximum in KE during the transient phase increases with the boosting factor for the energy generation, and that the overall KE for each model increases as the boosting factor is increased. This is intuitive as an increase in energy generation alone, results in a larger flux of KE at the temperature peak near the bottom of the shell.

The specific KE evolution over the radius of the computational domain for each model is shown as separate contour plots in Fig. 6.3; the colour-bars show values of the KE in units of $10^{13}\,\mathrm{erg\,g^{-1}}$. Each panel is labelled for the respective model. Each

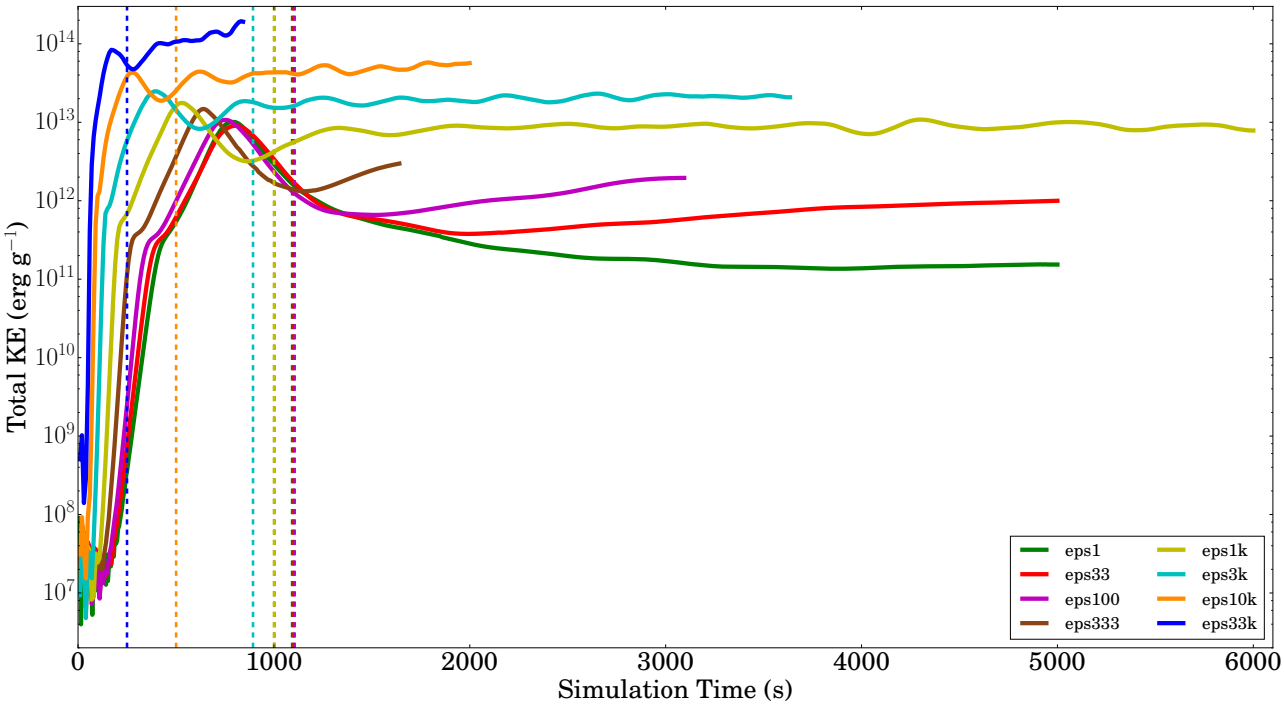

Figure 6.2: Specific total kinetic energy over the simulation time of each model. The initial transient is characterised by a sharp rise to a local maximum, followed by a shallow decrease. The roughly horizontal parts of each profile that follow, denote the quasi-steady turbulent phases of each model, the start of which are denoted by the relevant vertical dashed lines. Note though, that the lower energy models (eps1, eps33, eps100 and eps333) have likely entered this phase for only a short amount of time, due to such long transient time-scales and relatively short simulation times. The end of each profile indicates the end of each model.

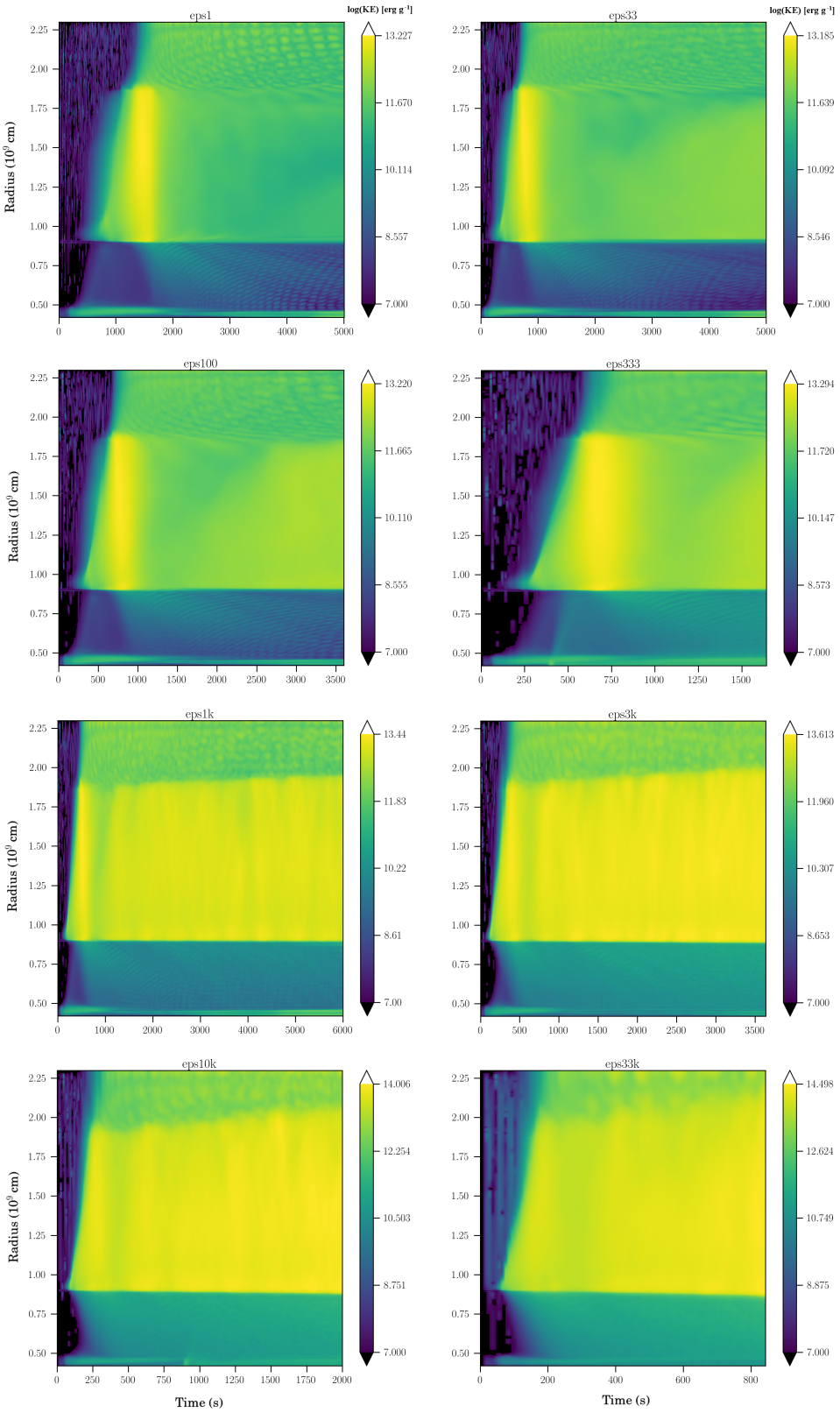

Figure 6.3: Contour plots of the logarithm of the KE evolution in the radial direction for each model. Each panel has the same radial scale (vertical axis) but has individual scales for each colour bar representing the KE magnitude and thus each model should be compared qualitatively and not quantitatively. Each model passes through an initial transient phase characterised by a strong pulse in KE near the start of each simulation. The eps1k, eps3k, eps10k and eps33k models, clearly show extended periods of turbulent entrainment, characterised by the migration of the upper boundary into the stable region above, which can be seen from the radial extension of the relatively higher KE in the turbulent region compared with the upper stable region. The eps1, eps33, eps100 and eps333 models have either not reached or have only entered the quasi-steady state for a short amount of time.

model passes through an initial transient phase characterised by a strong pulse in KE near the start of each simulation. The models eps1k, eps3k, eps10k and eps33k show semi-regular pulses in KE over the evolution of the models, a characteristic of convective transport. Such strong turbulent motions also lead to turbulent entrainment. This is best seen at the upper boundary by the gradual migration of the boundary into the stable region above. In all models, excited gravity modes can be seen in the upper stable region, identified by short, horizontal light blue streaks.

At first glance, the eps33k model may appear to still be transitioning through the transient phase, but actually this transition is shown by the light blue region spanning the convective region at around 200 s, followed by strong entrainment at the upper boundary. Towards the end of the model (> 700 s) a strong increase ($> 3 \times 10^{14}$ erg g^{-1}) in KE can be seen; at this point in the simulation the driving luminosity is so great that the shell is becoming dynamically unstable, and at later times (> 1000 s) the shell is completely disrupted. This can be seen in the time series of the velocity magnitude for this model in Fig. 6.4, where the velocity magnitude is plotted at 340 s, 840 s, 1020 s and 1180 s. Comparing the velocity magnitudes at 340 s and 840 s (top two panels), it can be seen that the upper boundary migrates, almost entirely encompassing the stable region above. By 1020 s (lower left panel) the upper boundary no longer exists and the entire previously upper stable region is now turbulent. These turbulent motions are no longer decelerated by approaching a stable region above, but still over-turn (as if these motions were approaching a boundary with an extremely high bulk Richardson number) due to the reflective boundary condition at the edge of the simulation domain. By 1180 s, the removal of the upper stable region leads to the turbulent velocities increasing dramatically (lower right panel) as turbulence is still driven by a large nuclear energy generation rate at the bottom of the shell, and the up-flowing radial velocities produced from this turbulence are not reduced by a negative buoyancy force due to the presence of an upper boundary. Instead the strong radial deceleration and turning of fluid elements at the upper domain boundary results in a band of material ($\geqslant 2 \times 10^9$ cm) with visibly reduced velocities. Regardless, the removal of the boundary results in an un-damped, runaway acceleration within the convective region and the velocities become so high, that the fluid approaches the transonic regime ($|v| \sim 10^8$ cm s^{-1}) and the shell becomes dynamically unstable.

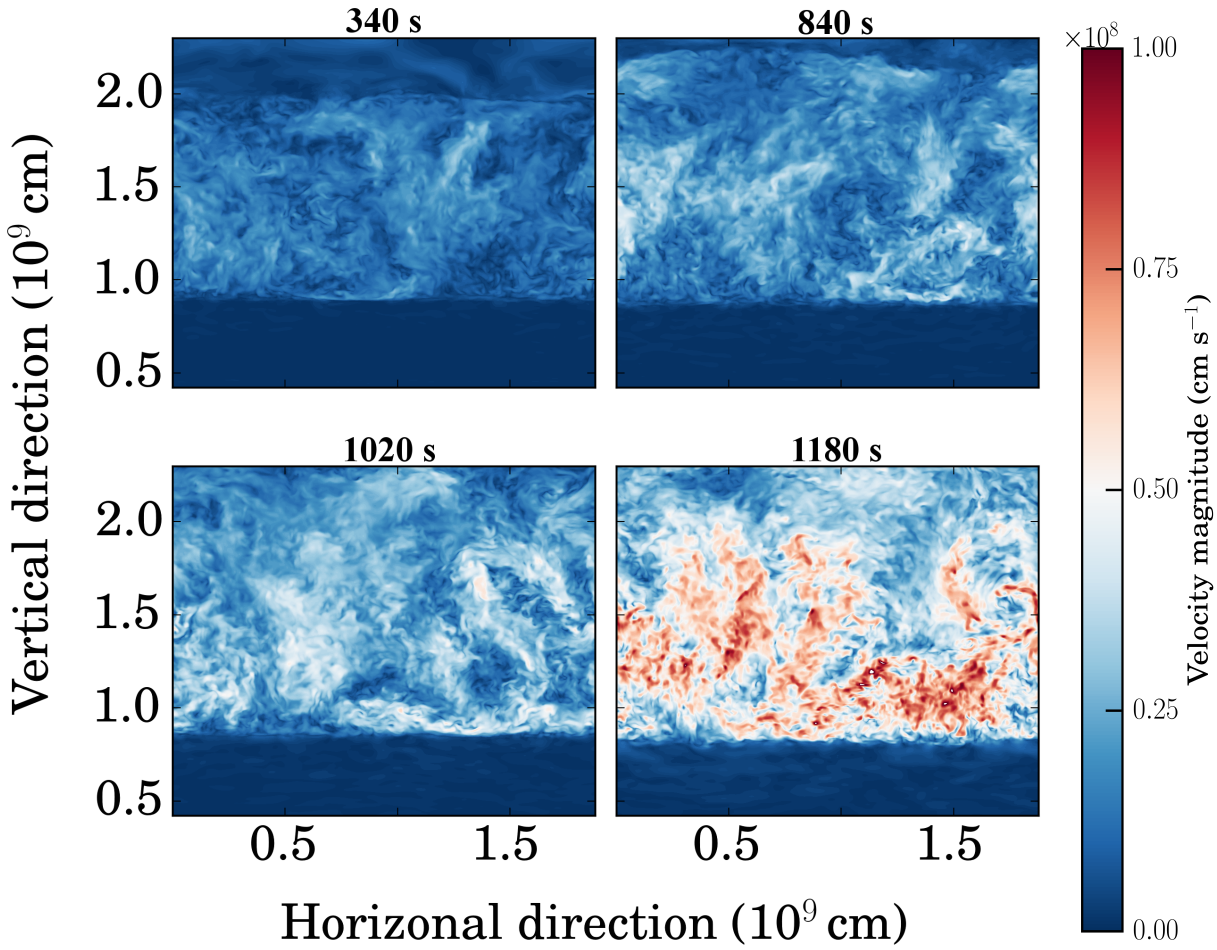

Figure 6.4: Sequential vertical cross-sections in the x-y plane of the velocity magnitude ($|v| = \sqrt{v_r^2 + v_y^2 + v_z^2}$) for the eps33k model. Snapshots are taken at 340 s (upper left), 840 s (upper right), 1020 s (lower left) and 1180 s (lower right). The colour bar presents the values of the velocity magnitude in units of cm s^{-1}. The upper panels reveal the progressive expansion of the upper boundary layer into the surrounding stable region. The lower panels reveal that the upper boundary is now completely disrupted and the entire previously upper stable region has become turbulent.

Despite such dynamic and violent behaviour, the short time period between 450 s - 900 s still represents turbulent entrainment at a greatly boosted rate, and such a time period is used in the further boundary analysis for this model.

Similarly to §5.2.1, the properties of the inertial range when varying the luminosity are explored by comparing velocity spectra for each model. Each spectrum is calculated in the same manner as described in §5.2.1 (including time-averaging over the quasi-steady state period), and are shown in Fig. 6.5. Similarly to Fig. 5.4, the inertial sub-ranges are shown by the roughly horizontal section of each profile. These represent the scales of the model which are no longer affected by the initial or boundary conditions, driving force or dissipation. The extent of the inertial sub-range over wave-number increases as the driving luminosity is increased, but is roughly located between $k = 20$

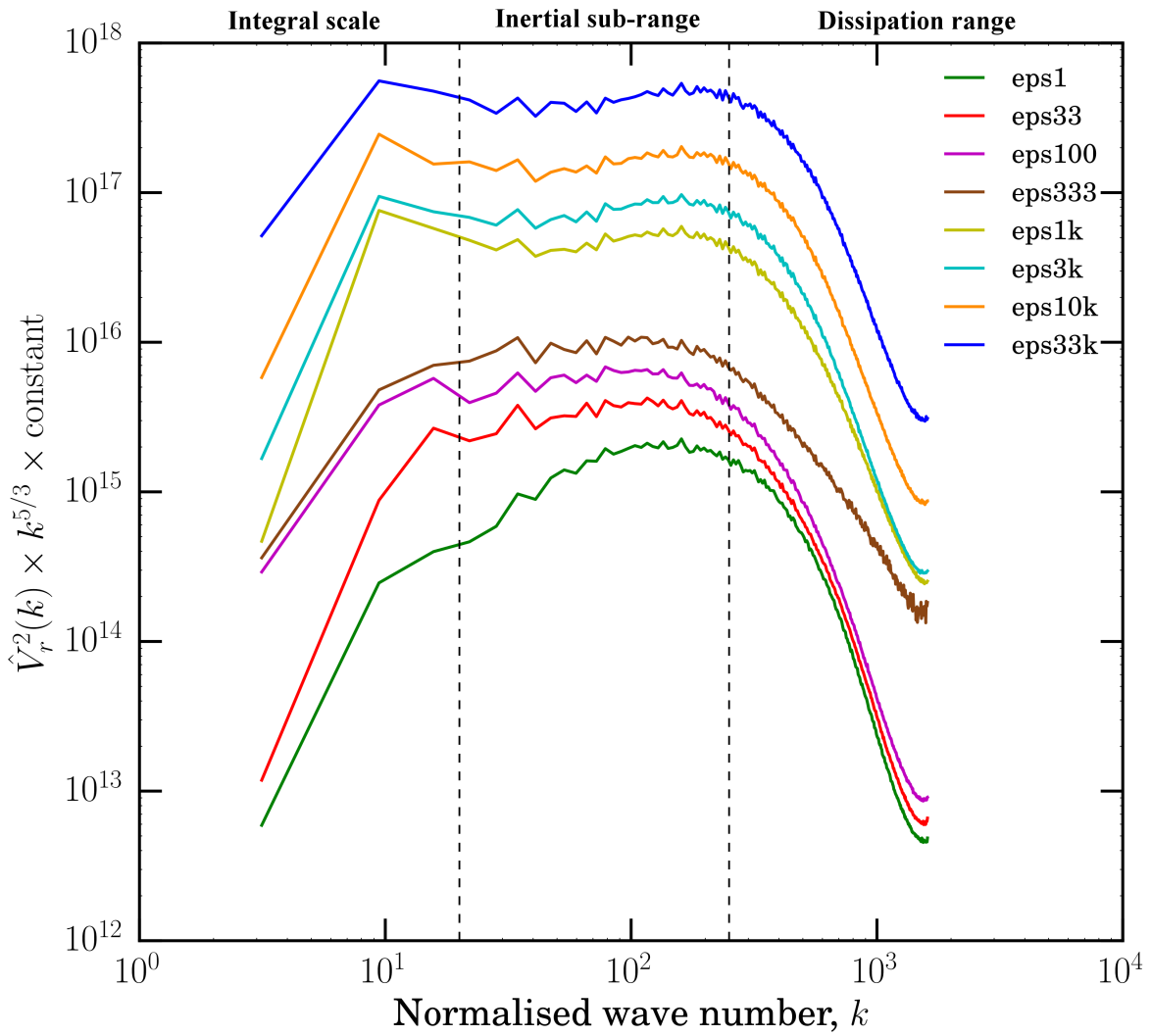

Figure 6.5: Specific kinetic energy spectrum for all of the simulations in the luminosity study. Spectra were obtained from a 2D Fourier transform (in the centre of the convective region) of the vertical velocity. The vertical axis consists of the square of the Fourier transform, scaled by a 'Kolmogorov factor', $k^{5/3}$, and a constant. The horizontal axis is the normalised wave-number, $k = \sqrt{k_y^2 + k_z^2}$. The eps333 (brown) and eps1k (yellow) models follow slightly different trends to the other models within the dissipation range. This is likely due to a relative decrease and increase in time averaging for these models, respectively.

and $k = 250$ for all models. The magnitude of the specific kinetic energy (velocity squared) also increases with driving luminosity, as expected. The differing trends beyond the inertial sub-range for the eps333 (brown) and eps1k (yellow) models is likely due to a relative decrease and increase in time averaging for these models, respectively, but the renormalisation makes such a comparison difficult.

Using heuristic arguments within turbulence theory; from Kolmogorov (1941) it can be shown that $\epsilon \sim v_{rms}^3/\ell$. Assuming that the energy generation rate is proportional to the luminosity, it can be shown that the cube of the vertical/radial velocity is directly proportional to the luminosity, or that

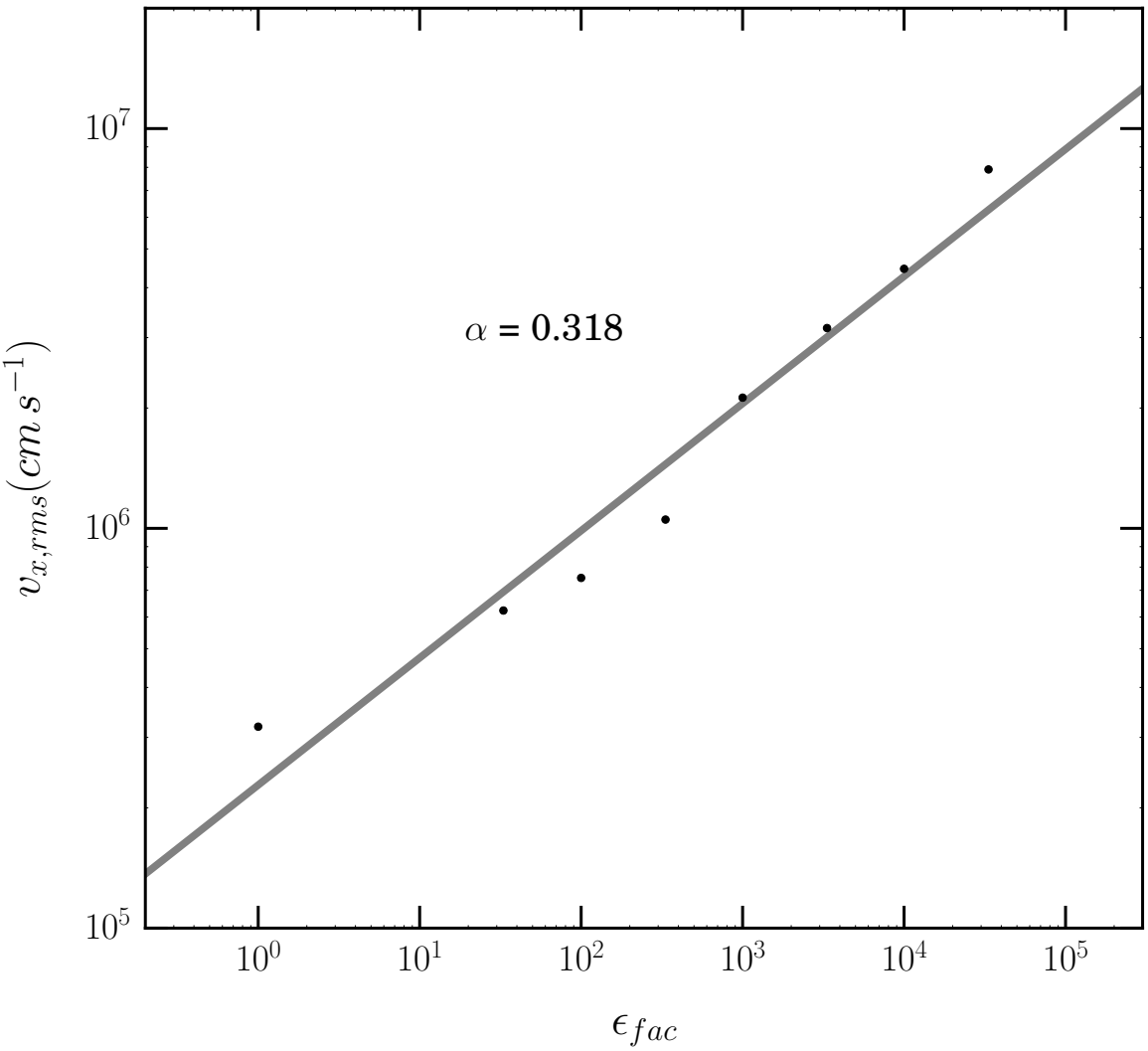

Figure 6.6: Vertical/radial (x-direction) RMS velocity averaged over the convective zone versus nuclear energy generation rate, for each model. This plot can help determine the scaling between these two quantities, assuming $v_{x,rms} \propto \epsilon^{\alpha}$. A linear regression on this data provides a line of best fit with a gradient of $\alpha = 0.318 \pm 0.034$, implying that the vertical flow velocity is roughly proportional to the energy generation rate (or luminosity) to the power one third, or $v_{x,rms} \propto L^{1/3}$.

$$v_{x,rms} \propto L^{1/3}, \tag{6.2.1}$$

where $v_{x,rms}$ is the vertical RMS velocity, assuming that the integral scale, ℓ, is constant and that $v_{x,rms} \sim v_{rms}$. Several other studies (Porter and Woodward, 2000; Arnett, Meakin and Young, 2009; Arnett et al., 2015; Jones et al., 2017) have also confirmed this proportionality.

For the eight models in this study, the cube of the vertical/radial velocity does indeed have a positive correlation with the nuclear energy generation rate. This is shown by Fig. 6.6, where the vertical velocity of each model is plotted against the boosting factor, ϵ_{fac}. A linear regression on these values reveals a line of best fit with a gradient of 0.318 ± 0.034. This is in agreement with Eq. 6.2.1 when the energy generation rate is considered to be proportional to the luminosity.

As explained in §5.1.3 the time-scale of the transient phase is approximately one convective turnover time. The above scaling implies that, as the energy generation rate is increased over the same initial structure (for each model), then the convective turnover time will decrease. This is confirmed in Fig. 6.2 by the relatively shorter initial transient times for the more energetic models. The lower energy models (i.e. eps1, eps33, eps100 and eps333) may have reached the quasi-steady state, but have not completed enough convective turnover times during this state for statistically valid analyses of the boundaries. This is apparent from their convective turnover times in Table 6.1. The number of turnovers completed during the simulation time of each model is shown in Fig. 6.7, where it can be seen that the eps1, eps33, eps100 and eps333 models have all completed two or less convective turnovers. In such models the turbulent velocity field may have developed but there is insufficient time during the quasi-steady state to provide statistically reliable results, this also leads to lower averages for the velocities, v_{rms}. The absence of sustained turbulence is also apparent from the relevant panels (eps1 - eps333) in Fig. 6.3, where it can be seen that there is a strong pulse in specific KE during the initial transient phase, but following this there is little activity in terms of the KE. For the eps100 and eps333 models though, it can be seen that there is a slight increase in KE towards later times, suggesting that these

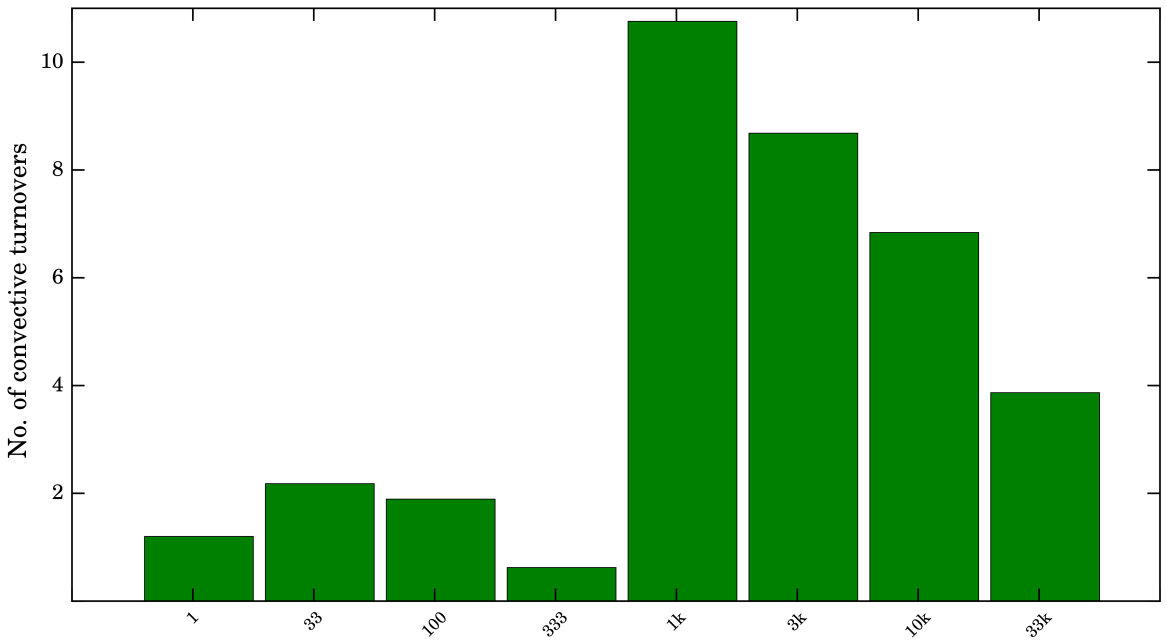

Figure 6.7: Approximate number of convective turnovers following the initial transient for each model. Convective turnover times were calculated as the time taken for a convective eddy with speed v_{rms}, to traverse twice the height of the convective region. The approximate time for entrainment to occur over a statistically significant period following the establishment of the turbulent velocity field is roughly between 3 and 5 convective turnover times. Hence, models eps1, eps33, eps100 and eps333 have not been evolved sufficiently, such that the convective region has been within a quasi-steady state for a significant time. The models which have evolved for one convective turnover or less are likely still adjusting to the initial conditions. Hence, only models eps1k, eps3k, eps10k and eps33k are included in the detailed boundary analysis.

models may be close to the equilibrium state during the quasi-steady state period. For the reasons described above the four models eps1, eps33, eps100 and eps333 are likely not entraining material at the boundaries, and certainly not over time-scales where a temporal average can reliably be taken. As such these models were excluded from all analysis involving turbulent entrainment.

6.2.2 Turbulent entrainment at convective boundaries

As mentioned earlier, only the more energetic models show signs of entrainment. This is not due to the energetics directly, but the shorter time-scales associated with the higher energy models (see the discussion in §5.1.3). The positions of the convective boundaries (calculated from a horizontal mean over the boundary surface, see §5.2.4 for more details on this method) over the simulation times are plotted in Fig. 6.8. The positions of the upper (top panel) and lower (bottom panel) boundaries are shown by solid lines, and the shaded envelopes represent twice the standard deviation from the calculated means. The eps1k, eps3k, eps10k and eps33k models show clear entrainment of the boundary over time. On the other hand, the eps1, eps33, eps100 and eps333 models do not show the same behaviour and the boundary positions remain fairly constant over the simulation time. For the lower boundary of the eps100 model, despite the shorter simulation time, the boundary appears to be migrating to a lower position towards the end of the simulation. Again, the analysis of an extension of this model would confirm if the boundaries will migrate further due to turbulent entrainment.

The variance in the boundary positions increases as the driving luminosity is increased. This agrees with the notion that the boundaries become softer with an increased driving luminosity due to a higher TKE flux at the boundaries, and that a larger distortion in the boundary surface (relative to the mean) is characteristic of plume penetration. The increase in softness of the boundaries with luminosity is also verified by the bulk Richardson numbers[51] given in Table 6.1.

The evolution of the convective boundary positions for the eps1k (top figure) and eps3k (bottom figure) models are shown separately in Fig. 6.9. The evolution of the

[51]Note that the bulk Richardson numbers for the eps1k model are different to those calculated from the hrez model (Table 5.2), as the eps1k model is an extension of the hrez model up to 6,000 s. Hence, the mean value of the bulk Richardson number is more accurate in this case due to the increased averaging time-scale.

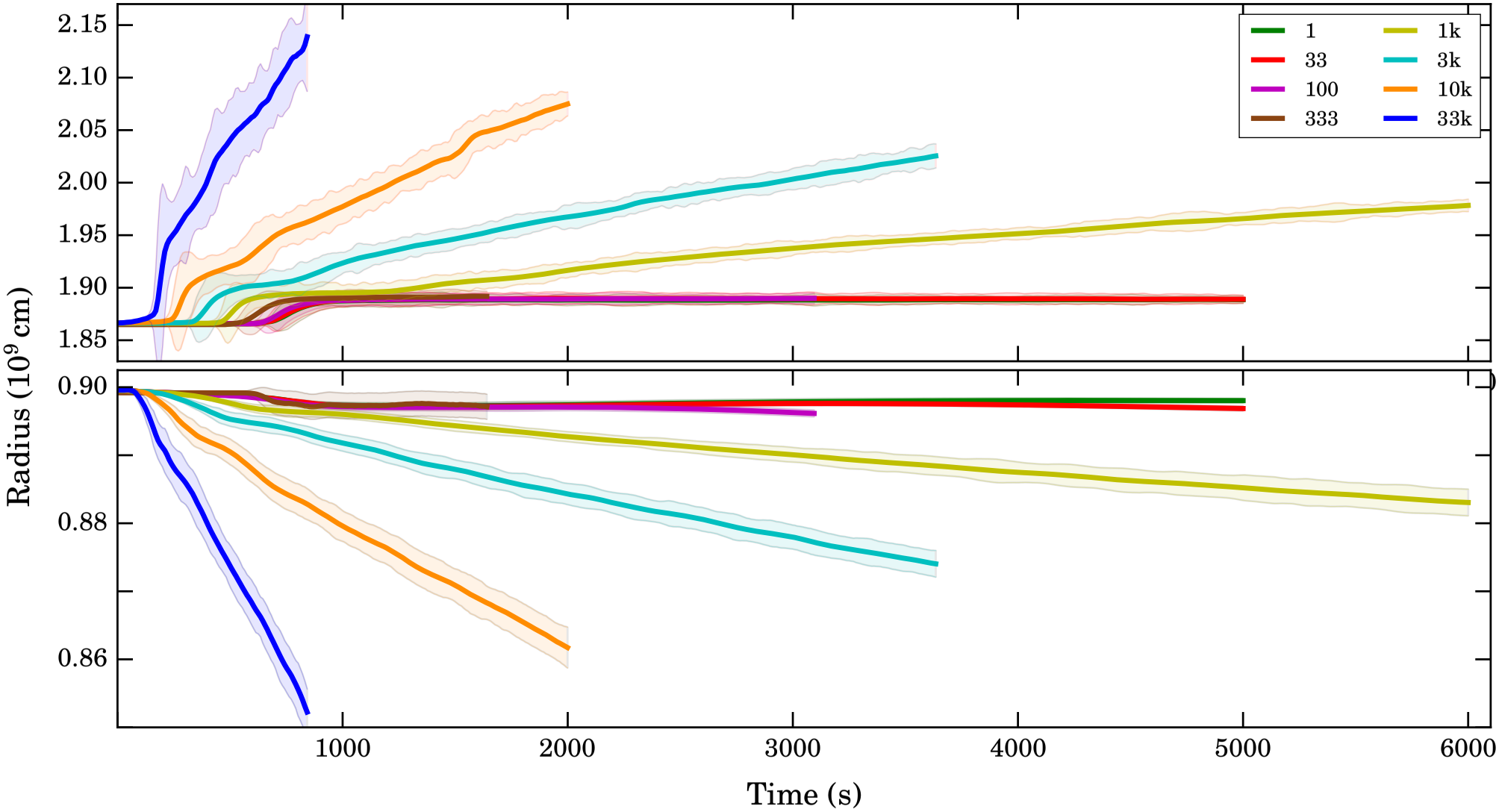

Figure 6.8: Time evolution of the mean radial position of the upper (top panel) and lower (bottom panel) convective boundaries, averaged over the horizontal plane for eight simulations which each use a different strength of driving luminosity. Shaded envelopes are twice the standard deviation from the mean boundary position. Variance in the mean boundary position generally increases with increasing driving luminosity, which can be associated with the occurrence of stronger and more frequent plume penetration of the boundary region.

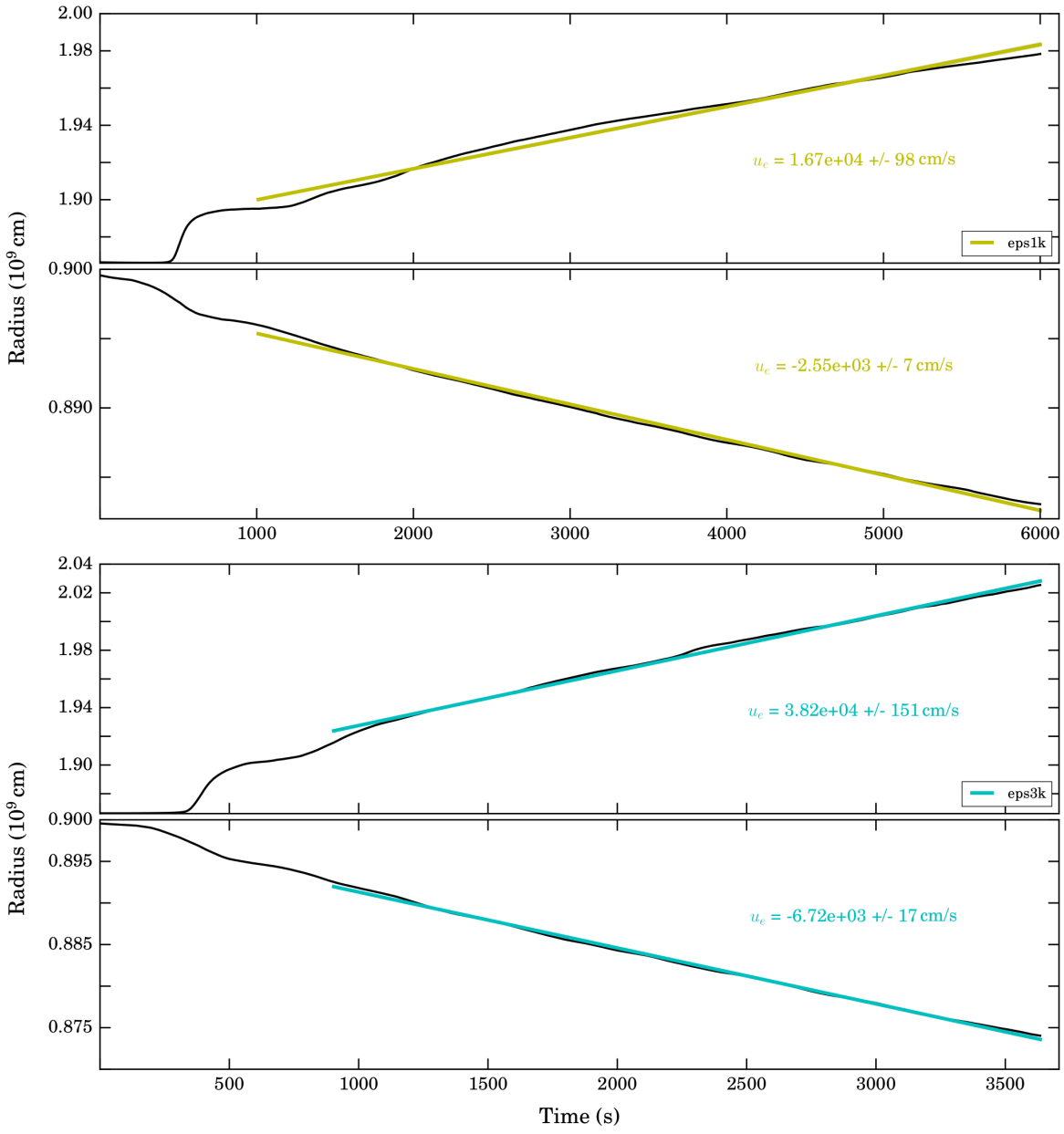

Figure 6.9: Time evolution of the mean radial position of the upper (top panel) and lower (second panel) convective boundaries for the eps1k model and the upper (third panel) and lower (bottom panel) convective boundaries for the eps3k model. Instantaneous boundary positions over the simulation times are shown by black lines, the coloured lines in each panel represent the best fit line following a linear regression of the boundary position over the quasi-steady state period. The corresponding entrainment velocity given by the best fit gradient and respective error are shown in coloured text beside each fit.

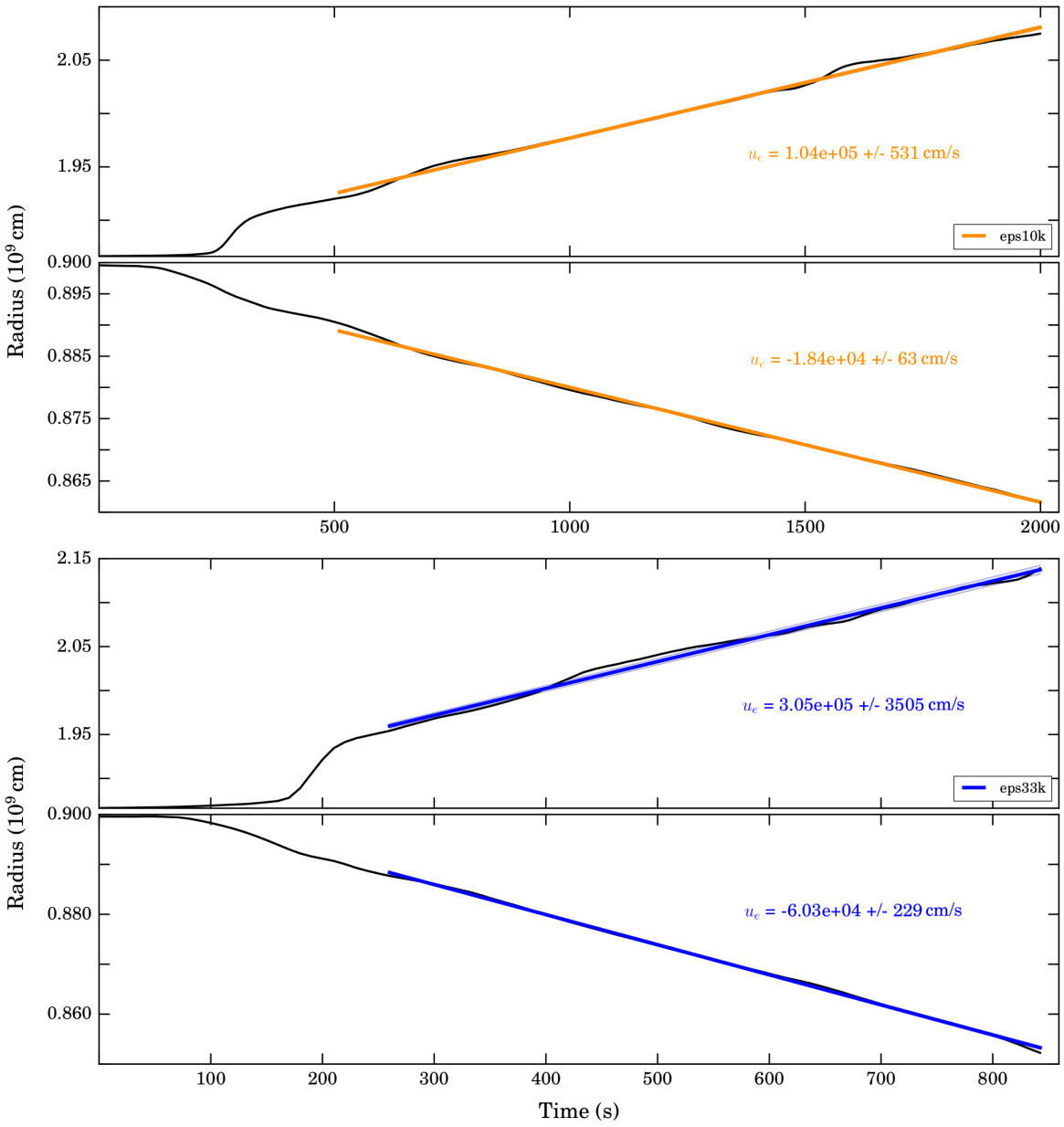

Figure 6.10: Time evolution of the mean radial position of the upper (top panel) and lower (second panel) convective boundaries for the eps10k and the upper (third panel) and lower (bottom panel) convective boundaries for the eps33k model. See the caption of Fig. 6.9 for details on the curves, colours and calculation of the best fit gradients.

convective boundary positions for the eps10k (top figure) and eps33k (bottom figure) models are shown separately in Fig. 6.10. These plots are very similar to Fig. 6.8, but allow an individual assessment of the entrainment and boundary migration for each model. The positions of the boundaries are shown by black solid lines. The best fit line from a linear regression of the boundary positions during the quasi-steady state for each model is shown by a solid coloured line. The corresponding best fit gradient and relative error are shown in coloured text beside each fit. This gradient is the entrainment velocity, and is remarkably linear in each case; the small errors in the best fit gradient show this, for which the largest is 1.5% for the upper boundary of the eps33k model.

The entrainment law and a boundary stiffness scaling

The eps1k, eps3k, eps10k and eps33k models have been interpreted within the framework of the entrainment law (Eq. 2.2.12). These models simulate a significant fraction ($\gtrsim 3$ convective turnover times) of the quasi-steady state (see Fig. 6.7). The entrainment speed (normalised by the RMS turbulent velocity) is plotted as a function of the bulk Richardson number for these models in Fig. 6.11. The coloured circles and triangles represent the values for the upper and lower boundaries, respectively, for the eps1k (yellow), eps3k (cyan), eps10k (orange) and eps33k (blue) models. The solid line is the best fit line following a linear regression of each data point. The slope (n) and intercept (A) along with the respective errors for this best fit are noted to the left of the line as $n = 0.74 \pm 0.04$ and $A = 0.05 \pm 0.06$, respectively. These values are obtained by performing a linear regression on the data points in (logarithmic) $E - \mathrm{Ri}_B$ space. The line of best fit is then of the form $y = mx + c$, where $m = -n$ and $c = \log A$. The black points in Fig. 6.11 represent the entrainment rate, E (as a function of the bulk Richardson number) obtained in the oxygen shell burning study by Meakin and Arnett (2007*b*), and the dashed line is the best fit curve following a linear regression of their data points. The slope and intercept are also noted beside this fit as $n = 1.05 \pm 0.21$ and $A = 1.06 \pm 2.40$, respectively.

Comparing the values obtained for the constants in this luminosity study with those obtained in the resolution study ($A = 0.03 \pm 0.01$ and $n = 0.62 + 0.09/-0.15$), it can be seen that the values for n are in reasonable agreement, and point towards a value in the

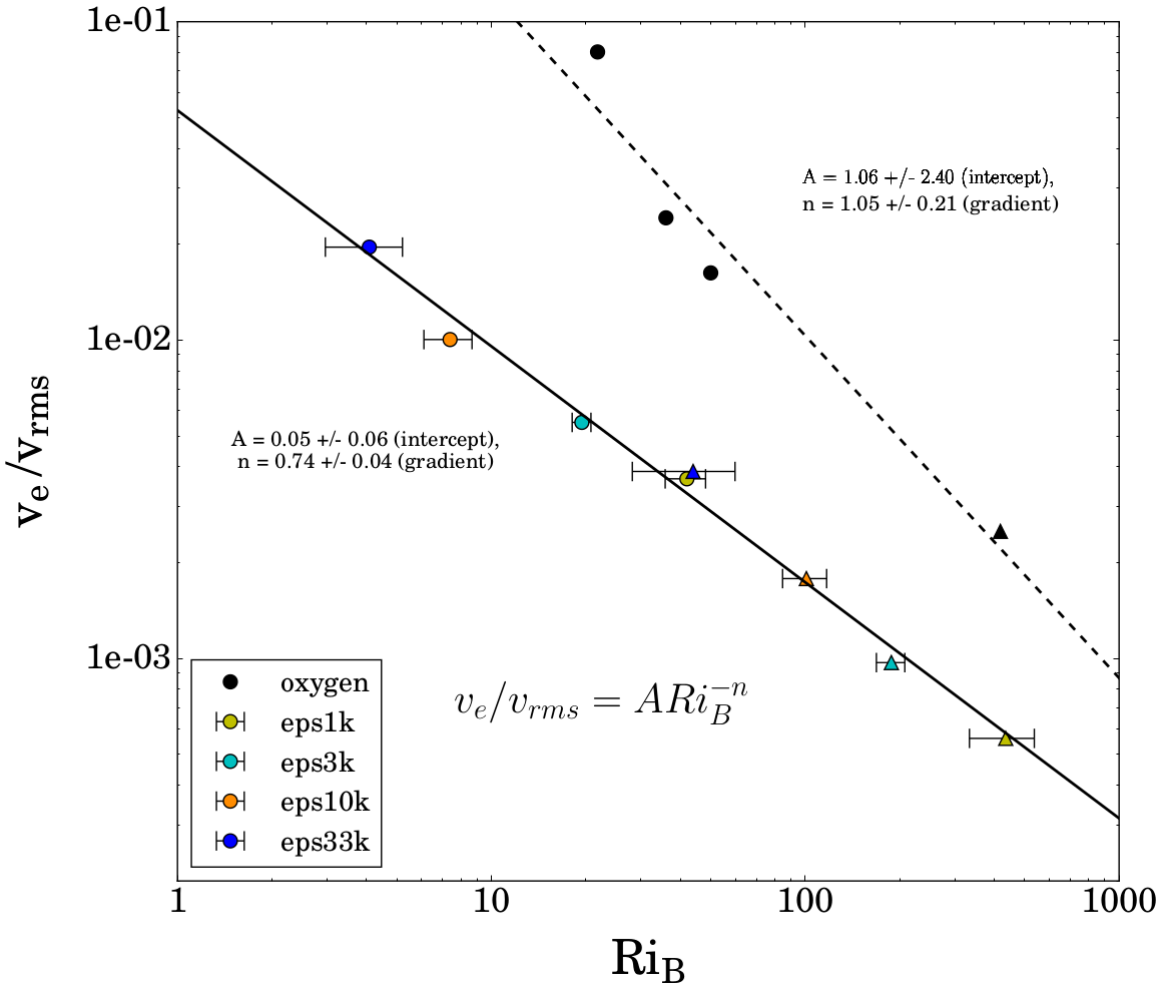

Figure 6.11: Logarithm of the entrainment speed (normalised by the RMS turbulent velocity) versus the bulk Richardson number. Coloured points represent data obtained in this luminosity study: eps1k (yellow); eps3k (cyan); eps10k (orange); and eps33k (blue). Triangles represent the values for the lower boundary and circles represent the values for the upper boundary. The horizontal error bars in the bulk Richardson number are the standard deviations from the mean over the quasi-steady state period. The black points represent data obtained in the oxygen burning study by Meakin and Arnett (2007*b*). The solid and dashed lines show the best fit power laws to the respective data, obtained through linear regressions. The corresponding best fit slope and intercept along with the respective errors are shown for the current data (solid line) as $n = 0.74 \pm 0.04$ and $A = 0.05 \pm 0.06$, respectively, and for the oxygen shell (dashed line) as $n = 1.05 \pm 0.21$ and $A = 1.06 \pm 2.40$, respectively.

range $1/2 \leq n \leq 1$ for fusion driven (neutrino cooling dominated) turbulent convection in the carbon shell burning of massive stars. The value of A is slightly smaller than the values quoted in other laboratory and numerical studies. The lower value of A as compared with that of the oxygen shell burning simulation (black points) suggests that the efficiency of the work done by turbulent eddies on the stable stratification at the boundary of the carbon shell is less than that of the oxygen shell. The error in the calculation of A from the linear regression of the data points in this luminosity study is higher than the best fit intercept value. It is therefore unreliable and states the need for more data points over the $E - \mathrm{Ri}_B$ parameter space. Also, models which span larger fractions of the quasi-steady state are needed in order to reduce the errors in the mean values of the bulk Richardson numbers. The variance of n between the carbon and oxygen shells suggests that there may be additional mixing processes occurring besides entrainment in the carbon shell. Uncertainties in the 'correct' value of n for turbulent entrainment are present throughout terrestrial simulations, where $n = 1/2$ was found by Jonker et al. (2013) while $n = 1$ was found by Fernando (1991), for example.

An approximate scaling relation can be obtained between the Ri_B and the luminosity, this can then allow the determination of the stiffness of convective boundaries in 1D stellar models. This relation can be obtained by starting with the formula for the bulk Richardson number (Eq. 2.2.8) and substituting for v_{rms} using Eq. 2.2.1 leads to

$$\mathrm{Ri}_B \propto v_{rms}^{-2} \propto L^{-2/3}, \tag{6.2.2}$$

if the integral scale and buoyancy jump (ΔB) are assumed to be constant (reasonable assumptions given an initial hydrostatic stratification and short dynamical time-scales), and the nuclear energy generation rate proportional to the luminosity.

This scaling between the driving luminosity and bulk Richardson number can easily be tested within the current luminosity study. As previously mentioned only the four models eps1k - eps33k are used to test this relation, as the remaining models do not contain a sufficient number of convective turnovers over which entrainment can occur. The bulk Richardson numbers for the upper (bottom line) and lower (top line) boundaries of these four models are plotted in Fig. 6.12 as a function of the boosting factor, ϵ_{fac}.

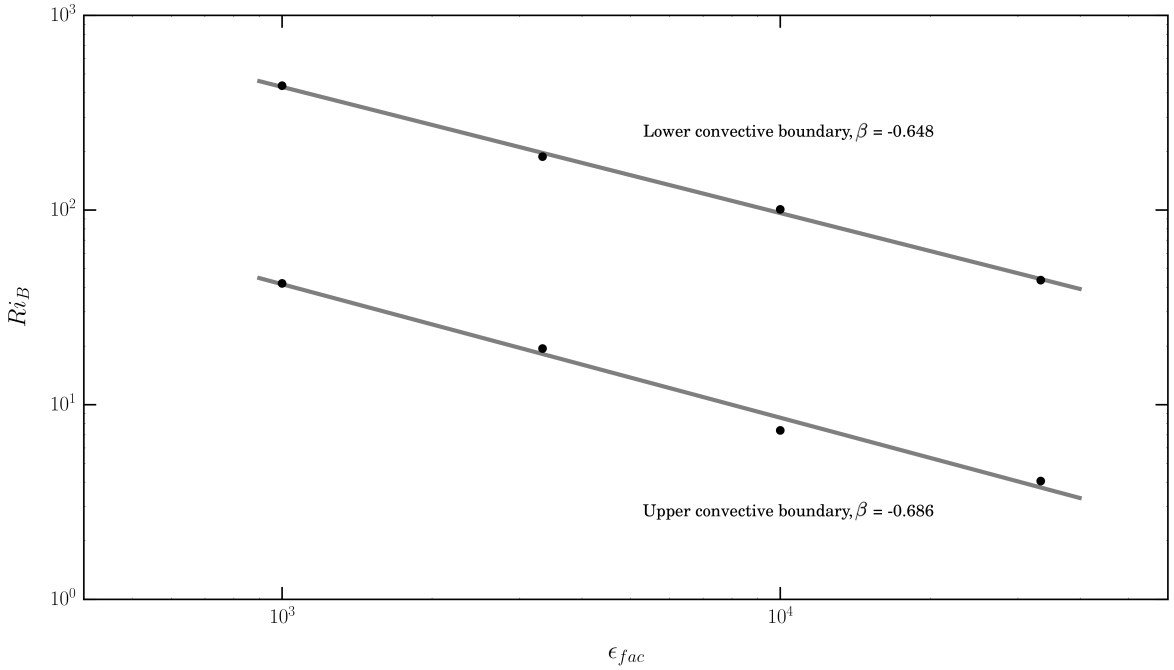

Figure 6.12: Bulk Richardson number as a function of the nuclear energy generation rate boosting factor. The upper points represent values for the lower convective boundary and the lower points represent values for the upper convective boundary for the eps1k, eps3k, eps10k and eps33k models. The grey lines are linear interpolations of each set of points, with the best fit gradient noted next to each fit by β. In this form the scaling between the boundary stiffness and driving luminosity is given by $\mathrm{Ri}_B \propto L^\beta$, where $\beta = -2/3$ (-0.667) is the expected value.

A linear regression of the data points for each boundary is performed over logarithmic space in order to determine a best fit power law and scaling exponent, β, assuming $\mathrm{Ri}_B \propto L^\beta$. This best fit power law is shown by the grey line for each boundary and the corresponding value of the scaling exponent is noted beside each one, $\beta = -0.686$ for the upper boundary and $\beta = -0.648$ for the lower boundary. For both boundaries, the value obtained is close to the expected value of $\beta = -0.667$. Unfortunately due to the sparse data sets it is not possible to obtain errors in the values of the slope. Nevertheless, such an agreement between theory and simulation is encouraging, and with more data points and longer time sampling for each model the confidence in these estimates can be improved.

From the best fit power laws calculated in Fig. 6.12, the bulk Richardson numbers of natural carbon burning luminosities can be extrapolated; these are $\mathrm{Ri}_{B,u} = 4750$ and $\mathrm{Ri}_{B,l} = 3.77 \times 10^4$ for the upper and lower boundaries, respectively. These values are in agreement (to within a factor of around 3) with the values calculated in the eps1 model (see Table 6.1), although arguably, the eps1 model values are not well constrained either, due to the short number of convective turnovers simulated (e.g. see

Fig. 6.7). The above values also agree (also to within a factor of around 3) with the values calculated from the stellar model initial conditions (see Table 4.2), which also have inherent uncertainties, due to the difficulty of calculating the bulk Richardson numbers over coarse stellar model grids. This difficulty arises from the lack of a precise definition for the buoyancy jump within a complex, stratified medium such as stellar interiors. The length scale over which this jump is calculated is therefore somewhat arbitrary. The entrainment velocities for the `eps1` model can also be estimated using the above values for the bulk Richardson numbers. Inserting the above values for the bulk Richardson numbers into the entrainment law (Eq. 2.2.12) with the values for A and n determined in Fig. 6.11 and the RMS velocity from Table 6.1 yields entrainment velocities of around $14\,\mathrm{cm\,s^{-1}}$ and $65\,\mathrm{cm\,s^{-1}}$ for the lower and upper boundaries, respectively.

Despite such uncertainties, the reliable estimation of the bulk Richardson number is still best pursued through long time-scale (ideally $\gtrsim 10$ convective turnovers), three-dimensional hydrodynamic simulations of turbulent convection, the results of which can populate the entrainment law parameter space ($E - \mathrm{Ri}_B$) and constrain the free parameters A and n. The agreement with the scaling relation, $\mathrm{Ri}_B \propto L^{-2/3}$, for several models over a range of different driving luminosities, demonstrates the applicability of this scaling relation to stellar flows. The discrepancy between the extrapolated values of the bulk Richardson number for natural carbon burning luminosities and the stellar model initial conditions, can be used to fit free parameters within the formulation of the bulk Richardson number for stellar models, namely the integration length, Δr, and the integral scale, ℓ (see §2.2.2).

With better constrained values of A and n as well as more accurate estimates of the bulk Richardson numbers within stellar models, new mixing prescriptions can be incorporated into stellar models, such as the one suggested by Meakin and Arnett (2007*b*)

$$\dot{m}_e = \frac{\partial m}{\partial r}\, v_e = 4\pi r^2 \rho\, v_{rms}\, A\, \mathrm{Ri}_B^{-n}, \tag{6.2.3}$$

where v_{rms} can be substituted for either v_{mlt} (Eq. 2.1.23) or v_c (Eq. 4.2.2).

6.2.3 Effects of driving luminosity on the turbulent kinetic energy budget

In the same manner as in §5.2.3, I will interpret the TKE budget of the models in this luminosity study within the RANS framework. All of the terms in Eq. A.2 are calculated for the eps1k and eps3k models in the top and bottom panels of Fig. 6.13, respectively, and for the eps10k and eps33k models in the top and bottom panels of Fig. 6.14, respectively. The radial profiles of each term are presented in the left panels of these figures, with the inferred viscous dissipation shown by a dashed line. Each profile is time averaged over multiple convective turnover times and normalised by the surface area of the domain. The right panels show bar charts of the radial integration of each term in the left panel. It can be seen that all profiles increase in magnitude as the driving luminosity is increased, simply because more nuclear energy is being put into the system.

The main driving term for the TKE is the buoyancy work, $\mathbf{W_b}$, which for the eps1k, eps3k and eps10k models is balanced by the numerical dissipation at the grid scale, ϵ_k. Due to such a balance, the shell is in a statistically steady state, as shown by the negligible values of the Eulerian time derivative of the TKE, $\rho\mathbf{D_t}E_k$. For the eps33k model, the driving term is so large that while most of the TKE is dissipated, some of the energy affects the shell dynamically, hence it is now no longer in a statistically steady state and the shell itself is eventually completely disrupted.

The peak in the residual TKE (dashed curve) at the bottom of the convective shell decreases in amplitude with increased driving luminosity, and the profile also broadens with increased driving luminosity. This could be due to an actual broadening of the boundary itself, as the boundary is more easily overwhelmed by turbulent motions as the driving luminosity increases. Hence, for the most energetic model, eps33k, the lower boundary is now broad enough that the spatial resolution is sufficient to model this boundary physically and without any adverse numerical effects due to poor resolution.

The residual TKE is compared between these four models for the upper and lower boundary in Fig. 6.15. In these figures the numerical dissipation is normalised by a value at a common position within the convective region close to the boundary. This normalisation value is numerically converged at these spatial resolutions (512^3) and so

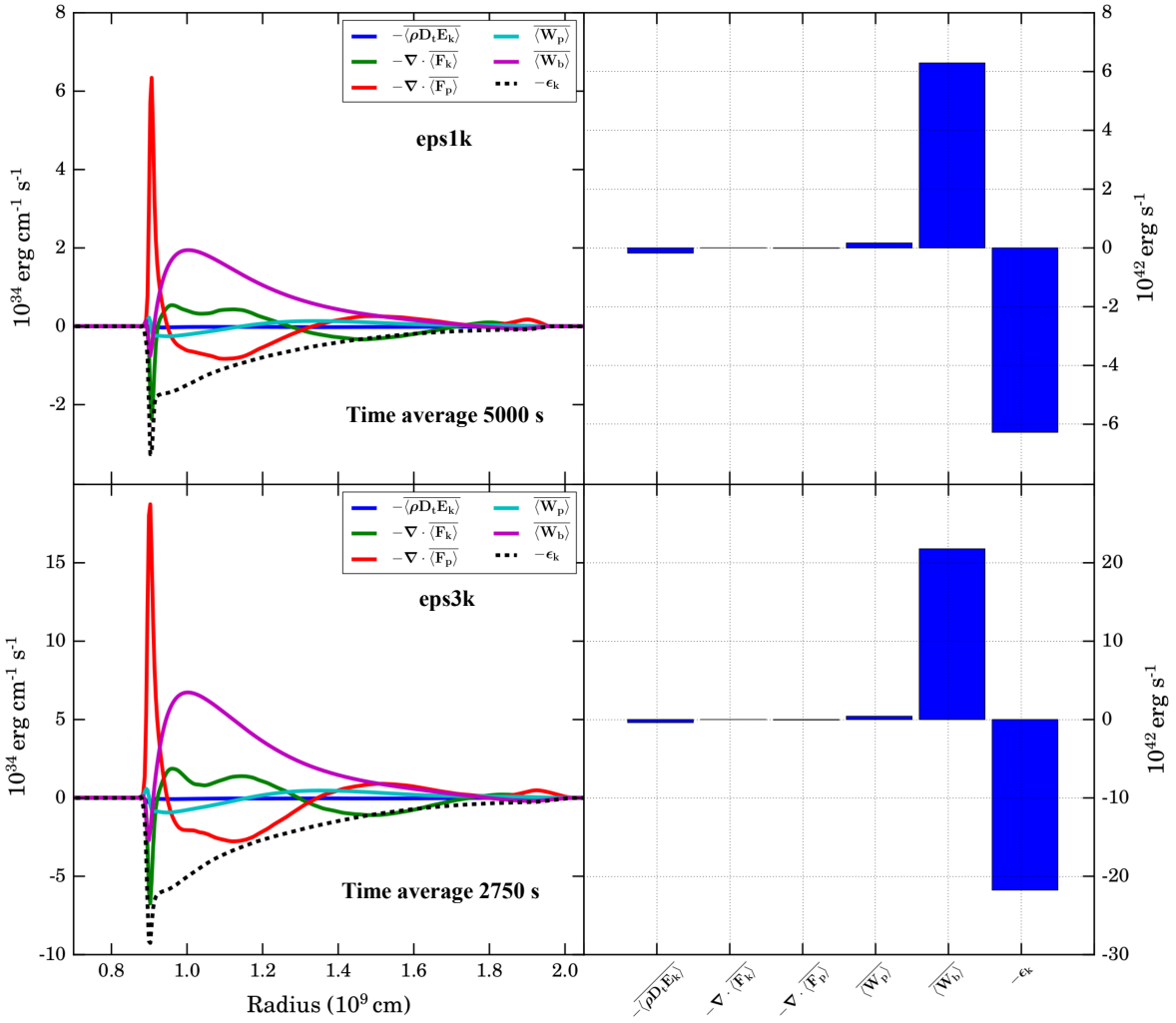

Figure 6.13: *Left*: Decomposed terms of the mean kinetic energy equation (Eq. A.2), which have been horizontally averaged, normalised by the domain surface area and time averaged over the quasi-steady state. Time averaging windows are over 5,000 s and 2,750 s for the `eps1k` (top) and `eps3k` (bottom) models, respectively. *Right*: Bar charts representing the radial integration of the profiles in the left panel. This plot is analogous to Fig. 8 of Viallet et al. (2013).

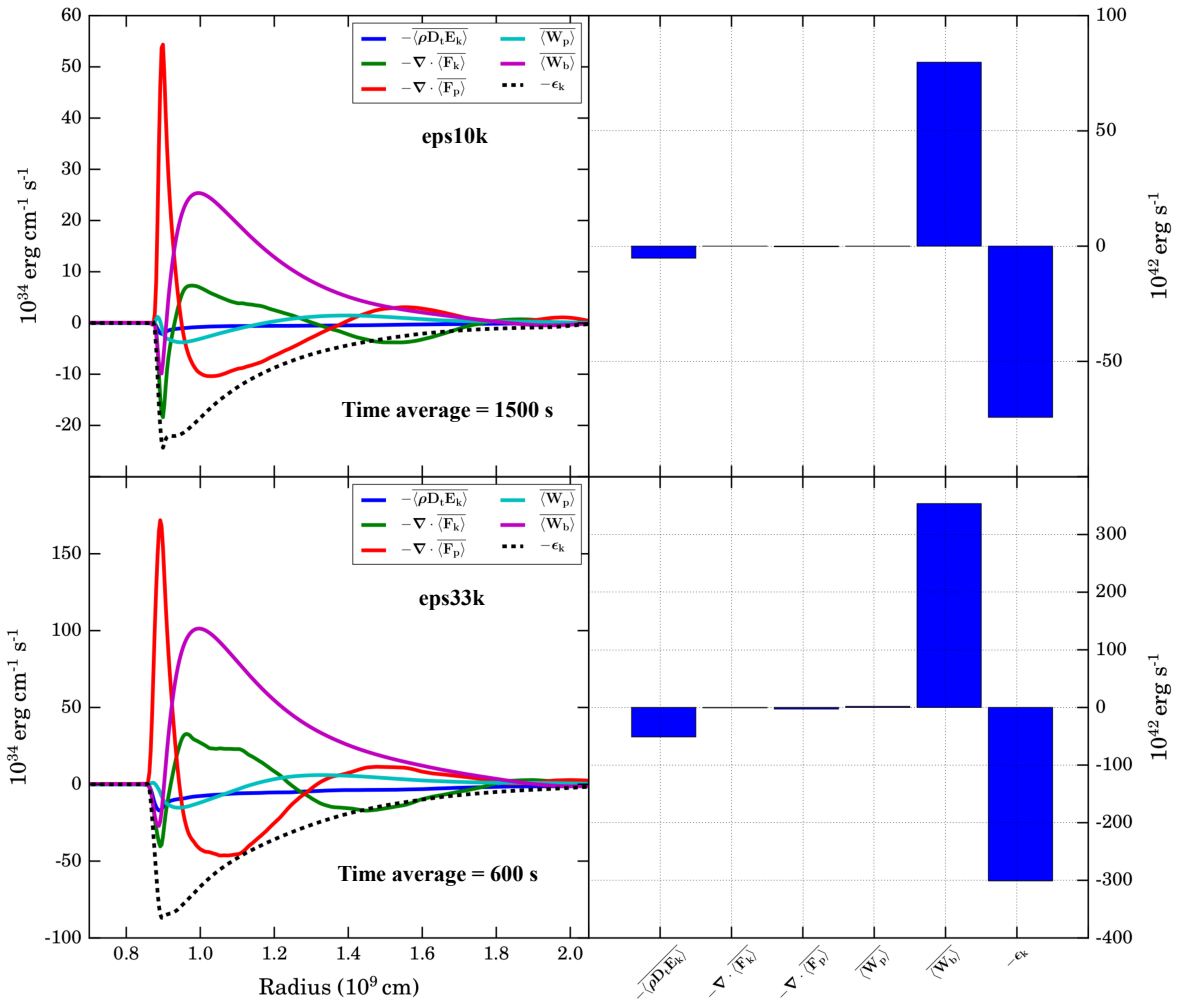

Figure 6.14: Same as Fig. 6.13 but for the eps10k (top) and eps33k (bottom) models. Time averaging windows are over 1500 s and 600 s, respectively.

	eps1k	eps3k	eps10k	eps33k
δr_l(cm)	4.04×10^7	5.14×10^7	6.24×10^7	5.88×10^7
δr_u(cm)	1.18×10^8	1.29×10^8	1.40×10^8	2.02×10^8
$\delta r_l/H_{p,l}$	0.141	0.181	0.218	0.201
$\delta r_u/H_{p,u}$	0.339	0.366	0.389	0.535

Table 6.2: δr_l and δr_u are the approximate boundary widths, determined from the composition profiles of the lower and upper convective boundaries respectively (see Fig. 6.16 and §5.2.5). These measurements of the boundary represent the size of the boundary region which is formed due to Kelvin-Helmholtz instabilities and shear mixing at the boundaries. $H_{p,l}$ and $H_{p,u}$ are the average pressure scale heights across the lower and upper convective boundary regions, respectively.

poor spatial resolution at the boundary is revealed by peaks in the dissipation curves.

For the upper boundary (top panel in Fig. 6.15), the absence of any peaks suggests that the adopted resolution is adequate in representing this boundary for the energy configuration of these four models. With the exception of the eps33k model, all of the models steadily decrease in relative dissipation towards the boundary, followed by a steeper gradient beyond the boundary, and eventually plateauing to a small value within the radiative region. For the eps33k model, however, the TKE is so great that the reduction in dissipation across the boundary region occurs at an almost constant gradient. A possible explanation for such behaviour is that the TKE of this model is so great that it destroys the boundary layer altogether (see Fig. 6.4).

The lower boundary is much narrower than the upper boundary (see e.g. Table 5.3). This is also apparent in Fig. 6.15 from the appearance of spurious peaks in the relative dissipation curves in all models except eps33k. The increase in driving luminosity broadens the lower boundary, resulting in an increase in the effective resolution for the higher energy models, and reduces the amplitude of the dissipation peaks. In the eps10k model the dissipation peak is small and in the eps33k it is almost non-existent.

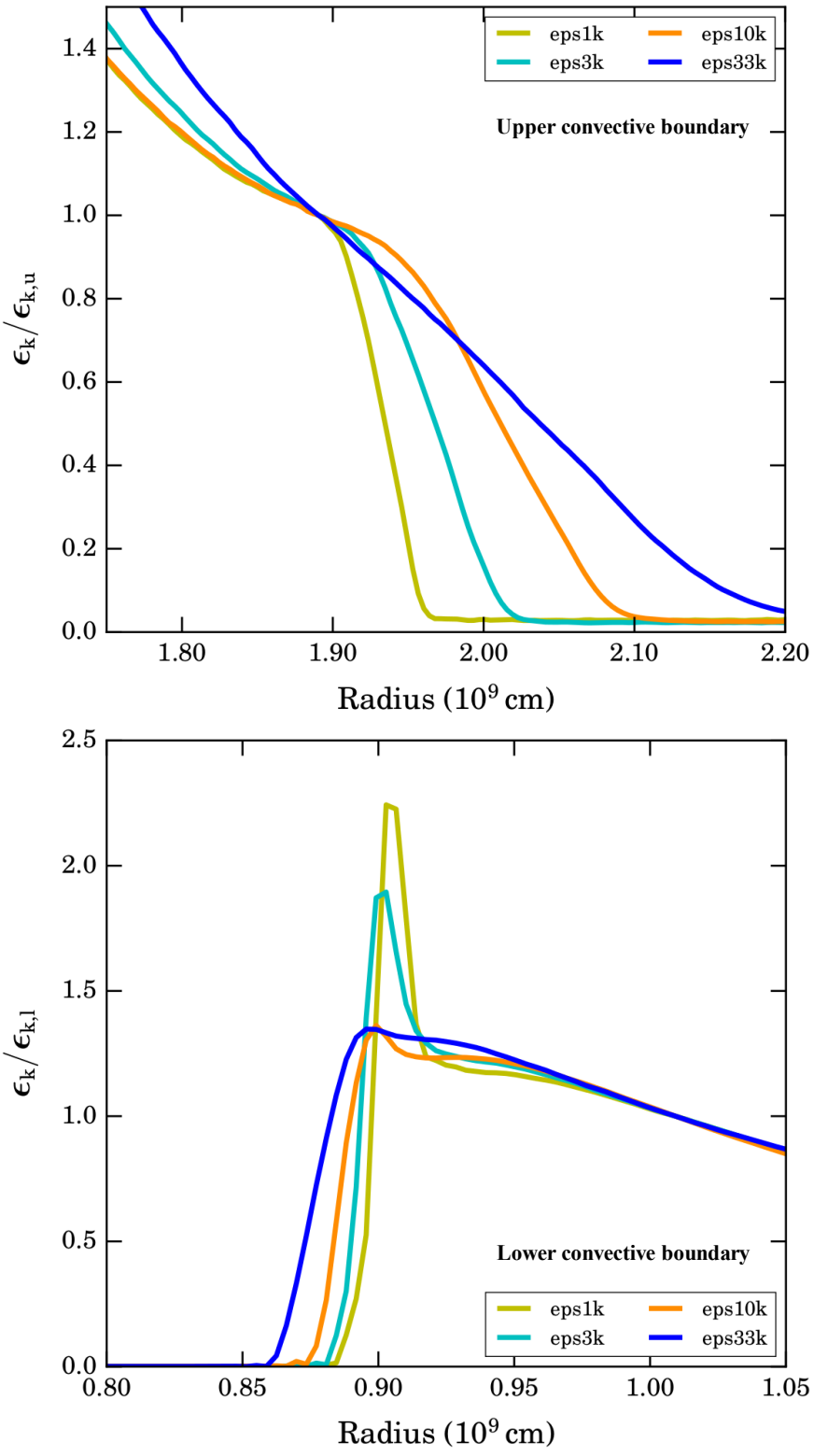

Figure 6.15: Turbulent kinetic energy residual dissipation curves of the upper (top) and lower (bottom) convective boundary regions for the: eps1k (yellow); eps3k (cyan); eps10k (orange); and eps33k (blue) models. The numerical dissipation for each boundary has been normalised by a value at a common position within the convective region near to the boundary ($\sim 1.9 \times 10^9$ cm and $\sim 1.0 \times 10^9$ cm). Therefore, any sensitivity to the spatial resolution should be revealed by sharp peaks in the dissipation profiles, of which there are none at the upper boundary but all models except the eps33k model possess sharp peaks at the lower boundary.

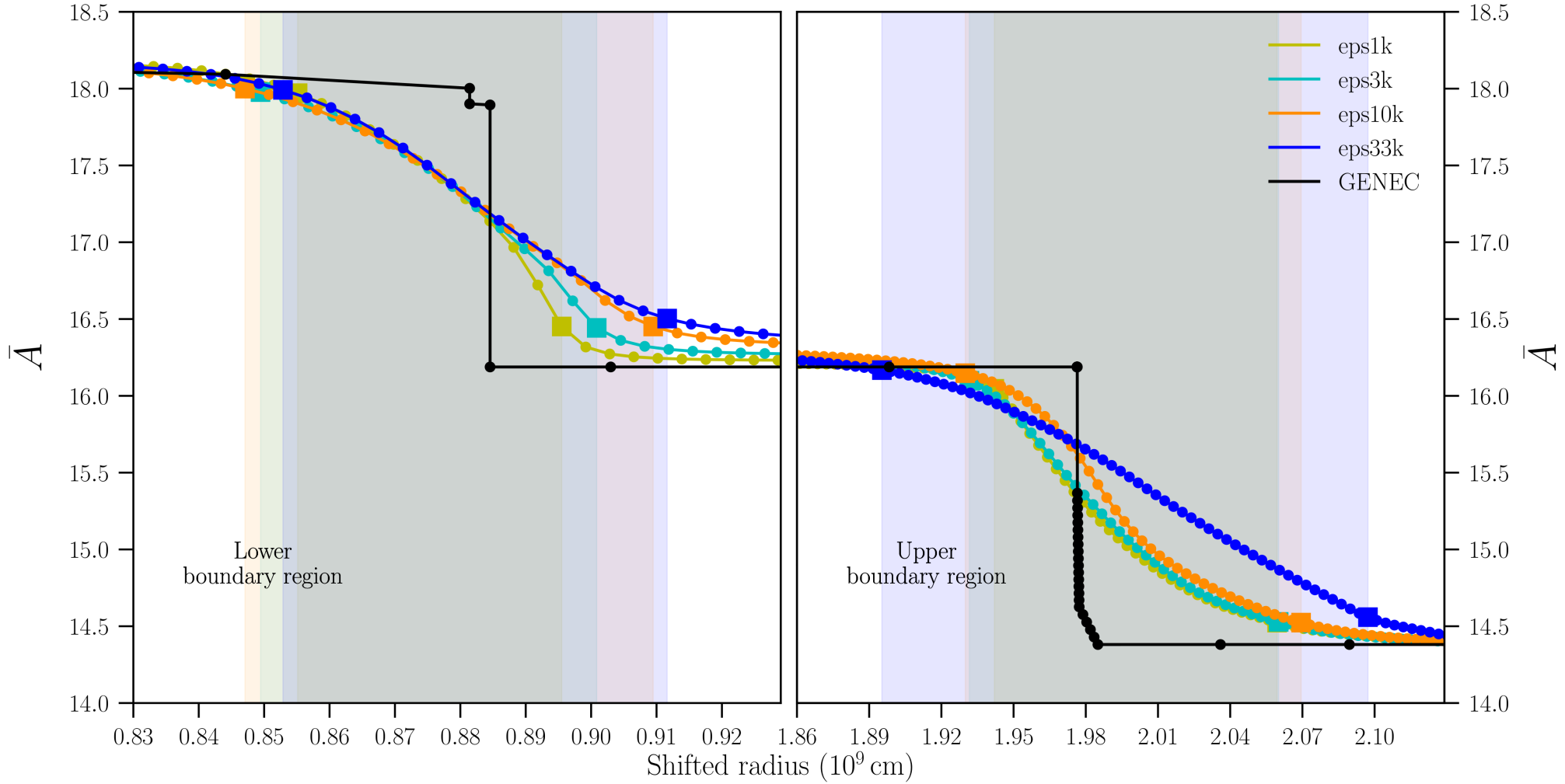

Figure 6.16: Radial compositional profiles at the lower (*left*) and upper (*right*) convective boundary regions for the last time step of the: eps1k (yellow); eps3k (cyan); eps10k (orange); and eps33k (blue) models. The radius of each model is shifted such that the boundary position, $\overline{r}$ (see §5.2.4), coincides with the boundary position of the eps1k model. In this sense, it is easier to compare the gradient and position of each boundary at the final time-step based on the driving luminosity. Individual mesh points are denoted by filled circles. Approximate boundary extent (width) is indicated by the distance between two filled squares for each model, and is shown by the correspondingly coloured shaded regions. See §5.2.5 for details on the definition of the boundary width.

6.2.4 Effects of driving luminosity on boundary widths

The composition profiles at both boundaries for the final time-step of each of the four models (eps1k - eps33k) are shown in Fig. 6.16. Each composition profile has been shifted in radius such that the boundary position, $\overline{r}$ (defined in §5.2.4), coincides with the boundary position of the eps1k model (for ease of comparison). The boundary width (as defined in §5.2.5) is denoted for each model by the distance between two filled squares at the edges of the boundary region, and is shown by the respectively coloured shaded region. These boundary widths, along with the standard deviation of the boundary position (Fig. 6.8) and their fractions of the pressure scale height are shown in Table 6.2.

For the upper boundary (right panel of Fig. 6.16) the composition profiles are similar except for the eps33k model, which has a shallower gradient over the boundary region. In this model the upper boundary is much broader, and the increased driving leads to a dramatic smoothing in the abundance gradient; this is not seen in the other models. As noted in §6.2.3, the strong increase in driving luminosity is likely leading to a structural readjustment of the shell at this time-step and will eventually result in the complete disruption of the shell.

At the lower boundary (left panel) the abundance profiles are very similar in gradient between all of the different cases, with an increase in driving luminosity leading to a clear increase in boundary width. As entrainment becomes more effective with stronger driving luminosity the composition in the convective region near the boundary also increases slightly, as an increased amount of heavier material from the stable region below is mixed into the turbulent region.

The smoothing of the horizontally averaged abundance profile due to the boundary deformation, can be measured by the standard deviation of the boundary position (Fig. 6.8) which can be associated with the vertical fluctuations in the boundary surface, possibly due to plume penetration events. The extent of the boundary region (its width), can be associated with the strength of shear mixing (or Kelvin-Helmholtz instabilities) at the boundary, caused by the overturning of turbulent fluid elements which carry large horizontal velocities.

Generally, the boundary widths (Table 6.2) have a weaker dependence on the boost-

ing factor, ϵ_{fac}, than originally expected. Longer time-scale and statistically significant simulations with lower values of ϵ_{fac} will help to test this expectation.

6.3 Comparison to similar studies

Similarly to §5.3 where similarities between the resolution study and other studies were identified, the results from this luminosity study can also be compared to similar simulations from other authors. The bulk Richardson number of the boosted carbon burning simulation `eps1k` has similar values to the bulk Richardson number for the oxygen shell burning simulation by Meakin and Arnett (2007*b*). From Eq. 6.2.2, this may be expected though, as the luminosity of the two shells are similar. These similarities between the bulk Richardson numbers give hope that a general prescription applicable to all or most evolutionary phases can be developed.

Chapter 7

Conclusions and future perspectives

Massive stars have a significant impact on the formation, dynamics and evolution of the universe, through their radiation, winds, explosions and chemical enrichment. The understanding of the interiors of massive stars is limited in observations to asteroseismology, progenitor structures inferred through supernovae and galactic chemical evolution. Such observational techniques do not directly test the deep internal dynamics of the stellar fluid, and also cannot directly test the specific compositional structure. The burden for detailed analysis of stellar interiors therefore lies with numerical modelling of the structure and evolution of these stars. Stellar evolution models are extremely useful tools for predicting the stellar structure and composition at various epochs. However, there are many areas which are poorly understood in terms of stellar evolution, not least of all convection, and in particular convective boundary mixing which has a large impact on the lifetime of the star and also the subsequent explosion energetics. Multi-dimensional simulations can model stellar flows from first principles for relatively short times. These simulations can provide great insight into the underlying physical processes responsible for convective boundary mixing and help in designing improved prescriptions for implementation into stellar evolution models.

An exploratory parameter study on various (but not all) convective regions during the evolution of a $15\,\mathrm{M}_{\odot}$ stellar model was performed. Over the evolution of the star there was a general trend for the gravitational acceleration, peak luminosity and mean molecular weight to increase, due to an increase in density and temperature within the central regions of the star. The pressure scale height tends to decrease as the star evolves due to an increase in the pressure and its radial gradient. As

the star evolves there is also an increasing trend for the convective velocity, Mach, Péclet and Damköhler numbers, pointing to a general acceleration in the evolutionary time-scales as the star proceeds through each burning phase. The bulk Richardson number was found to be highest (stiffer boundaries) during the maximum mass extent of the convective region, and the smallest values were found towards the end of each burning phase. The defining conclusion from this parameter study was that the lower convective boundaries of convective shells are stiffer, according to the bulk Richardson number, than the corresponding upper convective boundary. This finding was also confirmed in three-dimensional hydrodynamical simulations of the carbon shell, using initial conditions from the same stellar model, and also in oxygen burning simulations by Meakin and Arnett (2007*b*). Such a finding has implications for other areas of astrophysics, where CBM at lower boundaries of shells is important, such as novae and flame front propagation, for which the latter also affects EC-SN and type Ia SN.

The first 3D hydrodynamic simulations of carbon shell burning in a massive star were performed using the PROMPI code. These hydrodynamic simulations were designed with a focus on the convective boundary regions in mind. Hence, certain idealisations to the model set-up were made, such as a Cartesian geometry within the plane parallel approximation. Such simplifications allow for maximum effective resolution of the boundaries in these models. The effects of varying the grid resolution, were tested within the same initial carbon shell structure provided by the $15\,\mathrm{M}_{\odot}$ stellar model mentioned above. These variations in resolution revealed that a resolution of $512 \times 512 \times 512$ grid points are required to resolve the upper boundary of this carbon shell. The required number of grid points to resolve the lower boundary in this case is greater than $1024 \times 1024 \times 1024$, and estimated to be $1536 \times 1536 \times 1536$. Below these resolutions, the boundaries are incorrectly modelled as highlighted by peaks in the numerical viscosity. The widths of the boundaries were also estimated from the $512 \times 512 \times 512$ model to be roughly 10% and 30% of the local pressure scale height for the lower and upper convective boundaries, respectively.

In these simulations, the boosting of the nuclear energy generation rate by a factor of 1000 was required. This was following the realisation that the time required to evolve the model through the initial transient phase and set-up the turbulent velocity field, is approximately one convective turnover time. For natural carbon burning luminosi-

ties this would render high resolution, long time-scale (multiple convective turnovers) simulations computationally unaffordable.

The effects of varying the driving luminosity was also investigated using the same initial carbon shell structure. The results show that over the short dynamical time-scales which these models were run over (due to limited computational resources), the shell structure is not adversely affected by this boosting (except in the most extreme case) and serves to accelerate the evolution of the shell through increased rates of entrainment and mixing. As the structure is unchanged, the vigour of turbulence is also increased for the same stable stratification and so the representation of entrainment in the most energetic cases ($\epsilon_{fac} \geq 10^4$) is far from being physically realistic during the current evolutionary state. Such a luminosity study allows one to populate the parameter space ($E - \mathrm{Ri}_B$) of the entrainment law (Eq. 2.2.12) and constrain the values of A and n for high Péclet number, fusion driven convection.

This luminosity study has confirmed the scaling relation between the vertical RMS velocity and the driving luminosity, $v_{x,rms} \propto L^{1/3}$, as found by several other authors. This study has also confirmed the expected scaling between the bulk Richardson number (stiffness) of the boundary and the driving luminosity of the shell, $\mathrm{Ri}_B \propto L^{-2/3}$. Such a relation will prove useful in developing new CBM prescriptions for entrainment in stellar evolution models. For example, it helps to extrapolate values of the bulk Richardson number at nominal carbon burning luminosities. Comparing these extrapolated values to those from the initial 1D stellar evolution model calculations reveals that they are similar to within a factor of around 3.

Looking at the composition profiles of the boundaries, the slope of these profiles helps to give an idea of the boundary shape. From the 1D stellar evolution model this profile is discontinuous, like a step function, whereas in the 3D hydrodynamical models it is smooth and sigmoid-like. The boundary also possesses a sub-structure of significant width unlike in the 1D model which represents the boundary as a sharp discontinuity. The over-turning of fluid elements near the boundary leads to shear mixing, most likely due to Kelvin-Helmholtz instabilities. This type of mixing broadens the boundary region, and implies a similarity in the limiting behaviour of rotating and non-rotating convective boundary mixing.

Additional hydrodynamical simulations of different phases of evolution, will help

to further populate the entrainment parameter space in order to test the robustness of boundary scaling relations. They will also allow further exploration of the structure of the boundary region, and the processes responsible for creating such regions.

7.1 Future studies

One-dimensional stellar evolution models are currently the only viable way to simulate the entire life-time of a star, and are used as initial conditions for more sophisticated simulations as well as being the main theoretical framework to interpret observations. The improvement of these models and their underlying physical assumptions is paramount for the field of computational stellar astrophysics. There are many outstanding areas of improvement for such models which will undoubtedly keep the community occupied for decades to come:

- Convection
- Rotation
- Mass loss
- Magnetic fields
- Multiplicity

This thesis presents the work (carried out on the carbon shell of a $15\,M_\odot$ star) which provides a small contribution to the problem of convection, by providing the first three-dimensional hydrodynamic simulations of carbon shell burning in a massive star.

Despite the many outstanding problems listed above, many other astrophysical communities are under the assumption that stellar evolution is a solved problem. With the dawn of new state-of-the-art observational programs such as LIGO (Abramovici et al., 1992) and GAIA (Gaia Collaboration et al., 2016), as well as future missions such as LSST (Ivezić et al., 2008), ELT (Gilmozzi and Spyromilio, 2007) and JWST (Gardner et al., 2006), reliable stellar evolution models are needed in order to classify the many observations that will arise from these global efforts.

Concerning convection, the development of improved prescriptions is one way to improve its treatment in stellar evolution models. The goal of 1D stellar evolution models, is to capture the long-term (secular) evolution of the convective zone and its boundaries, while 3D hydrodynamic simulations probe the short-term (dynamical) evolution. Keeping this in mind, the key points to take from these and previous three-dimensional hydrodynamic studies for the development of new prescriptions in 1D stellar evolution codes are the following:

- Entrainment of the boundary and mixing across it occurs both at the top and bottom boundaries. Thus 1D stellar evolution models should include convective boundary mixing at both boundaries. Furthermore, the boundary shape is not a discontinuity in the 3D hydrodynamic simulations but a smooth function of radius, sigmoid-like, a feature that should also be incorporated in 1D models.

- At the lower boundary, which is stiffer, the entrainment is slower and the boundary width is narrower. This confirms the dependence of entrainment and mixing on the stiffness of the boundary. CBM prescriptions applied to lower boundaries should therefore reflect the decreased efficiency of mixing (compared to the upper).

- Since the boundary stiffness varies both in time and with the convective boundary, a single constant parameter will unlikely represent the dependence of the mixing on the instantaneous convective boundary properties correctly. Therefore, future prescriptions for entrainment in 1D stellar evolution codes would benefit from using the bulk Richardson number, or a similar measure of the boundary stiffness.

Further hydrodynamic simulations of stellar convection are also needed to improve the understanding of the evolution of entrainment at different epochs of phases of evolution. One specific question which I would be interested in finding the answer to is: "towards the end of carbon burning, does entrainment result in the further migration of the boundary position into the surrounding stable region, or does the boundary position remain roughly constant in mass/radius, as predicted by 1D stellar models, or does the boundary position even recede?"

Of course, just like 1D stellar evolution models, 3D hydrodynamical models should be subject to V&V in order to strengthen their predictive power. Verification can

similarly be achieved through code comparison by providing benchmark problems which can be simulated by several codes. The computation of well known fluid instabilities such as a simple Rayleigh-Taylor instability, can also help to verify that the simulated flows represent physical flows.

Validation ultimately requires the reproduction of observables. The level of agreement between the simulations and these observables, may help in determining if the physical assumptions and simplifications adopted significantly affect the solutions obtained. Generally, there are three areas of astrophysics which provide observables for the numerical modelling of stellar interiors: asteroseismology; galactic chemical evolution; and supernova progenitor structures. CBM prescriptions inspired by the results of multi-dimensional hydrodynamic simulations which are incorporated into 1D stellar evolution models should help to reproduce the observables from all three of these areas.

Multi-dimensional hydrodynamic simulations can also help simulate astrophysical problems where 1D stellar evolution models cannot reproduce observations. Of course, these simulations may not reproduce the observables either but will likely provide some insight into the problem.

As computing power increases, and the porting of existing codes to GPU technologies is becoming more common, more numerous and longer time-scale simulations will be possible. Such developments will help in the maturing of the stellar hydrodynamics field.

Appendix A

Useful derivations

A.1 Radiative temperature gradient

A radiative flux can be realised by applying Fick's law of diffusing particles to photons, by replacing the number density of particles, n, with the energy density of photons, $u = aT^4$, where a is the radiation constant

$$\mathbf{F_r} = -D\boldsymbol{\nabla} u. \tag{A.1.1}$$

The diffusion coefficient, D, is a measure of the dissipation of particles with a characteristic velocity over a characteristic length-scale. For photons, their velocity is the speed of light, and their characteristic length-scale can be taken as their mean free path, which for photons with a specific radiative cross-section, κ (averaged over all frequencies), propagating through a medium of density, ρ, is $1/\kappa\rho$. Of course, Fick's law can only be applied if the heat transport by photons is diffusive; this is indeed the case as the mean free path ($\sim 10^{-4}\,\mathrm{cm}$) is much smaller than the stellar radius ($\sim 10^{13}\,\mathrm{cm}$).

From spherical symmetry there is only a radial component of the flux and so

$$\boldsymbol{\nabla} u = 4aT^3\,\frac{\partial T}{\partial r}, \tag{A.1.2}$$

therefore the radiative flux can be written as

$$F_r = -\frac{1}{3}\,c\,\frac{1}{\kappa\rho}\,4aT^3\,\frac{\partial T}{\partial r}, \tag{A.1.3}$$

where the factor 1/3 comes from the consideration of inflowing and out-flowing fluxes on one side of a cube, where the cube represents a fluid element. Writing the flux as the luminosity at a given surface of area $4\pi r^2$, and rearranging for the temperature gradient yields

$$\frac{\partial T}{\partial r} = -\frac{3\kappa\rho L}{16\pi ac\, r^2 T^3}. \tag{A.1.4}$$

Transforming the independent variable to mass through the continuity equation $dm = \rho 4\pi r^2 dr$

$$\frac{\partial T}{\partial m} = -\frac{3\kappa L}{64\pi^2 ac\, r^4 T^3}, \tag{A.1.5}$$

and then using the equation for hydrostatic equilibrium

$$\frac{\partial p}{\partial m} = -\frac{Gm}{4\pi r^4}, \tag{A.1.6}$$

to change the independent variable again to pressure this time

$$\frac{\partial T}{\partial p} = \frac{3\kappa L}{16\pi ac\, GmT^3}. \tag{A.1.7}$$

Finally, using the nabla notation introduced in Eq. 2.1.9, and switching out the luminosity for flux again, the radiative flux can be expressed in terms of the radiative temperature gradient, ∇_{rad},

$$F_r = \frac{4ac\, GmT^4}{3\kappa p r^2}\nabla_{rad}. \tag{A.1.8}$$

A.2 Turbulent Kinetic Energy Equation

The Eulerian equation of turbulent kinetic energy can be written as (eq. A12 of Meakin and Arnett 2007*b*):

$$\partial_t\left(\rho E_k\right) + \boldsymbol{\nabla}\cdot\left(\rho E_k \boldsymbol{v}\right) = -\boldsymbol{v}\cdot\boldsymbol{\nabla}p + \rho\,\boldsymbol{v}\cdot\boldsymbol{g}, \tag{A.2.1}$$

where v is the velocity and $E_k = \frac{1}{2}(v\cdot v)$ is the specific kinetic energy.

Applying horizontal and temporal averaging to the above equation yields the mean turbulent kinetic energy equation, which can be written as

$$\overline{\langle \rho \mathbf{D_t} E_k \rangle} = - \boldsymbol{\nabla} \cdot \overline{\langle \mathbf{F_p} + \mathbf{F_k} \rangle} + \overline{\langle \mathbf{W_p} \rangle} + \overline{\langle \mathbf{W_b} \rangle} - \epsilon_k, \tag{A.2.2}$$

where E_k is the kinetic energy (KE);

$\mathbf{D_t} = \partial_t + \boldsymbol{\nabla} \cdot \mathbf{u}$ is the material derivative;

$\mathbf{F_p} = p'\mathbf{u}'$ is the turbulent pressure flux;

$\mathbf{F_k} = \rho E_k \mathbf{u}'$ is the TKE flux;

$\mathbf{W_p} = p' \boldsymbol{\nabla} \cdot \mathbf{u}'$ is the pressure dilatation;

$\mathbf{W_b} = \rho' \mathbf{g} \cdot \mathbf{u}'$ is the work due to buoyancy; and

ϵ_k is the numerical dissipation of KE.

A.3 Stellar Model Profile Fitting

The entropy (s), average atomic mass ($\bar{A}$) and average atomic number ($\bar{Z}$) were remapped by considering five distinct sections of the domain. The lower stable region (below the lower convective boundary), the convective region and the upper stable region (above the upper boundary) were fitted linearly in the form $\alpha + \beta\, x$, where α and β are constants, and x is the radius on a grid point. The two remaining sections are the upper and lower convective boundaries; these were fitted using sigmoid functions, f_{sig}, of the form

$$f_{sig} = \theta + \frac{\phi - \theta}{1 + e^{\,\eta\, z}}, \tag{A.3.1}$$

where θ, ϕ and η are constants, and z is a normalised grid index. The fitting constants for the three variables are presented in Table A.3; the subscripts for each constant represent the section of the domain for which the fit refers to. Subscripts $1, 2, 3$ denote the lower stable, convective and upper stable sections, respectively. Subscripts l and u refer to the lower and upper convective boundary sections, respectively.

Variable	Lower stable		Lower boundary			Convective		Upper boundary			Upper stable	
	α_1	β_1	θ_l	ϕ_l	η_l	α_2	β_2	θ_u	ϕ_u	η_u	α_3	β_3
s	1.65×10^8	0.24	2.81×10^8	3.43×10^8	-0.5	3.43×10^8	0	3.43×10^8	3.56×10^8	-0.5	3.56×10^8	0.08
$\bar{A}$	18.17	0	18.17	16.19	0.5	16.19	0	16.19	14.38	0.5	14.38	0
$\bar{Z}$	9.07	0	9.07	8.08	0.5	8.08	0	8.08	7.18	0.5	7.18	0

Table A.1: Constants used in the fitting functions (Eq. A.3.1) for the five sections of the entropy, $\bar{A}$ and $\bar{Z}$ profiles. Subscripts $1, 2$ and 3 refer to the lower stable, convective and upper stable sections, respectively. Subscripts l and u refer to the lower and upper convective boundary sections, respectively.

Appendix B

Additional information

B.1 Other hydrodynamic simulations

Here is a non-exhaustive list of some of the studies that have used the piecewise parabolic method to model stellar fluids: Arnett, Fryxell and Müller (1989); Fryxell, Arnett and Müller (1991); Shankar, Arnett and Fryxell (1992); Arnett and Livne (1994); Ruffert and Arnett (1994); Arnett (1994); Shankar and Arnett (1994); Bazan and Arnett (1994); Chen, Porter and Woodward (1994); Bazán and Arnett (1997); Kane et al. (1997); Bazán and Arnett (1998); Nelson et al. (1998); Jacobs, Porter and Woodward (1999); Kane, Arnett, Remington, Glendinning, Bazán, Müller, Fryxell and Teyssier (2000); Kane, Arnett, Remington, Glendinning, Bazan, Drake and Fryxell (2000); Porter and Woodward (2000); Mercer, Blondin and De Pree (2003); Meakin and Arnett (2007*b*); Herwig et al. (2007, 2011); Viallet et al. (2013); Herwig et al. (2014); Woodward, Herwig and Lin (2015); Cristini et al. (2016*a*); Jones et al. (2017).

B.2 Computational costs

The following table lists the computational costs required to run each model presented in this thesis. These costs are in units of 10^3 CPU-hrs, where 1 CPU-hr is equivalent to using one CPU (not necessarily at 100% of its resources) for one continuous hour. Hence, when using thousands of cores at one time for a single calculation, the accrued cost can be significant.

Model	lrez	mrez	hrez	vhrez	eps1	eps33	eps100	eps333	eps1k	eps3k	eps10k	eps33k	**Total**
CPU cost (kCPU-hrs)	1.4	22.6	511.0	1026.0	563.0	569.0	424.1	136.6	225.6	477.5	282.8	293.0	**4532.6**

Table B.1: Computational costs for the lrez, mrez, hrez, vhrez, eps1, eps33, eps100, eps333, eps1k, eps3k, eps10k and eps33k models in units of kCPU-hrs.

B.3 Glossary of acronyms

The following two tables list the various acronyms used throughout the thesis and their meanings.

Acronym	Definition
2D	Two-dimensional
3D	Three-dimensional
AGB	Asymptotic giant branch
AIAA	American institute of aeronautics and astronautics
APOGEE	Apache Point observatory galactic evolution experiment
BH	Black hole
CBM	Convective boundary mixing
CC-SN	Core-collapse supernova
CFL	Courant-Friedrichs-Lewy
CPU	Central processing unit
DNS	Direct numerical simulation
EC-SN	Electron capture supernova
ELT	Extremely large telescope
EOS	Equation of state
FLOPS	Floating point operations per second
FRANEC	Frascati Raphson Newton evolutionary code
FVM	Finite-volume method
GAIA	Global astrometric interferometer for astrophysics
GENEC	Geneva stellar evolution code
GPU	Graphics processing unit
HRD	Hertzsprung-Russell diagram
ILES	Implicit large eddy simulation
ISM	Inter-stellar medium
JWST	James-Webb space telescope
KE	Kinetic energy

Table B.2: Table listing all of the acronyms used throughout the thesis and their definitions.

Acronym	Definition
KH	Kelvin-Helmholtz
LES	Large eddy simulation
LIGO	Laser interferometer gravitational-wave observatory
LSST	Large synoptic survey telescope
MESA	Modules for experiments in stellar astrophysics
MLT	Mixing length theory
MPI	Message passing interface
NACRE	Nuclear astrophysics compilation of reaction rates
NIF	National ignition facility
NS	Neutron star
OPAL	Opacity project at Livermore
PARSEC	Padova and Trieste stellar evolution code
PPM	Piecewise parabolic method
PROMPI	Prometheus MPI
RANS	Reynolds-averaged Navier-Stokes
RMS	Root mean square
RSG	Red super giant
SGS	Sub-grid scale
SN	Supernova
TKE	Turbulent kinetic energy
UNIVAC	Universal automatic computer
V&V	Verification and validation
WD	White dwarf
YREC	Yale rotating stellar evolution code
ZAMS	Zero-age main sequence

Table B.3: Continuation table listing all of the acronyms used throughout the thesis and their definitions.

Appendix C

Publications and other dissemination methods

Refereed publications

1. **A. Cristini**, C. Meakin, R. Hirschi, D. Arnett, C. Georgy, M. Viallet and I. Walkington. "3D Hydrodynamic Simulations of Carbon Burning in Massive Stars." Submitted to MNRAS Oct 2016, accepted for publication Jun 2017.

2. **A. Cristini**, C. Meakin, R. Hirschi, D. Arnett, C. Georgy and M. Viallet. "Linking 1D evolutionary to 3D hydrodynamical simulations of massive stars." Physica Scripta 91(3):034006. (2016)

Other publications

1. **A. Cristini**, R. Hirschi, C. Georgy, C. Meakin, D. Arnett and M. Viallet, "The First 3D Simulations of Carbon Burning in a Massive Star", IAUS, 329 (2017; in press)

2. R. Hirschi, D. Arnett, **A. Cristini**, C. Georgy, C. Meakin and I. Walkington, "Progenitors of Core-Collapse Supernovae", IAUS, 331 (2017; in press)

3. **A. Cristini**, R. Hirschi, C. Georgy, C. Meakin, D. Arnett and M. Viallet, "Linking 1D Stellar Evolution to 3D Hydrodynamic Simulations", IAUS, 307:98-99 (2015)

4. R. Hirschi, J. den Hartogh, **A. Cristini**, C. Georgy and M. Pignatari, "Stellar structure, evolution and nucleosynthesis", PoS(NIC XIII)001 (2014)

In preparation for submission to a refereed journal

A. Cristini, C. Meakin, R. Hirschi, D. Arnett, C. Georgy, M. Viallet and I. Walkington. "3D Hydrodynamic Simulations of Carbon Burning within the Context of a Luminosity Study." To be submitted to MNRAS.

Talks

1. Stellar Hydro Days IV, Canada. Jun 2017.
2. IAUS 329 - The Lives and Death-throes of Massive Stars, New Zealand. Dec 2016.
3. BRIDGCE Workshop, UK. Sep 2016.
4. Asteroseismology and Stellar Evolution Workshop, UK. Dec 2014.
5. BRIDGCE Workshop, UK. Sep 2014.
6. Turbulent Mixing and Beyond Workshop, Italy. Aug 2014.
7. Nucleosynthesis in AGB stars, Germany. July 2014.
8. 17th Workshop on Nuclear Astrophysics, Germany. Apr 2014.

Posters

1. Dirac Day, UK. Sep 2016.
2. IAUS 307 - New Windows on Massive Stars, Switzerland. Jun 2014.

Appendix D

Bibliography

Abramovici, A., W. E. Althouse, R. W. P. Drever, Y. Gursel, S. Kawamura, F. J. Raab, D. Shoemaker, L. Sievers, R. E. Spero and K. S. Thorne. 1992. "LIGO - The Laser Interferometer Gravitational-Wave Observatory." *Science* 256:325–333.

Aerts, C., J. Christensen-Dalsgaard and D. W. Kurtz. 2010. *Asteroseismology*.

AIAA. 1998. *Guide: Guide for the Verification and Validation of Computational Fluid Dynamics Simulations (AIAA G-077-1998(2002))*. Reston, VA.

Alexander, D. R. and J. W. Ferguson. 1994. "Low-temperature Rosseland opacities." *ApJ* 437:879–891.

Almgren, A. S., J. B. Bell and M. Zingale. 2007. "MAESTRO: A Low Mach Number Stellar Hydrodynamics Code." *Journal of Physics Conference Series* 78(1):012085.

Angulo, C., M. Arnould, M. Rayet, P. Descouvemont, D. Baye, C. Leclercq-Willain, A. Coc, S. Barhoumi, P. Aguer, C. Rolfs, R. Kunz, J. W. Hammer, A. Mayer, T. Paradellis, S. Kossionides, C. Chronidou, K. Spyrou, S. degl'Innocenti, G. Fiorentini, B. Ricci, S. Zavatarelli, C. Providencia, H. Wolters, J. Soares, C. Grama, J. Rahighi, A. Shotter and M. Lamehi Rachti. 1999. "A compilation of charged-particle induced thermonuclear reaction rates." *Nuclear Physics A* 656:3–183.

Arnett, D. 1994. "Oxgen-burning hydrodynamics. 1: Steady shell burning." *ApJ* 427:932–946.

Arnett, D. 1996. *Supernovae and Nucleosynthesis: An Investigation of the History of Matter from the Big Bang to the Present*.

Arnett, D., B. Fryxell and E. Müller. 1989. "Instabilities and nonradial motion in SN 1987A." *ApJ* 341:L63–L66.

Arnett, D., C. Meakin and P. A. Young. 2009. "Turbulent Convection in Stellar Interiors. II. The Velocity Field." *ApJ* 690:1715–1729.

Arnett, D. and E. Livne. 1994. "The delayed-detonation model of a type IA supernovae. 1: The deflagration phase." *ApJ* 427:315–329.

Arnett, David. 2016. Private communication. University of Arizona.

Arnett, W. D. and C. Meakin. 2011*a*. "Toward Realistic Progenitors of Core-collapse Supernovae." *ApJ* 733:78.

Arnett, W. D. and C. Meakin. 2011*b*. "Turbulent Cells in Stars: Fluctuations in Kinetic Energy and Luminosity." *ApJ* 741:33.

Arnett, W. D., C. Meakin, M. Viallet, S. W. Campbell, J. C. Lattanzio and M. Mocák. 2015. "Beyond Mixing-length Theory: A Step Toward 321D." *ApJ* 809:30.

Asida, S. M. and D. Arnett. 2000. "Further Adventures: Oxygen Burning in a Convective Shell." *ApJ* 545:435–443.

Audouze, J., C. Chiosi and S. E. Woosley. 1986. Nucleosynthesis and chemical evolution. In *Saas-Fee Advanced Course 16: Nucleosynthesis and Chemical Evolution*, ed. J. Audouze, C. Chiosi and S. E. Woosley.

Bardina, J., J. H. Ferziger and W. C. Reynolds. 1980. Improved subgrid-scale models for large-eddy simulation. In *American Institute of Aeronautics and Astronautics, Fluid and Plasma Dynamics Conference, 13th, Snowmass, Colo., July 14-16, 1980, 10 p.*, ed. J. Bardina, J. H. Ferziger and W. C. Reynolds.

Battino, U., M. Pignatari, C. Ritter, F. Herwig, P. Denisenkov, J. W. Den Hartogh, R. Trappitsch, R. Hirschi, B. Freytag, F. Thielemann and B. Paxton. 2016. "Application of a Theory and Simulation-based Convective Boundary Mixing Model for AGB Star Evolution and Nucleosynthesis." *ApJ* 827:30.

Bazan, G. and D. Arnett. 1994. "Convection, nucleosynthesis, and core collapse." *ApJ* 433:L41–L43.

Bazán, G. and D. Arnett. 1997. "Large Nuclear Networks in Presupernova Models." *Nuclear Physics A* 621:607–610.

Bazán, G. and D. Arnett. 1998. "Two-dimensional Hydrodynamics of Pre–Core Collapse: Oxygen Shell Burning." *ApJ* 496:316–332.

Beaudet, G., V. Petrosian and E. E. Salpeter. 1967. "Energy Losses due to Neutrino Processes." *ApJ* 150:979.

Bersten, M. C., O. G. Benvenuto, G. Folatelli, K. Nomoto, H. Kuncarayakti, S. Srivastav, G. C. Anupama, R. Quimby and D. K. Sahu. 2014. "iPTF13bvn: The First Evidence of a Binary Progenitor for a Type Ib Supernova." *AJ* 148:68.

Bertelli, G., E. Nasi, L. Girardi and P. Marigo. 2009. "Scaled solar tracks and isochrones in a large region of the Z-Y plane. II. From 2.5 to 20 solar mass stars." *A&A* 508:355–369.

Boehly, T. R., R. S. Craxton, T. H. Hinterman, J. H. Kelly, T. J. Kessler, S. A. Kumpan, S. A. Letzring, R. L. McCrory, S. F. B. Morse, W. Seka, S. Skupsky, J. M. Soures and C. P. Verdon. 1995. "The upgrade to the OMEGA laser system." *Review of Scientific Instruments* 66:508–510.

Böhm-Vitense, E. 1958. "Über die Wasserstoffkonvektionszone in Sternen verschiedener Effektivtemperaturen und Leuchtkräfte. Mit 5 Textabbildungen." *Z. Astrophys.* 46:108.

Boldyrev, S. and F. Cattaneo. 2004. "Magnetic-Field Generation in Kolmogorov Turbulence." *Physical Review Letters* 92(14):144501.

Bressan, A., P. Marigo, L. Girardi, B. Salasnich, C. Dal Cero, S. Rubele and A. Nanni. 2012. "PARSEC: stellar tracks and isochrones with the PAdova and TRieste Stellar Evolution Code." *MNRAS* 427:127–145.

Brocchini, M., R. Bernetti, A. Mancinelli and G. Albertini. 2001. "An efficient solver for nearshore flows based on the WAF method." *Coastal Engineering* 43(2):105 – 129.

Brott, I., S. E. de Mink, M. Cantiello, N. Langer, A. de Koter, C. J. Evans, I. Hunter, C. Trundle and J. S. Vink. 2011. "Rotating massive main-sequence stars. I. Grids of evolutionary models and isochrones." *A&A* 530:A115.

Calder, A. C., N. T. Taylor, K. Antypas, D. Sheeler and A. Dubey. 2006. A Case Study of Verifying and Validating an Astrophysical Simulation Code. In *Numerical Modeling of Space Plasma Flows*, ed. G. P. Zank and N. V. Pogorelov. Vol. 359 of *Astronomical Society of the Pacific Conference Series* p. 119.

Canuto, V. M., I. Goldman and I. Mazzitelli. 1996. "Stellar Turbulent Convection: A Self-consistent Model." *ApJ* 473:550.

Canuto, V. M. and I. Mazzitelli. 1991. "Stellar turbulent convection - A new model and applications." *ApJ* 370:295–311.

Castellani, V., P. Giannone and A. Renzini. 1971. "Overshooting of Convective Cores in Helium-Burning Horizontal-Branch Stars." *Ap&SS* 10:340–349.

Chandrasekhar, S. 1931. "The highly collapsed configurations of a stellar mass." *MNRAS* 91:456–466.

Chandrasekhar, S. 1967. *An introduction to the study of stellar structure*.

Chassaing, P. 2002. *Variable density fluid turbulence*. Kluwer Academic Publishers.

Chatzopoulos, E., C. Graziani and S. M. Couch. 2014. "Characterizing the Convective Velocity Fields in Massive Stars." *ApJ* 795:92.

Chemel, C., C. Staquet and J.-P. Chollet. 2010. "Estimating the diffusive heat flux across a stable interface forcednewpage by convective motions." *Nonlinear Processes in Geophysics* 17:187–200.

Chen, H., D. H. Porter and P. R. Woodward. 1994. 3D High Resolution Simulation of Stellar Convection. In *American Astronomical Society Meeting Abstracts #184*. Vol. 26 of *Bulletin of the American Astronomical Society* p. 926.

Chieffi, A. and M. Limongi. 2013. "Pre-supernova Evolution of Rotating Solar Metallicity Stars in the Mass Range 13-120 M and their Explosive Yields." *ApJ* 764:21.

Choi, J., A. Dotter, C. Conroy, M. Cantiello, B. Paxton and B. D. Johnson. 2016. "Mesa Isochrones and Stellar Tracks (MIST). I. Solar-scaled Models." *ApJ* 823:102.

Christensen-Dalsgaard, Jørgen. 2003. "Stellar Oscillations." University Lecture. Aarhus University.

Clark, R. A., J. H. Ferziger and W. C. Reynolds. 1979. "Evaluation of subgrid-scale models using an accurately simulated turbulent flow." *Journal of Fluid Mechanics* 91:1–16.

Colella, P. and P. R. Woodward. 1984. "The Piecewise Parabolic Method (PPM) for Gas-Dynamical Simulations." *J. Comput. Phys.* 54:174–201.

Couch, S. M., E. Chatzopoulos, W. D. Arnett and F. X. Timmes. 2015. "The Three-dimensional Evolution to Core Collapse of a Massive Star." *ApJ* 808:L21.

Courant, R., K. Friedrichs and H. Lewy. 1928. "Über die partiellen Differenzengleichungen der mathematischen Physik." *Mathematische Annalen* 100:32–74.

Cristini, A., C. Meakin, R. Hirschi, D. Arnett, C. Georgy and M. Viallet. 2016*a*. "3D Hydrodynamic Simulations of Carbon Burning in Massive Stars." *ArXiv e-prints* .

Cristini, A., C. Meakin, R. Hirschi, D. Arnett, C. Georgy and M. Viallet. 2016*b*. "Linking 1D evolutionary to 3D hydrodynamical simulations of massive stars." *Phys. Scr.* 91(3):034006.

Cyburt, R. H., A. M. Amthor, R. Ferguson, Z. Meisel, K. Smith, S. Warren, A. Heger, R. D. Hoffman, T. Rauscher, A. Sakharuk, H. Schatz, F. K. Thielemann and M. Wiescher. 2010. "The JINA REACLIB Database: Its Recent Updates and Impact on Type-I X-ray Bursts." *ApJS* 189:240–252.

de Jager, C., H. Nieuwenhuijzen and K. A. van der Hucht. 1988. "Mass loss rates in the Hertzsprung-Russell diagram." *A&AS* 72:259–289.

Deardorff, J. W. 1980. "Stratocumulus-capped mixed layers derived from a three-dimensional model." *Boundary-Layer Meteorology* 18:495–527.

Decressin, T., S. Mathis, A. Palacios, L. Siess, S. Talon, C. Charbonnel and J.-P. Zahn. 2009. "Diagnoses to unravel secular hydrodynamical processes in rotating main sequence stars." *A&A* 495:271–286.

Demarque, P., D. B. Günther, L. H. Li, A. Mazumdar and C. W. Straka. 2008. "YREC: the Yale rotating stellar evolution code. Non-rotating version, seismology applications." *Ap&SS* 316:31–41.

Denissenkov, P. A. and C. A. Tout. 2003. "Partial mixing and formation of the ^{13}C pocket by internal gravity waves in asymptotic giant branch stars." *MNRAS* 340:722–732.

Denissenkov, P. A., F. Herwig, J. W. Truran and B. Paxton. 2013. "The C-flame Quenching by Convective Boundary Mixing in Super-AGB Stars and the Formation of Hybrid C/O/Ne White Dwarfs and SN Progenitors." *ApJ* 772:37.

Denissenkov, P. A., F. Herwig, L. Bildsten and B. Paxton. 2013. "MESA Models of Classical Nova Outbursts: The Multicycle Evolution and Effects of Convective Boundary Mixing." *ApJ* 762:8.

Deupree, R. G. 1976. "Nonlinear convective motion in shallow convective envelopes." *ApJ* 205:286–294.

Dongarra, J. 2014. *Performance of Various Computers Using Standard Linear Equations Software.*

Dore, V., M. Moroni, M. Le Menach and A. Cenedese. 2009. "Investigation of penetrative convection in stratified fluids through 3D-PTV." *Experiments in Fluids* 47:811–825.

Durst, F. and B. Ünsal. 2006. "Forced laminar-to-turbulent transition of pipe flows." *Journal of Fluid Mechanics* 560:449–464.

Eggenberger, P., G. Meynet, A. Maeder, R. Hirschi, C. Charbonnel, S. Talon and S. Ekström. 2008. "The Geneva stellar evolution code." *Ap&SS* 316:43–54.

Ekström, S., C. Georgy, P. Eggenberger, G. Meynet, N. Mowlavi, A. Wyttenbach, A. Granada, T. Decressin, R. Hirschi, U. Frischknecht, C. Charbonnel and A. Maeder.

2012. "Grids of stellar models with rotation. I. Models from 0.8 to 120 $M_\odot$ at solar metallicity (Z = 0.014)." *A&A* 537:A146.

Ergma, E. and E. P. J. van den Heuvel. 1998. "On the initial progenitor masses of stellar mass black holes and neutron stars." *A&A* 331:L29–L32.

Ertl, T., H.-T. Janka, S. E. Woosley, T. Sukhbold and M. Ugliano. 2016. "A Two-parameter Criterion for Classifying the Explodability of Massive Stars by the Neutrino-driven Mechanism." *ApJ* 818:124.

Eymard, R., T. Gallouët and R. Herbin. 2003. "Finite volume method." *Handbook of Numerical Analysis* 7:713–1020.

Fedorovich, E., R. Conzemius and D. Mironov. 2004. "Convective Entrainment into a Shear-Free, Linearly Stratified Atmosphere: Bulk Models Reevaluated through Large Eddy Simulations." *J. Atmos. Sci.* 61:281.

Fernando, H. J. S. 1991. "Turbulent mixing in stratified fluids." *Annual Review of Fluid Mechanics* 23:455–493.

Fewell, M. P. 1995. "The atomic nuclide with the highest mean binding energy." *American Journal of Physics* 63:653–658.

Fleming, S. W., S. Mahadevan, R. Deshpande, C. F. Bender, R. C. Terrien, R. C. Marchwinski, J. Wang, A. Roy, K. G. Stassun, C. Allende Prieto, K. Cunha, V. V. Smith, E. Agol, H. Ak, F. A. Bastien, D. Bizyaev, J. R. Crepp, E. B. Ford, P. M. Frinchaboy, D. A. García-Hernández, A. E. García Pérez, B. S. Gaudi, J. Ge, F. Hearty, B. Ma, S. R. Majewski, S. Mészáros, D. L. Nidever, K. Pan, J. Pepper, M. H. Pinsonneault, R. P. Schiavon, D. P. Schneider, J. C. Wilson, O. Zamora and G. Zasowski. 2015. "The APOGEE Spectroscopic Survey of Kepler Planet Hosts: Feasibility, Efficiency, and First Results." *AJ* 149:143.

Frey, W., R. Schofield, P. M. Hoor, F. Ravegnani, A. Ulanovsky, S. Viciani, F. D'Amato and T. P. Lane. 2014. "The impact of deep overshooting convection on the water vapour and trace gas distribution in the TTL and lower stratosphere." *AGU Fall Meeting Abstracts* .

Freytag, B., H.-G. Ludwig and M. Steffen. 1996. "Hydrodynamical models of stellar convection. The role of overshoot in DA white dwarfs, A-type stars, and the Sun." *A&A* 313:497–516.

Frischknecht, U., R. Hirschi, G. Meynet, S. Ekström, C. Georgy, T. Rauscher, C. Winteler and F.-K. Thielemann. 2010. "Constraints on rotational mixing from surface evolution of light elements in massive stars." *A&A* 522:A39.

Fryxell, B., D. Arnett and E. Müller. 1991. "Instabilities and clumping in SN 1987A. I - Early evolution in two dimensions." *ApJ* 367:619–634.

Fryxell, B., E. Müller and D. Arnett. 1989. Computation of multi-dimensional flows with non-uniform composition. In *Nuclear Astrophysics*, ed. W. Hillebrandt and E. Müller. p. 100.

Fryxell, B., K. Olson, P. Ricker, F. X. Timmes, M. Zingale, D. Q. Lamb, P. MacNeice, R. Rosner, J. W. Truran and H. Tufo. 2000. "FLASH: An Adaptive Mesh Hydrodynamics Code for Modeling Astrophysical Thermonuclear Flashes." *ApJS* 131:273–334.

Fuller, J., M. Cantiello, D. Lecoanet and E. Quataert. 2015. "The Spin Rate of Pre-collapse Stellar Cores: Wave-driven Angular Momentum Transport in Massive Stars." *ApJ* 810:101.

Gabriel, M., A. Noels, J. Montalbán and A. Miglio. 2014. "Proper use of Schwarzschild Ledoux criteria in stellar evolution computations." *A&A* 569:A63.

Gaia Collaboration, T. Prusti, J. H. J. de Bruijne, A. G. A. Brown, A. Vallenari, C. Babusiaux, C. A. L. Bailer-Jones, U. Bastian, M. Biermann and D. W. et al. Evans. 2016. "The Gaia mission." *A&A* 595:A1.

Garay, G. and S. Lizano. 1999. "Massive Stars: Their Environment and Formation." *PASP* 111:1049–1087.

Garcia, J. and J. Mellado. 2014. "The two-layer structure of the entrinament zone in the convective boundary layer." *J. Atmos. Sci.* pp. 1935–1955.

Gardner, J. P., J. C. Mather, M. Clampin, R. Doyon, M. A. Greenhouse, H. B. Hammel, J. B. Hutchings, P. Jakobsen, S. J. Lilly, K. S. Long, J. I. Lunine, M. J. McCaughrean, M. Mountain, J. Nella, G. H. Rieke, M. J. Rieke, H.-W. Rix, E. P. Smith, G. Sonneborn, M. Stiavelli, H. S. Stockman, R. A. Windhorst and G. S. Wright. 2006. "The James Webb Space Telescope." *SSRv* 123:485–606.

Garnier, E., N. Adams and P. Sagaut. 2009. *Large Eddy Simulation for Compressible Flows*.

Gastine, T., J. Wicht and J. M. Aurnou. 2015. "Turbulent Rayleigh-Bénard convection in spherical shells." *J. Fluid Mech.* 778:721–764.

Georgy, C., H. Saio and G. Meynet. 2014. "The puzzle of the CNO abundances of α Cygni variables resolved by the Ledoux criterion." *MNRAS* 439:L6–L10.

Ghosal, S. 1996. "An Analysis of Numerical Errors in Large-Eddy Simulations of Turbulence." *Journal of Computational Physics* 125:187–206.

Gilet, C., A. S. Almgren, J. B. Bell, A. Nonaka, S. E. Woosley and M. Zingale. 2013. "Low Mach Number Modeling of Core Convection in Massive Stars." *ApJ* 773:137.

Gilmozzi, R. and J. Spyromilio. 2007. "The European Extremely Large Telescope (E-ELT)." *The Messenger* 127.

Godunov, S.K. 1959. "Eine Differenzenmethode für die Näherungsberechnung unstetiger Lösungen der hydrodynamischen Gleichungen." *Mat. Sb., Nov. Ser.* 47:271–306.

Godunov, S.K., A.V. Zabrodin and G.P. Prokopov. 1962. "A computational scheme for two-dimensional non stationary problems of gas dynamics and calculation of the flow from a shock wave approaching a stationary state." *USSR Computational Mathematics and Mathematical Physics* 1(4):1187 – 1219.

Graboske, H. C., H. E. Dewitt, A. S. Grossman and M. S. Cooper. 1973. "Screening Factors for Nuclear Reactions. II. Intermediate Screen-Ing and Astrophysical Applications." *ApJ* 181:457–474.

Grinstein, F., L. Margolin and W. Rider. 2007. *Implicit Large Eddy Simulation - Computing Turbulent Fluid Dynamics.*

Hansen, C. J. and S. D. Kawaler. 1994. *Stellar Interiors. Physical Principles, Structure, and Evolution.*

Heger, A., N. Langer and S. E. Woosley. 2000. "Presupernova Evolution of Rotating Massive Stars. I. Numerical Method and Evolution of the Internal Stellar Structure." *ApJ* 528:368–396.

Heger, A., S. E. Woosley, C. L. Fryer and N. Langer. 2003. Massive Star Evolution Through the Ages. In *From Twilight to Highlight: The Physics of Supernovae*, ed. W. Hillebrandt and B. Leibundgut. p. 3.

Henyey, L. G., J. E. Forbes and N. L. Gould. 1964. "A New Method of Automatic Computation of Stellar Evolution." *ApJ* 139:306.

Henyey, L. G., L. Wilets, K. H. Böhm, R. Lelevier and R. D. Levee. 1959. "A Method for Automatic Computation of Stellar Evolution." *ApJ* 129:628.

Henyey, L. G., R. Lelevier and R. D. Levee. 1959. "Evolution of Main-Sequence Stars." *ApJ* 129:2.

Herwig, F. 2000. "The evolution of AGB stars with convective overshoot." *A&A* 360:952–968.

Herwig, F., B. Freytag, T. Fuchs, J. P. Hansen, R. M. Hückstädt, D. H. Porter, F. X. Timmes and P. R. Woodward. 2007. Convective and Non-Convective Mixing in AGB Stars. In *Why Galaxies Care About AGB Stars: Their Importance as Actors and Probes*, ed. F. Kerschbaum, C. Charbonnel and R. F. Wing. Vol. 378 of *Astronomical Society of the Pacific Conference Series* p. 43.

Herwig, F., M. Pignatari, P. R. Woodward, D. H. Porter, G. Rockefeller, C. L. Fryer, M. Bennett and R. Hirschi. 2011. "Convective-reactive Proton-^{12}C Combustion in Sakurai's Object (V4334 Sagittarii) and Implications for the Evolution and Yields from the First Generations of Stars." *ApJ* 727:89.

Herwig, F., P. R. Woodward, P.-H. Lin, M. Knox and C. Fryer. 2014. "Global Non-spherical Oscillations in Three-dimensional 4π Simulations of the H-ingestion Flash." *ApJ* 792:L3.

Iglesias, C. A. and F. J. Rogers. 1996. "Updated Opal Opacities." *ApJ* 464:943.

Itoh, N., H. Hayashi, A. Nishikawa and Y. Kohyama. 1996. "Neutrino Energy Loss in Stellar Interiors. VII. Pair, Photo-, Plasma, Bremsstrahlung, and Recombination Neutrino Processes." *ApJS* 102:411.

Itoh, N., T. Adachi, M. Nakagawa, Y. Kohyama and H. Munakata. 1989. "Neutrino energy loss in stellar interiors. III - Pair, photo-, plasma, and bremsstrahlung processes." *ApJ* 339:354–364.

Ivezić, Z., J. A. Tyson, B. Abel, E. Acosta, R. Allsman, Y. AlSayyad, S. F. Anderson, J. Andrew, R. Angel, G. Angeli, R. Ansari, P. Antilogus, K. T. Arndt, P. Astier, E. Aubourg, T. Axelrod, D. J. Bard, J. D. Barr, A. Barrau, J. G. Bartlett, B. J. Bauman, S. Beaumont, A. C. Becker, J. Becla, C. Beldica, S. Bellavia, G. Blanc, R. D. Blandford, J. S. Bloom, J. Bogart, K. Borne, J. F. Bosch, D. Boutigny, W. N. Brandt, M. E. Brown, J. S. Bullock, P. Burchat, D. L. Burke, G. Cagnoli, D. Calabrese, S. Chandrasekharan, S. Chesley, E. C. Cheu, J. Chiang, C. F. Claver, A. J. Connolly, K. H. Cook, A. Cooray, K. R. Covey, C. Cribbs, W. Cui, R. Cutri, G. Daubard, G. Daues, F. Delgado, S. Digel, P. Doherty, R. Dubois, G. P. Dubois-Felsmann, J. Durech, M. Eracleous, H. Ferguson, J. Frank, M. Freemon, E. Gangler, E. Gawiser, J. C. Geary, P. Gee, M. Geha, R. R. Gibson, D. K. Gilmore, T. Glanzman, I. Goodenow, W. J. Gressler, P. Gris, A. Guyonnet, P. A. Hascall, J. Haupt, F. Hernandez, C. Hogan, D. Huang, M. E. Huffer, W. R. Innes, S. H. Jacoby, B. Jain, J. Jee, J. G. Jernigan, D. Jevremovic, K. Johns, R. L. Jones, C. Juramy-Gilles, M. Juric, S. M. Kahn, J. S. Kalirai, N. Kallivayalil, B. Kalmbach, J. P. Kantor, M. M. Kasliwal, R. Kessler, D. Kirkby, L. Knox, I. Kotov, V. L. Krabbendam, S. Krughoff, P. Kubanek, J. Kuczewski, S. Kulkarni, R. Lambert, L. Le Guillou, D. Levine, M. Liang, K. Lim, C. Lintott, R. H. Lupton, A. Mahabal, P. Marshall, S. Marshall, M. May, R. McKercher, M. Migliore, M. Miller, D. J. Mills, D. G. Monet, M. Moniez, D. R. Neill, J. Nief, A. Nomerotski, M. Nordby, P. O'Connor, J. Oliver, S. S. Olivier,

K. Olsen, S. Ortiz, R. E. Owen, R. Pain, J. R. Peterson, C. E. Petry, F. Pierfederici, S. Pietrowicz, R. Pike, P. A. Pinto, R. Plante, S. Plate, P. A. Price, M. Prouza, V. Radeka, J. Rajagopal, A. Rasmussen, N. Regnault, S. T. Ridgway, S. Ritz, W. Rosing, C. Roucelle, M. R. Rumore, S. Russo, A. Saha, B. Sassolas, T. L. Schalk, R. H. Schindler, D. P. Schneider, G. Schumacher, J. Sebag, G. H. Sembroski, L. G. Seppala, I. Shipsey, N. Silvestri, J. A. Smith, R. C. Smith, M. A. Strauss, C. W. Stubbs, D. Sweeney, A. Szalay, P. Takacs, J. J. Thaler, R. Van Berg, D. Vanden Berk, K. Vetter, F. Virieux, B. Xin, L. Walkowicz, C. W. Walter, D. L. Wang, M. Warner, B. Willman, D. Wittman, S. C. Wolff, W. M. Wood-Vasey, P. Yoachim, H. Zhan and for the LSST Collaboration. 2008. "LSST: from Science Drivers to Reference Design and Anticipated Data Products." *ArXiv e-prints* .

Jacobs, M. L., D. H. Porter and P. R. Woodward. 1999. Three Dimensional Computational Simulations of Convection in AGB Stars. In *American Astronomical Society Meeting Abstracts*. Vol. 31 of *Bulletin of the American Astronomical Society* p. 1447.

Jones, S., R. Andrassy, S. Sandalski, A. Davis, P. Woodward and F. Herwig. 2017. "Idealized hydrodynamic simulations of turbulent oxygen-burning shell convection in 4π geometry." *MNRAS* 465:2991–3010.

Jones, S., R. Hirschi, K. Nomoto, T. Fischer, F. X. Timmes, F. Herwig, B. Paxton, H. Toki, T. Suzuki, G. Martínez-Pinedo, Y. H. Lam and M. G. Bertolli. 2013. "Advanced Burning Stages and Fate of 8-10 M Stars." *ApJ* 772:150.

Jones, S., R. Hirschi, M. Pignatari, A. Heger, C. Georgy, N. Nishimura, C. Fryer and F. Herwig. 2015. "Code dependencies of pre-supernova evolution and nucleosynthesis in massive stars: evolution to the end of core helium burning." *MNRAS* 447:3115–3129.

Jones, S. W. 2014. Evolution of electron capture supernova progenitors: new models, improved nuclear physics and hydrodynamic mixing uncertainties. PhD thesis Keele Univ., (2014).

Jonker, Harm J. J., Maarten van Reeuwijk, Peter P. Sullivan and Edward G. Patton. 2013. "On the scaling of shear-driven entrainment: a DNS study." *Journal of Fluid Mechanics* 732:150–165.

Kane, J., D. Arnett, B. A. Remington, S. G. Glendinning, G. Bazán, E. Müller, B. A. Fryxell and R. Teyssier. 2000. "Two-dimensional versus Three-dimensional Supernova Hydrodynamic Instability Growth." *ApJ* 528:989–994.

Kane, J., D. Arnett, B. A. Remington, S. G. Glendinning, G. Bazan, R. P. Drake and B. A. Fryxell. 2000. "Supernova Experiments on the Nova Laser." *ApJS* 127:365–369.

Kane, J., D. Arnett, B. A. Remington, S. G. Glendinning, J. Castor, R. Wallace, A. Rubenchik and B. A. Fryxell. 1997. "Supernova-relevant Hydrodynamic Instability Experiments on the Nova Laser." *ApJ* 478:L75–L78.

Käppeler, F., R. Gallino, S. Bisterzo and W. Aoki. 2011. "The s process: Nuclear physics, stellar models, and observations." *Reviews of Modern Physics* 83:157–194.

Kippenhahn, R., A. Weigert and A. Weiss. 2013. *Stellar Structure and Evolution*.

Kippenhahn, R., A. Weigert and E. Hofmeister. 1967. "Methods for Calculating Stellar Evolution." *Methods in Computational Physics* 7:129–190.

Kolmogorov, A. 1941. "The Local Structure of Turbulence in Incompressible Viscous Fluid for Very Large Reynolds' Numbers." *DoSSR* 30:301–305.

Kolmogorov, A. N. 1962. "A refinement of previous hypotheses concerning the local structure of turbulence in a viscous incompressible fluid at high Reynolds number." *Journal of Fluid Mechanics* 13:82–85.

Kuhlen, M., W. E. Woosley and G. A. Glatzmaier. 2003. 3D Anelastic Simulations of Convection in Massive Stars. In *3D Stellar Evolution*, ed. S. Turcotte, S. C. Keller and R. M. Cavallo. Vol. 293 of *Astronomical Society of the Pacific Conference Series* p. 147.

Kuranz, C. C., H.-S. Park, B. A. Remington, R. P. Drake, A. R. Miles, H. F. Robey, J. D. Kilkenny, C. J. Keane, D. H. Kalantar, C. M. Huntington, C. M. Krauland, E. C. Harding, M. J. Grosskopf, D. C. Marion, F. W. Doss, E. Myra, B. Maddox, B. Young, J. L. Kline, G. Kyrala, T. Plewa, J. C. Wheeler, W. D. Arnett, R. J. Wallace, E. Giraldez and A. Nikroo. 2011. "Astrophysically relevant radiation hydrodynamics experiment at the National Ignition Facility." *Ap&SS* 336:207–211.

Kurucz, R. L. 1991. New Opacity Calculations. In *NATO Advanced Science Institutes (ASI) Series C*, ed. L. Crivellari, I. Hubeny and D. G. Hummer. Vol. 341 of *NATO Advanced Science Institutes (ASI) Series C* p. 441.

Langer, N., J.-P. Arcoragi and M. Arnould. 1989. "Neutron capture nucleosynthesis and the evolution of 15 and 30 solar-mass stars. I - The core helium burning phase." *A&A* 210:187–197.

Large, W. G., J. C. McWilliams and S. C. Doney. 1994. "Oceanic vertical mixing: A review and a model with a nonlocal boundary layer parameterization." *Reviews of Geophysics* 32:363–403.

Lautrup, B. 2011. *Physics of Continuous Matter: Exotic and Everyday Phenomena in the Macroscopic World*. CRC press.

Ledoux, P. 1947. "Stellar Models with Convection and with Discontinuity of the Mean Molecular Weight." *ApJ* 105:305.

Liu, Y. and R. E. Ecke. 2011. "Local temperature measurements in turbulent rotating Rayleigh-Bénard convection." *Phys. Rev. E* 84(1):016311.

Lorenz, E. N. 1963. "Deterministic Nonperiodic Flow." *J. Atmos. Sci.* 20:130–148.

Maeder, A. 2009. *Physics, Formation and Evolution of Rotating Stars*.

Maeder, A. and G. Meynet. 2010. "Evolution of massive stars with mass loss and rotation." *NewAR* 54:32–38.

Maeder, A., G. Meynet, N. Lagarde and C. Charbonnel. 2013. "The thermohaline, Richardson, Rayleigh-Taylor, Solberg-Høiland, and GSF criteria in rotating stars." *A&A* 553:A1.

Martins, F. and A. Palacios. 2013. "A comparison of evolutionary tracks for single Galactic massive stars." *A&A* 560:A16.

Meakin, C. A. and D. Arnett. 2006. "Active Carbon and Oxygen Shell Burning Hydrodynamics." *ApJ* 637:L53–L56.

Meakin, C. A. and D. Arnett. 2007*a*. "Anelastic and Compressible Simulations of Stellar Oxygen Burning." *ApJ* 665:690–697.

Meakin, C. A. and D. Arnett. 2007*b*. "Turbulent Convection in Stellar Interiors. I. Hydrodynamic Simulation." *ApJ* 667:448–475.

Mercer, A., J. Blondin and C. G. De Pree. 2003. Hydrodynamic Simulations of Ultracompact HII Regions. In *American Astronomical Society Meeting Abstracts*. Vol. 36 of *Bulletin of the American Astronomical Society* p. 592.

Miernik, J., G. Statham, L. Fabisinski, C. D. Maples, R. Adams, T. Polsgrove, S. Fincher, J. Cassibry, R. Cortez, M. Turner and T. Percy. 2013. "Z-Pinch fusion-based nuclear propulsion." *Acta Astron.* 82:173–182.

Mocák, M., L. Siess and E. Müller. 2011. "Multidimensional hydrodynamic simulations of the hydrogen injection flash." *A&A* 533:A53.

Moroni, M. and A. Cenedese. 2006. "Penetrative convection in stratified fluids: velocity and temperature measurements." *Nonlinear Processes in Geophysics* 13:353–363.

Müller, B. and H.-T. Janka. 2015. "Non-radial instabilities and progenitor asphericities in core-collapse supernovae." *MNRAS* 448:2141–2174.

Müller, B., M. Viallet, A. Heger and H.-T. Janka. 2016. "The Last Minutes of Oxygen Shell Burning in a Massive Star." *ApJ* 833:124.

Nelson, A. F., W. Benz, F. C. Adams and D. Arnett. 1998. "Dynamics of Circumstellar Disks." *ApJ* 502:342–371.

Nieva, M.-F. and N. Przybilla. 2014. "Fundamental properties of nearby single early B-type stars." *A&A* 566:A7.

Nishimura, N., T. Fischer, F.-K. Thielemann, C. Fröhlich, M. Hempel, R. Käppeli, G. Martínez-Pinedo, T. Rauscher, I. Sagert and C. Winteler. 2012. "Nucleosynthesis in Core-collapse Supernova Explosions Triggered by a Quark-Hadron Phase Transition." *ApJ* 758:9.

Nomoto, K., C. Kobayashi and N. Tominaga. 2013. "Nucleosynthesis in Stars and the Chemical Enrichment of Galaxies." *ARA&A* 51:457–509.

O'Connor, E. and C. D. Ott. 2011. "Black Hole Formation in Failing Core-Collapse Supernovae." *ApJ* 730:70.

Pavelyev, A. A., A. I. Reshmin, S. Kh. Teplovodskii and S. G. Fedoseev. 2003. "On the Lower Critical Reynolds Number for Flow in a Circular Pipe." *Fluid Dynamics* 38(4):545–551.

Paxton, B., L. Bildsten, A. Dotter, F. Herwig, P. Lesaffre and F. Timmes. 2011. "Modules for Experiments in Stellar Astrophysics (MESA)." *ApJS* 192:3.

Phillips, A. C. 1999. *The Physics of Stars, 2nd Edition*.

Pignatari, M., F. Herwig, R. Hirschi, M. Bennett, G. Rockefeller, C. Fryer, F. X. Timmes, C. Ritter, A. Heger, S. Jones, U. Battino, A. Dotter, R. Trappitsch, S. Diehl, U. Frischknecht, A. Hungerford, G. Magkotsios, C. Travaglio and P. Young. 2016. "NuGrid Stellar Data Set. I. Stellar Yields from H to Bi for Stars with Metallicities Z = 0.02 and Z = 0.01." *ApJS* 225:24.

Pignatari, M., R. Gallino, M. Heil, M. Wiescher, F. Käppeler, F. Herwig and S. Bisterzo. 2010. "The Weak s-Process in Massive Stars and its Dependence on the Neutron Capture Cross Sections." *ApJ* 710:1557–1577.

Porter, D. H. and P. R. Woodward. 2000. "Three-dimensional Simulations of Turbulent Compressible Convection." *ApJS* 127:159–187.

Porter, D. H., P. R. Woodward and A. Pouquet. 1998. "Inertial range structures in decaying compressible turbulent flows." *Physics of Fluids* 10:237–245.

Radice, D., C. D. Ott, E. Abdikamalov, S. M. Couch, R. Haas and E. Schnetter. 2016. "Neutrino-driven Convection in Core-collapse Supernovae: High-resolution Simulations." *ApJ* 820:76.

Rauscher, T. and F.-K. Thielemann. 2000. "Astrophysical Reaction Rates From Statistical Model Calculations." *Atomic Data and Nuclear Data Tables* 75:1–351.

Renzini, A. 1987. "Some embarrassments in current treatments of convective overshooting." *A&A* 188:49–54.

Reynolds, O. 1883. "An Experimental Investigation of the Circumstances Which Determine Whether the Motion of Water Shall Be Direct or Sinuous, and of the Law of Resistance in Parallel Channels." *Royal Society of London Philosophical Transactions Series I* 174:935–982.

Richardson, L. F. 1922. "Weather prediction by numerical processes." *Quarterly Journal of the Royal Meteorological Society* 48(203):282–284.

Rogers, F. J., F. J. Swenson and C. A. Iglesias. 1996. "OPAL Equation-of-State Tables for Astrophysical Applications." *ApJ* 456:902.

Ruffert, M. and D. Arnett. 1994. "Three-dimensional hydrodynamic Bondi-Hoyle accretion. 2: Homogeneous medium at Mach 3 with gamma = 5/3." *ApJ* 427:351–376.

Salpeter, E. E. 1955. "The Luminosity Function and Stellar Evolution." *ApJ* 121:161.

San, O., A. E. Staples, Z. Wang and T. Iliescu. 2011. "Approximate deconvolution large eddy simulation of a barotropic ocean circulation model." *Ocean Modelling* 40:120–132.

Schaller, G., D. Schaerer, G. Meynet and A. Maeder. 1992. "New grids of stellar models from 0.8 to 120 solar masses at Z = 0.020 and Z = 0.001." *A&AS* 96:269–331.

Schwarzschild, K. 1992. *Gesammelte Werke Vol.1, Vol.2, Vol.3.*

Shankar, A. and D. Arnett. 1994. "Thermonuclear runaways in nova outbursts. 2: Effect of strong, instantaneous, local fluctuations." *ApJ* 433:216–228.

Shankar, A., D. Arnett and B. A. Fryxell. 1992. "Thermonuclear runaways in nova outbursts." *ApJ* 394:L13–L15.

Shu, F. H. 1992. *The physics of astrophysics. Volume II: Gas dynamics.*

Siess, L. and M. L. Pumo. 2006. "Evolutionary properties of massive AGB stars." *Mem. Soc. Astron. Ital.* 77:822.

Simpson, C. M., G. L. Bryan, C. Hummels and J. P. Ostriker. 2015. "Kinetic Energy from Supernova Feedback in High-resolution Galaxy Simulations." *ApJ* 809:69.

Stevens, B. and D. H. Lenschow. 2001. "Observations, Experiments, and Large Eddy Simulation." *Bulletin of the American Meteorological Society* 82:283–294.

Stothers, R. B. and C.-W. Chin. 1991. "Metal opacities and convective core overshooting in Population I stars." *ApJ* 381:L67–L70.

Sullivan, P. P., C.-H. Moeng, B. Stevens, D. H. Lenschow and S. D. Mayor. 1998. "Structure of the Entrainment Zone Capping the Convective Atmospheric Boundary Layer." *J. Atmos. Sci.* 55:3042–3064.

Sullivan, P. P. and E. G. Patton. 2011. "The Effect of Mesh Resolution on Convective Boundary Layer Statistics and Structures Generated by Large-Eddy Simulation." *J. Atmos. Sci.* 68:2395–2415.

Sytine, I. V., D. H. Porter, P. R. Woodward, S. W. Hodson and K.-H. Winkler. 2000. "Convergence Tests for the Piecewise Parabolic Method and Navier-Stokes Solutions for Homogeneous Compressible Turbulence." *Journal of Computational Physics* 158:225–238.

Tayar, J., G. Somers, M. H. Pinsonneault, D. Stello, A. Mints, J. A. Johnson, O. Zamora, D. A. García-Hernández, C. Maraston, A. Serenelli, C. Allende Prieto, F. A. Bastien, S. Basu, J. C. Bird, R. E. Cohen, K. Cunha, Y. Elsworth, R. A. García, L. Girardi, S. Hekker, J. Holtzman, D. Huber, S. Mathur, S. Mészáros, B. Mosser, M. Shetrone, V. Silva Aguirre, K. Stassun, G. S. Stringfellow, G. Zasowski and A. Roman-Lopes. 2017. "The Correlation Between Mixing Length and Metallicity on the Giant Branch: Implications for Ages in the Gaia Era." *ArXiv e-prints* .

Timmes, F. X. and D. Arnett. 1999. "The Accuracy, Consistency, and Speed of Five Equations of State for Stellar Hydrodynamics." *ApJS* 125:277–294.

Timmes, F. X. and F. D. Swesty. 2000. "The Accuracy, Consistency, and Speed of an Electron-Positron Equation of State Based on Table Interpolation of the Helmholtz Free Energy." *ApJS* 126:501–516.

Todini, P. and A. Ferrara. 2001. "Dust formation in primordial Type II supernovae." *MNRAS* 325:726–736.

Toro, Eleuterio F. 1999. *Riemann Solvers and Numerical Methods for Fluid Dynamics: A Practical Introduction*. Springer.

Turner, J. S. 1973. *Buoyancy Effects in Fluids*.

Turner, J. S. 1986. "Turbulent entrainment - The development of the entrainment assumption, and its application to geophysical flows." *Journal of Fluid Mechanics* 173:431–471.

van Dyke, M. 1982. "An album of fluid motion." *NASA STI/Recon Technical Report A* 82.

van Reeuwijk, M., G. R. Hunt and H. J. Jonker. 2011. Direct simulation of turbulent entrainment due to a plume impinging on a density interface. In *Journal of Physics Conference Series*. Vol. 318 of *Journal of Physics Conference Series* p. 042061.

Viallet, M., C. Meakin, D. Arnett and M. Mocák. 2013. "Turbulent Convection in Stellar Interiors. III. Mean-field Analysis and Stratification Effects." *ApJ* 769:1.

Viallet, M., C. Meakin, V. Prat and D. Arnett. 2015. "Toward a consistent use of overshooting parametrizations in 1D stellar evolution codes." *A&A* 580:A61.

Viallet, Maxime. 2015. Private communication. Max-Planck-Institut für Astrophysik.

Vink, J. S., A. de Koter and H. J. G. L. M. Lamers. 2001. "Mass-loss predictions for O and B stars as a function of metallicity." *A&A* 369:574–588.

Wanajo, S., Y. Sekiguchi, N. Nishimura, K. Kiuchi, K. Kyutoku and M. Shibata. 2014. "Production of All the r-process Nuclides in the Dynamical Ejecta of Neutron Star Mergers." *ApJ* 789:L39.

Winteler, C., R. Käppeli, A. Perego, A. Arcones, N. Vasset, N. Nishimura, M. Liebendörfer and F.-K. Thielemann. 2012. "Magnetorotationally Driven Supernovae as the Origin of Early Galaxy r-process Elements?" *ApJ* 750:L22.

Wood, D. O. S. and E. Churchwell. 1989. "The morphologies and physical properties of ultracompact H II regions." *ApJS* 69:831–895.

Woodward, P. R., F. Herwig and P.-H. Lin. 2015. "Hydrodynamic Simulations of H Entrainment at the Top of He-shell Flash Convection." *ApJ* 798:49.

Woosley, S. E., A. Heger and T. A. Weaver. 2002. "The evolution and explosion of massive stars." *Rev. Mod. Phys.* 74:1015–1071.

Woosley, S. and T. Janka. 2005. "The physics of core-collapse supernovae." *Nature Physics* 1:147–154.

Yakovlev, D. G. and D. A. Shalybkov. 1989. "Degenerate Cores of White Dwarfs and Envelopes of Neutron Stars - Thermodynamics and Plasma Screening in Thermonuclear Reactions." *Astrophysics and Space Physics Reviews* 7:311.

Young, P. A., C. Meakin, D. Arnett and C. L. Fryer. 2005. "The Impact of Hydrodynamic Mixing on Supernova Progenitors." *ApJ* 629:L101–L104.

Zahn, J.-P. 1991. "Convective penetration in stellar interiors." *A&A* 252:179–188.